UNIVERSITE DE NICE-SOPHIA ANTIPOLIS - UFR Sciences
Ecole Doctorale Sciences Fondamentales et Appliquees
ONERA - Office National d'Etudes et Recherches Aerospatiales

Ph.D. DISSERTATION

In Partial Fulfilment of the Requirements for the
Degree of Doctor of Philosophy of the University of Nice-Sophia Antipolis

Presented by
Noah SCHWARTZ

Precompensation of turbulence effects by adaptive optics: application to free-space optics

Ph.D Supervisor
Julien BORGNINO

Publically Presented on the 17th of December 2009 before the jury composed of:

M. Julien BORGNINO	Ph.D Supervisor
M. Vincent MICHAU	Ph.D Supervisor
M. Claude AMRA	Reviewer
M. Alain BARTHELEMY	Reviewer
M. Mikhail VORONTSOV	Member
M. Frederic CHAZALLET	Member
Mme Marie-Therere VELLUET	Invited

WARNING: THIS DOCUMENT IS A TRANSLATION. PLEASE REFER TO THE ORIGINAL DOCUMENT FOR QUOTATION

Résumé

En propagation endo-atmosphérique et sur des longues distances (supérieure à quelques kilomètres), les effets de la turbulence atmosphérique sont importants pour les liaisons de télécommunication optique en espace libre (LOA). Le champ de l'onde subit des perturbations de phase qui modulent l'intensité reçue par le récepteur, dans des proportions pouvant être rédhibitoires pour la fiabilité de la liaison. La précompensation du champ émis à l'aide d'une optique adaptative (OA) a été proposée afin de limiter cet effet et de permettre d'augmenter la distance de propagation ainsi que le débit des LOA. L'objectif de cette thèse est d'évaluer les performances et les limites, en termes d'efficacité vis-à-vis des LOA, des différentes méthodes de corrections par OA et d'étudier la possibilité de concepts plus efficaces.

Nous avons montré qu'une approche itérative de correction de phase et d'amplitude - qualifiée de correction optimale - permet d'atteindre des performances excellentes, la meilleure parmi les approches proposées jusque-là. L'étude de cette approche théorique, nous a permis de fixer les limites de l'apport d'un système d'OA et de montrer que la correction a encore un intérêt largement au-delà de la limite des faibles perturbations.

Dans le régime de fortes turbulences, nous montrons les limites des approches classiques - OA par mesure de front d'onde (ASO), par modulation de phase ou itérative de phase (qualifiée de sous-optimale) - notamment à cause de la scintillation, des enroulements de phase et de la présence de bruit de mesure. Nous avons quantifié la baisse de leurs performances vis-à-vis de la correction optimale et proposé une solution permettant de s'affranchir des effets de la scintillation sur la mesure de front d'onde. Nous avons finalement proposé un dispositif pour la précompensation de phase et d'amplitude et plus particulièrement de la mesure et de la commande qui devrait permettre de mettre en oeuvre la correction optimale.

Mots-clés : OPTIQUE ADAPTATIVE - TÉLÉCOMMUNICATION OPTIQUE - PROPAGATION OPTIQUE - CORRECTION EN FORTES PERTURBATIONS.

Abstract

Effects of atmospheric turbulence, on long distance endo-atmospheric propagation (over a few miles), can be seriously detrimental to free-space optical communications (FSO). The field of the optical wave undergoes phase perturbations that modulate the received intensity. These perturbations can seriously afflict FSO reliability. Precompensation by adaptive optics (AO) has been proposed to mitigate these effects and enable the possibility to increase propagation distance and data throughput. The purpose of this thesis is to evaluate the performance and limitations, in terms of FSO effectiveness, of different AO correction methods and to study the possibility of more efficient concepts.

We demonstrate that a phase and amplitude iterative correction approach - latter described as optimal correction - enables excellent performance, among the best so far proposed. The study of this theoretical approach enables us to set boundaries to the effectiveness of AO system. We showed that an efficient correction can be achieved greatly beyond the weak perturbation regime.

In strong turbulence, it appears that classical approaches - AO by wavefront measurement, phase modulation or iterative phase correction (described as sub-optimal) - are limited. These limitations are due to scintillation, phase branch points and noise. We quantify the drop of performance relative to the optimal correction and propose a solution enabling the minimization of scintillation effects on phase measurements. We finally propose a method to precompensation for phase and amplitude and in particular for measurement and control, that should enable the implementation of the optimal correction.

Keywords: ADAPTIVE OPTICS - OPTICAL COMMUNICATIONS - OPTICAL PROPAGATION - CORRECTION IN STRONG TURBULENCE.

Warning

This document is a translation. Please refer to the original document (in French) presented to the University of Nice-Sophia Antipolis in partial fulfillment of the requirements for the degree of doctor of philosophy.

Contents

List of Figures

Table of Acronyms and Abbreviations

Table of Physical Parameters:

Name	Definition
C_n^2	Index of refraction structure function
D	Telescope diameter
$\mathcal{F}_d(x,y)$	Fresnel propagator over distance d
$\mathcal{G}_{1\to 2}$	Propagation through turbulence from point 1 to point 2
I	Intensity or irradiance
J	Objective function
λ	Wavelength
L_F	Fresnel distance ($\sqrt{\lambda L}$)
L	Total propagation distance
l_0	Turbulence inner scale
L_0	Turbulence outer scale
$\mathcal{P}$	Telescope pupil
r_0	Fried parameter
ρ_0	Coherence distance of an electromagnetic wave
σ_R^2	Rytov variance ($1.23k^2C_n^2L^{11/6}$)
$V_\perp$	Transverse wind speed
W_x	3D spectral power density of variable x
z	Distance in the plan transverse to the propagation direction
ψ	Complex electromagnetic field
φ	Phase of the electromagnetic field
χ	Log-amplitude of the electromagnetic field

Table of Abbreviations:

Name	Definition
AO	Adaptive Optics
APD	Avalanche photodiode
BER	Bit Error Rate
CoG	Centre of gravity
DM	Deformable Mirror
D-SPGD	Decoupled Stochastic Parallel Gradient Descent
f_e	Sampling frequency
FSO	Free-Space Optics
FORTUNE43G	Free Space Optical Receiver and Transmitter UNit Evaluation for 3G
FoV	Field of view
FW	Full-wave
FWHM	Full Width at Half Maximum
IDL	Interactive Data Language
IR	Infrared
ONERA	Office National d'Etudes et de Recherches Aerospatiales
OOK	On-Off Keying
PIB	Power In the Bucket
PILOT	Propagation et Imagerie Laser ou Optique a travers la Turbulence
PDF	Power Density Function
PO	Phase Only
PPM	Pulse Position Modulation
RTC	Real Time Computer
SH	Shack-Hartmann
SNR	Signal to Noise Ratio
SPGD	Stochastic Parallel Gradient Descent
T_1	Telescope number 1 of the FSO system
T_2	Telescope number 2 of the FSO system
WFS	Wavefront Sensor

General Introduction

La maturité de l'homme, c'est d'avoir retrouvé le sérieux qu'on avait au jeu quand on était enfant.

"Par-delà le bien et le mal"
Friedrich Nietzsche

Many factors contribute to the development and expansion of free-space optical communications sytems: their implementation simplicity, their high-data throughput or the fact that the infrastructure involved is cheaper than for optical fibers. However, as propagation distance increases, atmospheric turbulence reduces the quality of the link. Turbulence induces random laser beam movements, beam spreading and scintillation that disrupts communications. Despite the great advantage offered by free-space optical communication systems, perturbations introduced by the atmosphere limit both propagation distances and throughput.

In 1953 was proposed the first concept to correct for atmospheric turbulence using adaptive optics [Babcock-a-53], helping to increase the quality of astronomy images. At the time technical difficulties, especially in terms of computing power, delayed the expansion of such correction techniques. Today most major telescopes in the world are equipped with adaptive optics systems. Exploration of the solar system and the need to communicate with spacecrafts, particularly within the Strategic Defense Initiative (SDI) project, motivated the implementation of devices capable of transmitting data from ground to space. Throughput, power and size are essential features for such systems. Laser communications can meet these demanding requirements. In free-space optical communication systems, atmospheric turbulence notably reduces mean received flux. It can lead to a total disappearance of the signal and has great temporal variability. Bit-error-rate becomes much higher than in the absence of turbulence, which can be incompatible with classical link objectives in terms of throughput, error rate and permanency. One possible solution is to reduce these effects by using adaptive optics (AO). AO consists in measuring phase perturbations and correcting them by means of a deformable mirror. The correction is used to concentrate and stabilise the flux at the reception. Fante [Fried-a-72, Fante-p-75] was one of the first to suggest AO to solve the issue of transmitting information from ground to space. This method is particularly adapted to this specific configuration. Atmospheric turbulence is concentrated near the ground-based telescope and correction of the emitted electromagnetic field can be limited to phase. A deformable mirror is typically used to correct phase perturbations.

In the case of horizontal propagations (either for imaging or laser communications), turbulence is distributed along the optical path. Correction strategies using AO systems have also

been developed [Primmerman-a-95, Vorontsov-a-97] to cope with these particular perturbations distribution. However, the use of a single deformable mirror is usually insufficient and the exploitation of more mirrors needs to be investigated to control both phase and amplitude of the field [Primmerman-a-95]. Unfortunately, diffractive effects make the control of the second mirror difficult. A linear model for the control is no longer adapted. Firstly, when phase perturbations distributed over the volume are sufficiently strong, amplitude fluctuations of the field can disrupt wavefront measurements [Mahe-p-00, Voitsekhovich-a-01]. In addition, phase discontinuities appear in the field [Fried-a-92], making correction by a continuous deformable mirror problematic.

In order to dissociate control and correction issues, we will first limit our study to a theoretical approach of phase and amplitude correction. I first studied chapter 6, an approach initially proposed by Barchers [Barchers-a-02-a, Barchers-a-02-b]. The control consists in an iterative method leading to a correction he describes as optimal. He suggested the correction principle and studied its contribution in weak perturbations. His work suggests that pupil truncation has a large impact on the amplitude of the corrected field after propagation over a long distance. In order to understand the performance of the optimal correction in the case of horizontal propagation, we use a multi-layered turbulence propagation model. Barchers′ work is characterised within a larger framework than previously studied (i.e. weak and strong turbulence) using typical free-space optics criterions. Obtained results serve as a reference to test other correction methods. We study the impact of pupil truncation on laser propagation using the optimal correction over all propagation regimes. Propagation regimes are categorised by the overall strength of phase perturbations along the propagation path. To understand the limitations of this approach, we also study the so-called sub-optimal correction. This approach [Barchers-a-02-b] is similar to the optimal correction but this time we limit ourselves to only correcting the phase part of the wave.

The second part the problem focuses on the study and comparison of the optimal and sub-optimal corrections with respect to classical methods used in AO. Corrections are restricted to the phase part of the field. Two mains categories of control applied to the deformable mirror are developed. The first, studied in chapter 7, is based on a linear model of the relation between phase perturbations created by atmospheric turbulence and measurements by a wavefront sensor [Fried-a-72, Fante-p-75]. Unfortunately, this approach gives limited improvements for endo-atmospheric propagations over a long distance where amplitude fluctuations cannot be disregarded. We will study the arrival of such a limitation and propose a simple solution to partially overcome this issue. The second method is based on an iterative control of the deformable mirror by optimising an objective function [Buffington-a-77, Omeara-a-77, Vorontsov-a-97]. This approach does not rely on wavefront measurements and has the advantage to be insensitive to scintillation. Chapter 8, we will study the influence of the algorithm on the correction quality and on convergence time.

We show (chapter 7 and 8) that for most turbulence strengths of interest in free-space optical communication, phase-only correction drastically limits link quality. This restriction leads us to the study (chapter 9) of a practical implementation strategy for the optimal correction enabling phase and amplitude precompensation of the emitted field. The impact of spatial sampling of the field is essential. Several approached were proposed [Primmerman-a-95, Yu-a-04] to modulate

both phase and amplitude but measurement and control are still an issue. We propose in this chapter a practical solution for both measuring and controlling phase and amplitude.

Part I

Context

Chapter 1

Free-Space Optical Communications

Contents

This first chapter briefly introduces the framework of the work presented in the following chapters. Its goal is to put the presented work into perspective by putting it in the larger context of free-space optical communications. We will first present a brief history of atmospheric optical links along with their general properties. In order to further characterise the framework and the challenges created by the propagation channel (i.e. Earth's atmosphere), we will put forth horizontal line-of-sight channels that are close to ground level.

1.1 Optical Communications

1.1.1 History of Optical Communications

It is out of the scope of this paper to write a complete background of the techniques humankind has used throughout history in order to establish communication links using optical signals. Nevertheless, important technical achievements must be highlighted because they establish the principles of todays free-space optical (FSO) systems. For instance, Claude Chappe's

optical telegraph based on the principle of semaphores is of particular importance [Bouchet-l-04]. In 1844, 500 'Chappe tours' cover most important French cities, establishing one of the first optical communication networks.

In addition, Mangin's optical telegraph can be a presented as precursor of today's free-space optical telecommunication systems. It is by many ways comparable to modern systems. Mangin's optical telegraph (see figure 1.1) uses a petrol lamp as the light source in order to create a collimated beam and an obstructer to transmit data using Morse code. A telescope is used to align instruments and to receive the messages.

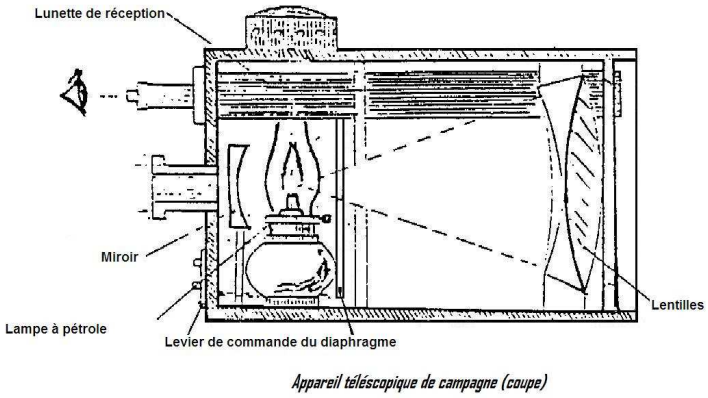

Figure 1.1: Mangin optical telegraph (source: *http ://fortdebourlemont.fr*).

With the invention of the photophone in 1880 (see figure 1.2), Alexandre Graham Bell [Bell-a-1880] demonstrated the efficiency of using optical signals (here the Sun's radiations) for transmitting information. He was able to demonstrate the transmission of voice using intensity modulation over a distance of about 200 m [Killinger-a-02]. The variability of the source (the Sun) and the short propagation distance limited by the detection capability of the receiving system will not allow his invention to become widely used.

The scientific community has been trying, since the $1960s$ and the invention of the laser, to establish FSO communications using optical signals in a line-of-sight configuration. First applications were developed for links to space [Lucy-a-68, Lipsett-a-69]. Unfortunately, the limited live span of lasers, their size and limited luminous power triggered a rapid downfall of this technology.

The arrival in the $1980s$ of semi-conductor lasers having long life expectancies, reduced size and high efficiency enabled laser communication programs both in Europe and in the United States [Begley-p-02] to emerge. Lasers are light sources with a high directivity and power. They enable systems to work at a high signal-to-noise ratio (SNR) when associated with modern detectors. Bell lacked such detectors. We will see in chapter 3, that working with high SNRs is a sine qua none condition to achieve high throughput communication channels. A number of FSO systems were then proposed for numerous scenarios: air-to-air, satellite-to-submarine,

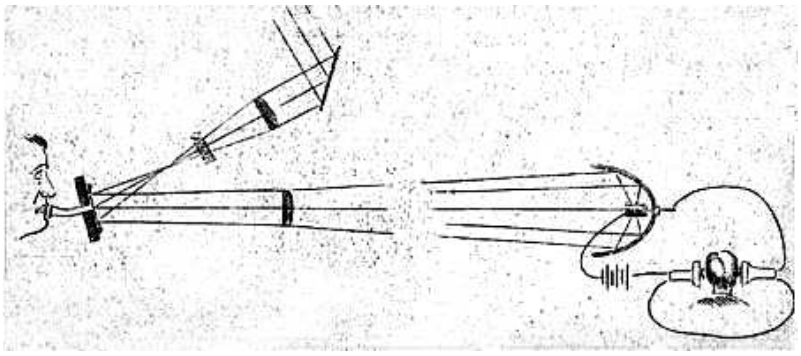

Figure 1.2: Diagram of Graham Bell's photophone (figure from [Breguet-a-1880]). Under the influence of voice, the mirror would change its shape and modulate luminous intensity coming from the sum at the level of the receiver. The receiver made of selenium sees it resistance vary as a function of received luminous intensity enabling the transmission of information.

air-to-submarine, air-to-satellite or satellite-to-satellite. However, most of these programs were abandoned for various reasons: time to market suspected to be too long due to necessary technology development, high cost, and lack of political support favouring other projects deemed a priority.

Since the $1990s$, a high increase in data throughput and technology maturity of components developed for fibre communication systems re-stimulates the development of FSOs. First systems were developed for short distances (typically a few hundred meters) due to variability of the transmission channel induced by the changing atmospheric conditions (rain, aerosols...) and the necessity of having a highly reliable and available link.

1.1.2 Principle and Characteristics of Atmospheric Optical Link

Free-Space Optics (FSO) relies on light propagation through the atmosphere to transmit information between two points. They are generally point-to-point links but point-to-multipoint configurations also exist. The various areas of application (air-to-air, satellite-to-submarine, satellite-to-satellite...) have a great impact on their characteristics and implementation. It is therefore, difficult to have a general description for all FSO systems. In the following chapters, we will focus on air-to-air FSO systems with direct line-of-sight. Figure 1.3 represents a typical point-to-point FSO link between two urban locations. FSOs can usually overcome issues posed by fibre optics systems which are often long and expensive to put in place. Furthermore, such systems do not require any licencing, are immune to interference, are by nature secure (low divergence) and can be full-duplex [1]. The possibility of reaching high data throughputs makes FSO systems also highly competitive with their radio counterpart.

From a conceptual point of view, FSOs only differ from guided optics by the propagation channel. In the case of guided optics, the channel is composed of an emitter-fibre coupler, a fibre

[1] A telecommunication system where information is transmitted in both direction simultaneously.

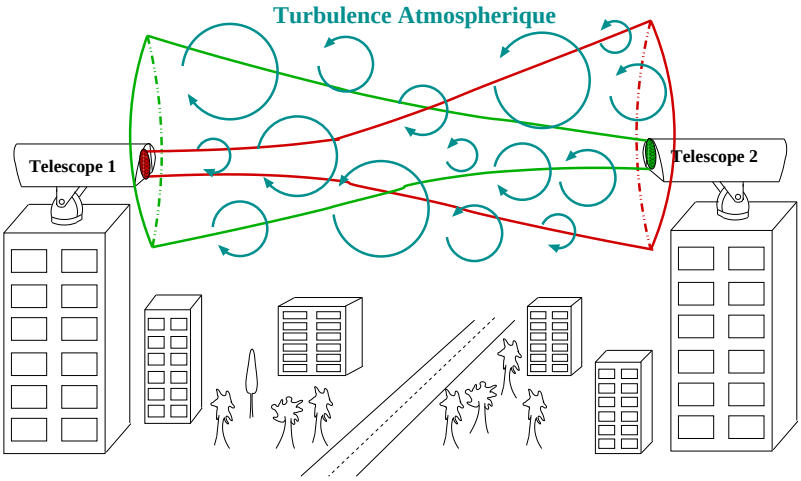

Figure 1.3: Diagram of a atmospheric optical link in a point-to-point configuration between two urban locations. Green and red beams respectively represent one of the communication channels.

and of a fibre-receptor coupler. In the case of free-space optics, the emitter coupler is an optical system (often a telescope) that launches a beam into free-space. After propagating through atmosphere, the beam is coupled into a detector by means of a collecting system optical. FSOs require a full line-of-sight visibility between emitter and receiver. In fiber optics the wavelength must be selected to match the absorption spectra of the fibre. In the same way, for FSO it is imposed by the necessity to minimise atmospheric attenuations. Atmospheric windows in the visible or near infrared are the most used (see paragraph 1.2.3).

In terms of applications, FSOs play an important role in today's last mile systems (local loop). Numerous other applications are envisioned: high-definition television, backbone network for mobiles or high-speed data transfer for temporary links (temporary events, natural disaster ...). These applications typically require an increased propagation range that is inaccessible with currently available systems.

1.1.3 Free-Space Optics Challenges

The numerous advantages gained by using free-space optical links are counterbalanced by the randomness of the propagation channel [Bloom-a-03]. This leads to an increase complexity of communications systems. The main sources of the propagation channel variability are:

- absorption and diffusion by aerosols and precipitation (rain, fog, snow, hail ...) [Bouchet-l-04],
- atmospheric turbulence, that as we will see can make the transmission vary in a very short timescale (typically of the order the millisecond).

Diffusion by aerosols and atmospheric absorption are out of the scope of the following chapters. We will mainly focus on the influence of the optical wave distortions introduced by the

atmosphere namely by atmospheric turbulence. To these two fundamental issues another technological one must be added. It is related to the stabilisation of the optical axis both of the emitting and receiving systems due to thermal and mechanical drifts and vibrations. Depending on the configuration of the link and the desired application, one or the other will be predominant.

1.2 Endo-Atmospheric Optical Links

This document is dedicated to the study of endo-atmospheric optical links with a horizontal line-of-sight. These links constitute a communication channel where both emitter and receiver are within Earth's atmosphere and where atmospheric turbulence will perturb electromagnetic waves propagation. Firstly, this paragraph will focus on short and long range FSO systems, showing several newly established applications. Secondly, we will study the importance of wavelength and discuss the modulation strategy. Finally, we will present the specific application framework studied throughout this document.

1.2.1 Short-Range FSOs

Most systems developed for terrestrial applications have been limited to short propagation distances. As we have seen, these configurations enable the minimisation of the impact of environmental factors related to the transmission channel. As early as 1995, authors [Eardley-p-95] proposed broadband links with 1 Gbit/s over a very short distance (several tens of meters). In order to illustrate the large variety of applications one can see [Wakamori-a-07] for the last mile application. It is a typical example of FSO system for a terrestrial broadband application currently in use in Japan. A number of companies (Shaktiware, AOptix, fSONA, CableFree ...) offer off-the-shelf systems with a typical range limited to between 500 m and a few kilometers. It demonstrates that it is possible to establish a horizontal link over a short-distance with high-bandwidth. The impact of aerosols, atmospheric turbulence, thermal and mechanical drifts are limited for these distances of propagation. It enables the use of small telescopes without the need for complex correction systems such as adaptive optics.

1.2.2 Long-Range FSOs

Some applications require long-distance connexions (e.g. communication between the coast and a boat at sea, between ships, rural or temporary links...). A study of a 61 km link [Giggenbach-p-02] demonstrates the importance of atmospheric turbulence perturbations in FSO systems. For this particular experiment however, the turbulence distribution over the propagation path is favourable. The emitter is located on the top of a mountain where atmospheric turbulence is weaker. In addition, the system is composed of several emitters mitigating turbulence effects. Increasing propagation distance for terrestrial FSOs introduces more perturbations related to atmospheric turbulence and pointing. In order to mitigate these problems and reach high bandwidths, it is possible to increase the size of the receptors (i.e. telescopes). Unfortunately, this leads to very large telescopes, with diameters of a few meters, usually incompatible with typical commercial

applications. Novel solutions are therefore required to reduce the impact of turbulence. Adaptive optics, already applied in astronomy to reduce atmospheric turbulence effects, appears as a possible solution. A 150 km link has been recently successfully demonstrated [Young-p-07] using adaptive optics. Problems related to atmospheric turbulence are nevertheless rather limited at these altitudes (≈ 3000 m) and are not particularly representative of low altitudes optical links. A low altitude communication link [Plett-t-07] above Chesapeake Bay, Maryland, United States, has been established over a distance of 16 km. This link used a modulated retro-reflector to transmit data but only reached a data rate of a few Mbit/s.

1.2.3 Wavelength Selection

Wavelength is an important parameter for atmospheric optical links. Within the transmission window, greater wavelengths (far infrared) have a better atmospheric transmission that the lower ones[Hutchinson-l-08], and that regardless of weather conditions. In addition, higher wavelengths are less degraded by atmospheric turbulence effects. We will see chapter 4.1 that the Fried parameter, which can be used to characterise the strength of perturbations is proportional to $\lambda^{6/5}$.

However, transmission windows do not exist for all wavelengths. Moreover, telecommunication systems require electronics that can work with a high data bandwidth ($\approx$ Gbit/s). This is true for both the source and the detectors. Numerous electronics systems have been developed for fibre optics and wavelengths between $\lambda = 0.8$ µm and 1.5 µm. Technologies at these wavelengths are now mature. For all these reasons (atmospheric transmission, turbulence impact and technology maturity), current systems favour the near infrared, mainly $\lambda = 850$ nm and 1.5 µm.

Optical transmissions in the mid-infrared ($3-5$ µm) [Prasad-l-08] or even the far-infrared up to 10 µm are being studied [Hutchinson-l-08, Manor-a-03]. The far-infrared has a better penetration rate in fog [Achour-a-03], and is up to 2 to 10 times better than near-infrared. Unfortunately, electronics issues for both the source and the detector make the construction of long wavelength FSOs difficult.

1.2.4 Modulation

Most current FSO systems are based on technologies (modulation sources, detectors, demodulators) developed for optical communications using fibre optics. FSO systems typically use On-Off Keying (OOK) modulation that is widely used in fibre optics technology. Other modulation strategies exist and can be used such as the pulse position modulation (PPM) [Wright-a-08]. PPM is more energy efficient then OOK [Xu-p-09] because on-off keying modulation requires more mean energy to achieve the same error rate. However, PPM requires a higher bandwidth and requires accurate synchronisation at the reception [Wilson-p-05] that is more difficult to achieve. In this document we will limit our study assuming OOK modulation.

1.2.5 The Fortune43G Project

Shaktiware launched in September 2008 a collaboration with ONERA, OKO Tech and Turkcell to develop the Fortune43G project. Its objective is to realise a high-bandwidth telecommunication system between two fix stations. These points should typically be separated by a distance of ten kilometers. The goal by the end of the project is to propose a technology solution to transmit in free-space data with a bit-rate higher than the Gbit. The expansion of FSO systems to longer distances will enable the use of this technology for example in wireless networks for the local loop or for mobile telephone infrastructures. One of the desired application is the development of a high-bandwidth communication system that can be used in major natural disasters such as earthquakes [Aljada-p-06] when the normal network is down.

In this project, the wavelength will be set to 1.5 μm. It corresponds to an atmospheric window and is the wavelength choice for fiber based communication systems. For this wavelength and propagation distance, atmospheric turbulence effects cannot be neglected. This is the reason this system shall include adaptive optics. The size of such a system is a major issue and the telescope diameter shall not exceed 30 cm. Field tests are expected by summer 2010 to validate the initial design. Fortune43G will enable by the end of 2010 the development of a full FSO system using adaptive optics. Propagation conditions defined in this project will serve as framework application for this document.

Chapter 2

Optical Propagation through Turbulence

Contents

The work presented in this document is motivated by adaptive optics correction of atmospheric turbulence effects in free-space optics communication systems (FSOCS). This chapter describes perturbations caused by atmospheric turbulence. I will first present the physical phenomenon of turbulence and then introduce typical quantities used to describe effects of optical propagation through turbulence. Propagation model and in particular weak and strong perturbation regimes will be discussed. Secondly, I will introduce the impact of atmospheric turbulence on laser beam propagation. Gaussian beam propagation will serve as the beam model for atmospheric optical communication links.

2.1 Atmospheric Turbulence

In this paragraph, after presenting the physical phenomenon generating optical perturbations (§2.1.1), we will focus on the statistical properties of refraction index fluctuations introduced by atmospheric turbulence (§2.1.2).

2.1.1 Physical Phenomenon

Earth's atmosphere is a combination of gas that is subject to solar radiations on the one hand and radiative transfer coming for the ground on the other. Wind shear in the atmosphere produces turbulent air movements. Following Kolmogorov [Kolmogorov-a-41], the kinetic energy of these vortices is then transmitted to smaller and smaller one (energy cascade theory) until dissipation by viscous friction. Diagram 2.1 illustrates the energy cascade process. These air movements produce in-homogeneities. Statistical properties of index of refraction in-homogeneities follow the statistics of temperature in-homogeneities. It can be shown [Obukhov-a-49] that statistics are governed by Kolmogorov energy cascades.

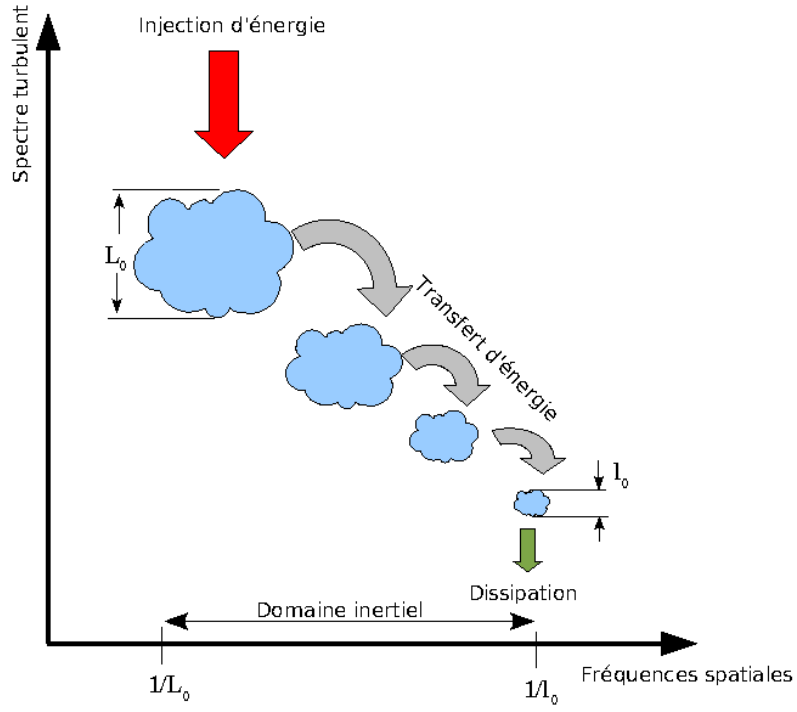

Figure 2.1: Diagram of energy cascade and turbulent cell division in the atmosphere (diagram adapted from [Wheelon-l-01]).

2.1.2 Air Refraction Index

2.1.2.1 Refraction Index Fluctuations

Let $n(\mathbf{r})$ be the refraction index at a point $\mathbf{r}$ in space and $n(\mathbf{r}+\boldsymbol{\rho})$ the refraction index at a distant point $\boldsymbol{\rho}$. Vectors $\mathbf{r}$ and $\boldsymbol{\rho}$ represent respectively a position and a separation distance in a three-dimensional space.

For established turbulent regimes (i.e. temporally and spatially stationary) in the inertial domain, the variance of the difference in refractive index between two points in space (i.e. the structure function) is given by [Obukhov-a-49, Yaglom-a-49]:

$$D_n(\boldsymbol{\rho}) = \left\langle |n(\mathbf{r}) - n(\mathbf{r}+\boldsymbol{\rho})|^2 \right\rangle = C_n^2 \rho^{\frac{2}{3}}, \tag{2.1}$$

where $\langle . \rangle$ represents the ensemble average. $D_n(\mathbf{r})$ is called the index of refraction structure function and C_n^2 is the index of refraction structure constant. C_n^2 is expressed in $\mathrm{m}^{-2/3}$ and $\rho = |\boldsymbol{\rho}|$ in m.

2.1.2.2 Inertial Domain

The inertial domain defines the scales where turbulence is fully developed. It is defines for the larger scale vortices by the turbulence outer-scale L_0 and the smaller ones by turbulence inner-scale l_0. Equation 2.1 is actually only an approximation and valid as long as $\boldsymbol{\rho}$ is smaller than the outer-scale. For large distances $\boldsymbol{\rho}$, indexes $n(\mathbf{r})$ and $n(\mathbf{r}+\boldsymbol{\rho})$ will become completely independent. Following equation 2.1, refraction index fluctuations are then equal to infinity which does not make any physical sense. $D_n(\boldsymbol{\rho})$ is therefore only valid for $l_0 < \boldsymbol{\rho} < L_0$.

2.1.2.3 Inner and Outer Scales

Let us detail inner and outer scales further. The inner-scale $l_0(\mathbf{r},t)$ corresponds to the spatial scale from which the kinetic energy is dissipated into heat by viscous friction. It is therefore, strongly dependant on atmospheric density. $l_0(\mathbf{r},t)$ can vary from a few millimetres near the ground to several centimetres in the tropopause.

Outer-scale $L_0(\mathbf{r},t)$ is conditioned by the size of the physical phenomenon triggering air masses movements and corresponds to the greater macroscopic phenomenon (i.e. air flows, winds, weather perturbations). It sets the lower frequencies amplitudes of the perturbations triggered by turbulence. Only few measurements have been made of the outer-scale in the optical region. Measurements by [Borgnino-a-92, Ziad-a-04] lead to mean values of the order of a few tens of meters. These values present a high temporal and spatial variability. In addition, these measurements were realised for vertical profiles for altitudes higher than a few hundred of meters. Near the grounds, that is for $h < 100\,\mathrm{m}$, we generally consider that $L_0 \propto h$, where h is the altitude over the ground. In this document, we will consider altitudes below 100 meters.

2.1.2.4 Spectral Density of Refractive Index Fluctuations

Another solution to characterise the fluctuations of the index of refraction is to consider the power spectral density. Following the Wiener-Khinchine theorem, the power spectrum of the

Kolmogorov index of refraction spatial fluctuations can be calculated from the structure function by a Fourier transform [Tatarski-l-61]:

$$W_n(\mathbf{f}) = 0.033(2\pi)^{-\frac{2}{3}} C_n^2 f^{-\frac{11}{3}}, \tag{2.2}$$

where f is the spatial frequency modulus expressed in m^{-1}. Kolmogorov spectrum (equation 2.2) is theoretically only valid in the inertial area, that is for: $1/L_0 < f < 1/l_0$. It assumes an inner and outer scales respectively equal to zero and infinity. It also diverges for $f = 0$.

To justify the use of a spectrum over the entire range of frequencies, we can introduce in the Kolmogorov spectrum L_0 and l_0. The introduction of these parameters in the Kolmogorov spectrum leads to the modified von Karman spectrum [Tatarski-l-61] saturating for $f < L_0$ and cutting at $f = l_0$. Its analytical expression is given equation 2.3. This saturation guaranties a spectrum without any singularity to the cost of a currently not properly know parameter L_0. Figure 2.2 shows the von Karman spectrum for various values of L_0 and l_0. All the results shown in this document where obtained using a modified von Karman spectrum.

$$W_n(\mathbf{f}) = 0.033(2\pi)^{-\frac{2}{3}} C_n^2 \left(f^2 + \frac{1}{L_0^2} \right)^{-\frac{11}{6}} e^{-\left(\frac{2\pi l_0}{5.91} f\right)^2}, \; 0 \leq f < \infty \tag{2.3}$$

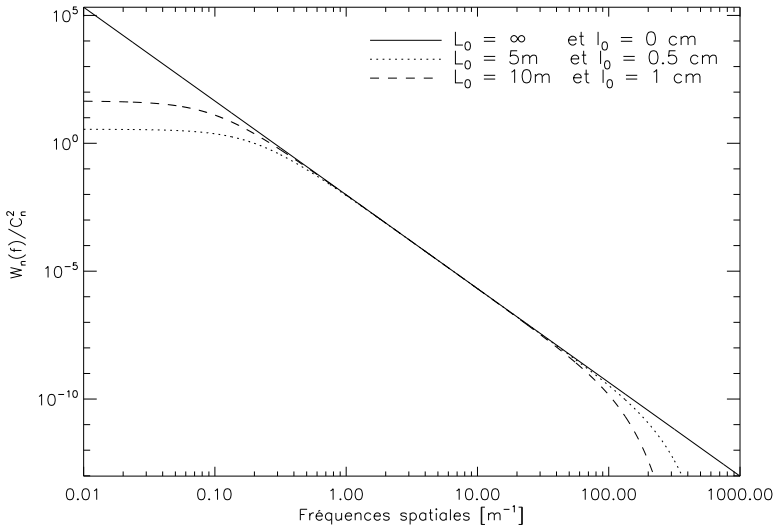

Figure 2.2: Power spectral density of refractive index fluctuations for different values of (l_0, L_0). The spectrums are normalised by the squared structure constant of the index of refraction (C_n^2).

2.1.2.5 C_n^2 Vertical Profile Models

The index of refraction fluctuations structure constant, noted C_n^2, is dependent on a number of meteorological parameters (temperature, humidity, solar radiation) but also on orography

(terrain type and arrangement) [Hufnagel-p-74, Mahe-t-00] and altitude. It has a strong spatial and temporal variability. C_n^2 is a parameter describing turbulence strength distribution along the propagation path. Near ground level (below the first couples of hundreds of meters) thermodynamic atmospheric properties are essentially set by interactions with the ground. Due to these exchanges, optical turbulence is particularly strong in this area, named the planetary boundary layer. For the first few hundred meters above the ground (typical high for low-altitude endo-atmospheric FSO systems), $C_n^2(h)$ can typically vary from $10^{-13}\,\mathrm{m}^{-2/3}$ to $10^{-15}\,\mathrm{m}^{-2/3}$.

Meteorological models, the so-called Monin-Obukhov similitude laws [Monin-a-54], have been proposed for the planetary boundary layer [Wyngaard-a-71] and depend on the stability state of turbulence. These models usually present a dependence on height such as $C_n^2(h) \propto h^{-q}$. q can respectively take the value of $4/3$, $2/3$ of 0 for instable, stable and neutral atmospheric conditions respectively [Mironov-l-81]. Stability is set by the temperature difference between ground and the atmosphere. When the ground is warmer than air, the less dense heated air goes up and is replaced near the ground by colder air. The atmosphere is said to be instable and typically corresponds to terrestrial observations during the day. In the adverse case, the air is warmer then the ground. The atmosphere is stable and typically corresponds to either terrestrial night-time observations or maritime day-time environments.

In the rest of the document, we will use for free-space optical links a constant C_n^2 profile along the propagation path. This is justified by the fact that we will only consider horizontal line-of-sight links. Considering the C_n^2 decrease as a function of altitude (for example $-4/3$ for day-time links), we will be able to determine a ground-level turbulence strength and calculate this strength at the desired altitude for the FSOCS.

2.2 Optical Propagation in Turbulent Media

When an electromagnetic wave with a visible or infrared wavelength propagates through a turbulent media such as the atmosphere, phase and amplitude parts of the electric field are subject to fluctuations. These fluctuations are due to variations in the index of refraction presented in the previous paragraph. Several theoretical approaches have been developed to describe these fluctuations. These theories are generally based on an analytical resolution of the propagation equation. Unfortunately, rigorously solving the propagation equation in the general case, that is for all propagation regimes, is far from simple. This intrinsic difficulty has lead to the development of numerous heuristic theories mainly for strong perturbation regimes.

The perturbed electromagnetic field follows the wave equation. In the case of the atmosphere it can be reduced to the Helmholtz equation (paragraph 2.2.1). First were proposed analytical resolutions based on perturbative methods (paragraph 2.2.3). These methods can in particular, give analytical expressions of certain moments of the electromagnetic field but are limited to weak perturbations only. In order to straightforwardly solve the propagation equations beyond weak perturbations, in strong perturbation regimes (paragraph 2.2.4), we will use a Monte Carlo approach. It consists in using a numerical approximation by splitting up turbulent volume in perturbative phase screens (paragraph 2.2.5). We will use a monochromatic plane wave for the rest of the chapter to describe its properties. Results obtain for a spherical wave are quantita-

tively similar to those obtained for plane waves. Specificities due to the finite size of beams are presented at the end of this chapter (paragraph 2.3).

2.2.1 Electromagnetic Wave Propagation Equations

2.2.1.1 Helmholtz Equation

Propagation of an electromagnetic wave in a dielectric such as air follows Maxwell laws. Considering the oscillation period of the wave as negligible when compared to the time evolution of the index of refraction fluctuations, it can be shown [Tatarski-l-61] that the wave electromagnetic field $\mathbf{E}(\mathbf{r})$ follows the propagation equation:

$$\nabla^2\mathbf{E}(\mathbf{r}) + k_0^2 n(\mathbf{r})^2 \mathbf{E}(\mathbf{r}) + 2\nabla(\mathbf{E}(\mathbf{r}).\nabla(log(n(\mathbf{r})))) = 0, \tag{2.4}$$

where $\mathbf{r} = (x, y, z)$ is a point in space, $n(\mathbf{r})$ the index of refraction, $k_0 = 2\pi/\lambda$ the wave number of the electromagnetic field propagating in the void and $\nabla^2 = \Delta = \partial^2/\partial x^2 + \partial^2/\partial y^2 + \partial^2/\partial z^2$ the Laplacian. It has been shown [Clifford-l-78] that the propagation equation 2.4 can be simplified by neglecting $\nabla(\mathbf{E}(\mathbf{r}).log(n(\mathbf{r})))$. This quantity represents the change in polarisation of the wave as it propagates. It is negligible in visible wavelengths and infrared (IR) because the wavelength λ is extremely small compared to the scale of the index fluctuations [Tatarski-l-71]. Equation 2.4, also called Helmholtz equation, can thus be simplified to:

$$\nabla^2\mathbf{E}(\mathbf{r}) + k_0^2 n(\mathbf{r})^2 \mathbf{E}(\mathbf{r}) = 0 \tag{2.5}$$

The Helmholtz equation 2.5 can be decomposed into three equations, one for each spatial components of the field $\mathbf{E}$ (scalar Helmholtz equation) and can be studied separately.

2.2.1.2 Helmholtz Equation Paraxial Approximation

Let us consider a wave that can be decomposed onto a plane wave basis and propagating in a turbulent media with direction $\vec{e}_z$. Amplitude of the scalar field $E(\mathbf{r})$ can been written as:

$$E(\mathbf{r}) = \psi(\mathbf{r}) e^{ikz}, \tag{2.6}$$

where $\Psi(\mathbf{r})$ represents the complex amplitude of the non-plane part of the wave. The wave propagates in a media of average index of refraction $\langle n\rangle$ where $\langle .\rangle$ is the temporal average. The wave number is $k = \langle n\rangle k_0$. The field $\psi(\mathbf{r})$ is solution to the Helmholtz equation. After development:

$$\nabla^2\Psi(\mathbf{r}) + 2i\langle n\rangle k_0 \frac{\partial\Psi(\mathbf{r})}{\partial z} + k_0\left(n^2 - \langle n\rangle^2\right)\Psi(\mathbf{r}) = 0 \tag{2.7}$$

In the case where spatial variations of Ψ are slow relative to the wavelength, it is possible to neglect $\left|\frac{\partial^2\Psi}{\partial z^2}\right|$ relative to $\left|k\frac{\partial\Psi}{\partial z}\right|$ in equation 2.7. This approximation is called the paraxial or the parabolic approximation.

In parallel, by writing the index of refraction as $n = \langle n\rangle + N$, where N is the index of refraction fluctuations around the average, the development of n^2 to the first order gives with

$N \ll 1$ [Rytov-l-87]: $n^2 \approx \langle n \rangle^2 + 2 \langle n \rangle N$. Equation 2.7 is simplified to obtain the paraxial equation (or parabolic equation) of the electromagnetic field:

$$\frac{\partial^2 \Psi(\mathbf{r})}{\partial x^2} + \frac{\partial^2 \Psi(\mathbf{r})}{\partial y^2} + 2i \langle n \rangle k_0 \frac{\partial \Psi(\mathbf{r})}{\partial z} + 2k_0 \langle n \rangle N \psi(\mathbf{r}) = 0 \tag{2.8}$$

The solution of this equation in a homogeneous media is given by the Fresnel approximation (see equation 2.27).

2.2.2 Spatial Coherence of the Propagated Field

The spatial coherence function B_Ψ of the complex field Ψ can be used to quantify loss of spatial coherence introduced by the propagation through turbulence. In the case of a plane wave, the spatial coherence function is defined by:

$$B_\Psi = \langle \Psi(\mathbf{r}) \Psi^*(\mathbf{r} + \boldsymbol{\rho}) \rangle \tag{2.9}$$

It can be shown [Yura-a-74] that:

$$B_\psi = exp^{-\left(\frac{\rho}{\rho_0}\right)^{\frac{5}{3}}}, \tag{2.10}$$

where $\rho = |\boldsymbol{\rho}|$. By taking $C_n^2(z)$ as the turbulence strength distribution along the propagation path:

$$\rho_0 = \left[1.46 k_0^2 \int_0^L dz C_n^2(z)\right]^{-\frac{3}{5}} \tag{2.11}$$

ρ_0 is the field coherence length. It corresponds to the distance between two points of the field in the reception plane where the spatial correlation has dropped to $1/e$.

The field coherence length can be written as a function of the Fried parameter r_0 [Fried-a-66] even if these quantities are not defined in the same plane (respectively focal and pupil plane). ρ_0 is linked to r_0 by the relation:

$$r_0 = 2.11 \rho_0 \tag{2.12}$$

2.2.3 Weak Perturbation: Analytical Resolution of the Helmholtz Equation

The propagation equation 2.5 cannot be solved analytically in the general case. Further hypothesis are necessary. The weak perturbation hypothesis enables a perturbative resolution of the wave equation. Two different approaches have been developed: the Rytov approximation [Tatarski-l-61] and the Born approximation [Clifford-l-78]. The Rytov approximation consists in considering perturbations as multiplicative relative to the unperturbed field. The Born approximation, on the other hand, considers perturbations as additives. In this document, we will only consider the Rytov approximation that enables us to establish principal statistical expression of the field in weak perturbations.

2.2.3.1 The Rytov Approximation

Let a monochromatic wave be solution of the propagation equation in a homogeneous media of index $\langle n \rangle$: $E_0(\mathbf{r}) = e^{\psi_0(\mathbf{r})}$. After propagation through turbulence, the field sees its amplitude altered by index of refraction fluctuations following equation 2.5. The field after propagation is: $E(\mathbf{r}) = e^{[\psi_0(\mathbf{r})+\psi_1(\mathbf{r})+\ldots]}$. The perturbation $\psi_1(\mathbf{r})$ is only taken to the first order. All other orders are neglected. By applying the Helmholtz equation 2.5 to the field E, we have:

$$\nabla^2\left(e^{\psi_0+\psi_1}\right) + k_0^2 n^2\left(e^{\psi_0+\psi_1}\right) = 0 \tag{2.13}$$

By further developing this equation:

$$\left(\nabla^2(\psi_0+\psi_1) + (\nabla(\psi_0+\psi_1))^2 + k_0^2 n^2\right) e^{\psi_0+\psi_1} = 0 \tag{2.14}$$

The index of refraction $n = \langle n \rangle + N$ can be approximated by $n \approx 1 + N$ by considering the mean value of n unitary and N a random variable of zero mean. We can thus consider that $n^2 \approx 1 + 2N$. Incidentally, the unperturbed field E_0 also follows this equation, that is:

$$\nabla^2(\psi_0) + (\nabla(\psi_0))^2 + k_0^2 = 0 \tag{2.15}$$

By taking into account the previous approximation on the square index of refraction, we obtain from equation 2.15:

$$\nabla^2(\psi_1) + \nabla(\psi_1)(\nabla(\psi_1) + 2\nabla(\psi_0)) + 2Nk_0^2 = 0 \tag{2.16}$$

The Rytov approximation de Rytov consist in considering $|\nabla\psi_1| \ll |\nabla\psi_0|$. We have [Tatarski-l-61, Fante-p-75]:

$$\nabla^2(\psi_1) + 2\nabla(\psi_1)\nabla(\psi_0) + 2Nk_0^2 = 0 \tag{2.17}$$

The solution can therefore be written as:

$$\psi_1(\mathbf{r}) = \frac{k^2}{2\pi E_0(\mathbf{r})}\int_{\mathcal{V}} d\mathbf{r}' N(\mathbf{r}') E_0(\mathbf{r}') \frac{e^{ik|\mathbf{r}-\mathbf{r}'|}}{|\mathbf{r}-\mathbf{r}'|} \tag{2.18}$$

Imposing that $|\nabla\psi_1| \ll |\nabla\psi_0|$ implies important constrains on perturbations affecting E. The validity domain of the Rytov approximation will be considered as the weak perturbations regime.

2.2.3.2 Weak Perturbations Limit

The validity of the results presented in the previous paragraphs is limited to the Rytov approximation. Empirically, it has been shown that Rytov approximation is valid when the log-amplitude variance σ_χ^2 derived from this approximation is lower than 0.3 [Fante-p-75, Clifford-a-74]. This limit is usually expressed as intensity fluctuations variance. It is calculated in the case of

weak turbulence from C_n^2 profile and a Kolmogorov spectrum. It is called the Rytov variance and is expressed as:

$$\sigma_R^2 = 4\int_0^\infty df 2\pi f W_\chi(f) \tag{2.19}$$

$$= 2.26k^{7/6}\int_0^L dz C_n^2(z) z^{5/6}, \tag{2.20}$$

where L is the propagation distance and C_n^2 the structure constant of the index of refraction. The Rytov variance represents intensity (irradiance) fluctuations of a plane wave. Rytov variance for a constant turbulence profile can be simplified to:

$$\sigma_R^2 = 1.23 C_n^2 k^{7/6} L^{11/6} \tag{2.21}$$

When the amplitude of perturbations increases, σ_χ^2 and therefore the value of the intensity variance σ_I^2 increases without limit. This is in contradiction with experiments where the value of the intensity fluctuations saturates [Gracheva-a-65]. Weak perturbations can be characterised by $\sigma_R^2 < 1$ and strong perturbations by $\sigma_R^2 \gg 1$. One can also define a moderate perturbation regime for $\sigma_R^2 \approx 1$ and a saturation regime where $\sigma_R^2 \to \infty$. This behaviour is illustrated figure 2.3.

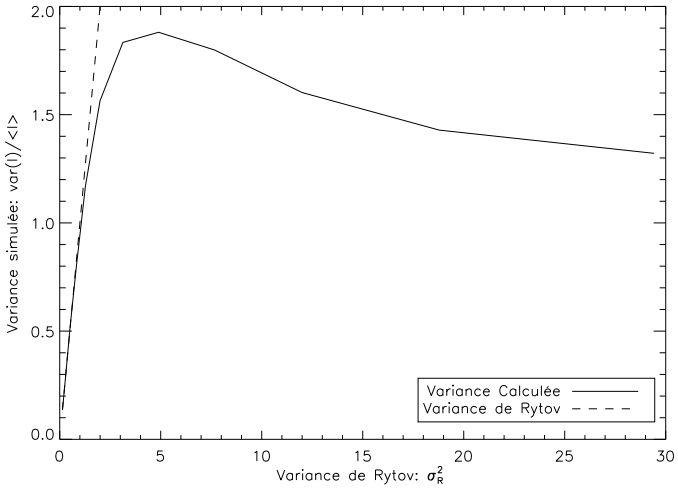

Figure 2.3: Intensity fluctuations variance as a function of C_n^2 for plane wave propagation. The variance value have been obtained by numerical simulations for $\lambda = 1.5$ µm, $L = 10$ km and $l_0 = 5$ mm. The turbulence strength is constant along the propagation path.

The limit defined by $\sigma_R^2 = 1.23 C_n^2 k^{7/6} L^{11/6} = 1$ enables us to determine for a fixed turbulence profile, the maximum propagation distance L_{Rytov} guaranteeing weak perturbation regime. Figure 2.4 shows on one side L_{Rytov} as a function of C_n^2 for two different wavelength values. On

the other side it shows Monin-Obukhov similitude laws (in red on the diagram) for C_n^2 following $h^{-4/3}$, where h represents the height above the ground. The strong chromaticity of this limit can easily be seen and this figure, favouring longer wavelengths. If one is to choose 1.5 µm as the wavelength and 10 km for the propagation distance, it is not possible to rise above a turbulence strength higher than $7\ 10^{-16}\,\mathrm{m}^{-2/3}$ if one wants to stay in the weak perturbation regime. One can reach this value for example for ground value of C_n^2 of $10^{-14}\,\mathrm{m}^{-2/3}$ (resp. $10^{-13}\,\mathrm{m}^{-2/3}$) and a propagation altitude of $h = 15\,\mathrm{m}$ (resp. $h > 50\,\mathrm{m}$). As we have seen, in paragraph 2.1.2.5, these values are actually in the lower limit of the variations of the structure constant. It thus appears that the Rytov variance, in the case of long distance endo-atmospheric FSOCS, goes clearly beyond the weak perturbation limit.

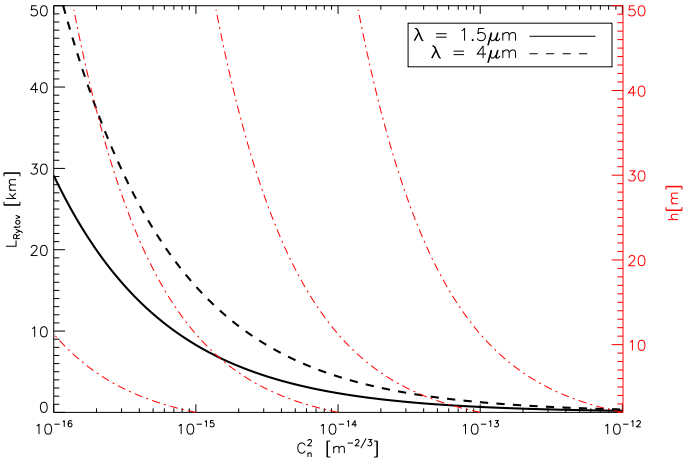

Figure 2.4: Theoretical limit for the Rytov theory as function of C_n^2 for two different wavelengths (C_n^2 is constant along the propagation path). Plots in red represent the decreasing Monin-Obukhov similitude laws for C_n^2 as a function of altitude for different values of ground C_n^2 values.

2.2.3.3 Field Properties in Weak Perturbation Regimes

Statistical Properties of the Propagated Intensity

An important parameter for characterising signal transmission in FSOs (see chapter 3) is the received intensity. One of the important parameters of interest is therefore the intensity density probability function that is directly related to the log-amplitude. Within the weak perturbation Rytov approximation, first order perturbations can be expressed as: $\psi_1 = \chi_1 + i\varphi_1$ where χ_1 is the log-amplitude and φ_1 the phase of the perturbation. For the rest of the document, we will use a simplifying hypothesis where the mean index of refraction is equal to one: $\langle n \rangle = 1$. For weak perturbations χ as well as φ, are the sum of independent Gaussian random variables as shown in equation 2.18 [Fried-a-66, Fante-p-75, Goodman-l-85]. The probability density of χ is therefore

a centred Gaussian function (within the Rytov framework, $\langle\chi\rangle = 0$) of full width half maximum (FWHM) $2\sqrt{2\ln 2}\sigma\chi$.

For the rest of the document we will mainly concentrate on intensity $I = \Psi\Psi^* = I_0 e^{2\chi}$. We have seen that χ follows a normal distribution. Probability density function of I therefore follows log-normal statistics [Goodman-l-85]:

$$p(I) = \frac{1}{2\sqrt{2\pi}I\sigma_\chi} exp\left[-\frac{\left(\ln\frac{I}{I_0} - 2\langle\chi\rangle\right)^2}{8\sigma_\chi^2}\right], I > 0, \tag{2.22}$$

where $\sigma_\chi^2 = \langle\chi^2\rangle - \langle\chi\rangle^2$ is the log-amplitude variance of χ. Energy conservation $\langle I\rangle = I_0$ implying that $\langle\chi\rangle \neq 0$, we observe the difficulty of Rytov approximation to describe strong perturbations.

The normalised intensity variance, i.e. scintillation index, is related to log-amplitude variance by:

$$\sigma_I^2 = \frac{\langle I^2\rangle}{\langle I\rangle^2} - 1 = exp\left[4\sigma_\chi^2\right] - 1 \tag{2.23}$$

For weak perturbations it is possible to develop to the first order the expression of the intensity: $e^{2\chi} \approx 1 + 2\chi$. Normalised intensity probability density can be approximated by a normal law with:

$$\sigma_I^2 \simeq 4\sigma_\chi^2 \tag{2.24}$$

A scintillation rate of 20% therefore corresponds to a log-amplitude variance of $\sigma_\chi^2 = 0.05$.

Power Spectral Density

For a homogeneous distribution of turbulence strength along the propagation path, one can calculate power spectral density for log-amplitude $W_\chi(f)$ and phase $W_\varphi(f)$ from equation 2.18:

$$W_\chi(f) = k^2 \int_0^L dz W_n(f) sin^2(\pi z\lambda f^2), \tag{2.25}$$

$$W_\varphi(f) = k^2 \int_0^L dz W_n(f) cos^2(\pi z\lambda f^2), \tag{2.26}$$

where W_n is the power spectral density of index fluctuation and L the propagation distance.

Figure 2.5 represents the intensity fluctuations spectrum $W_I(f)$ in the plane of the receiver after propagation of a plane wave. Propagation distance was set to $L = 10\,\text{km}$ and wavelength to $\lambda = 1.5$ µm. The turbulence strength is taken constant along the propagation path: $C_n^2 = 10^{-16}\,\text{m}^{-2/3}$. In addition, propagation parameters have been chosen so that the weak perturbation approximation is valid ($\sigma_R^2 = 0.14 < 1$). The intensity fluctuations spectrum presents a maximum value that defines the characteristic size of intensity fluctuations (scintillation grain). Scintillation is created by constructive interferences (high intensities) and destructives interferences (low intensities) between different points of the field. For weak perturbations, the maximum is around $1/\sqrt{\lambda L}$, where $\sqrt{\lambda L}$ is the Fresnel distance, for a plane wave.

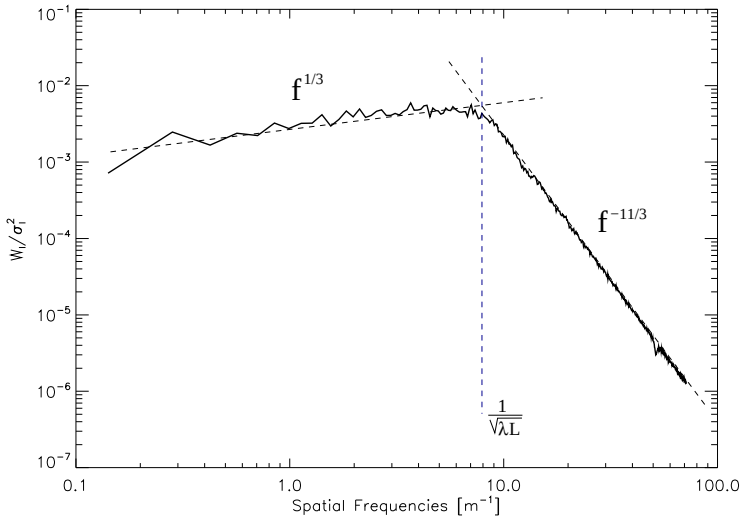

Figure 2.5: Intensity spectrum of a plane wave after propagation. Propagation distance is set to $L = 10\,\text{km}$, wavelength to $\lambda = 1.5$ µm and $C_n^2 = 10^{-16}\,\text{m}^{-2/3}$ is constant along the propagation path leading to $\sigma_R^2 = 0.14$. Index fluctuations are described by a von Karman spectrum. The blue dashed vertical line represents the cut-off frequency at $1/\sqrt{\lambda L}$.

2.2.4 Strong Perturbations

The different analytical expressions presented in the previous paragraph (paragraph 2.2.3) are not valid in strong perturbation. The field's behaviour can nevertheless be describe by numerically solving the propagation equation [Martin-a-88] or by applying heuristic models. Heuristic model can be used to describe certain properties of the field and in particular its intensity [Andrews-a-99]. Results presented in this paragraph are obtained by numerical simulation. Details of the method are presented in the following paragraph.

Figure 2.6 shows two different intensity distributions after plan wave propagation through atmospheric turbulence. The first case corresponds to weak perturbation ($\sigma_R^2 = 0.14$) and the second to a strong perturbation regime ($\sigma_R^2 = 7$). In weak perturbation regimes, scintillation grains have a circular shape. Oppositely, in strong perturbation conditions, scintillation grains take a filament shape.

Modification in speckles geometry translates directly onto intensity fluctuations spectrum by the appearance of two characteristic sizes. On figure 2.7 is represented intensity fluctuations spectrum for plane wave propagation in strong perturbation regime. Propagation distance is set to $L = 10\,\text{km}$ and wavelength to $\lambda = 1.5$ µm. Turbulence strength is constant along propagation path and equal to $C_n^2 = 5\ 10^{-15}\,\text{m}^{-2/3}$. These parameters were chosen to insure a normalised intensity fluctuation variance of $\sigma_R^2 \simeq 7$ and be in the strong perturbation regime. The intensity fluctuation spectrum presents two characteristic sizes for intensity fluctuations corresponding to the characteristic dimensions observed on figure 2.6. The characteristic frequencies are $r_0/(\lambda L)$ and $1/r_0$, where r_0 if the Fried parameter. For the chosen simulation values $r_0 = 2.9\,\text{cm}$.

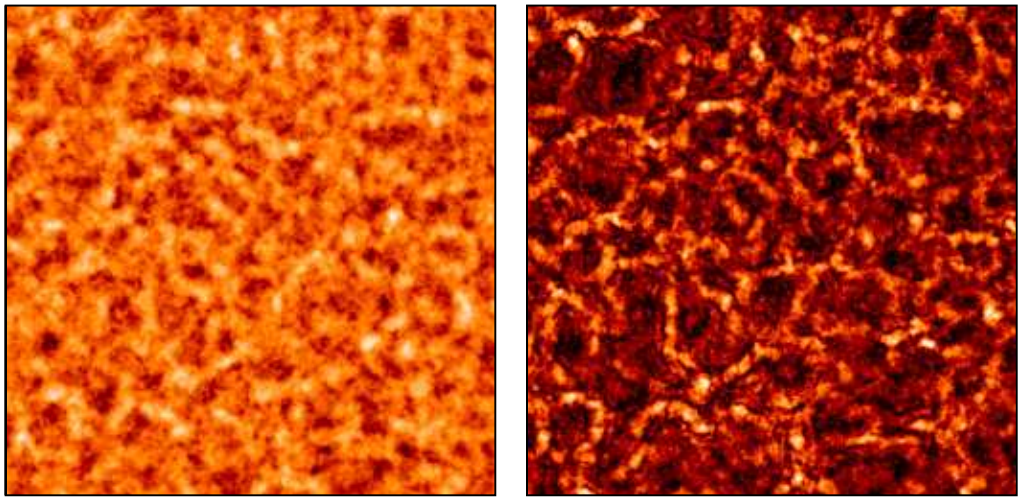

Figure 2.6: Propagation through turbulence for $\sigma_R^2 = 0.14$ (left), $\sigma_R^2 = 7$ (right). The length of each side of the square is 25 cm. Logarithmic colour scale.

2.2.5 Propagation Simulation by Phase Screens

The Helmholtz equation (Eq. 2.5) has no analytical solution in the general case. On the other hand, by using Markov approximation [Tatarski-l-61], it is possible to solve the Helmholtz equation locally [Lee-p-69]. It is then possible to numerically model wave propagation in a turbulent media[Martin-a-88]. The main advantage of this technique is that it enables to go beyond the analytical models, limited to weak perturbations. It enables, by a Monte Carlo approach, to reach statistical properties of the propagated field in strong perturbation regimes.

2.2.5.1 Modelling Principle

The phase screen propagation method of electromagnetic waves is based on the separation between propagation and turbulence. The approach consists in sampling the turbulent volume into several turbulent layers. We then consider that the turbulence contained in one turbulence slab can be modelled by a thin layer that we call a phase screen.

Between phase screens, propagation is performed in vacuum. The thickness of each layer must be sufficiently small so that propagation of phase aberrations within the layers can be neglected. On the other hand, the layers' thickness must be sufficiently large so that two consecutive layers can be considered decorrelated.

Within the parabolic approximation, propagation in vacuum of a perturbation $\psi(x, y, z)$ over a distance d can be described by a simple Fresnel propagation:

$$\Psi(x, y, z + d) = \Psi(x, y, z) * \frac{e^{ikd}}{i\lambda d} e^{ik\frac{x^2+y^2}{2d}} \tag{2.27}$$

$$= \Psi(x, y, z) * \mathcal{F}_d(x, y), \tag{2.28}$$

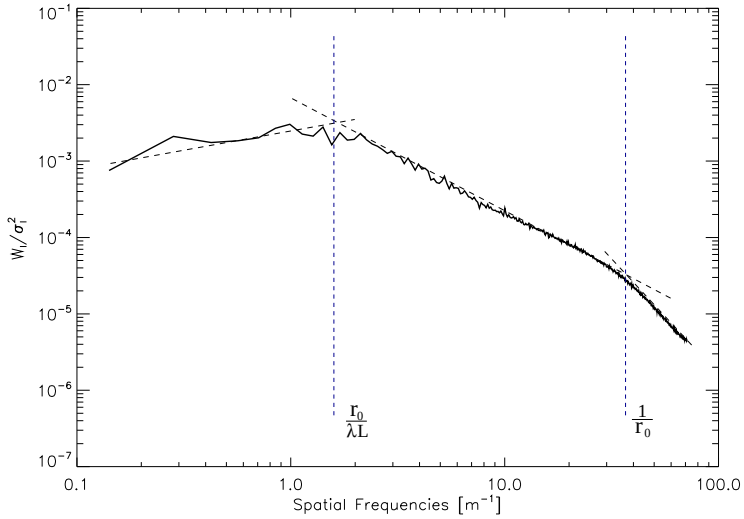

Figure 2.7: Intensity distribution spectrum after propagation of a plane wave. Propagation distance is set to 10 km, wavelength to $\lambda = 1.5$ µm and $C_n^2 = 5\ 10^{-15}\,\mathrm{m}^{-2/3}$ is constant along the propagation path. Intensity fluctuations are described by the von Karman spectrum. The two vertical dashed lines represent the cut-off frequencies at $r_0/(\lambda L)$ and $1/r_0$.

where $\mathcal{F}_d(x,y)$ is the Fresnel propagator over a distance d, $*$ the convolution product and $\Psi(x,y,z)$ the incident field.

Figure 2.8 presents the modelling principal of propagation through a turbulent media by the phase screen method. The turbulent volume is decomposed into layers, here in blue. Phase perturbations introduced by one layer are represented as a phase screen, here in gray. The propagation scheme is the following:

$$\begin{aligned}
\Psi(x,y,z) &= A_0(x,y,z).e^{i\varphi_0(x,y,z)} \\
\Psi'(x,y,z) &= \Psi(x,y,z).e^{i\varphi_1(x,y,z)} \\
\Psi(x,y,z+d) &= \left(\Psi(x,y,z).e^{i\varphi_1(x,y,z)}\right) * \frac{e^{ikd}}{i\lambda d} e^{ik\frac{x^2+y^2}{2d}} \\
&= \Psi'(x,y,z) * \mathcal{F}_d(x,y) \\
\Psi'(x,y,z+d) &= \Psi(x,y,z+d).e^{i\varphi_2(x,y,z+d)} \\
\Psi(x,y,z+2d) &= \Psi'(x,y,z+d) * \mathcal{F}_d(x,y) \\
\cdots &= \cdots
\end{aligned}$$

The propagated field is a succession of phase perturbations introduced by phase screens and of phase and amplitude perturbations introduced by propagation of phase aberrations between layers (diffraction).

This modelling principal has been put in place at ONERA by the PILOT (Propagation et Imagerie Laser ou Optique à travers la Turbulence) code [Mahe-t-00]. Turbulence is sampled by a finite number of independent phase screens. Each phase screen is modelled by a Fourier approach

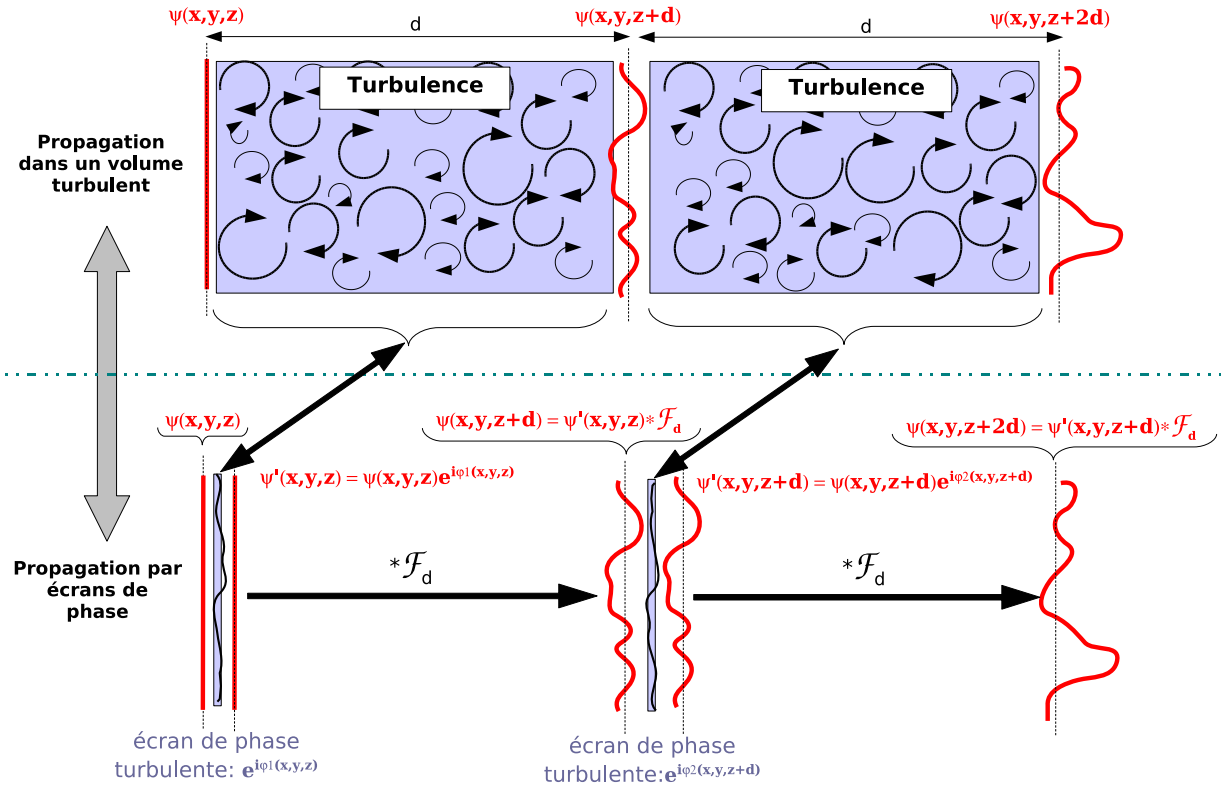

Figure 2.8: Diagram of the principal of phase screen propagation.

[McGlamery-p-76] following von Karman statistics. Numerical simulation results presented in this document have been obtained using the PILOT code.

2.2.5.2 Temporal Effects Modelling

For the time scales considered (i.e. a few tens of seconds) the temporal evolution of turbulence follows Taylor's frozen turbulence hypothesis. This hypothesis enables us to model air mass movements between two instances in time by a simple translation. Its amplitude is equal to speed vector component $V_\perp$, orthogonal to the direction of observation. The index of refraction at time t can thus be calculated by: $n(\mathbf{r}, t) \approx n(\mathbf{r} - V_\perp(\mathbf{r})\, t)$. To model temporal evolution we will perform phase screens translations perpendicular to the propagation direction.

2.3 Turbulence Effects on Laser Propagation

Laser beams are essential to establish a high signal-to-noise link. Results presented so far do not take into account the impact spatial limitation of the field on FSOs. This paragraph will address the impact of turbulence on a spatially limited electromagnetic wave.

2.3.1 Properties and Conventions for Gaussian Beams

In this document, we will mainly consider mono-mode Gaussian laser beams, that is TEM_{00} electromagnetic waves. The amplitude of the Gaussian beam complex field U_0 is:

$$U_0(\mathbf{r}, z) = A(z)\, exp\left(-\frac{\mathbf{r}^2}{w(z)^2} - i\frac{k\mathbf{r}^2}{2R(z)}\right), \tag{2.29}$$

where:

- $A(z)$ represents the on-axis electric field amplitude;
- $k = \frac{2\pi}{\lambda}$ the wave number;
- $w(z)$ the $1/e$ beam radius in amplitude;
- $R(z)$ the radius of curvature.

Figure 2.9 presents the conventions used in this document. The beam radius is calculated on the amplitude at $1/e$.

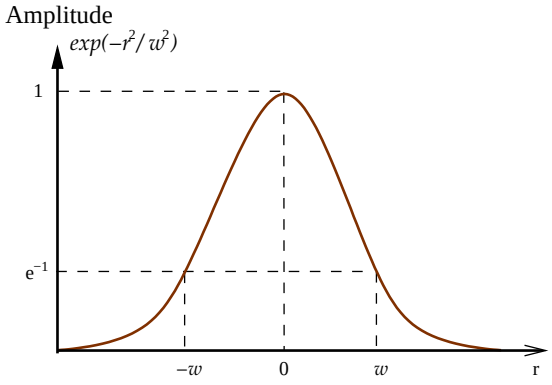

Figure 2.9: Conventions for a Gaussian beam in amplitude.

For a beam propagating in vacuum, the minimal size w_0 defines the beam waist. The wavefront is flat at the level of the beam waist (infinite radius of curvature). Let z_0 be the plane where the beam waist is located. The distance dependence of the beam size $w_{z=L}$ as a function of $z - z_0$ and the beam waist w_0 is governed by this equation:

$$w(z)^2 = w_0^2\left(1 + \left(\frac{z - z_0}{Z_R}\right)^2\right) \tag{2.30}$$

where $Z_R = \frac{\pi w_0^2}{\lambda}$ is the Rayleigh distance. For long propagation distances (i.e. $z \gg Z_R$), we can use the approximation: $w(z) \approx \theta_0 z$, with the angle $\theta_0 = \frac{\lambda}{\pi w_0}$. Figure 2.10 presents a diagram of the diameter evolution at $1/e$ in amplitude as a function of propagation distance.

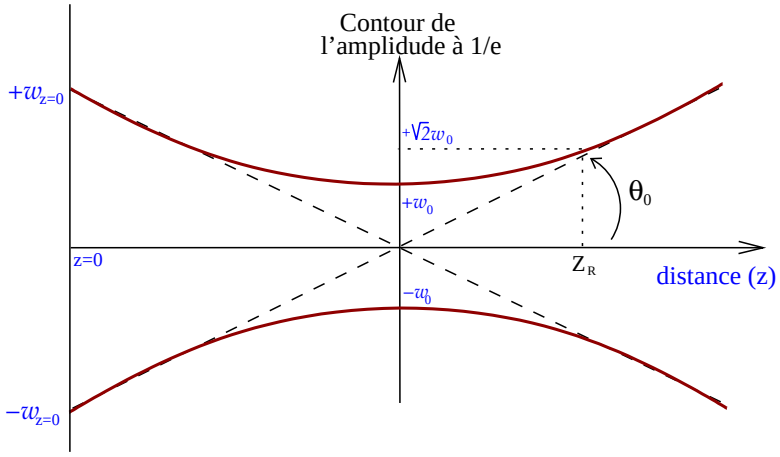

Figure 2.10: Propagation of a convergent (radius of curvature > 0 at origin) Gaussian beam in vacuum.

The radius of curvature $R(z)$ evolution as a function of propagation distance is given by:

$$R(z) = (z - z_0)\left(1 + \left(\frac{Z_R}{z - z_0}\right)^2\right) \tag{2.31}$$

2.3.2 Turublence Effects on Propagation

2.3.2.1 Beam Wander and Beam Spreading

Introduction

As we have seen, turbulence introduces index variations along the propagation path. For a finite size beam such as a Gaussian beam it will introduce on the one hand, random displacement of the beam as it propagates and on the other beam broadening (larger than that predicted by diffraction). Random displacements of the beam (or beam wander ρ_c), are mainly due to turbulence cells larger than the beam size. Oppositely, turbulence cells smaller than the beam will tend to break-up the beam but not really bend it. As a consequence of these smaller cells, the beam will be made broader. We can consider two different cases, short and long exposures. Short exposures do not take beam displacement into account, the beam spreading is then expressed by the radius ρ_s (i.e. *short-term beam spreading*). Long exposures characterised by the radius ρ_L (or *long-term beam spreading*) take into account both effects. Figure 2.11 schematically illustrates ρ_c, ρ_s and ρ_L in the reception plane and where the hashed red disks represent a laser impact i at a given time t_i.

In strong turbulence regime, the beam will be highly broken up. The beam will mainly suffer from beam spreading and beam wander will be moderate. If we look at short-exposure images, the beam will be broken up and composed of a multitude of speckles. Figure 2.12 shows intensity distribution in the plane of reception for several turbulence strengths. These propagation

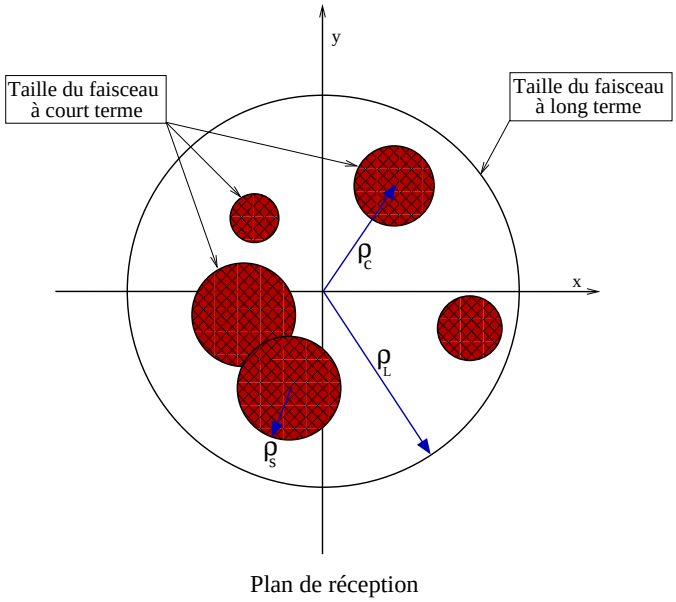

Figure 2.11: Diagram of the beam-wander (ρ_c), short exposure beam-spreading (ρ_s) and long-exposure beam-spreading (ρ_L). Each hashed red disks represent an individual laser impact after propagation for several independent realisation of turbulence (source [Fante-p-75]).

conditions lead to a Rytov variance, from left to right, of respectively: $\sigma_R^2 \simeq 0.28$, 2.8, 9.8 and 28.

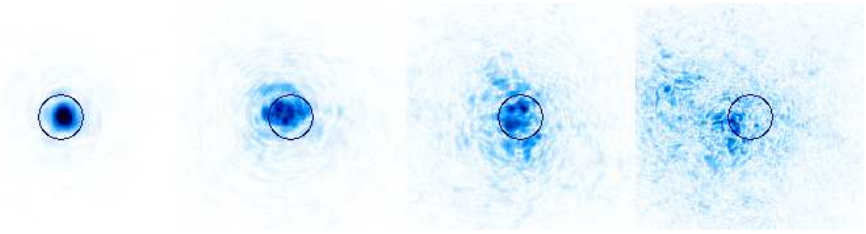

Figure 2.12: Illustration of the impact of atmospheric turbulence on free-space laser beam propagation. From left to right, turbulence strength is: $C_n^2 = 2.10^{-16}$, 2.10^{-15}, 7.10^{-15}, $2.10^{-14}\,\mathrm{m}^{-2/3}$. Propagation distance is set to $10\,\mathrm{km}$ and wavelength to $\lambda = 1.5$ µm. Black circles represent a $30\,\mathrm{cm}$ diameter.

Analytical Expressions

Beam wander can be statistically characterised by the variance of the intensity distribution centre of gravity in a plan perpendicular to the optical axis. In an isotropic medium, position variance relative the optical axis can be characterised when $\rho_0 \ll \sqrt{2}w_o < z$ et $z \lesssim 2kw_o$, by

[Fante-p-75, Churnside-a-90]:

$$\left\langle \rho_c^2 \right\rangle \simeq \frac{2.64 z^2}{k^2 \rho_0^{5/3} w_{z=0}^{1/3}}, \tag{2.32}$$

Where z represents propagation distance and $\rho_0 = \left[1.46 k^2 z \int_0^1 d\xi \, (1-\xi)^{5/3} \, C_n^2(\xi z)\right]^{-3/5}$ field coherence distance calculated for a convergent spherical wave in reception plane. In an isotropic medium, beam wander is identical in both axis [Andrews-p-08]. The variance for only one axis is simply $\left\langle \rho_c^2 \right\rangle / 2$.

Considering a Gaussian laser beam propagating over a distance z with an initial beam radius $w_{z=0}$ and radius of curvature $R_{z=0}$, the long-term beam spreading ρ_L can be described as [Fante-p-75] when $z \ll \left(k^2 C_n^2 l_o^{5/3}\right)^{-1}$:

$$\left\langle \rho_L^2 \right\rangle \simeq \frac{2z^2}{k^2 w_{z=0}^2} + \frac{w_{z=0}^2}{2}\left(1 - \frac{z}{R_{z=0}}\right)^2 + \frac{4z^2}{k^2 \rho_0^2} \tag{2.33}$$

ρ_L is defined as the radius at which the mean intensity distribution is reduced by a factor $1/e$ from its maximal value. Short-term and long-term beam spreading are related by [Fante-p-75]:

$$\left\langle \rho_L^2 \right\rangle = \left\langle \rho_c^2 \right\rangle + \left\langle \rho_s^2 \right\rangle \tag{2.34}$$

Beam wander and beam spreading are obtained without the need of making the weak perturbation approximation. Moreover, when the radius of curvature is small, we are brought back to the spherical wave case.

Numerical Validations

Figure 2.13 present a comparison between numerical simulations obtained by the PILOT simulation tool and analytical expressions given by Fante [Fante-p-75]. We see a very good correlation between theory and simulations. The relative error stays, for the beam wander, below 20% for the studied parameters range (below 12% on average). It is difficult to measure accurately the

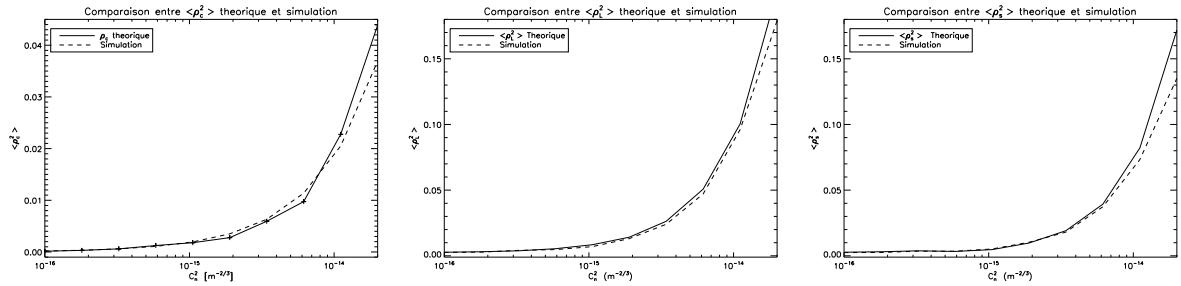

Figure 2.13: Comparison between theoretical and simulated values. From left to right: beam wander, long-term beam spreading and short-term beam spreading. Propagation distance is $10\,$km, wavelength $1.5\ \mu$m and $w_{z=0} = 6\,$cm.

short-exposure beam size because it is highly fragmented and not longer resembles a Gaussian intensity distribution. In order to measure beam spreading, it is possible to use the radius of a circle within which 86.47% of the energy is contained [Dios-a-08]. Comparison between simulated and theoretical data for ρ_L and ρ_s seem to coincide well despite this restriction.

2.3.2.2 Intensity Fluctuations and Power in the Bucket

Gaussian Beam and Scintillation

We have presented average effects of turbulence on Gaussian beams. Scintillation can also modify collected intensity after propagation. Due to the spatial limitation of the Gaussian profile, it is not possible to make the assumption of a spatially stationary process. Mean intensity evolves radially as a function of distance from the optical centre. Similarly, normalised log-amplitude variance will change throughout the field. Log-amplitude variance of the field is:

$$\sigma_\chi^2(\rho) = \frac{\text{Var}[\chi(\rho)]}{\langle\chi(\rho)\rangle^2} \tag{2.35}$$

Variance $\sigma_\chi^2(\rho)$ generally increases with distance ρ. This equation has no analytical solution but can be evaluated by numerical simulations [Frehlich-a-00]. However, for weak perturbations, Velluet *et al.* [Velluet-p-07] suggests a simplified model to estimate these fluctuations. Fluctuations of χ can be explained by a combination of beam wander and small-scale fluctuations (scintillation) of the laser beam log-amplitude. By considering a Gaussian beam χ in the absence of perturbation is equal to $\chi_0 = -\frac{\rho}{w}^2$, where ρ is the distance from the optical axis and w the radius of the beam, the variance of χ introduced by Gaussian beam displacement (beam wander) can be written as:

$$\sigma_{\chi,bw}^2(\rho) = 4\frac{\rho}{w}^2 \langle\rho_c^2\rangle \tag{2.36}$$

An estimation of the weak perturbations variance (equation 2.37) $\sigma_\chi^2(\rho)$, can be obtained by adding beam wander effects and on-axis variance. The on-axis variance $\sigma_\chi^2(0)$ can be estimated by Rytov variance for a spherical wave.

$$\sigma_\chi^2(\rho) = \sigma_\chi^2(0) + \sigma_{\chi,bw}^2(\rho) \tag{2.37}$$

In strong turbulence conditions, equation 2.37 is not longer valid. In fact, the beam is strongly broken up which increases fluctuations near the axis. Figure 2.14 presents intensity radial variance for several turbulence strengths: $\sigma_R^2 = 0.147$ and $\sigma_R^2 = 14.7$.

Power in the Bucket

When using non-negligible pupil sizes, it is possible to integrate the received flux over the entire pupil surface instead of only considering a single point. Let the power in the bucket (PIB) be the intensity integral of field ψ_R received by the telescope pupil $\mathcal{P}_R$ and normalised by the total emitted flux:

$$PIB = I = \frac{\int |\psi_R(\mathbf{r}')|^2 \mathcal{P}_R(\mathbf{r}') d\mathbf{r}'}{\int |\psi_E(\mathbf{r})|^2 d\mathbf{r}}, \tag{2.38}$$

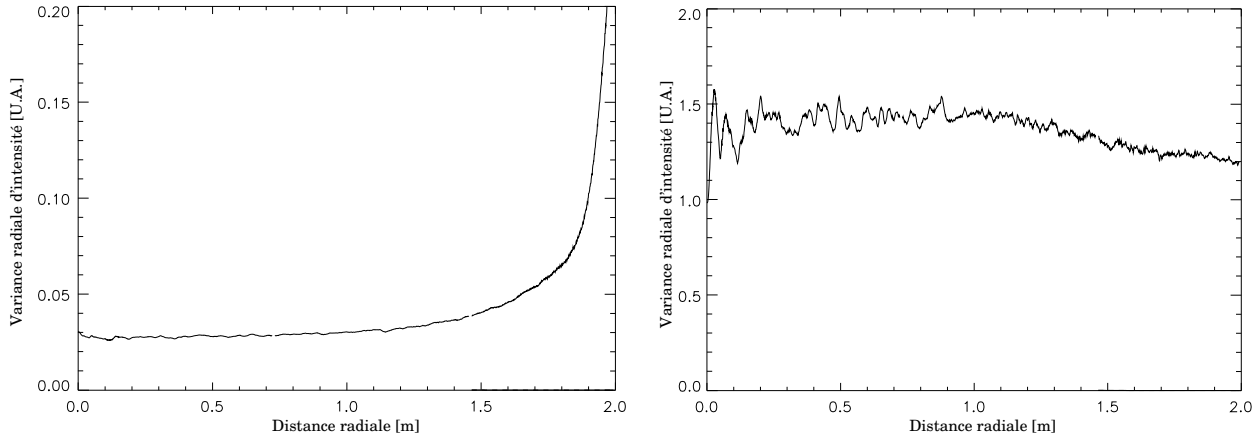

Figure 2.14: Normalised intensity radial variance. Left: $\sigma_R^2 = 0.15$, right: $\sigma_R^2 = 14.7$.

where ψ_E is the emitted field. Let ψ_E be the field emitted by one of the FSO ends and ψ_R the field received at the other end by the pupil. In other terms, the normalised PIB represents the coupling coefficient between the two ends of the communication link. This parameter is at the heart of the quality estimation of atmospheric optical links. In fact, for FSO systems using OOK modulation and integrating flux over the entire pupil, the signal-to-noise ratio is proportional to PIB. In addition, as we will see in the followings paragraphs (see paragraph 3.1.1), the bit-error-rate (BER) is also directly linked to the PIB. Another important parameter for optical communications is the link margin [Majumdar-l-08]. It is expressed as the ratio between received power and the required power to achieve a given BER at a given transmission data rate.

The combined effect of beam wander, beam spreading and scintillation makes the collected intensity (PIB) in the collecting pupil evolve over time. Qualitatively, beam wander generally introduces variations of large amplitude and low frequencies whereas scintillation and beam spreading leads to variations of higher frequencies. Figure 2.15 illustrates the temporal evolution for three turbulence forces with a collecting pupil diameter of $25\,\text{cm}$. Turbulence strength is constant along the propagation path to represent an endo-atmospheric link. We have chosen wind speeds between $2.5\,\text{m.s}^{-1}$ and $10\,\text{m.s}^{-1}$. We can see that when turbulence strength or wind speed increases temporal variations also increase, leading to a deterioration of the link quality.

Curves shown figure 2.16, illustrate the PIB density probability function evolution as turbulence strength varies. Simulation parameters have been chosen so that the Rytov variance is respectively of $\sigma_R^2 = 0.14$, 1.4 and 14 for the different turbulence strengths. We therefore consider the entire regimes of perturbations, from weak to strong. We notice that as turbulence increases, the more the distribution departs from a log-normal distribution (mainly for $C_n^2 = 10^{-14}\,\text{m}^{-2/3}$). When perturbations are extremely severe (deep saturation), the PDF becomes a negative exponential law [Gochelashvily-a-71, Bissonnette-a-79].

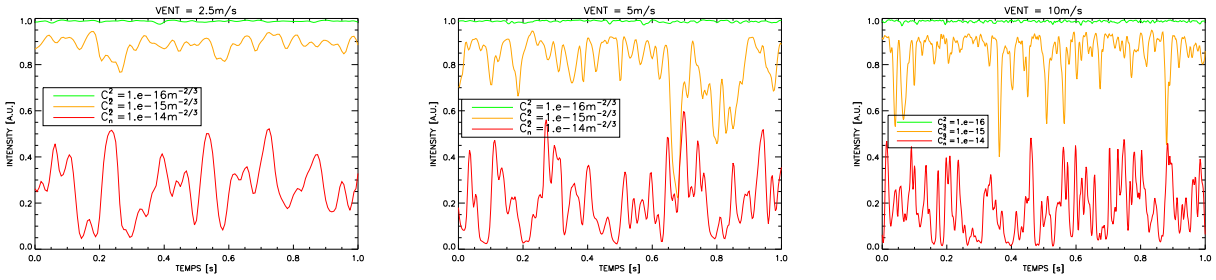

Figure 2.15: Intensity (PIB) temporal evolution. Propagation distance is $10\,$km, wavelength $\lambda = 1.5$ µm and collecting pupil diameter $\phi = 25\,$cm.

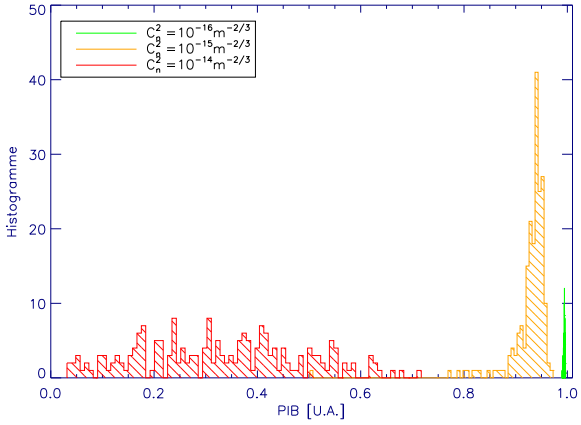

Figure 2.16: Intensity probability density for a propagation through turbulence. Wavelength: $\lambda = 1.5$ µm, propagation distance: $10\,$km. Intensity is integration over a $30\,$cm diameter pupil. Histograms realised over 300 propagations.

2.3.2.3 Strong Turbulence Regime

The turbulence strength classification based exclusively on Rytov variance is only theoretically applicable to a plane or spherical wave. Weak perturbation conditions correspond to regimes where the scintillation index is inferior to unity. For Gaussian beams propagating a quasi-horizontal path, weak perturbation regimes are fulfilled by two conditions [Miller-a-94, Andrews-a-01]:

$$\sigma_R^2 < 1 \text{ and } \sigma_R^2 \left(\frac{2L}{k w_{z=L}^2} \right)^{5/6} < 1, \tag{2.39}$$

where σ_R^2 is the Rytov variance, and $w_{z=L}$ the beam radius after propagation over a distance L in the vacuum. If one of these conditions is not satisfied, weak perturbation regime is no longer valid. This additional condition is to take into account the beam profile and insure that the

inequality $\sigma_R^2 < 1$ stays valid over the whole field.

In the rest of the document, we will mainly study propagation distances of $L = 10\,\text{km}$, wavelengths of $\lambda = 1.5$ µm and relatively large beam diameters ($> 7\,\text{cm}$). With these typical values, the second criterion, that is $\sigma_R^2 \left(\frac{2L}{kw_{z=L}^2}\right)^{5/6} < 1$, will always be satisfied. We can therefore concentrate exclusively on σ_R^2 to characterise turbulence regimes. By setting the beam size to $w_{z=L} > 7\,\text{cm}$, we obtain: $\left(\frac{2L}{kw_{z=L}^2}\right)^{5/6} \simeq 1$.

2.4 Nominal Conditions

In the rest of this document, we will present numerical simulation results relative to laser beam propagation through turbulent media. Typical conditions taken for the numerical modelling are chosen to be representative of a long-distance atmospheric FSO system. The wavelength, in the near infrared, will be set to $\lambda = 1.5$ µm and propagation distance to $10\,\text{km}$. In addition, to simplify the study, we will set as a general value the telescope diameter between $D = 25 - 30\,\text{cm}$ to limit the bulk of the system. These telescopes will emit a coherent wave and do not rely on emission diversity. Table 2.1 summarises the chosen numerical values for the simulations presented in the following chapters. We will consider a mean propagation altitude of $30\,\text{m}$ above the ground in order to be above obstacles along the path (trees, buildings, landscape ...)

	Numerical Values
Wavelength	$\lambda = 1.5$ µm
Propagation Distance	$L = 10\,\text{km}$
Telescope Diameter	$D = 25 - 30\,\text{cm}$
Height of Propagation	$h \simeq 30\,\text{m}$

Table 2.1: Table presenting typical numerical values used for modelling.

C_n^2 profile is taken constant along the propagation path. This turbulence is typical of horizontal line-of-sight link. Dependence of C_n^2 with altitude is set by the Monin-Obukhov similitude laws that state the turbulence strength decreases as $h^{-4/3}$ for daytime Earth propagation (and as $h^{-2/3}$ for night time). For information, we can consider C_n^2 values presented in table 9.1, where σ_R^2 is the Rytov variance and ρ_0 is the wave spatial coherence. Weak perturbations propagation

	Weak	Median	Strong
C_n^2 ($h = 2\,\text{m}$)	$3.7\ 10^{-15}\,\text{m}^{-2/3}$	$3.7\ 10^{-14}\,\text{m}^{-2/3}$	$3.7\ 10^{-13}\,\text{m}^{-2/3}$
C_n^2 ($h = 30\,\text{m}$)	$10^{-16}\,\text{m}^{-2/3}$	$10^{-15}\,\text{m}^{-2/3}$	$10^{-14}\,\text{m}^{-2/3}$
σ_R^2 ($h = 30\,\text{m}$)	0.14	1.4	14
ρ_0 ($h = 30\,\text{m}$)	14 cm	3.5 cm	0.9 cm

Table 2.2: C_n^2, σ_R^2 and ρ_0 values, typical for continental climate and horizontal propagation.

conditions enable us to estimate the behaviour of the link in favourable condition. In most real

life cases, the presented framework will preferably be in strong perturbations. However, three atmospheric turbulence cases will enable us to study different perturbation regimes: weak, intermediate and strong. We remind here that the correction performance will be done considering two metrics: mean intensity $\langle I \rangle$ or PIB and normalised intensity fluctuations $\frac{\sigma_I}{\langle I \rangle}$. The influence of vibrations and pointing errors will not be studied here.

Results are presented for an outer-scale L_0 of the order of a few meters. The reason of this limitation is related to the use of phase screens (see paragraph 2.2.5) that imposes a strong constrain on the physical size of screens. It is necessary to correctly sample the inner-scale in addition to keeping a sufficient screen width to minimize aliasing. Inner-scale is of the order of a few millimetres. In order to minimise calculation time and memory size taken by phase screens, we will limit screens to a few meter in width. Outer-scale will thus be limited in size and its effects (mainly on beam wander) under-estimated. Methods have been proposed [Frehlich-a-00] to improve outer-scale sampling. As we will see in the following paragraphs, this limitation will have an important impact on the case we will study (see paragraph 2.3).

Part II

The Optical Channel

Chapter 3

Atmospheric Turbulence Effects

Contents

In the previous chapter we studied the effects of atmospheric turbulence on laser beam propagation. In order to further characterise perturbations effects on FSOs, we will study in this chapter how to estimate link quality for a free-space optical communication system (paragraph 3.1). This estimation can be in particular, expressed in terms of bit-error rate (BER). Unfortunately, it generally relies on precise knowledge of the intensity density probability function. For strong perturbations, there is no satisfactory method to properly characterise it. For this very reason, we propose to estimate link quality in the case of numerical simulations, mainly by mean intensity and intensity fluctuations (paragraph 3.1.4). For links of more than a few kilometres, turbulence has a major impact on link quality and mitigating its effects is essential. Before proceeding directly to the original research work presented in this document part three, paragraph 3.2 presents different methods and implementations that can be found in the literature. It will help us to understand the importance and efficiency of each of them. More specifically linked to the work presented here, we will put forward the importance of adaptive optics pre-compensation for atmospheric optical link. This aspect will be further developed in the following chapters.

3.1 Telecommunication Link Characterisation

3.1.1 Bit-Error Rate

3.1.1.1 Transmission Channel Capacity

Channel capacity is the maximal amount of information that can be transmitted reliably (i.e. without information loss) through a communication channel. Channel capacity C with an additive white Gaussian noise (ASWGN) is given by the Shannon-Hartley theorem by [Shannon-l-49, Viterbi-l-79]:

$$C(t) = B\, log_2(1 + SNR(t)) \tag{3.1}$$

Channel capacity C is given in bit/s, bandwidth B in Hertz and SNR is the signal-to-noise ratio. A reliable transmission information can only be performed when data throughput is inferior to C. The time-scale at which signal-to-noise ratio and channel capacity varies is typically of a few orders of magnitude lower that the modulation speed of the carrier signal. In the case of FSOs, B is of the order of the GHz and temporal variations of SNR of the order of the millisecond. The signal-to-noise ratio varies over time because of the received flux variations caused by atmospheric turbulence. Channel capacity $C(t)$ because linked to the SNR, will also vary over time. When data throughput is made larger channel capacity, the communication link will suffer from information loss.

3.1.1.2 Bit-Error Rate in Absence of Turbulence

Bit-error rate or BER is defined by:

$$BER = \frac{\text{Number of errors}}{\text{Number of bits transmitted}} = Pr(E) \tag{3.2}$$

In absence of atmospheric turbulence, it is possible to calculate the error occurrence probability $Pr(E)$ for an On-Off Keying (OOK) modulation where each bit is coded by a luminous pulse respectively turned on or off for the duration of the bit. Figure 3.1 illustrates the derivation of different error probabilities as a function of the detection threshold. For the derivation, we assume a Gaussian noise adding to the detection signal. Noise will create two different error types:

- Detection of a '1' when a '0' has been transmitted: green section on figure 3.1
- Detection of a '0' when a '1' has been transmitted: red section on figure 3.1

Such probability errors are respectively $Pr(1|0)$ (false alarm probability) and $Pr(0|1)$ (missed detection probability). Let i_T be the threshold level, I the signal without noise and σ_N^2 the noise variance (see annex A.1):

$$\begin{aligned} Pr(1|0) &= \frac{1}{\sqrt{2\pi}\sigma_N}\int_{i_T}^{\infty} e^{-I^2/2\sigma_N^2} dI = \frac{1}{2} erfc\left(\frac{i_T}{\sqrt{2}\sigma_N}\right) \\ Pr(0|1) &= \frac{1}{\sqrt{2\pi}\sigma_N}\int_{-\infty}^{i_T} e^{-(I-is)^2/2\sigma_N^2} dI = \frac{1}{2} erfc\left(\frac{I - i_T}{\sqrt{2}\sigma_N}\right) \end{aligned}$$

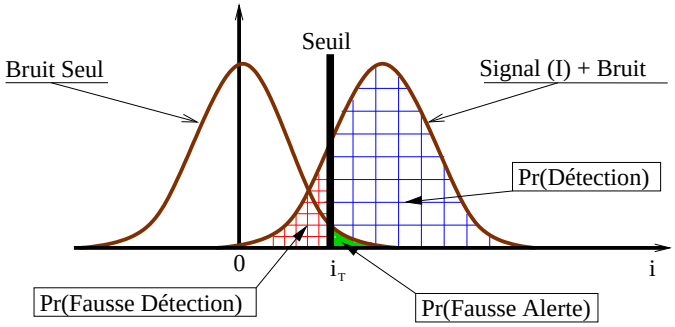

Figure 3.1: False alarm detection probability (source [Andrews-l-98]).

By letting the threshold at half the dynamic range $i_T = I/2$, we obtain $Pr(0|1) = Pr(1|0)$. Supposing the probability of sending a '1' p_1 equal to the probability p_0 of sending a '0' (with $p_0 = p_1 = 0.5$), we can calculate the total error probability without turbulence $Pr(E)^{no\ turb}$ [Gagliardi-l-76]:

$$\begin{aligned} Pr(E)^{no\ turb} &= p_0 Pr(1|0) + p_1 Pr(0|1) \\ &= \frac{1}{2}\left(\frac{1}{2} erfc\left(\frac{i_T}{\sqrt{2}\sigma_N}\right)\right) + \frac{1}{2}\left(\frac{1}{2} erfc\left(\frac{I - i_T}{\sqrt{2}\sigma_N}\right)\right) \\ &= \frac{1}{2} erfc\left(\frac{SNR_0}{2\sqrt{2}}\right), \end{aligned}$$

where $SNR_0 = \frac{I}{\sigma_N}$ is the detection signal-to-noise ratio.

3.1.1.3 Bit-Error Rate in Turbulence

Two different methods have been developed in order to characterise bit-error rates in presence of turbulence. The first by calculating BER based on an analytical probability density function expressions of the physical phenomenon itself. In the second method, the BER is directly evaluated by an end-to-end Monte Carlo modelling of the physical phenomenon. We will see that both methods have serious limitations.

Why Turbulence Increases Error Probability?

We have shown that the bit-error rate is function of the signal-to-noise ratio (SNR), that is for a constant noise level to the received signal amplitude. This is verified for every detector type using a detection threshold (non-coherent detection). Atmospheric turbulence makes the received signal amplitude fluctuate randomly over time. The received signal $I(t)$ therefore becomes a random variable with probability density $PDF\,(I)$. In the same way, the error probability $Pr(E)$ will also become a random variable. The error probability of the both random phenomenon (noise and turbulence) must be evaluated by integrating over turbulence the previous error probability calculated over noise.

For optical propagations inferior to a kilometre [Andrews-l-01], systems usually have enough link-margin to ensure their performance is not degraded by scintillation. For longer distance links, turbulence is a determining factor for the error rate.

BER Estimation by Probability Density Function

We have seen paragraph 3.1.1.2 that:

$$Pr(E)^{no\ turb} = BER_0 = \frac{1}{2} erfc\left(\frac{SNR_0}{2\sqrt{2}}\right) \tag{3.3}$$

In the case where the received signal and thus the SNR varies, in particular in presence of atmospheric turbulence, error probability is a conditional probability that must be averaged over the density probability function (PDF) of the collected signal I. We obtain the error probability in presence of turbulence in the case of an adaptive threshold:

$$Pr(E)^{turb} = \langle BER \rangle = \int_0^\infty P_r(E|I=s)^{no\ turb} p_I(s) ds \tag{3.4}$$

$$= \frac{1}{2}\int_0^\infty erfc\left(\frac{s}{2\sqrt{2}\sigma_N}\right) p_I(s) ds \tag{3.5}$$

Unfortunately, the probability distribution $p_I(s)$ is not well known (cf. paragraph 3.1.2.2) as soon as turbulence is strong. In order to calculate the BER, some authors [Sandalidis-a-08] consider a *K* model for the probability distribution, whereas others [Andrews-p-08] propose a $\Gamma\Gamma$ model. In both cases, these are empirical models and their validity regime is not well defined. The estimation of such a quantity thus requires a numerical estimation of $p_I(s)$ or a direct estimation of BER.

BER Direct Estimation by Monte Carlo Methods

Direct estimation of BER is performed by counting modelled events with a complete simulation of propagation and detection processes. A complete simulation is extremely time-consuming and it is important to evaluate the number of simulation rounds that need to be performed in order to evaluate the BER.

The confidence level *CL* that the BER is smaller than a given level gives us the percentage of change of having the BER estimate equal to the actual BER. If one is to choose a confidence level of $CL = 90\%$ of having a BER smaller than 10^{-9}, one needs to simulate $n = 2.3 * 10^9$ bit transmissions if the number of measured error is $N = 0$ and $n = 3.88 * 10^9$ bits for $N = 1$ (see annex A.2). This extremely high number of required transmission makes it impossible to use numerical simulation methods using phase screens which is costly in terms of computation time.

Limitations of the Average Bit-Error Rate

The average BER enables us to characterise the mean behaviour of telecommunication links but not to access instantaneous error rates. Atmospheric turbulence limits the relevance of using

mean statistical values to evaluate link quality. In fact, in the case of propagation through turbulence, instantaneous BER increases dramatically because of signal attenuation. The time scale of signal extinction (of the order of the millisecond) is of a few orders of magnitude larger than the time duration of a bit. Other metrics exist to characterise link quality (mean fade time, probability of fade) thus limiting the relevance of average BER as absolute metric for characterising FSOs.

3.1.2 Intensity Statistical Properties

3.1.2.1 Intensity Density Probability Function Estimation

We have seen paragraph 2.2 that different turbulence regimes lead to intensity probability density functions that are either log-normal for weak turbulence or badly theoretically described in the case of strong perturbations. As soon as we leave the Rytov regime, intensity is no longer log-normal.

In the case of atmospheric optical links, the probability density function can be used to calculate the error rate (see paragraph 3.1.1). It is therefore an important quantity for characterising FSO systems. Unfortunately, its theoretical description is badly known. It is difficult to use mean bit-error rate to characterise link quality with numerical simulations. For FSOCS one requires a very low BER (of the order of 10^{-9} or even 10^{-12}). This requires an accurate analytical expression of density probability function and to undertake an extensive statistical study.

Some authors [Majumdar-p-07] have proposed the use of higher-order statistical moment to estimate the PDF. These estimates are still an issue for end-to-end numerical simulations. In parallel, non-parametric methods for estimating PDFs a posteriori exist (Parzen estimator [Parzen-a-62] for example). However they do not significantly decrease the number of realisations required to estimate the PDF relative to a classic Monte Carlo approach.

3.1.2.2 The Gamma –Gamma Law

Some authors [Al-Habash-a-01] propose the use of an empirical law called Gamma – Gamma ($\Gamma - \Gamma$) to describe the intensity probability density collected by a circular aperture. This law is currently frequently used in FSO studies and in particular in signal processing. The model assumes that small-scale intensity fluctuations (diffractive phenomenon) are modulated multiplicatively by large-scale intensity fluctuations (refractive phenomenon). Let $I = I_x I_y$ be the intensity after propagation where I_x and I_y are respectively small and large scale intensity fluctuations. Furthermore we assume that I_x and I_y are statistically independent and can be described by a Gamma distribution. The intensity I will follow a $\Gamma - \Gamma$ distribution.

$$p(I) = \frac{2(\alpha\beta)^{(\alpha+\beta)/2}}{\Gamma(\alpha)\Gamma(\beta)} I^{(\alpha+\beta)/2-1} K_{\alpha-\beta}\left(2\sqrt{\alpha\beta I}\right), I > 0 \tag{3.6}$$

where K_p is the modified Bessel function of the second kind and of order p. α (resp. β) represents the effective number of small (resp. large) turbulent cells. These values can be calculated from

propagation conditions:

$$\frac{1}{\alpha} = \sigma_x^2 = exp\left[\frac{0.49\beta_0^2}{\left(1+0.18d^2+0.56\beta_0^{12/5}\right)^{7/6}}\right]$$
$$\frac{1}{\beta} = \sigma_y^2 = exp\left[\frac{0.21\beta_0^2\left(1+0.69\beta_0^{12/5}\right)^{-5/6}}{(1+0.90d^2+0.62\beta_0^{12/5})}\right]$$

With L the propagation distance, $\beta_0 = 0.5C_n^2k^{7/6}L^{11/6}$ the Rytov variance for a spherical wave, $d = \sqrt{\frac{kD^2}{4L}}$ the dimensionless ratio of the optical diameter by the Fresnel distance and D the diameter of the reception optics.

In weak perturbations, the $\Gamma-\Gamma$ model gives similar results to the log-normal model [Al-Habash-a-01] and is in accordance with simulations done by Flatté et al. [Flatte-a-94]. When turbulence strength increases (up to saturation regime) the intensity probability density function at the level of the collecting lens approaches a negative exponential function [Gochelashvily-a-71, Bissonnette-a-79]. The heuristic $\Gamma - \Gamma$ function can be used to describe the entire spectrum of turbulence regimes and has a good correlation with simulation data [Al-Habash-a-01]. Nevertheless, it is not derived from any analytical model and its validity domain is still to be quantified.

3.1.2.3 Aperture Averaging

An efficient way to mitigate atmospheric turbulence effects is to increase the physical size of the telescope's aperture: called aperture averaging. We have studied paragraphs 2.2.3.3 and 2.2.4 the characteristic size of scintillation grains at the receiver. By averaging several scintillation grains, it is possible to reduce the global scintillation rate. In order to quantify the impact of aperture averaging on the received signal we need to multiply the scintillation rate σ_I^2 calculated for a point receiver by aperture averaging factor A [Fried-a-67, Tatarski-l-71]:

$$\sigma_I'^2 = A\sigma_I^2 \tag{3.7}$$

The aperture averaging factor A is given for a Gaussian collimated beam by [Ricklin-l-08]:

$$A = \frac{16}{\pi}\int_0^1 x\, exp\left(-\frac{D^2x^2}{\beta_0^2} * \left[2 + \frac{\beta_0^2}{w_{z=0}^2\left(\frac{2z}{kw_{z=0}}\right)^2} - \frac{\beta_o^2\phi^2}{w_{z=L}^2}\right]\right) * \left(Arccos\,(x) - x\sqrt{1-x^2}\right) dx, \tag{3.8}$$

where D is the receiver pupil diameter, $w_{z=0}$ and $w_{z=L}$ respectively the beam radius at receiver and emitter without turbulence, $\beta_0 = (0.55C_n^2k^2L)^{-3/5}$ the coherence length of a spherical wave and $\phi \triangleq \frac{kw_{z=0}^2}{2z} - \frac{2z}{k\beta_0^2}$ for a collimated beam. Figure 3.2 shows aperture averaging efficiency for different perturbation regimes and wavelengths. Aperture averaging appears less effective for longer wavelengths. This is due to the fact the pupil averages over less scintillation grains.

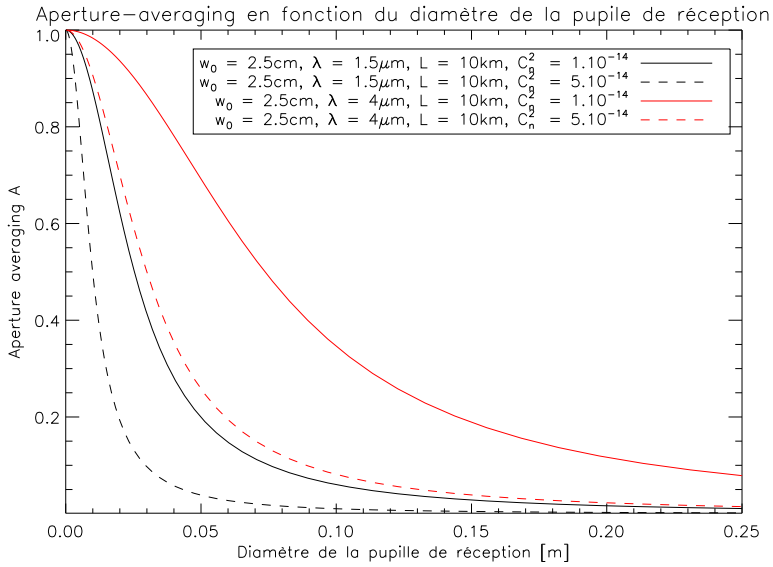

Figure 3.2: PIB fluctuations attenuation factor as a function of receiver pupil diameter for different propagation conditions.

3.1.3 Terrestrial Link

In order to give typical FSOCS link quality in terms of mean BER, this paragraph presents an estimate for typical turbulence conditions. We have shown that the error probability in absence of turbulence is:

$$Pr(E)^{no\ turb} = \frac{1}{2} erfc\left(\frac{I}{2\sqrt{2}\sigma_d}\right), \tag{3.9}$$

where σ_d represents the detection noise taken as constant and I the received intensity. In the presence of turbulence, error probability must be calculated by the conditional probability averaged over the probability density p_I of the collected signal I.

$$Pr(E)^{turb} = \frac{1}{2}\int_0^{\infty} erfc\left(\frac{s}{2\sqrt{2}\sigma_d}\right) p_I(s)ds \tag{3.10}$$

This equation can be used to calculate the error probability with turbulence for a threshold level calculated adaptively [Majumdar-l-08]. Figure 3.3 presents the mean BER $\langle BER\rangle$ with and without turbulence as a function of the mean received intensity $\langle I\rangle$. Various turbulence strengths are presented and are distinguished by their normalised variance $\frac{\sigma_I}{\langle I\rangle}$. Left-hand side curves (resp. right) shows the evolution of the mean BER for a fixed detection noise at $\sigma_d = 1/20$ (resp. $\sigma_d = 1/25$). The probability density function p_I is log-normal. When the pupil diameter at the receiver is sufficiently large to ensure $D > \frac{\lambda L}{r_0}$ or when correction by adaptive optics is efficient, one can indeed assume log-normal statistics. However, it has been shown that log-normal statistics underestimates the behaviour of the tail of the PDF relative to experimental data. Underestimating the tail can lead to important mis-estimations of FSO bit-error rates because

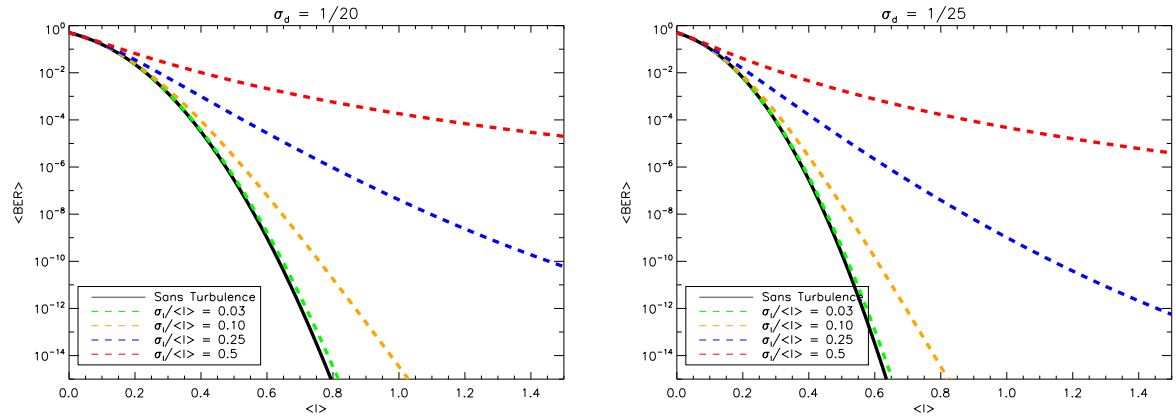

Figure 3.3: Mean BER in presence of atmospheric turbulence as a function of mean received intensity. Right: $\sigma_d = 1/20$. Left: $\sigma_d = 1/25$.

its value is mainly calculated with the tail of the PDF. Nevertheless, we have performed our calculation assuming a log-normal law. Even if it gives slightly optimistic values in terms of link quality, it enables us to give values in terms of classical telecommunication metrics.

Detection noise diminution leads to a better signal-to-noise ratio and a better BER. Without turbulence whereas a received intensity of $I = 0.55$ at $\sigma_d = 1/25$ can lead to a BER of 10^{-12}, one needs to increase received intensity to $I = 0.7$ at $\sigma_d = 1/20$ to reach the same BER value. Let set, as an example, intensity fluctuations to $\frac{\sigma_I}{\langle I \rangle} = 0.25$ and mean intensity to $\langle I \rangle = 0.7$ for a detection noise of $\sigma_d = 1/25$ (in bleu on the right hand side figure). The error rate is $\langle BER_{\sigma_d=1/25} \rangle = 10^{-6}$. In order of achieve a BER of 10^{-12}, closer to typical desired value in optical telecommunications, one needs to double the emitted intensity or equivalently decrease normalised intensity fluctuations by a factor 2.5 (yellow curve).

When turbulence increases, on one hand it will increase the normalised variance $\frac{\sigma_I}{\langle I \rangle}$ and on the other it will decrease the mean received intensity $\langle I \rangle$. In the same way, when atmospheric turbulence is such that we can reach a normalised variance of $\frac{\sigma_I}{\langle I \rangle} = 0.1$ (yellow curve) and an intensity of $\langle I \rangle = 0.7$, the error rate will be $BER_{\sigma_d=1/20} = 10^{-7}$. When turbulence increases to $\frac{\sigma_I}{\langle I \rangle} = 0.25$ (blue curve) and mean intensity drops to $\langle I \rangle = 0.50$, BER is multiplied by a factor 1000. In a less favourable case ($\frac{\sigma_I}{\langle I \rangle} = 0.5$ in red), one cannot reach a rate smaller than 10^{-6} for studied SNRs.

For terrestrial link, turbulence effects are not tolerable. Typical atmospheric conditions lead to intensity fluctuation of the order of $\frac{\sigma_I}{\langle I \rangle} = 0.5$. Increasing optical power in order to limit the error rate is only possible in a certain range of powers and its effectiveness is limited to high $\frac{\sigma_I}{\langle I \rangle}$. The development of system lowering BER significantively is essential.

3.1.4 Estimation of FSO Link in Simulations

We have seen that evaluating performance for FSO links relies on a precise knowledge of the intensity probability density function. In weak perturbations, the distribution is known to be log-normal. Calculating its average and its variance are sufficient to characterise it. Oppositely, in strong perturbations, no satisfactory method exists for characterising it with sufficient precision. It is clear that average and variance will not be sufficient to fully characterise the link quality. However, we will make use of these two statistical moments as criterions to evaluate FSO quality studied in this document and to compare different correction methods envisaged. This approach enables us to free us from limitations related to turbulence regimes (weak or strong) and stay as general as possible. In this document we will thus characterise transmission quality through atmosphere by the average total collected intensity and the normalised standard deviation (or intensity fluctuations):

$$I_{mean} = \langle I \rangle = PIB \text{ mean} \tag{3.11}$$

$$\frac{\sigma_I}{\langle I \rangle} = \frac{\sqrt{\langle I^2 \rangle - \langle I \rangle^2}}{\langle I \rangle} \tag{3.12}$$

where $\langle . \rangle$ represents the ensemble average and I the intensity integral of field ψ_R in the reception telescope pupil $\mathcal{P}_R$ normalised over the total emitted flux:

$$I = PIB = \frac{\int |\psi_R(\mathbf{r}')|^2 \mathcal{P}_R(\mathbf{r}') d\mathbf{r}'}{\int |\psi_E(\mathbf{r})|^2 d\mathbf{r}}, \tag{3.13}$$

where index R (resp. E) represents the reception plane (resp. emission) and ψ the complex field. Using two separate metrics to evaluate link quality can lead to problems when evaluating performance. Some authors [Xiao-p-07] have proposed a meta-metric Δ containing the two previous metrics: $\Delta = \langle I \rangle (1 - \sigma_I / \langle I \rangle)$. This choice is clearly arbitrary and other meta-metrics could be equally used. In this document the two metrics will be studied independently.

3.2 Turbulence Effects Attenuation Methods

We have seen that turbulence can highly perturb link quality and even more so when propagation distances are large. Several techniques have been put forward to mitigate turbulence effects. We will briefly present them in this paragraph. The presented methods are not exhaustive but represent the classical techniques used to improve the link budget of an FSOCS in a terrestrial environment.

3.2.1 Diversity Methods

Diversity methods consist in using the transmission's channel (here Earth's atmosphere) decorrelation (either spatial, temporal or in wavelength) to mitigate the impact of turbulence.

Each channel being statistically independent, atmospheric turbulence will have a different impact and turbulence will be mitigated by averaging its effects. To a first approximation, it is equal to dividing σ_I^2 by N where N is the number of channels. The different possible methods are not exclusive and can be used in synergy within a FSO system. All diversity methods require a synchronisation procedure between received signals. These different atmospheric turbulence mitigation techniques have been studied from a signal processing point of view by Khalighi [Xu-a-09, Khalighi-a-09-b].

3.2.1.1 Wavelength Diversity

Wavelength diversity consists in emitting information redundantly, through the same optical path, by using several beams with different wavelengths. Unfortunately, an important part of scintillation effects are from geometric not diffractive origin. Atmospheric turbulence dependence to wavelength is small and the different propagation channels are only weakly decorroleted. For this reason, only a modest reduction in scintillation index is obtained when using diversity with several emitting wavelengths [Kiasaleh-a-06, Peleg-a-06]. The reduction in scintillation index is limited to the order of 10% [Kiasaleh-a-06]. A better mitigation would be obtained by using two beams with very different wavelengths. It is unfortunately, difficult to design a performing optical system optimised for such wavelengths.

3.2.1.2 Multiple Input and Multiple Output Diversity

In order to reduce the impact of turbulence, it is possible to use several emitting laser beams (multiple-input-single-output or MISO). Oppositely to the previous case, emitter diversity relies on the spatial decorrelation of turbulence. The different laser beams propagate in different optical channels. Adding several lasers incoherently to each other can be seen as reducing the emitting laser coherence [Polynkin-a-07]. This leads to a reduction of the scintillation rate [Voelz-p-04, Ricklin-l-08, Baykal-a-09]. Complexity and implementation costs, requiring a complex alignment source and the generation of a large number of incoherent sources, can lead to very expensive systems. In order to fully take advantage of emission diversity, it is best to separate beam from a distance of at least $\simeq \rho_0$.

It is similarly possible to use a reception system with several receptors: reception diversity (i.e. single-input-multiple-output or SIMO). Such systems generally are composed of several reception pupils that can be used to average received signals. From a conceptual point of view, such systems a very similar to using a large pupil (aperture averaging). Implementation simplicity of such a method has driven study of these systems [Belmonte-a-97, Razavi-p-05, Khalighi-a-09-b].

3.2.1.3 Temporal Diversity

Coherence time of the transmission channel (i.e. atmosphere) is relatively long compared to the typical duration of a bit. It is typically of the order of the millisecond compared to nanoseconds. It is therefore possible to transmit information several times [Xu-p-08, Xu-a-09] to take

advantage of the atmospheric turbulence temporal decorrelation. The latency between two successive data transmissions must be superior to the atmospheric correlation time. If the error probability is p_e then the joint probability of temporal diversity will be p_e^2. The typical correlation time is of the order of 10 ms [Davis-p-02]. Unfortunately, this technique has a relative small interest compared to classical wavelength multiplexing solutions (WDM). In addition, when the size of the reception pupil is large than coherence time is large compared to the total bit duration. Long coherence times imply large buffer memories (of the order of $\propto 10^6$ bits). In practice, it is difficult to use temporal diversity for large pupil diameters [Khalighi-a-09-b].

3.2.2 Beam Shaping

3.2.2.1 Static Case

So far we have only considered Gaussian beams. This particular beam geometry is not always the most appropriate one for FSOCS in turbulence. Some authors have proposed the use of other beam shapes [Li-p-05, Cai-a-08]. Analytical derivations by [Eyyuboglu-a-06] propose in particular dark hallow beams in the case of weak perturbations. As an example, the beam geometry modification can change the scintillation rate from 0.8 for Gaussian beams to 0.65 for asymmetric dark hallow beams. These results are only valid in weak perturbations. When turbulence strength increases towards strong perturbations, the initial beam geometry has little impact on the final state of the beam geometry after propagation. The beam tends to be Gaussian on average regardless of the beam geometry at origin.

Particular reception telescope pupil geometries (central obscuration for Cassegrain telescopes for example) can lead to optimal beam geometry other than Gaussian. Mansell [Mansell-p-06] proposed to use a relay mirror in order to shape the beam and maximise the coupled energy between two Cassegrain telescopes. Others [Li-p-05] proposed to modify the Gaussian shape to an annular beam to maximise coupling efficiency. Moreover, it has been shown [Henderson-p-08, Carbon-p-03] that it is possible to use a deformable mirror to shape the beam (super circular Gaussian, super square Gaussian, circular ring, square ring) at emission or reception.

3.2.2.2 Dynamical Case

Atmospheric turbulence effects evolve rapidly over time. In order to mitigate these effects, it is possible to modulate in real-time emission phase and amplitude to minimise flux fluctuation at the reception (PIB). Similar to static beam shaping that enables us to diminish turbulence effects on average, dynamic shaping can mitigate its effects at every instant in time by pre-compensating perturbations.

A possible option for dynamically modulating phase and amplitude of the emitted field is adaptive optics (AO). The purpose of this document is to estimate the possible gain and limitations using AO methods. The following chapter will discuss AO techniques as implemented and proposed in the literature.

3.3 Conclusion

In this chapter we have studied the characterisation of atmospheric turbulence effects on free-space optical communications. In typical turbulence conditions and for anticipated configurations, atmospheric turbulence makes communication link unreliable. This is the reason why numerous mitigation solutions have been proposed in the literature, such as diversity methods or adaptive optics. Diversity methods are simpler to implement but generally do not enable a sufficient gain for long distance FSOCS. AO appears as the only solution to mitigate turbulence sufficiently and improve FSO link quality.

Chapter 4

Precompensation Methods

Contents

Adaptive optics was first proposed by Babcock [Babcock-a-53] in 1953 and independently by [Linnick-a-57] Linnick in 1957 for improving astronomical images. Because of prohibitive costs of research and implementation it was not possible at the time to build such systems. One of the very first adaptive optics system dates from 1977 [Hardy-a-77]. One needs to wait until 1989 for astronomical applications with the COME-ON project [Rousset-a-90]. Nowadays, adaptive optics systems equip the vast majority of world's telescopes (VLT, Keck, Gemini...). Numerous other applications are emerging using adaptive optics such as retinal imaging or free-space optical communications. We will first introduce the principal of adaptive optics (§4.1.1) and of wavefront sensing (§4.1.2) to then elaborate on modal phase analysis in weak perturbations (§4.1.3) and limitations in strong perturbation regimes (§4.1.4).

Endo-atmospheric laser beam propagation through turbulence produces phase and amplitude perturbations. Adaptive optics, which can act directly on the phase of electromagnetic fields, seems the tool of choice for correcting perturbations. Laser beam precompensation by adaptive optics although promising, is hindered by its implementation complexity. Strong perturbations make wavefront sensing difficult and correction by classical adaptive optics approaches used in

astronomy generally inefficient. Various methods of mitigating atmospheric turbulence by AO in FSOSC have been proposed in the literature. The method that is the closest to AO correction concepts used in astronomy is a correction where the wavefront sensing is performed on a counter-propagating laser beam (§4.2.1) and was first proposed in the 70's. Another classical approach consists in directly optimising the received intensity in the pupil by modulating the emitted phase (§4.2.2). This method can free oneself form problems related to wavefront measurements. Finally, a theoretical approach proposed by Barchers [Barchers-a-02-b] leads to the optimal solution by using a phase and amplitude correction (§4.2.3). To conclude, and in order to clarify the numerical simulation framework, we will present the nominal conditions that will be used throughout the following chapters.

4.1 An Introduction to Adaptive Optics

4.1.1 Adaptive Optics Principle

Adaptive optics (AO) is a servo-controlled system that aims at the real time correction of wavefront distortions. Measurements of the optical distortions are done by a wavefront sensor. The correcting element is generally a deformable mirror. Adaptive optics bloc diagram is presented figure 4.1.

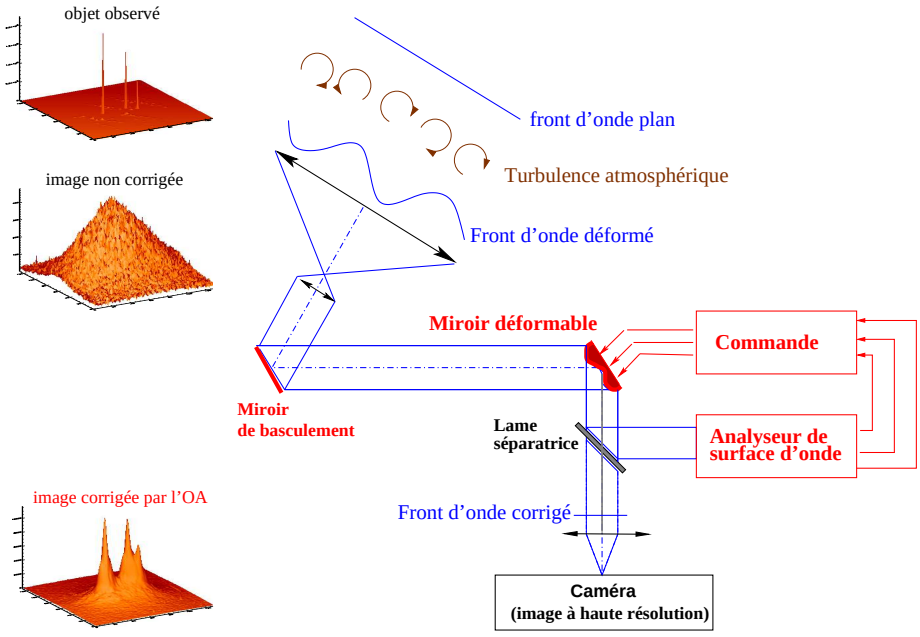

Figure 4.1: Adaptive optics bloc diagram for stellar imaging.

4.1.2 Wavefront Sensing

In is not possible with today's technology to directly measure the phase of a wavefront in the optical as it is possible for radio waves. No optical detector can work at the high temporal frequencies involved. One typically goes around this issue by indirect measurements that is by measuring the impact of phase perturbations on intensity distribution. Rousset [Rousset-l-99] has realised a complete description of wavefront sensors for adaptive optics. We will only mention here the properties of the Shack-Hartmann wavefront sensor. This sensor is the commonly used in adaptive optics and its limitations are representative of most pupil plan sensors.

Principle of the Shack-Hartmann

The Shack-Hartmann (SH) wavefront sensor (WFS) is a pupil plan wavefront sensor (cf. figure 4.2) relying on geometrical optics formalism [Shack-a-71]. A grid of lenslets samples the

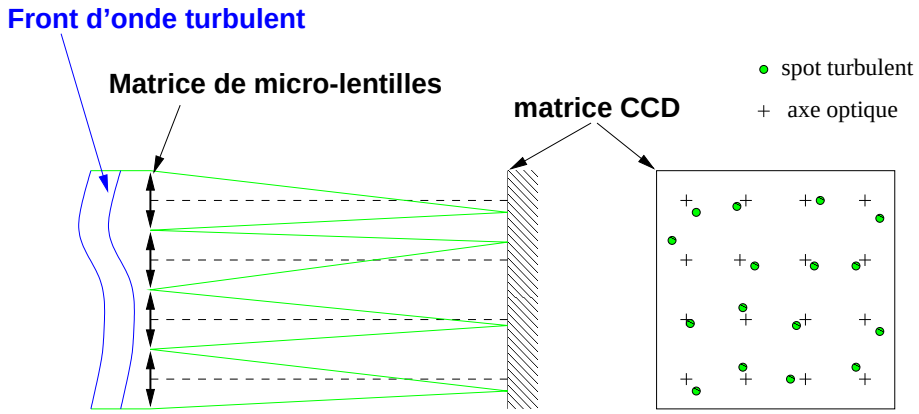

Figure 4.2: Shack-Hartmann wavefront sensor bloc diagram.

incoming wavefront in the pupil plan. The measured positions of the focal spots formed by each lenslet give access to the local slopes in the pupil plan for each lenslet. The measurement of the spot position is generally done by centre of gravity (COG), but other position estimators can be used such as correlation for example [Poyneer-a-03]. The slope measured with the COG in lenslet k is respectively for direction x and y:

$$p_x^k = \frac{\iint_{sspup} d\mathbf{r} \frac{\delta\varphi_k(\mathbf{r})}{\delta x} \left|\psi_k(\mathbf{r})\right|^2}{\iint_{sspup} d\mathbf{r} \left|\psi_k(\mathbf{r})\right|^2}$$

$$p_y^k = \frac{\iint_{sspup} d\mathbf{r} \frac{\delta\varphi_k(\mathbf{r})}{\delta y} \left|\psi_k(\mathbf{r})\right|^2}{\iint_{sspup} d\mathbf{r} \left|\psi_k(\mathbf{r})\right|^2}, \tag{4.1}$$

where the index $sspup$ indicates that the integration is performed over the surface of lenslet k, φ_k is the phase and $|\psi_k|$ the complex field amplitude. When the intensity is constant over the lenslet, slope measurement is an average over the lenslet surface.

Undersampling and Aliasing

Phase estimation is limited by the spatial sampling of phase in the pupil; that is directly linked to the number of lenslets. To a first approximation in astronomy (i.e. for weak perturbations) the number of lenslets used to measure phase is approximately equal to the radial order of Zernike polynomials used to decompose the phase. The phase estimation error due to undersampling is given by Noll's equation (see equation 4.8) which represents the wavefront estimation sampling error.

Wavefront spatial frequencies above the cut-off frequency will produce aliasing. One can admit that to a first approximation aliasing error is close to a few tens of percent of undersampling error.

Noise Sources

The centre of gravity measurement for each of the lenslets is affected by noise. Two main sources of noise are generally taken into account [Rousset-l-99].

- Photon noise:

$$\sigma^2_{photon} = \frac{\pi^2}{2}\frac{1}{N_{ph}}\frac{X_T^2}{X_D^2}\,[radian^2], \tag{4.2}$$

  where X_T is the full width half maximum of the focal plan image spot, X_D the full width half maximum of the image spot limited by diffraction and N_{ph} the number of photons received by each lenslet during integration time. X_T and X_D are given in pixels.

- Detector noise :

$$\sigma^2_{detector} = \frac{\pi^2}{3}\frac{\sigma^2_{e^-}}{N^2_{ph}}\frac{X_S^4}{X_D^2}\,[radian^2], \tag{4.3}$$

  where X_S^2 is the number of pixels taken into account in the centre of gravity calculation

Precision of wavefront measurement is directly function of SNR and of the collected flux over each lenslet.

4.1.3 Weak Perturbations: Modal Analysis of Turbulent Phase

4.1.3.1 Zernike Polynomials

Zernike polynomials form an orthogonal polynomial basis on a circular grid. The polynomials are expressed as function of their radial order n and of their azimuthal frequency m:

$$Z^{n,m}(\mathbf{r}) = R_n^m(r)\Theta_n^m(\theta) \tag{4.4}$$

They are arranged by index $i = n + m$. The analytical expression of $R_n^m(r)$ and $\Theta_n^m(\theta)$ are given by Noll [Noll-a-76]. Figure 4.3 represents the first 21 Zernike polynomials. We can recognise the first orders of the Seidel classical aberrations (coma, astigmatism ...).

4.1.3.2 Phase Statistical Properties and Zernike Polynomials

Using Zernike polynomials, it is possible to decompose turbulent phase $\varphi(\mathbf{r})$ by the following:

$$\varphi(\mathbf{r}) = \sum_{i=1}^{\infty} a_i Z_i(\mathbf{r}), \tag{4.5}$$

By choosing the Zernike polynomials normalisation proposed by Noll [Noll-a-76], the total phase variance $\varphi(\mathbf{r})$ can be expressed directly as:

$$\sigma_{\varphi}^2 = \frac{1}{S}\int_S \left\langle \varphi(\mathbf{r})^2 \right\rangle d\mathbf{r} = \sum_{i=1}^{\infty} \left\langle a_i^2 \right\rangle \tag{4.6}$$

By using Kolmogorov spectrum Noll [Noll-a-76] gives the analytical expression of the variance of theses coefficients. Figure 4.4 presents the Zernike coefficients variance for the first 200 orders. It illustrates the fact that low orders are the most highly stimulated orders and that they will have the most impact on the total phase variance. Expression of the total variance (after subtraction of the piston mode) of the turbulent phase is given by [Noll-a-76]:

$$\sigma_{\varphi}^2 = \sum_{i=2}^{\infty} \left\langle a_i^2 \right\rangle = 1.03 \left(\frac{D}{r_0}\right)^{\frac{5}{3}} \tag{4.7}$$

An empirical law [Noll-a-76] gives the residual variance after perfect correction of the first j Zernike polynomials:

$$\sigma_{\varphi,j}^2 = 0.2944 j^{\frac{-\sqrt{3}}{2}} \left(\frac{D}{r_0}\right)^{\frac{5}{3}} \tag{4.8}$$

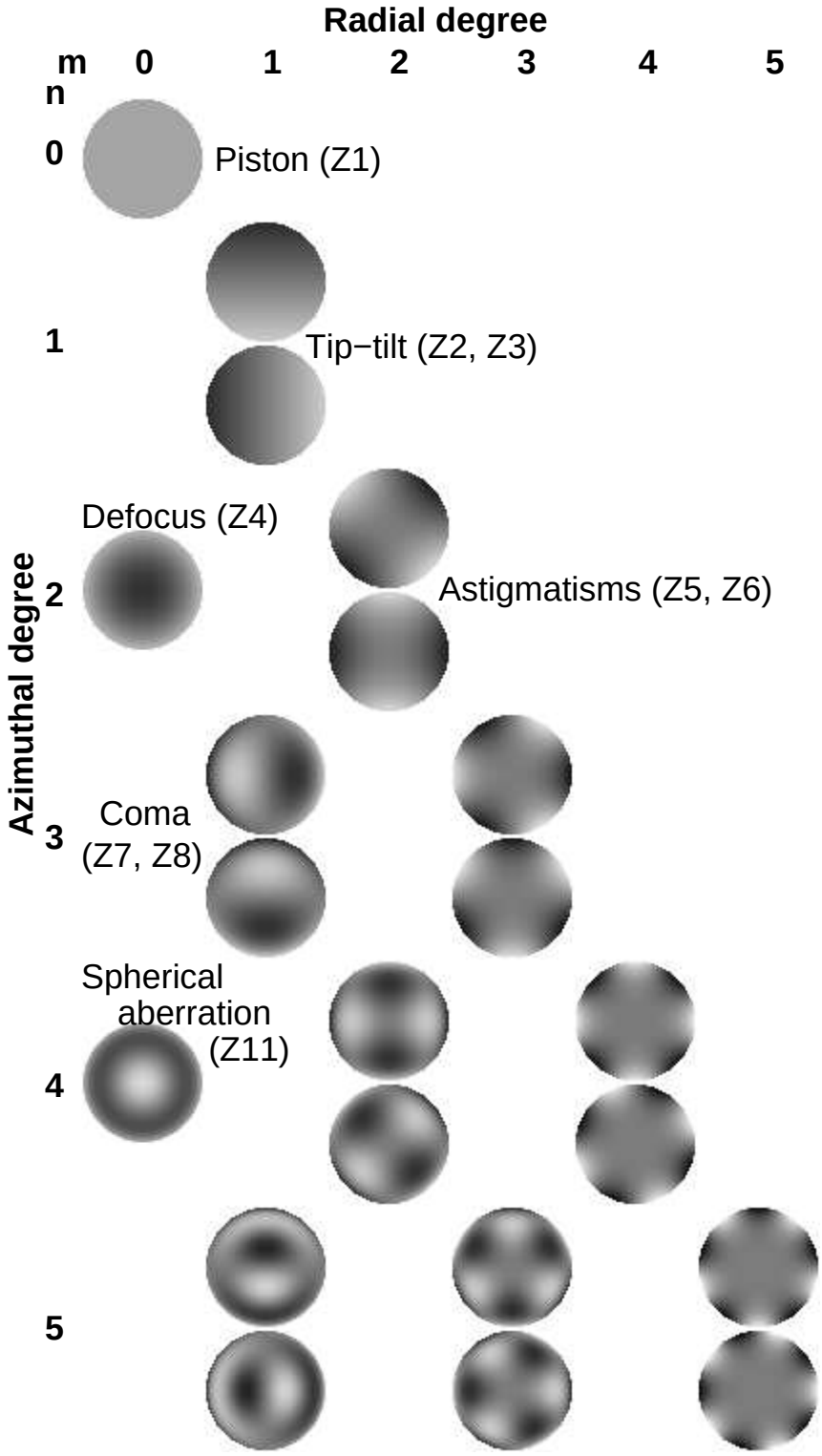

Figure 4.3: The first 21 Zernike polynomials arranged by radial orders and azimuthal. The first polynomial orders correspond to the classical optical aberrations.

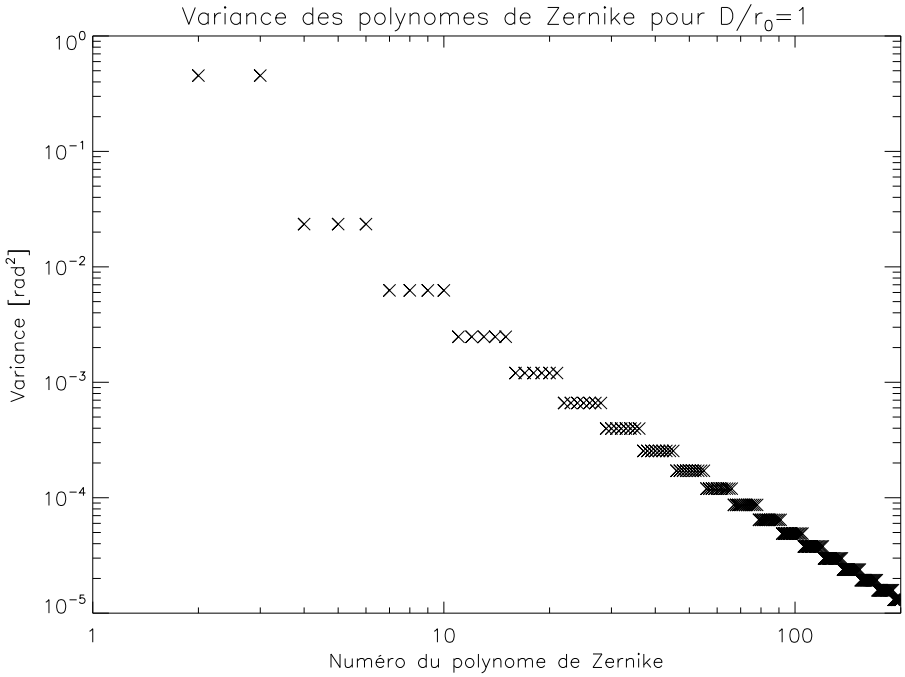

Figure 4.4: Theoretical Zernike coefficient variance for the first 200 orders by assuming Kolmogorov statistics for the turbulent phase. Numerical values correspond to a $D/r_0 = 1$.

4.1.4 Adaptive Optics Limitations in Strong Perturbations

First applications of adaptive optics where mainly developed for astronomical observations. In the case of endo-atmospheric propagations, characteristics of the highly perturbed field introduces new constrains in the use of classical adaptive optics[Primmerman-a-95]. The interest of adaptive optics in imaging configurations in highly turbulent conditions is still a subject of current research [Vedrenne-t-08]. These constrains and limitations are introduced by three highly coupled phenomenon: scintillation, branch points and anisoplanatism [Fried-a-92].

4.1.4.1 Scintillation Effects

Scintillation is the development of strong high-intensities and low-intensities or even zero intensity (i.e. non-uniform illumination). Its main impact is to create errors in the phase estimation. Firstly, according to equations 4.1, we have seen that local slope measurements are directly linked to the flux in each lenslet. When illumination is not uniform over the lenslet, slope measurement will be biased [Mahe-p-00, Voitsekhovich-a-01]. Secondly, when the lenslet receives no or very little flux, measurement noise will dominate the signal to be measured: phase will not be calculated correctly. These errors both depend on turbulence strength and lenslet size.

4.1.4.2 Branch Points

Let Ψ be the complex field of an electromagnetic wave. The wave phase φ is defined when the amplitude of the field is not equal to zero by: $\varphi \triangleq arctan\frac{\Im(\Psi)}{\Re(\Psi)} \triangleq arg\,(\Psi)\,[2\pi]$. Increase in turbulence strength leads to an increase in scintillation. The probability of obtaining points of zero intensity is no longer negligible in strong perturbations. When intensity is equal to zero, phase is undetermined. This singularity provokes a wavefront discontinuity called branch point [Fried-a-92]. Obviously, field and phase defined modulo 2π is continuous. Figure 4.5 presents module and phase of the electromagnetic field after propagation under strong turbulence conditions. Numerous phase wrapping and branch points (points 1 and 2 on figure) are present in the phase and are caused by field amplitude cancellation (points 1' et 2').

The appearance of phase discontinuities has several consequences. Firstly, geometric wavefront sensors measuring gradients or local curvatures of the wavefront become ill-fitted because they rely on geometric approximation and continuity of the wavefront [Lukin-a-02]. This is why certain authors have proposed to directly drive the deformable mirror without relying on a pupil plan sensor [Vorontsov-a-97]. Correction of phase perturbations by continuous surface (such as deformable mirrors) becomes ineffective justifying the use of segmented mirrors [Lukin-a-02].

4.1.4.3 Anisoplanatism

Two electromagnetic waves coming from two different directions will not go through the same turbulence volume. These two waves will not suffer from the same perturbations and are angularly decorrelated. For endo-atmospheric propagation, angular decorrelation in the field is very high and problems linked to the isoplanatic patch (that is the area of the field for which one can consider the point spread function as invariant) are even more important than for astronomy

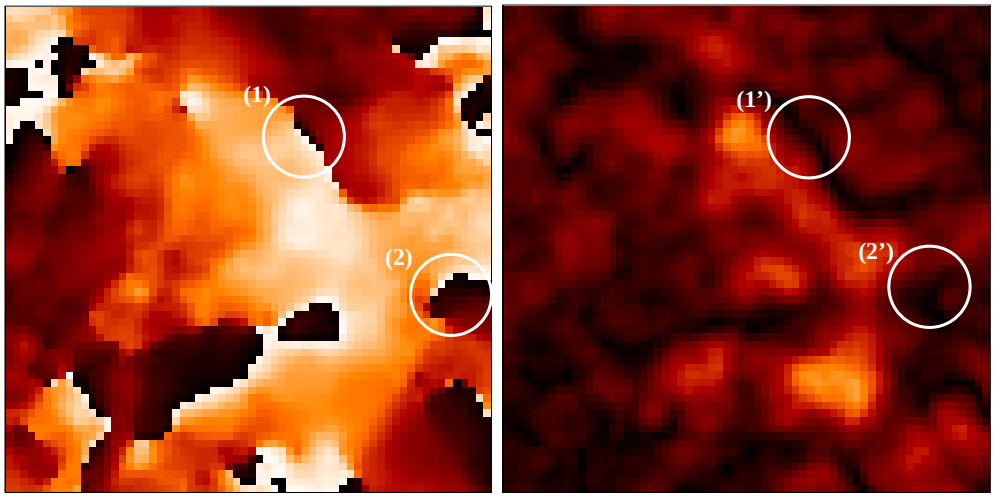

Figure 4.5: Phase φ (Left) and modulus $|\psi|$ (Right) of the field for strong perturbation conditions ($\sigma_R^2 = 7$).

[Fried-a-82]. Figure 4.6 presents a diagram of anisoplanatism. The two sources come from different directions and do not go through the same volume of turbulence: perturbations are angularly decorrelated.

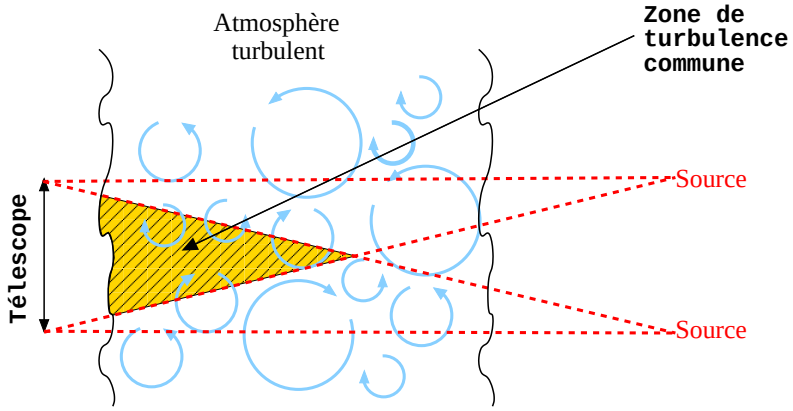

Figure 4.6: Anisoplanatism diagram.

As a consequence, correction performed by a DM located in the pupil plan is appropriate only in the direction of the sensor. It appears that anisoplanatism significantly limits the angular field of correction for classical AO systems design for imaging. For FSO, where the correction field is small (on-axis correction), this limitation will have only a small impact. However, as we will see paragraph 7.3 when reducing turbulence effects on the wavefront measurements, anisoplanatism will play a dominant role in the final correction quality, especially when several laser sources are used throughout the field.

4.2 FSO Precompensation by Adaptive Optics

An efficient way to correct the impact atmospheric turbulence on a free-space optical communication system is to use adaptive optics precompensation. In the following paragraph, we will present the principal methods of interest. We will study their implementation and expected performance in the following chapters. One of the biggest challenges of an AO correction for FSOCS is the presence of strong turbulence along the propagation path. Turbulence produces strong optical perturbations and makes AO implementation difficult and often inefficient. Another issue is the fact that turbulence is distributed over the volume of the propagation path whereas the correction is often performed in a single plane. Moreover, phase and amplitude are decorrelated in strong turbulence. One needs to correct them independently.

One can distinguish between three main AO corrections which are presented in more details later in the document. The classical approach, similar to AO applications in astronomy, consists in performing correction in a single iteration step by using a wavefront sensor (§4.2.1). Direct optimisation of a criterion without an *a priori* model for data formation (§4.2.2) can be seen as an attractive solution whenever wavefront sensing is difficult (i.e. strong turbulence). The third approach (§4.2.3) is a hybrid solution between classical method and iterative approach typical of criterion minimisation. This approach, that we will later called optimal correction, consists in correcting both phase and amplitude iteratively.

4.2.1 Correction on Counter-Propagating Beam

In 1972, Fried and Yura [Fried-a-72] then Fante [Fante-p-75] suggest using adaptive optics to compensate for angle of arrival fluctuations in laser communication between Earth and space. A laser beam launched for space towards the ground is sent to probe turbulence. Atmospheric channel reciprocity [Fried-a-72] enables in particular to precompensate for pointing errors due to turbulence on the beam emitted from the ground. The optimal beam to be sent from ground is simply obtained by inverting propagation direction of the received laser beam probe. If only the phase part of the beam is to be precompensated, the electromagnetic field is equal to:

$$\Psi'\left(z=0,\mathbf{r}'\right)=\Psi_0\left(z=0,\mathbf{r}'\right)exp\left[-i\varphi_1\left(z=0,\mathbf{r}'\right)\right], \tag{4.9}$$

where Ψ' is the emitted field, Ψ_0 the field we wish to send in the absence of turbulence and φ_1 is the phase of the received field (probe beam propagating from space to the ground).

It is possible to show on the one hand [Lutomirski-a-71] that solution to the propagation equation (see equation 2.7) can be obtained by:

$$\Psi\left(z,\mathbf{r}\right)=\frac{1}{\lambda iz}\iint_{-\infty}^{\infty}\Psi\left(z=0,\mathbf{r}'\right)exp\left[\frac{ik\left(\mathbf{r}-\mathbf{r}'\right)^2}{2z}+\chi_1\left(\mathbf{r},\mathbf{r}'\right)+i\varphi_1\left(\mathbf{r},\mathbf{r}'\right)\right]d^2\mathbf{r}', \tag{4.10}$$

where $\Psi\left(z=0,\mathbf{r}'\right)$ is the field at $z=0$ and $\chi_1\left(\mathbf{r},\mathbf{r}'\right)$ and $\varphi_1\left(\mathbf{r},\mathbf{r}'\right)$ are respectively log-amplitude and phase random fluctuations of a spherical wave propagating in a turbulent media from point $\left(z=0,\mathbf{r}'\right)$ towards a point $\left(z,\mathbf{r}\right)$. When atmospheric turbulence is close to the emitter (as for

example in ground to space links), log-amplitude fluctuations are negligible (that is $\chi_1 \simeq 0$) and only phase fluctuations need to be taken into account. It is obvious from equation 4.10 that only correcting for phase will be sufficient as soon as turbulence is close to the emitter. Furthermore, telescope pupil diameter needs to follow the inequality: $r_{0_{os}} > D$, where $r_{0_{os}}$ represents the Fried parameter for a spherical wave and D the telescope diameter. When D becomes greater than $r_{0_{os}}$, the DM is no longer able to correct for phase perturbations over the entire field because of anisoplanatism effects (see 4.1.4.3).

4.2.1.1 Principle

Phase correction diagram using a counter-propagating probe is shown figure 4.7. Telescope number 1 ($T1$) is the emitting telescope from which the beam carrying the information is launched. This beam will be later called the telecom beam (in red on the diagram). Telescope $T2$ is the reception telescope. The beam sent by $T2$ propagate in opposite direction relative to the telecom beam. The counter-propagating beam or probe is in blue on the diagram. The probe beam enables the system to measure the wavefront at $T1$.

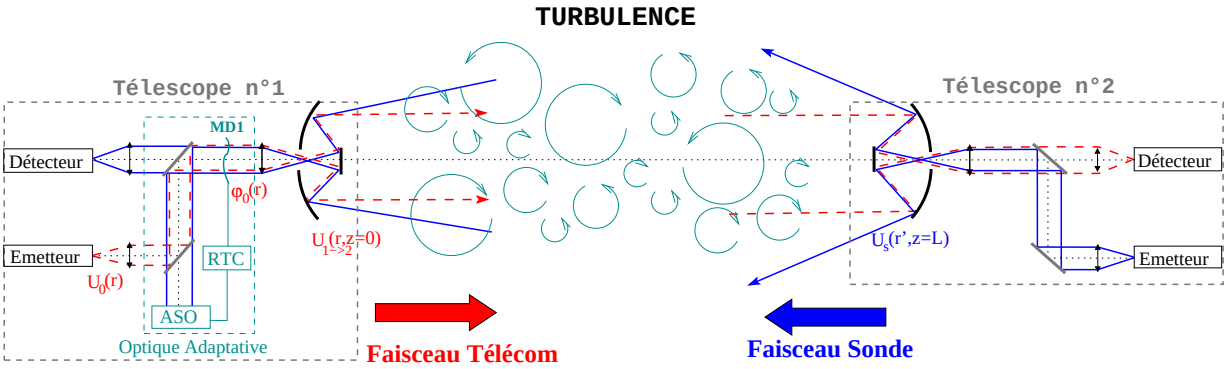

Figure 4.7: Phase correction diagram using a counter-propagating probe.

The steps needed to perform phase correction with a counter-propagating laser beam probe are the following:

- The laser beam probe $U_s(r', z = L)$ is launched from the reception telescope $T2$ towards the emission telescope $T1$. This beam must have sufficient beam divergence, as we will later see, in order to compensate for pointing errors and turbulence effects while still illuminating the entire telescope $T1$ pupil. This will enable the system to perform wavefront measurements.

- After propagation through turbulence, beam $U_s(r, z = 0) = |U_s(r, z = 0)| e^{i\varphi_s(r,z=0)}$ arrives at $T1$. In a similar way to guide stars (either natural or laser) used in astronomical adaptive optics, the probe beam helps measuring phase perturbations encountered by the laser beam.

- Telescope's $T1$ AO system modifies the DM surface ($MD1$ on diagram) in order to compensate for perturbations encountered by the laser probe when propagating through atmospheric turbulence.

Telecom beam $U_{1\to 2}(r, z=0)$ launched by telescope $T1$ sees its phase modified by $MD1$ so that:

$$U_{1\to 2}(r, z=0) = |U_0(r, z=0)|\, e^{-i\varphi_s(r,z=0)}$$

This implementation strategy (classical adaptive optics) is typically used in astronomy where the near field approximation is valid and where the impact of perturbations on data formation is linear. For endo-atmospheric propagations, it has been recorded that near field approximation is no longer valid. Strong scintillation reduces correction quality.

4.2.1.2 Implementation Strategies

Several implementation strategies have been proposed for wavefront correction with a counter-propagating laser probe. They can be distinguished by their configuration relative to turbulence distribution along the propagation path. One can classify them into three main categories: low-altitude horizontal propagation, slant-path propagation and high-altitude propagation (typically between two mountaintops).

Horizontal Propagations

Low-altitude horizontal propagation is the most restrictive configuration because turbulence is distributed almost uniformly along the propagation path and because C_n^2 values are generally high. Primmerman [Primmerman-a-95] in 1995 has undertaken a experimental validation for horizontal propagation over a distance of 5.5 km and an average height above ground of 68 m. Most investigations lead at that time have been for weak turbulence conditions [Primmerman-a-91]. Primmerman shows a strong AO correction quality degradation as turbulence strength increases. The main reason for the quality degradation is the appearance of branch points and scintillation. Numerous branch points can appear; over a hundred for $\sigma_R^2 > 12$ and a pupil diameter of $D = 15$ cm.

Laboratory experimental validations [Tyson-a-03, Tyson-p-05-b], have shown BER reduction for turbulence conditions between $0.8 < D/r_0 < 2.3$. Pre-compensation is limited to the first Zernike polynomials. However, BER estimation has been performed with the Gamma-Gamma model which validity domain is still unclear. Moreover, when turbulence strength increases, the improvement brought by AO drops dramatically. As an example, BER reduction is limited to approximately 1.4 for $D/r_0 = 2.3$.

Slant-Path Propagations

Propagation on a slant-path is a favourable case as far as turbulence distribution is concerned. Most of the turbulence is concentrated near the ground which generally reduces σ_R^2 and the number of branch points relative to a horizontal propagation. Moreover, as we have previously seen, it is a favourable distribution for AO correction whenever the emitter is located near the

ground. When the emitter is high above ground, turbulence is near the receptor. This does not create scintillation and only slightly perturbs the optical link. Field experiments have been carried out [Sova-p-06] between a ground station and aerostat located $1.2\,\mathrm{km}$ away and $1\,\mathrm{km}$ above ground. These favourable conditions for turbulence, the authors were able to reach a very high data throughput ($\simeq 40\,\mathrm{Gbit}$) for a small bit-error rate ($BER < 10^{-6}$). In parallel, AOptix Technologies Inc. sells military grade communication systems that can be used to create a data link between a summit and the ground, taking advantage of the favourable turbulence distribution once again.

Optical Link between two summits

A simple solution in order to increase propagation distance while keeping bit-error rate low is to increase the average propagation altitude. Turbulence strength decrease with altitude as $h^{-4/3}$, where h is the height above ground. By using an AO system correcting for the first 30 Zernike modes, Northcott et al. [Young-p-07, Northcott-p-07] have demonstrated the possibility of creating a FSOCS between two mountains on the Hawai'i islands. The average height for the telescopes of approximately $3000\,\mathrm{m}$, can free the system from most atmospheric turbulence issues. The authors have estimated turbulence strength approximately to $C_n^2 \simeq 2\ 10^{-17}\,\mathrm{m}^{-2/3}$ which keeps the turbulence within the intermediate or weak perturbation regimes. Only turbulence close to the reception and emission telescopes needs to be corrected for.

4.2.1.3 Limitations

We have seen that in order to mitigate the impact of anisoplanatism, it is necessary to guaranty $r_{0_{os}} > D$. This constrain puts a limit on correction effectiveness to small pupil sizes, not taking fully advantage of aperture averaging. Moreover, equation 4.10 shows that when log-amplitude fluctuations are no longer negligible, one must correct both phase and amplitude of the field. As currently no phase and amplitude system exists, correction system effectiveness is limited to weak perturbations.

4.2.2 Phase Modulation Correction

The classical approach for compensating atmospheric perturbations by adaptive optics is based on wavefront sensing and its reconstruction [Roddier-l-99]. In order to apply this technique to free-space optical communications, part of the received beam must be used to perform wavefront measurement. This strategy has been successfully implemented in a number of systems and in particular for astronomy applications [Rousset-a-90]. For these applications, phase perturbations are located in the near field of the receptor. It is generally possible to neglect scintillation effects. When phase perturbations are distributed in the volume along the propagation path and scintillation is no longer negligible, wavefront measurement and its reconstruction is difficult. This specific phase perturbations distribution is typically encountered in FSOCS.

In order to go around the problem of wavefront measurements in strong perturbations; wavefront control of the DM can be performed by a direct control of the DM shape without preliminary phase measurement. This optimisation is achieved by a model free optimisation. This

concept was proposed at the very beginning of adaptive optics end of 1970 in order to improve image quality and laser beam propagation [Buffington-a-77, McCall-a-77]. However, this technique was rapidly disregarded because the estimation of the objective function was incompatible with the bandwidth available at the time. Several optimisation methods have been proposed, such as le multi-dithering [Omeara-a-77] and sequential perturbations [Hardy-p-78]. More recently, Vorontsov *et al.* have proposed a stochastic parallel gradient descent (SPGD) optimisation [Vorontsov-a-97, Vorontsov-a-00] and the decoupled stochastic parallel gradient descent (D-SPGD) [Vorontsov-a-02] that can increase convergence speed.

Deformable mirrors developments, fast real-time calculators (RTC) in addition to powerful algorithms enables the implementation of such correction strategies. However, the necessary bandwidths still generally stays a few orders of magnitude higher that those necessary for systems using a WFS. In addition, it is impossible to guaranty the optimality of the solution due to the high non-convexity of the problem. The significance of this correction strategy lies in its capacity of overcoming strong turbulence issues (i.e. scintillation, branch points). This is only possible by degrading the bandwidth. Astronomy observation is generally performed in weak turbulence conditions. This is the reason this solution has not been kept as an implementation strategy.

4.2.2.1 Principle

Figure 4.8 presents a possible implementation diagram for the correction by optimisation. A field $U_E(r, z = 0)$ (in red on the diagram) is sent by telescope $T1$. This beam represents the telecom beam containing the information T_X to be transmitted. Field $U_R(r', z = L)$ is received by telescope $T2$ after propagation through atmospheric turbulence. $U_R(r', z = L)$ enables the transmission of the received signal R_X. From the received field, metric J (i.e. objective function) is calculated or measured. For example, this metric can be taken as phase, intensity distribution in the emitting pupil or the total collected intensity by the pupil ... Metric J (in blue on the diagram) is then sent back to by telescope $T1$. The transmission can, for example, either be performed by a low throughput radio connection or a counter-propagating optical link. Temporal evolution of the metric is used by the real-time calculator to compute the voltage to be sent to the DM. DM tensions computation and global performance of the system is strongly linked to the algorithm implemented.

4.2.2.2 Implementation for FSOs

Several implementation strategies of direct optimisation by phase modulation have been proposed [Weyrauch-l-08]. Classical methods using a single deformable mirror [Loizos-p-06, Vorontsov-a-00] have been studied both in simulations and experimentally. The use of hybrid solutions combining both wavefront sensing methods and direct optimisation [Vorontsov-a-02, Weyrauch-a-05] have also been proposed and validated experimentally over a distance of several kilometres. These systems take advantages of the fact that it is easier to measure low-orders of the turbulence with a sensor, even in the presence of scintillation, to correct tip-tilt independently. Higher-order modes are corrected by direct optimisation by algorithms such as SPGD. In order to circumvent strong scintillation and anisoplanatism issues on the laser beam probe, it is

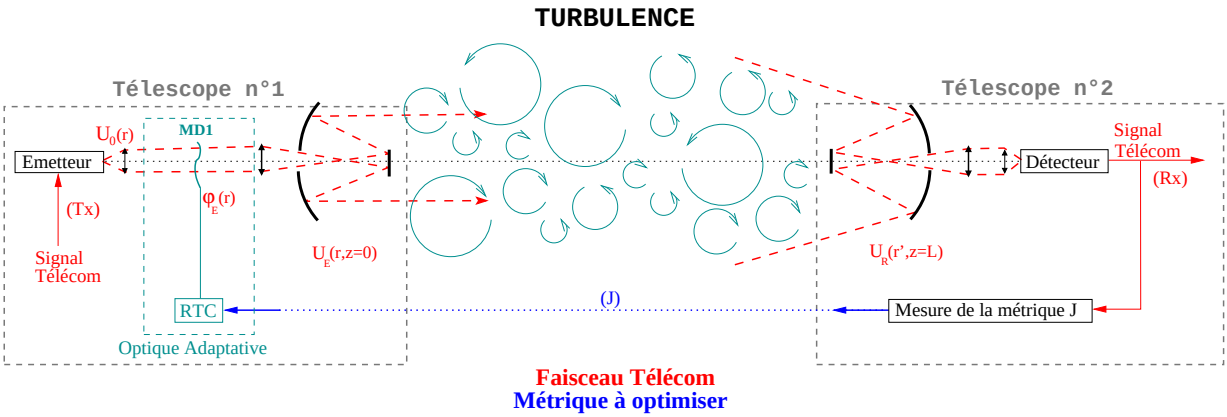

Figure 4.8: Implementation diagram for a phase correction using direct optimisation.

possible [Yu-p-03, Yu-a-04] to use multi-conjugate adaptive optics (MCAO). Such systems use several deformable mirrors conjugated at different planes and enables the precompensation both in amplitude and in phase of the emitted field.

4.2.2.3 Limitations

Modulation methods require, among others, a much higher control frequency relative to systems using wavefront sensing on a counter-propagating laser beam probe, presented previously. This higher frequency is mandatory in order to iteratively optimise for each turbulence realisation. It is indeed important to have reached convergence (or at least a satisfactory correction level) before turbulence changes. The characteristic modification time of turbulence is of the order of the millisecond. As an example, supposing that a hundred iterations are required before convergence, the control DM frequency must be of the order of 10 kHz. In addition, limits imposed by using such a correction strategy are not clearly established because no theoretical approach has yet been proposed. Furthermore, since the metric to be optimised is generally non-convex, optimality of the correction cannot be guaranteed.

4.2.3 Optimale Correction

4.2.3.1 Optimal Phase and Amplitude Correction

The approach proposed by Barchers [Barchers-a-02-b] is a hybrid solution between the classical approach and the iterative criterion minimising solution. Barchers proposed a theoretical implementation solution for the optimal correction of laser beam propagating through turbulent atmosphere. This approach consists of the use of an adaptive optics system capable of controlling both phase and amplitude of the field emitted by each telescope. The correction is iterative until convergence towards the optimal solution. The correction of phase and amplitude by adaptive optics generally implements several deformable mirrors. Figure 4.9 presents a functional diagram of the iterative optimal correction between two telescopes used for optical communications.

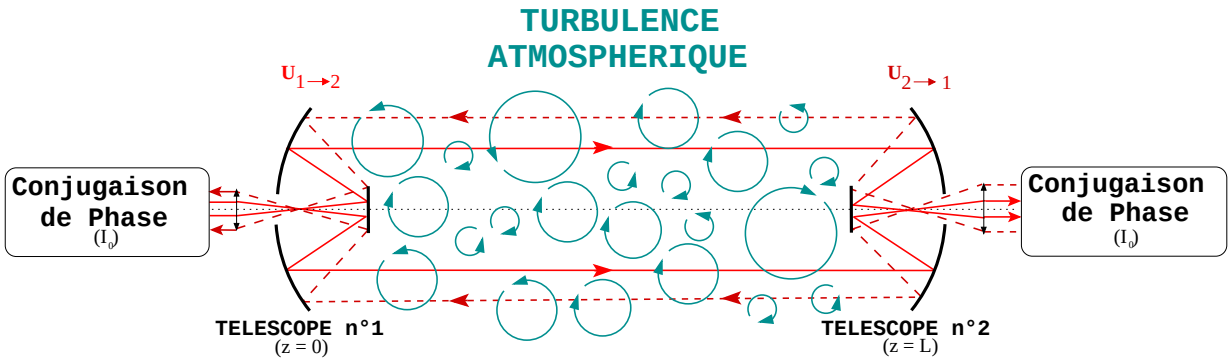

Figure 4.9: Diagram for phase and amplitude iterative correction.

The steps to implement optimal phase and amplitude correction are:

- A first uncompensated laser beam is launched from telescope 1.
- When received by telescope number 2, a phase and amplitude conjugation is performed. This conjugation consists in re-emitting the laser beam with a complex field noted $U_{2\to1}$ and equal to the complex conjugate of the received field $U_{1\to2}$. We obtain, in the absence of pupil truncation: $U_{2\to1} = U^*_{1\to2}$.
- The precompensated laser beam then propagates from telescope 2 to telescope 1.
- Arriving at telescope 1, the correction process is repeated: $U'_{1\to2} = U^*_{2\to1}$.

From this moment, both correction systems (located in telescope 1 and 2) are activated. Propagations between the two telescopes of the link are then performed iteratively. Correction convergence is monotonous and each iteration step brings the system closer to the optimal solution. The author stresses that the process must be preceded by an initial phase to align both telescopes.

The mathematical steps implementing optimal phase and amplitude correction are presented below with: $z = 0$ (resp. $z = L$) the position of telescope number 1 (resp. 2), $|A_0|^2 = I_0$ the maximal intensity emitted by the laser beams $\left(\int_{\mathcal{P}} |U_0(\mathbf{r}, z=0)|^2 d\mathbf{r} = I_0\right)$, $\mathcal{P}_1$ (resp. $\mathcal{P}_2$) corresponds to the pupil of telescope 1 (resp. 2). D is the pupils diameter. The operator $\mathcal{G}_{1\to2}$ (resp. $\mathcal{G}_{2\to1}$) represents propagation through atmospheric turbulence along increasing (resp. decreasing) z, that is from telescope 1 to telescope 2 (resp. from 2 to 1). The iteration index of the complex field is noted i and $U^{*(i)}$ is the complex conjugated field of $U^{(i)}$. The complex field propagating from telescope 1 towards telescope 2 at iteration step (i) is:

$$U^{(i)}_{1\to2}(\mathbf{r}', z=L) = \mathcal{G}_{1\to2}\left[\frac{A_0}{\sqrt{\int_{\mathcal{P}_2}\left|U^{(i)}_{2\to1}(\mathbf{r}, z=0)\right|^2 d\mathbf{r}}} U^{*(i)}_{2\to1}(\mathbf{r}, z=0)\times\mathcal{P}_1\right] \tag{4.11}$$

The complex field propagating from telescope 2 towards telescope 1 at iteration step (i)

$$U_{2\rightarrow 1}^{(i)}\left(\mathbf{r},z=0\right)=\mathcal{G}_{2\rightarrow 1}\left[\frac{A_0}{\sqrt{\int_{\mathcal{P}_1}\left|U_{1\rightarrow 2}^{(i-1)}(\mathbf{r}',z=L)\right|^2 d\mathbf{r}}}U_{1\rightarrow 2}^{*(i-1)}\left(\mathbf{r}',z=L\right)\times\mathcal{P}_2\right] \tag{4.12}$$

The nominal field that is injected into the system can be taken as a truncated Gaussian beam: $U_0\left(\mathbf{r},z=0\right)=A_0 exp\left(-\frac{\mathbf{r}^2}{{w_{z=0}}^2}-i\frac{k\mathbf{r}^2}{2F_{z=0}}\right)\times\mathcal{P}_1$, where $w_{z=0}^2$ is the emission beam size and $F_{z=0}$ the radius of curvature. The re-emitted field at the level of each telescope is normalised to obtain a field of intensity $I_0=\left|A_0\right|^2$ before each iteration step.

The necessity of realising iterations arises from the presence of pupil truncation at the level of each of the telescopes and their associated diffractive effects. In the absence of truncation, the optimal solution is simply the conjugated complex field $U_{2\rightarrow 1}=U_{1\rightarrow 2}^{*}$ and only a single iteration is required. However, access to the field $U_{2\rightarrow 1}$ (resp. $U_{2\rightarrow 1}$) is spatially limited to the pupil of telescope 1 (resp. 2). It is not possible to obtain a phase and amplitude conjugation on the entire plan $z=L$ (resp. $z=0$).

Barchers [Barchers-a-02-b] studied correction quality as a function of different metrics, namely PIB and Strehl ratio, for different turbulence strength. He limited his study to weak and intermediate perturbations with $0.4<\sigma_R^2<2.8$. He has shown that in order to obtain a sufficient correction quality (95% of coupled energy between the two telescopes), it important to have pupil diameters D such as $D>2\sqrt{\lambda L}$.

It is important to note that the article essentially deals with a novel solution to an existing problem. It's behaviour relative to FSOCS is barely mentioned. The selected wavelength used for the study ($\lambda=500\,\text{nm}$) does not correspond to typical wavelengths used in laser communications. In addition, strong turbulence conditions are not treated. However, the most important shortcoming is that no implementation concept has been proposed, which seriously limits the significance of the article. This very issue probably explains why no research work on this theme is mentioned in the literature. If one is to examine implementation possibility of such a correction strategy, two possibilities come to mind:

- The use of a optical phase conjugation, each iteration is performed optically. The use of optical phase conjugation for optical communications is still an important issue [McAulay-p-99, Bruesselbach-a-95]. In addition, both the telescopes and the turbulent volume can be considered as a cavity and nothing guarantees its stability.

- The use of counter-propagating laser beam shaped by adaptive optics [Roggemann-a-98]. Control of such systems is still to be invented; flux normalisation not being the least of problems.

4.2.3.2 Sub-optimal Phase Correction

By means of iterative phase and amplitude one achieves optimal correction. Optimality is possible by using highly complex correction systems where at least two deformable mirrors

are necessary. Similarly to iterative phase and amplitude conjugation, it is possible to degrade correction quality by performing a phase-only correction [Barchers-a-02-b]. The complex field propagating from telescope 2 towards telescope 1 at iteration step (i):

$$U_{2\to1}^{(i)}\left(\mathbf{r}, z=0\right) = \mathcal{G}_{2\to1}\left[U_0\left(\mathbf{r}', z=L\right)\frac{U_{1\to2}^{*(i-1)}\left(\mathbf{r}', z=L\right)}{\left|U_{1\to2}^{(i-1)}\left(\mathbf{r}', z=L\right)\right|}\times\mathcal{P}_2\right] \tag{4.13}$$

The complex field propagating from telescope 1 towards telescope 2 at iteration step (i):

$$U_{1\to2}^{(i)}\left(\mathbf{r}', z=L\right) = \mathcal{G}_{1\to2}\left[U_0\left(\mathbf{r}, z=0\right)\frac{U_{2\to1}^{*(i)}\left(\mathbf{r}, z=0\right)}{\left|U_{2\to1}^{(i)}\left(\mathbf{r}, z=0\right)\right|}\times\mathcal{P}_1\right] \tag{4.14}$$

The field's amplitude is no longer the amplitude of the field propagating in the opposite direction received at the previous iteration step, but the initial field U_0 (where $\int_{\mathcal{P}}\left|U_0 d\mathbf{r}\right|^2 = \left|A_0\right|^2 = 1$. Link quality is degraded relative to phase and amplitude optimal correction. However, it enables its implementation by classical AO means using a single deformable mirror. Barchers [Barchers-a-02-b] observes a strong decrease in correction quality and it is not possible to obtain a coupled energy higher than 95% for $D < 4.5\sqrt{\lambda L}$.

4.3 Conclusion

This chapter was dedicated on one hand to an introduction to the basic concepts of adaptive optics. In spite of its performance in weak perturbations, adaptive optics show serious limitations in strong turbulence mainly because of branch points in the phase and strong scintillation. For endo-atmospheric long-distance optical links, strong turbulence for realistic scenarios will be the norm.

On the other hand, we have presented possible methods available in the literature to correct for turbulence effects by AO for FSO. Three strategies have been proposed: wavefront measurements on a counter-propagating probe, direct optimisation and optimal approach. These three methods all have important limitations.

Chapter 5

Rationale

We have presented in the introductory chapters the influence of turbulence on optical communication links. In particular, it has been estimated by the use of two important metrics: mean intensity $\langle I \rangle$ and normalised intensity fluctuations $\frac{\sigma_I}{\langle I \rangle}$. Signal extinctions and attenuations lead to an increase in bit error rate which is incompatible with requirements. In particular true for long-distance links. We have seen that normalised intensity fluctuations can typically be of the order of $\frac{\sigma_I}{\langle I \rangle} = 0.5$ when a value of $\frac{\sigma_I}{\langle I \rangle} \simeq 0.1$ actually seems the maximal acceptable value. Reducing variance by a factor 25 or more is difficult to achieve with by diversity methods. Furthermore, when estimating probability density function, we have used a log-normal law. This law exhibits optimistic values for error rates (under-estimation of the tail of the PDF) and the value $\frac{\sigma_I}{\langle I \rangle} \simeq 0.1$ is probably also optimistic. Turbulence strongly limits FSOCS performance by significantly increasing BER. AO precompensation is one of the most promising methods to overcome this limitation. We have presented in the previous chapter two techniques that are currently implemented in existing systems: wavefront measurement using a counter-propagation probe and phase modulation. These methods mainly concern horizontal links near the ground limited to a few kilometres or to very special conditions (e.g. links between two high-altitude summits). On the other hand, a theoretical approach to the so-called optimal correction has been presented, but no implementation strategy has yet been proposed.

The objective of this document is to propose solutions to improve FSOCS performance by using the theoretical optimal approach. We will study long-distance horizontal links which is the most limiting case. In this document we will only study systems were both ends of the communication channel are cooperative, that is where control system can act on both emission and reception. This particular case is to be distinguished with military applications where the reception (or target) is not controlled. The application framework will be the Fortune43G project presented paragraph 1.2.5.

We will first study performance for the best possible AO corrected optical communication system in free-space. Iterative phase and amplitude optimal correction will be studied in details for optical communications in chapter 6. We will present expected performance for a large spectrum of atmospheric turbulence. We will then address the envisaged improvement brought by changing the wavelength and limitation generated by central obscuration. These implementation constrains for the optimal solution gives reasons for the study of iterative corrections limited to

phase. Secondly, we evaluate expected performance for classical approaches from the standpoint of the results obtained previously with the optimal correction. We first study correction by wavefront measurement on a counter-propagating laser beam (chapter 7). This correction type is strongly impacted by scintillation which perturbs phase measurements. We propose a mechanism to partially free the system from these limitations. We will also study the expected performance (chapter 8) of direct optimisation by a performance metric, in particular with stochastic algorithms. Finally, we propose a new concept for measuring and controlling phase and amplitude. We study its implementation in chapter 9.

Part III

Precompensation by Adaptive Optics

Chapter 6

Optimal and Sub-Optimal Correction

Contents

The optimal correction proposed by Barchers [Barchers-a-02-b] enables, for a given turbulence realisation, to iteratively reach a propagation mode. A propagation mode is a mode limiting energy losses between the two ends of the communication channel. This method relies on a phase and amplitude control of the emitted electromagnetic fields. We will study in this chapter (see paragraph 6.1) and in detail the contribution of this propagation mode for FSO systems. In particular, we will focus on typical propagation conditions found in the Fortune43G project. We will expand Barcher's study to the entire spectrum of perturbation regimes (i.e. weak to strong) and show that performance is in particular scaled by the size of the pupil and by the integrated turbulence strength over the propagation path. Finally, we evaluate performance of a degraded correction strategy, the so-called sub-optimal correction (see paragraph 6.2), where only the phase part of the emitted wave is control at each iteration.

6.1 Optimal Correction: Towards a Propagation Mode

6.1.1 Modelling Principle

Modelling of the phase and amplitude iterative control was realised using PILOT simulation code. We consider a perfect phase and amplitude (full-wave) correction in which the true phase is used for conjugation. True phase is the phase that actually arrives at the telescope's level after propagation. Figure 6.1 presents the basic principal diagram of the optical link with telescope positions ($T1$ at $z = 0$ and $T2$ at $z = L$) as well as the propagation direction of the field. Atmospheric turbulence is located between the two telescopes $T1$ and $T2$, perturbing fields $U_{1\to 2}$ and $U_{2\to 1}$ as they propagate.

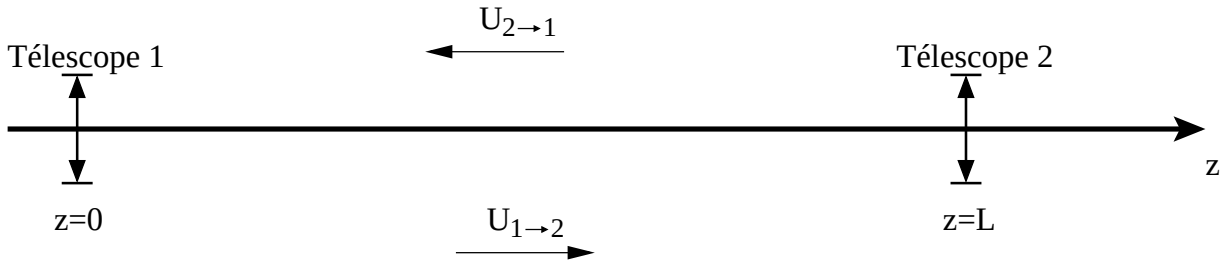

Figure 6.1: Diagram of the optical link.

We recall the various steps of the optimal iterative correction between telescope 1 and telescope 2.

$$\text{Iteration 0}\begin{cases} U_0^{(0)}(\mathbf{r}, z=0) & = \frac{U_0(\mathbf{r},z=0)}{\sqrt{\int_{\mathcal{P}_1}|U_0(\mathbf{r},z=0)|^2 d\mathbf{r}}} A_0 \times \mathcal{P}_1 \\ U_{1\to 2}^{(0)}(\mathbf{r}', z=L) & = \mathcal{G}_{1\to 2}\left[U_0^{(0)}(\mathbf{r}, z=0)\right] \times \mathcal{P}_2 \end{cases}$$

$$\text{Iteration 1}\begin{cases} U_{2\to 1}^{(1)}(\mathbf{r}, z=0) & = \mathcal{G}_{2\to 1}\left[\frac{U_{1\to 2}^{*(0)}(\mathbf{r}',z=L)}{\sqrt{\int_{\mathcal{P}_2}\left|U_{1\to 2}^{(0)}(\mathbf{r}',z=L)\right|^2 d\mathbf{r}'}} A_0\right] \times \mathcal{P}_1 \\ U_{1\to 2}^{(1)}(\mathbf{r}', z=L) & = \mathcal{G}_{1\to 2}\left[\frac{U_{2\to 1}^{*(1)}(\mathbf{r},z=0)}{\sqrt{\int_{\mathcal{P}_1}\left|U_{2\to 1}^{(1)}(\mathbf{r},z=0)\right|^2 d\mathbf{r}}} A_0\right] \times \mathcal{P}_2 \end{cases}$$

$$\vdots\vdots\vdots$$

$$\text{Iteration i}\begin{cases} U_{2\to 1}^{(i)}(\mathbf{r}, z=0) & = \mathcal{G}_{2\to 1}\left[\frac{U_{1\to 2}^{*(i-1)}(\mathbf{r}',z=L)}{\sqrt{\int_{\mathcal{P}_2}\left|U_{1\to 2}^{(i-1)}(\mathbf{r}',z=L)\right|^2 d\mathbf{r}'}} A_0\right] \times \mathcal{P}_1 \\ U_{1\to 2}^{(i)}(\mathbf{r}', z=L) & = \mathcal{G}_{1\to 2}\left[\frac{U_{2\to 1}^{*(i)}(\mathbf{r},z=0)}{\sqrt{\int_{\mathcal{P}_1}\left|U_{2\to 1}^{(i)}(\mathbf{r},z=0)\right|^2 d\mathbf{r}}} A_0\right] \times \mathcal{P}_2 \,, \end{cases}$$

Where $U_0(\mathbf{r}, z=0)$ is the initial field, $\mathcal{P}$ represents the pupil, $\mathcal{G}_{j\to k}[.]$ a turbulent propagation from telescope j to telescope k, $|A_0|^2$ the total emitted field intensity and $U_{j\to k}$ the receive field in k that has propagated from j. Without any loss of generality, we will set $|A_0|^2 = 1$. Each round trip between telescopes is considered as a single iteration step. The first iteration (iteration 0) is done without any precompensation. We remind the reader that the diagram of the telecommunication link has been presented figure 4.9.

Statistical values $\langle I_i \rangle$ and $\frac{\sigma_{I_i}}{\langle I_i \rangle}$ at iteration i are estimated by a Monte Carlo approach with approximately 300 independent turbulence realisations. At each iteration step the integrated intensity (PIB) is estimated at the level of each telescope by:

$$I_1^{(i)} = \frac{\int_{\mathcal{P}_1} U_{2\to 1}^{(i-1)}(\mathbf{r}, z=0)\, d\mathbf{r}}{\int_{\mathcal{P}_2} U_{1\to 2}^{(i-1)}(\mathbf{r}', z=L)\, d\mathbf{r}'} \tag{6.1}$$

$$I_2^{(i)} = \frac{\int_{\mathcal{P}_2} U_{1\to 2}^{(i)}(\mathbf{r}', z=L)\, d\mathbf{r}'}{\int_{\mathcal{P}_1} U_{2\to 1}^{(i)}(\mathbf{r}, z=0)\, d\mathbf{r}} \tag{6.2}$$

The total emitted intensity by telescope $T1$ (resp. $T2$) after truncation by the pupil $\mathcal{P}_1$ (resp. $\mathcal{P}_2$) will always be normalised in order to respect the following equality: $\int_{\mathcal{P}_1} U_{1\to 2}^{(i)} = I_0$ (resp. $\int_{\mathcal{P}_2} U_{2\to 1}^{(i)} = I_0$). $I_1^{(i)}$ and $I_2^{(i)}$ represents the coupling energy between the two telescopes at each iteration step. In the rest of the document, we will mainly focus on values relative to telescope $T2$. After convergence of the correction, statistical values at both ends of the communications link are identical. Any argument based on $T1$ or $T2$ will be equivalent.

6.1.2 Optimal Correction in Absence of Turbulence

In order of decrease convergence time, we first optimise the initial beam parameters $U_0(\mathbf{r}, z=0)$. We suppose the beam to be Gaussian. Figure 6.2 represents the optimisation of the initial Gaussian beam parameters that is of the waist radius w_o and radius of curvature R. Optimisation is performed with a turbulent free propagation over a distance of $L = 10\,\text{km}$, with a wavelength of $\lambda = 1.5\ \mu\text{m}$ and a pupil diameter of $D = 30\,\text{cm}$. Pupils truncation is added both at the level of $T1$ and $T2$. For the range of parameters studied here, the final intensity value after optimal correction does not seem to depend on the initial beam geometry. Variations on the final PIB value after 10 iterations are inferior to $5\ 10^{-3}$. In absence of turbulence, it is possible for pupils $D \geq 30\,\text{cm}$ to collect approximately 100% of the emitted flux. It seems that convergence is achieved faster for beams with a waist radius of $w_0 = 5\,\text{cm}$ focalised at the middle of the propagation path ($z_{w_o} = 5\,\text{km}$) because truncation effects by $T1$ and $T2$ are minimised. System parameters (pupil of $D = 30\,\text{cm}$, wavelength of $\lambda = 1.5\ \mu\text{m}$) lead to a symmetrical situation where the emitted and received beam size are identical (approximately $7\,\text{cm}$ in radius). Diffraction is negligible. Initial beam parameters in the presence of turbulence will therefore be taken as $w_0 = 5\,\text{cm}$ for the beam waist, focalised at the middle of the propagation distance ($z_{w_o} = 5\,\text{km}$).

Figure 6.3 illustrates the energy distribution in the plane of $T2$ before and after optimal correction on an optimised beam and without turbulence. This figure clearly shows that the

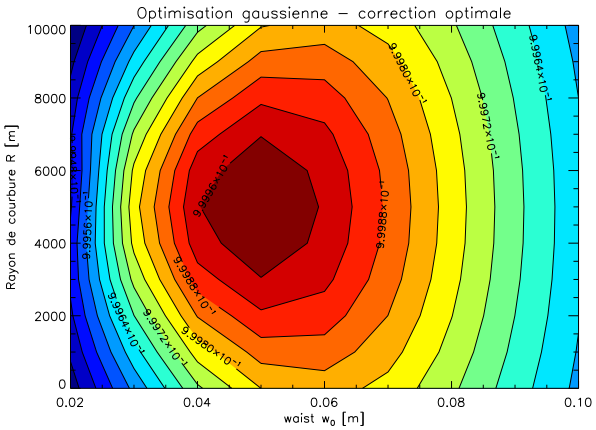

Figure 6.2: Curves of same energy: initial Gaussian beam parameters optimisation. Propagation without turbulence and truncation at both ends of the link. Full-wave optimal correction. Propagation distance: $L = 10\,\text{km}$, wavelength: $\lambda = 1.5$ µm and pupil diameter: $D = 30\,\text{cm}$. The number of iterations is limited to 10.

optimal Gaussian beam is extremely close to the beam after convergence.

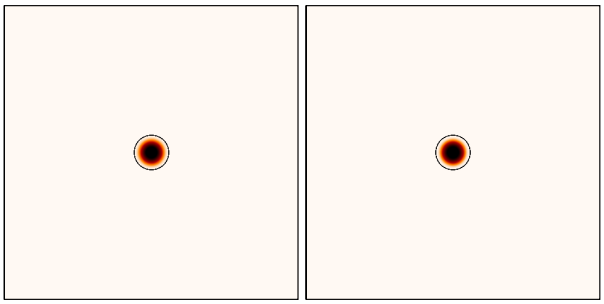

Figure 6.3: Influence of optimal correction without turbulence on an optimised Gaussian beam. Left: image without correction, right: image with optimal correction after 10 iterations. Propagation distance: $L = 10\,\text{km}$, wavelength: $\lambda = 1.5$ µm and pupil diameter: $D = 30\,\text{cm}$. The colour scale is logarithmic.

Figure 6.4 shows the evolution of integrated intensity (PIB) as a function of pupil diameter. It shows that without turbulence and as soon as the pupil diameter is larger than $D = 25\,\text{cm}$, it is possible to transmit approximately all the flux from one telescope to the other. This limit is actually imposed by diffraction. The entire emitted flux can be collected to the condition that the pupil diameter respects the following condition $D > 2\sqrt{\lambda L} \simeq 24.5\,\text{cm}$. When $D < 24.5\,\text{cm}$ the mode that is established in the cavity gives rise to energy losses oppositely to what happens in a waveguide. This curve will serve as the ultimate reference in terms of correction quality for propagations in presence of turbulence.

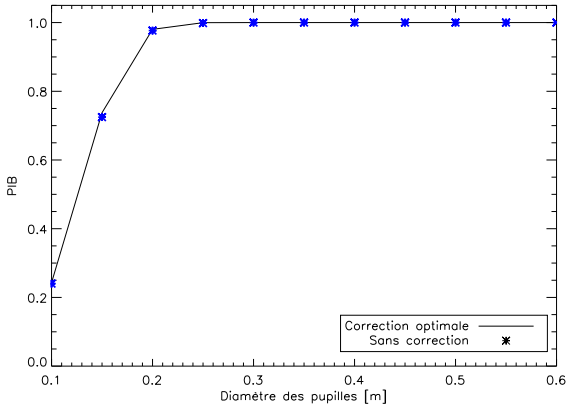

Figure 6.4: Intensity evolution as a function of pupil diameter for propagation without turbulence using optimal correction. Propagation distance: $L = 10\,\text{km}$, wavelength: $\lambda = 1.5$ µm and pupil diameter: $D = 30\,\text{cm}$.

6.1.3 Performance as a Function of Turbulence Strength

In this paragraph, we will suppose that telescope $T1$ and $T2$ are immersed in atmospheric turbulence and have circular apertures of diameter $D = 30\,\text{cm}$.

6.1.3.1 Short-Exposure Energy Distribution

As an illustration of the capacity of the system to concentrate energy within the reception aperture, on figure 6.5 is shown energy distributions for short-exposure at telescope $T2$ with and without correction. Three turbulence strengths are considered: $C_n^2 = 10^{-16}\,\text{m}^{-2/3}$, $C_n^2 = 10^{-15}\,\text{m}^{-2/3}$ and $C_n^2 = 10^{-14}\,\text{m}^{-2/3}$. Atmospheric turbulence strength has a strong impact over the integrated intensity value, both with and without correction. Table 6.1 gives integrated intensity values (PIB) obtained from intensity distributions presented figure 6.5. These values are only valid for this particular turbulence realisation. It gives evidence of the improvement brought by optimal correction which is more clearly visible for stronger turbulence conditions. For weak turbulence, the optical link is already very good without correction and improvement brought by any correction can only be small.

	$C_n^2 = 10^{-16}\,\text{m}^{-2/3}$	$C_n^2 = 10^{-15}\,\text{m}^{-2/3}$	$C_n^2 = 10^{-14}\,\text{m}^{-2/3}$
Without correction	$I_0 = 99.2\%$	$I_0 = 92.5\%$	$I_0 = 40.2\%$
Optimal correction	$I_{10} = 99.8\%$	$I_{10} = 98.2\%$	$I_{10} = 80.8\%$

Table 6.1: Table summarising intensity values obtained figure 6.5 for $\lambda = 1.5$ µm and a $D = 30\,\text{cm}$ diameter pupil .

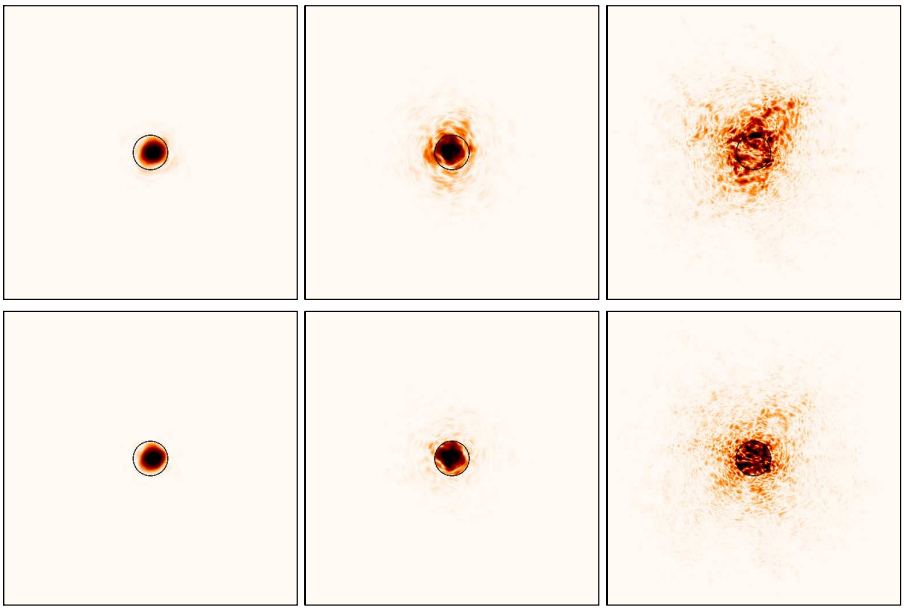

Figure 6.5: Influence of optimal correction. Top: short-exposure images without correction; bottom: short-exposure images after 10 iterations of phase and amplitude correction. From left to right: $C_n^2 = 10^{-16}\,\mathrm{m}^{-2/3}$, $C_n^2 = 10^{-15}\,\mathrm{m}^{-2/3}$, $C_n^2 = 10^{-14}\,\mathrm{m}^{-2/3}$. Propagation distance: $L = 10\,\mathrm{km}$, wavelength: $\lambda = 1.5$ µm and pupil diameter: $D = 30\,\mathrm{cm}$. The colour scale is logarithmic for better visualisation of contrasts.

6.1.3.2 Influence of Turbulence Strength

We first study and for four different turbulence strengths the evolution of two metrics $\langle I_i \rangle$ and $\frac{\sigma_{I_i}}{\langle I_i \rangle}$ as function of the iteration step i (see figure 6.6). Final values for both metrics after optimal correction convergence, depends on turbulence strength C_n^2. These curves clearly demonstrate that correction efficiency is function of turbulence strength. Barchers [Barchers-a-02-b] had limited his study to mean PIB in the case of weak perturbations. As Barchers, we observe that for $C_n^2 = 10^{-16}\,\mathrm{m}^{-2/3}$ correction is perfect in terms of average PIB (as long as $D > \sqrt{\lambda L}$). Curves figure 6.6 demonstrate that optimal correction can lead to a very satisfactory level of mean PIB well beyond weak perturbations limitation. If one is to consider the $C_n^2 = 10^{-14}\,\mathrm{m}^{-2/3}$ case, iterative correction can increase PIB form $\langle I_0 \rangle = 0.31$ to more than $\langle I_9 \rangle = 0.83$; or a mean increase of approximately 167%. We remind the reader that the Rytov variance is $\sigma_R^2 = 14$ for the turbulent case under consideration. It is important to emphasize that it is the case where correction is the most efficient. In the other cases studied, turbulence strength is lower and mean PIB is already very good without correction. For $C_n^2 = 7\ 10^{-14}\,\mathrm{m}^{-2/3}$, the average PIB level is very low ($\langle I_0 \rangle = 0.057$). After optimal correction, it is increased to $\langle I_9 \rangle = 0.333$, or an mean improvement of approximately 484%. This confirms that correction efficiency, in terms of mean PIB, increases with the turbulence strength.

We also characterised PIB residual intensity fluctuations. Its attenuation is capital for FSO

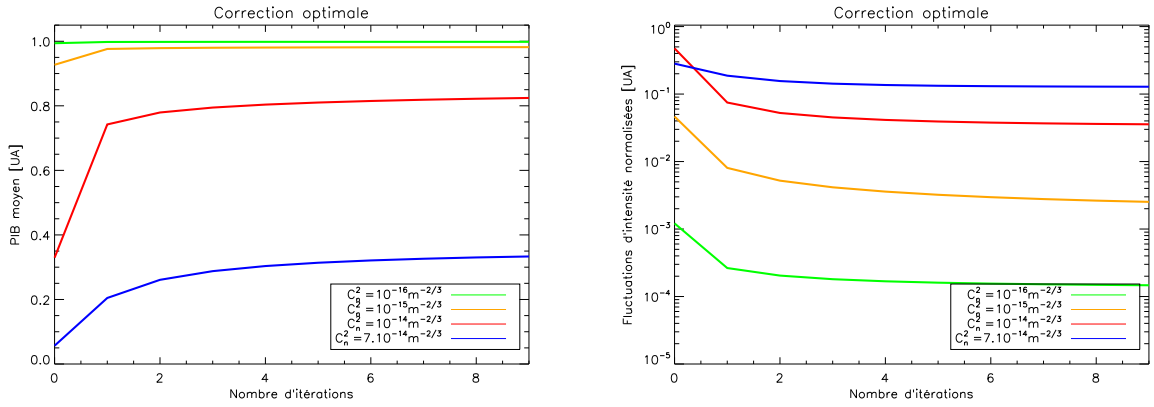

Figure 6.6: Optimal correction efficiency as a function of iteration number. Propagation distance: $10\,\text{km}$ and $\lambda = 1.5\ \mu\text{m}$. Green: $C_n^2 = 10^{-16}\,\text{m}^{-2/3}$, orange: $C_n^2 = 10^{-15}\,\text{m}^{-2/3}$, red: $C_n^2 = 10^{-14}\,\text{m}^{-2/3}$ and blue: $C_n^2 = 7\ 10^{-14}\,\text{m}^{-2/3}$. Left: mean PIB. Right: normalised intensity fluctuations.

systems. Regardless of the turbulence regime, and apart for $C_n^2 = 7\ 10^{-14}\,\text{m}^{-2/3}$, a reduction of a factor of approximately 10 is observed after 10 iterations. The strongest turbulence case (bleus curves) corresponds to a Rytov variance of $\sigma_R^2 \simeq 98$ and a propagation in deep saturation regime. Optimal correction can reduce residual intensity fluctuations by a factor 3 only. Figure 2.3 in chapter 2 has shown a small reduction of the true variance for strongly saturated cases. Curves figure 6.6 confirm that residual fluctuations are reduced for $C_n^2 = 7\ 10^{-14}\,\text{m}^{-2/3}$ compared to $C_n^2 = 10^{-14}\,\text{m}^{-2/3}$. However, perturbations are too strong for the optimal correction to sufficiently reduce fluctuations.

Concerning convergence speed, if one iteration is sufficient for weak turbulence and for mean PIB, it clearly appears that a larger number of iterations are necessary for the other cases. For the rest of the study, we have systematically insured that a sufficient number of iteration has been made in order to reach convergence. We have established that 5 iterations are generally sufficient.

6.1.3.3 Average Error Rate

Figure 6.7 presents mean BER evolution as a function of mean received intensity $\langle I \rangle$. Details of how BER is estimated using a log-normal law can be found paragraph 3.1.3. Three different turbulence strengths are studied with and without optimal correction: $C_n^2 = 7\ 10^{-14}\,\text{m}^{-2/3}$ (on the figure in blue), $C_n^2 = 10^{-14}\,\text{m}^{-2/3}$ (in red) and $C_n^2 = 10^{-15}\,\text{m}^{-2/3}$ (in orange). For the same emitted optical power, configuration without correction corresponding to $C_n^2 = 7\ 10^{-14}\,\text{m}^{-2/3}$ and $C_n^2 = 10^{-14}\,\text{m}^{-2/3}$ do not enable the system to reach a reasonable average BER for typical FSOCS standards. Table 6.2 gives a summary of the average error rate for the different turbulence strength studied both with and without correction. Values are obtained from figure 6.7. We have assumed the emitted optical power to be $I_{\text{emit}} = 1$ and calculated the error rate from the mean

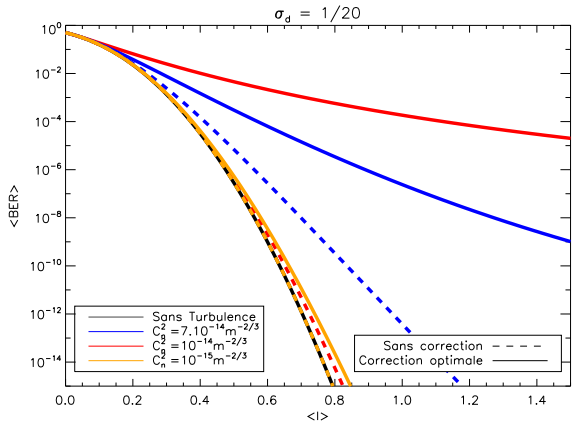

Figure 6.7: Mean BER evolution as a function of mean received intensity. Orange curves: $C_n^2 = 10^{-15}\,\mathrm{m}^{-2/3}$, red: $C_n^2 = 10^{-14}\,\mathrm{m}^{-2/3}$ and blue: $C_n^2 = 7\ 10^{-14}\,\mathrm{m}^{-2/3}$. Dashed lines: without correction, solid lines: optimal correction.

intensity $\langle I \rangle$ attenuation for each case.

C_n^2	$7\ 10^{-14}\,\mathrm{m}^{-2/3}$	$10^{-14}\,\mathrm{m}^{-2/3}$	$10^{-15}\,\mathrm{m}^{-2/3}$
Without correction	0.3	$2\ 10^{-2}$	$4\ 10^{-18}$
Optimal correction	$3\ 10^{-4}$	$3\ 10^{-15}$	$3\ 10^{-23}$

Table 6.2: Table summarising mean BER values as function of the turbulence strength for $\lambda = 1.5$ µm and a pupil of $D = 30$ cm diametre.

In order to decrease error rates in the least favourable case (i.e. when $\langle BER \rangle > 10^{-12}$), it is important either to increase signal-to-noise ratio (either by decreasing noise variance σ_d^2 or by increasing emitted optical power I_{emit}), or increase the pupil diameter. When residual fluctuations of the PIB are high, increasing signal to noise ratio can help lower mean BER below the threshold of 10^{-12}.

For $C_n^2 = 7\ 10^{-14}\,\mathrm{m}^{-2/3}$ and using optimal correction, mean PIB is equal to $\langle I \rangle \simeq 0.33$. A twofold increase (respectively threefold increase) of the emitted intensity makes it possible to reach $\langle BER \rangle = 3\ 10^{-8}$ (resp. $\langle BER \rangle = 3\ 10^{-14}$). However, such increase in optical fluxes is not always possible for endo-atmospheric FSOSC. In addition, these considerations can be questioned, especially for strong turbulence condition without correction. In this case, we go beyond the validity of log-normal density probability.

6.1.4 Pupil Diameter Influence

Correction efficiency will naturally depend on turbulence strength but also on pupil diameter, wavelength and propagation distance. If pupils are too small, it will be impossible to create a propagation mode minimising loses between the two ends of the optical link. In the opposite

case, we know that for an infinitely large pupil, phase conjugation is the immediate solution. Barchers put forward the reduced parameter $\sqrt{\lambda L}$ as a scaling parameter for pupil diameters in weak perturbations. Figure 6.8 shows pupil diameter influence for a typical wavelength of $\lambda = 1.5$ µm and various propagation regimes. As emphasized by Barchers we observe in weak

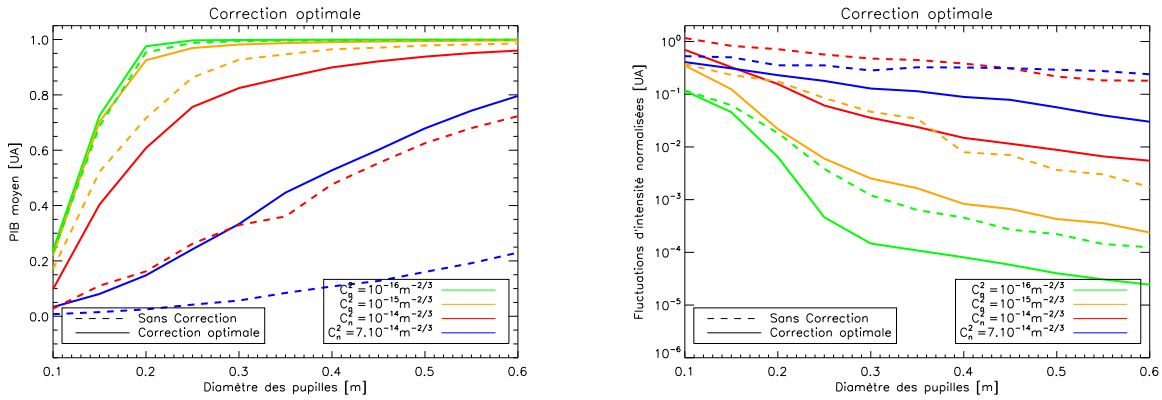

Figure 6.8: Optimal correction efficiency as function of pupil diameters for various turbulence strengths. Propagation distance $L = 10\,\text{km}$ and wavelength $\lambda = 1.5$ µm. Green: $C_n^2 = 10^{-16}\,\text{m}^{-2/3}$, orange: $C_n^2 = 10^{-15}\,\text{m}^{-2/3}$, red: $C_n^2 = 10^{-14}\,\text{m}^{-2/3}$ and blue: $C_n^2 = 7\ 10^{-14}\,\text{m}^{-2/3}$. Solid lines: optimal correction, dashed lines: no correction. Left: PIB, right: Normalised intensity fluctuations.

turbulence cases, when pupil diameters are smaller than $L_F = \sqrt{\lambda L}$, that it is impossible to obtain a propagation mode. Iterative correction is therefore inefficient in this case. We recall that $\sqrt{\lambda L} = 12\,\text{cm}$. One must emphasize that this is purely a diffractive effect without any direct link with atmospheric turbulence. As a matter of fact, we observe exactly the same characteristics in the absence of turbulence (see figure 6.4). A propagation mode can therefore only take place inside a pseudo-cavity of transverse dimension greater than L_F. This observation imposes a limit to the minimum size of usable pupils for this particular correction method. Regimes studied by Barchers are not relevant for typical FSO configurations (i.e. the expected gain is too small).

Let us first focus on the evolution of $\langle I \rangle$ as a function of pupil diameter D as shown figure 6.8. When the pupil diameter is too large, correction is barely more efficient that direct propagation without correction. The studied values for D do not enable us to see the appearance of such a characteristic for $C_n^2 = 7\ 10^{-14}\,\text{m}^{-2/3}$, located beyond $D = 0.6\,\text{m}$. This result shows that with correction, it is useless to increase the pupil diameter of the telescope beyond the natural expansion of the beam. Pupil averaging is then predominant and correction is unnecessary.

In diffractive regimes (weak perturbation: $\sigma_R^2 = 0.14$) and up to the appearance of saturation ($\sigma_R^2 = 1.4$), the characteristic value is L_F. Beyond $2L_F$ correction is unnecessary with regards to $\langle I \rangle$. In highly perturbed regimes (i.e. $\sigma_R^2 = 14$ and $\sigma_R^2 = 98$), L_F is replaced by $\frac{\lambda L}{\pi \rho_0}$ (see first part I) equal to $0.5\,\text{m}$. For the considered pupil diameter ($D < 0.6\,\text{m}$), it can be observed that correction is highly effective relative to $\langle I \rangle$.

Concerning intensity fluctuations, increasing the pupil diameter enables a significant reduction even beyond the characteristic size identified previously for $\langle I \rangle$. This is valid for all turbulence strengths studied. According to figure 3.3, it seems that normalised intensity fluctuations below approximately $\frac{\sigma_I}{\langle I \rangle} < 0.1$ are able to reduce bit error rate sufficiently. For these fluctuations, mean BER is very close to the no-turbulence case. For $\sigma_R^2 = 14$, decrease is proportional to D^{-1}. It is inversely proportional to the square root of the number of independent speckles in the pupil. For $\sigma_R^2 = 0.14$ and $\sigma_R^2 = 1.4$, the behaviour is different at least for diameters below 30 cm. For these cases, most of the perturbation is composed of beam wander.

In order to better understand the domain of interest of the correction, in figure 6.9 is presented the gain brought by optimal correction. We define gain in terms of PIB by the ratio:

$$G_{PIB} = \frac{\langle I \rangle_{\text{With Correction}}}{\langle I \rangle_{\text{Without Correction}}}, \tag{6.3}$$

The normalised intensity fluctuation gain is given by the inverse ratio:

$$G_{Fluct} = \frac{\left[\frac{\sigma_I}{\langle I \rangle}\right]_{\text{Without Correction}}}{\left[\frac{\sigma_I}{\langle I \rangle}\right]_{\text{With Correction}}} \tag{6.4}$$

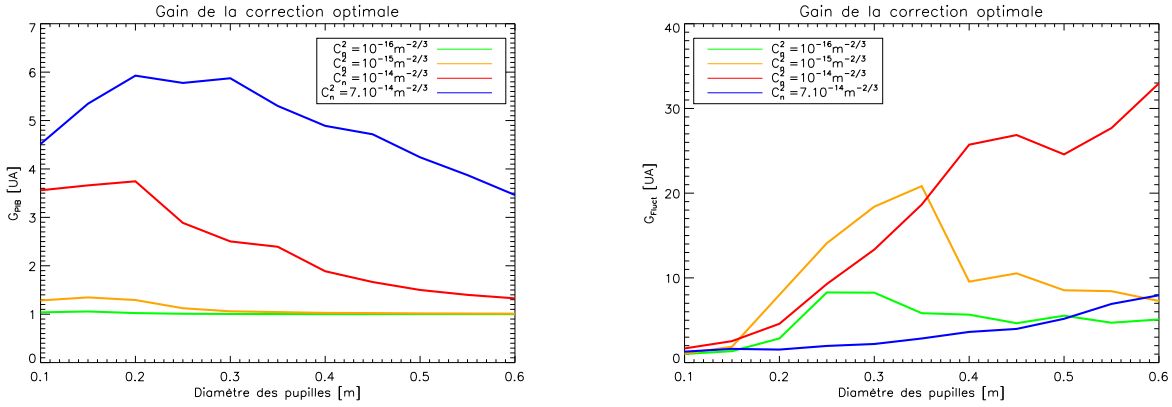

Figure 6.9: Gain of optimal correction as function of telescopes pupil diameter for various turbulence strength. Propagation distance 10 km, $\lambda = 1.5$ µm. Green: $C_n^2 = 10^{-16}\,\mathrm{m}^{-2/3}$, orange: $C_n^2 = 10^{-15}\,\mathrm{m}^{-2/3}$, red: $C_n^2 = 10^{-14}\,\mathrm{m}^{-2/3}$ and blue: $C_n^2 = 7\,10^{-14}\,\mathrm{m}^{-2/3}$. Left: PIB gain, right: normalised intensity fluctuations gain.

Let us first focus on mean PIB $\langle I \rangle$. As presented previously, optimal correction gain increases with turbulence strength. Curve for $C_n^2 = 10^{-16}\,\mathrm{m}^{-2/3}$ does not show significant increase relative to a propagation without correction. When turbulence increases beyond weak perturbation regime one can observe the appearance of an optimal pupil diameter maximising gain. When the diameter is too small, the gain stays small (no propagation modes appears). When using a

large pupil, the telescope collects almost all the flux even without correction (i.e. correction is unnecessary).

6.1.5 Probability Density Function

We have seen paragraph 3.1.1.3 that probability density functions can be used to derive error rates of atmospheric optical links. Intensity PDFs for laser beam propagation without any correction has been presented figure 2.16. Calculated BER rely on the hypothesis that PIB follows log-normal statistics. This hypothesis is justified in absence of precompensation when fluctuations of I are low in two cases:

- when perturbations are weak and the collecting pupil is small compared to $\sqrt{\lambda L}$ (i.e. the characteristic intensity grain size);
- when the collecting pupil is very large compared to the characteristic intensity grain size. Statistics approaches a normal law (central limit theorem) itself approaching a log-normal law.

The results we have presented here using an AO pre-compensation show that intensity fluctuations stay small for the studied conditions. It is important to examine probability density functions in presence of correction to validate the fact that BER evaluations, previously calculated for small intensity fluctuations with log-normal statistics, can still be carried out.

Figure 6.10 illustrates PDF modification following iterative phase and amplitude optimal correction. The distribution seems to be modified towards a log-normal function expected in weak

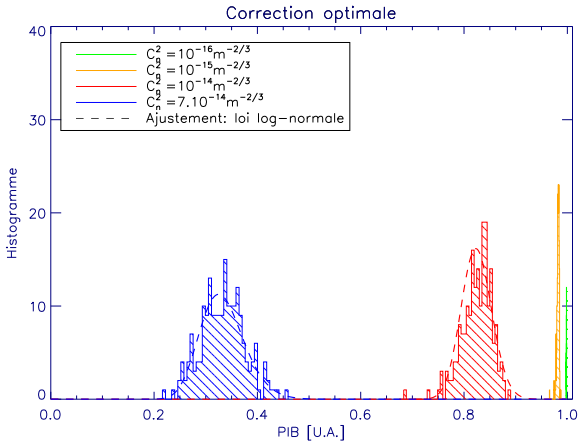

Figure 6.10: Intensity histograms for several turbulence strengths after optimal correction. Propagation distance $10\,\text{km}$, $\lambda = 1.5$ µm and pupil diameter $D = 30\,\text{cm}$. Dashed curves represent a log-normal fit.

perturbations or when pupil averaging is strong enough. Dashed curves represent a log-normal

fit for turbulence values of $C_n^2 = 10^{-14}\,\mathrm{m}^{-2/3}$ and $C_n^2 = 7\ 10^{-14}\,\mathrm{m}^{-2/3}$. This function is used to calculate the BER presented paragraph 6.1.3.3. For the studied turbulence strengths, optimal correction helps to retrieve a probability distribution resembling a log-normal distribution. This seems to hold even for strong turbulence conditions. The modification of the PDF as presented figure 6.10, will strongly reduce error rates. It brings an increase in mean signal to noise ratio and a reduction in flux variation.

6.1.6 Influence of Pupil Geometry

So far we have only considered un-obscured apertures. We have shown that efficiency of the selected propagation mode is function of the pupil diameter. Using an un-obscured aperture we modify the characteristic size of the pupil and thus diffractive effects at the same time as the total collecting area. In the perspective of a physical implementation of instruments with complex pupils (e.g. aperture synthesis) one can ask itself the role played by these two parameters separately. In order to study these parameters, we have chosen a pupil with central obscuration, particularly interesting from an implementation point of view. Centrally obscured telescopes (e.g. Cassegrain telescope) are often used, particularly for their implementation simplicity and low cost. Central obscuration simplifies optical set ups but slightly reduces the collecting surface available. On the other hand, central obscuration imposes a characteristic dimension - the width of the corona - that might strongly constrain the propagation mode efficiency.

6.1.6.1 Absence of Turbulence: an Adapted Propagation Mode

In order to study the impact of central obscuration, we first realised numerical simulations without atmospheric turbulence. The initial Gaussian beam is launched on the side of the pupil. This has no impact after optimal correction neither on final field distribution nor on studied parameters $\langle I \rangle$ and $\frac{\sigma_I}{\langle I \rangle}$.

Figures 6.11 and 6.12 represent different steps of phase and amplitude iterative correction for a central obscuration respectively with $OC = 0.5$ and $OC = 0.8$. They show in parallel phase and amplitude in the reception plane. Obtained propagation mode differs from the one obtain without central obscuration. In fact, the mode has changed from a Gaussian mode to a mode with radial symmetry composed of several lobes. The number of lobes increases with central obscuration and depends on the size of the pupils.

Intensity distributions of the thus obtained modes are similar to LP_{ml} spatial modes observed in a cylindrical multimode optical step-index fibre. The azimuth number m represents the number of mode divided by 2 (e.g. here $m = 3$ for a 50% central obscuration and $m = 4$ for 80%). The radial number l represents the number of coronas and LP_{01} mode corresponds to the Gaussian mode. In addition, as for fibre optics, the phases of the lobes are opposite side by side. We observe that part of the energy still lies outside the pupil but that globally the modes have a geometry compatible with a circular central obscuration. The phase has discontinuities at the level of zero intensity. It must be emphasized that oppositely to fibre optics, energy losses are not negligible. This is particularly true for an 80% central obscuration.

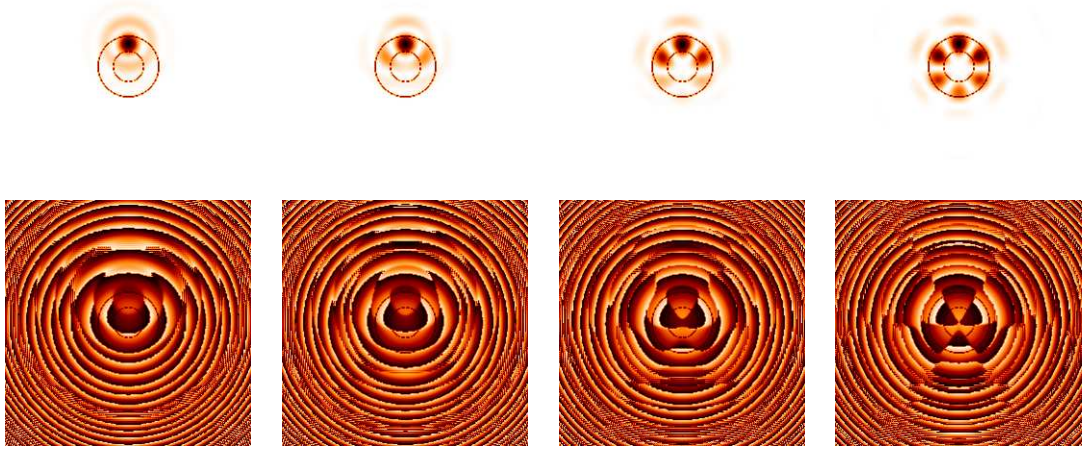

Figure 6.11: Intensity (top) and phase (bottom) evolution in reception plane after iterative optimal correction. Circles represent a $D = 25$ cm diameter pupil with central obscuration 50%. The propagation distance is 10 km and $\lambda = 1.5$ µm. From left to right are presented iteration number 1, 2, 5 and 14.

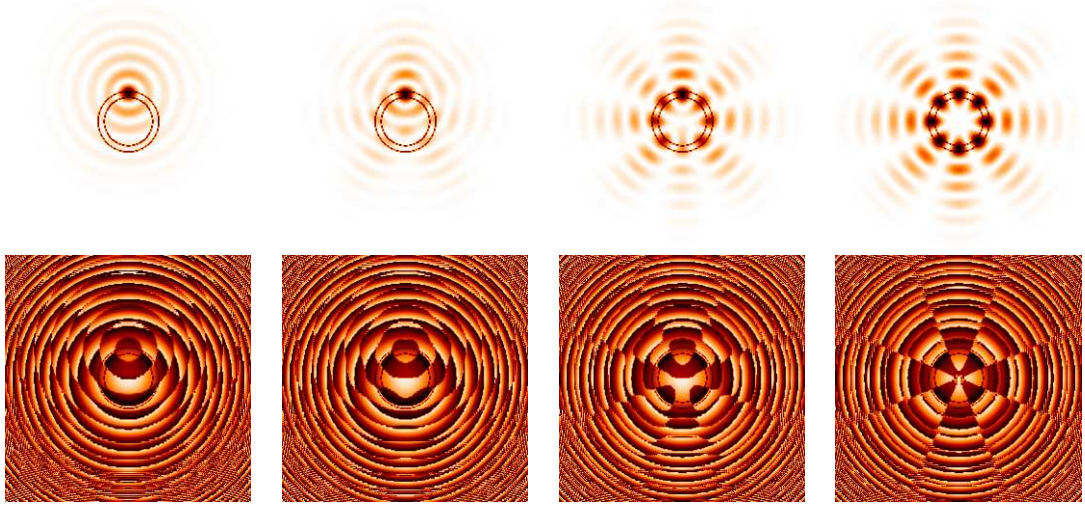

Figure 6.12: Intensity (top) and phase (bottom) evolution in reception plane after iterative optimal correction. Circles represent a $D = 25$ cm diameter pupil with central obscuration 80%. The propagation distance is 10 km and $\lambda = 1.5$ µm. From left to right are presented iteration number 1, 2, 5 and 14.

Perhaps more accurately, one can compare emitted phase of the propagation mode to a 4-quadrant phase mask [Roddier-a-97] proposed for stellar coronagraphy. The coronagraph is designed to block flux coming from a luminous star on the optical axis. In the same way, the

pseudo phase mask enables energy rejection from the optical axis towards to edges of the pupil. After iteration, an additional defocalisation appears in the phase compared to the classical phase quadrants.

Integrated intensity (PIB) evolution as function of central obscuration OC is presented figure 6.13 for a propagation without turbulence. The shape of the curves are the same as for an un-

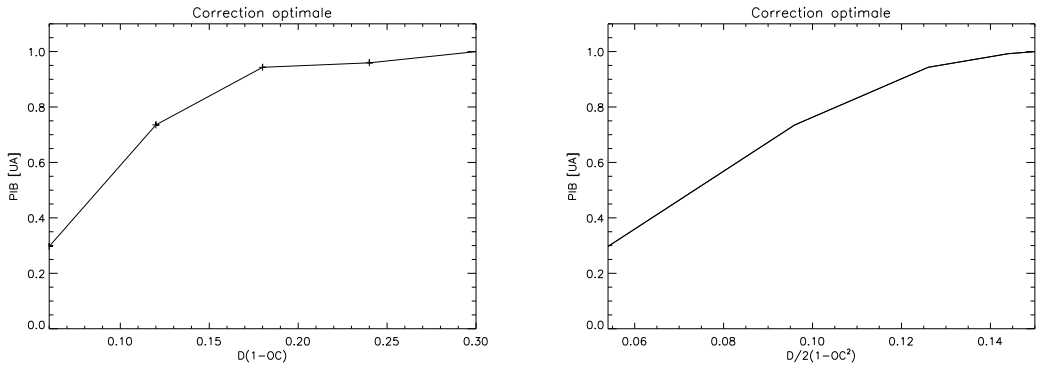

Figure 6.13: Intensity evolution for optimal correction without turbulence as function of $D\,(1-OC)$ (left) and $\frac{D}{2}^2\,(1-OC^2)$ (right). The propagation distance is $L = 10\,\text{km}$, $\lambda = 1.5$ µm and the pupil diameter is $D = 30\,\text{cm}$.

obscured pupil by replacing pupil diameter by D by $D\,(1-OC)$. We first observe a linear intensity increase proportional to the collecting surface ($\frac{D}{2}^2\,(1-OC^2)$), then the appearance of saturation when almost all the energy is collected by the pupil.

6.1.6.2 In Presence of Turbulence

Figure 6.14 compares energy distribution in reception plane for different turbulence strengths and different central obscuration values. For weak turbulence, the mode obtained without turbulence is almost retained. The same result was obtained for the un-obscured pupil case. Inversely and for strong turbulence conditions, the eigen-mode of the system differs from the geometry obtained without turbulence.

Mean intensity and normalised intensity fluctuations evolution as function of central obscuration are presented figure 6.15. Mean intensity decreases as obscuration increases. Unsurprisingly and for weak perturbations, mean attenuation after convergence is closely matched to the one obtained without turbulence. For strong perturbations (i.e $C_n^2 = 10^{-14}\,\text{m}^{-2/3}$), a quasi-linear increase is obtained for mean attenuation $\langle I \rangle$ as a function of collecting surface $d_c = 1 - OC^2$.

Regardless of perturbations, fluctuations reduction is obtained by increasing the characteristic size $1 - OC$. This was also observed for plain pupils with the same behaviour between weak and strong perturbations. Figure 6.15 right, presents mean PIB linearity for strong perturbations function of $d_c = 1 - OC^2$. No saturation is observed for $\langle I \rangle$ because the pupil diameter of

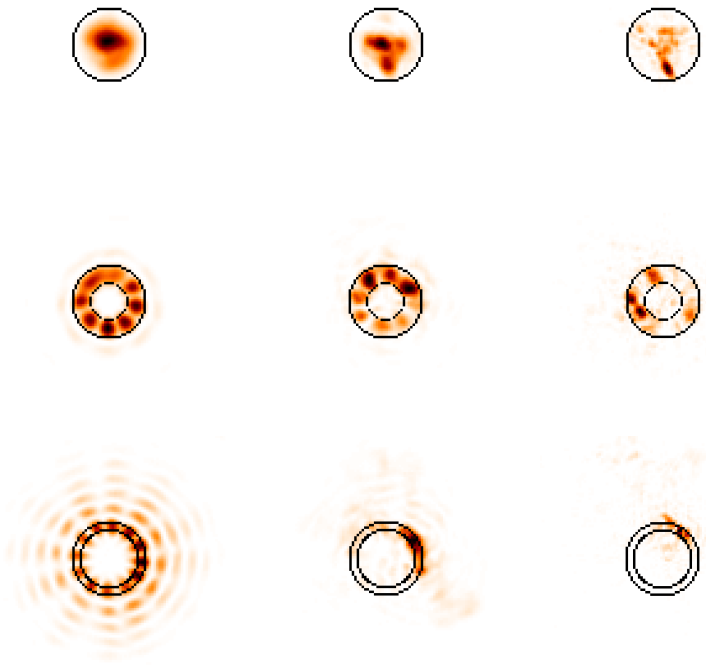

Figure 6.14: Typical intensity distribution after optimal full-wave correction (turbulence different for each realisation). Circles represent a $D = 30\,\text{cm}$ pupil. Propagation distance $L = 10\,\text{km}$, $\lambda = 1.5$ µm. From top to bottom: central obscuration 0%, 50% and 80%. From left to right, the turbulence strength is: $C_n^2 = 10^{-16}\,\text{m}^{-2/3}$, $C_n^2 = 10^{-15}\,\text{m}^{-2/3}$ and $C_n^2 = 10^{-14}\,\text{m}^{-2/3}$.

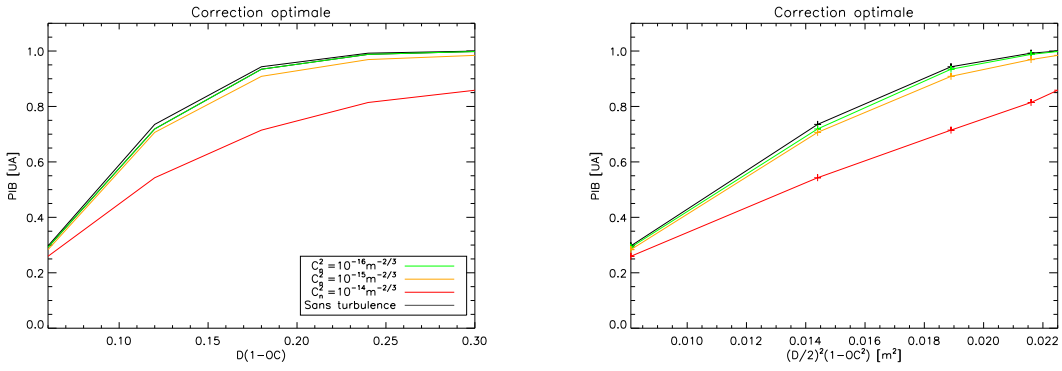

Figure 6.15: Mean intensity evolution after iterative full-wave correction function of central obscuration. Propagation distance $L = 10\,\text{km}$, $\lambda = 1.5$ µm and pupil diameter $D = 30\,\text{cm}$.

$D = 30\,\text{cm}$ is too small. Figure 6.16 presents intensity fluctuations evolution as function of $1 - OC$.

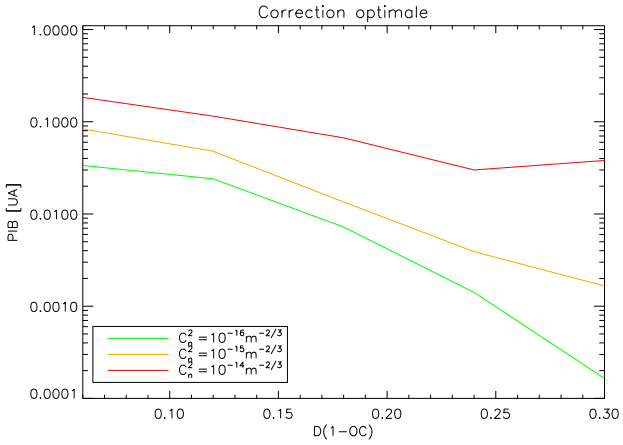

Figure 6.16: Intensity fluctuations evolution function of $d_c = 1 - OC$. Propagation distance $L = 10\,\text{km}$, $\lambda = 1.5$ µm and pupil diameter $D = 30\,\text{cm}$.

6.1.6.3 Conclusion

For annular pupils, we observe an adapted geometry similar to those found in fibre optics. We have observed two effects that are partially decoupled:

- loses proportional to surface S of the reception pupil,
- constant diffraction (related to $\frac{\lambda L}{D}$).

The behaviour of the mean PIB, when the pupil diameter D is constant, is principally related to S.

6.2 Sub-Optimal Correction

6.2.1 Modelling Principal

Iterative phase-only correction modelling is performed by the PILOT code, similarly to the optimal full-wave correction. We first consider perfect phase correction. Precompensation is realised with the true phase. Controlling only the phase part of the field will not enable a correction as good as one based on both phase and amplitude. Systems controlling only the phase part of the field are solutions one must resort to for lack of existing optimal solution implementations.

We remind the reader the principle steps for iterative phase correction or sub-optimal correction between telescope 1 and telescope 2.

$$\text{Iteration 0}\begin{cases} U_0^{(0)}(\mathbf{r}, z=0) & = \frac{U_0(\mathbf{r},z=0)}{\sqrt{\int_{\mathcal{P}}|U_0(\mathbf{r},z=0)|^2 d\mathbf{r}}} A_0 \times \mathcal{P} \\ U_{1\to 2}^{(0)}(\mathbf{r}', z=L) & = \mathcal{G}_{1\to 2}\left[U_0^{(0)}(\mathbf{r}, z=0)\right] \times \mathcal{P}_2 \end{cases}$$

$$\text{Iteration 1}\begin{cases} U_{2\to 1}^{(1)}(\mathbf{r}, z=0) & = \mathcal{G}_{2\to 1}\left[U_0(\mathbf{r}, z=0)\frac{U_{1\to 2}^{*(0)}(\mathbf{r}',z=L)}{\left|U_{1\to 2}^{(0)}(\mathbf{r}',z=L)\right|}\right] \times \mathcal{P}_1 \\ U_{1\to 2}^{(1)}(\mathbf{r}', z=L) & = \mathcal{G}_{1\to 2}\left[U_0(\mathbf{r}, z=0)\frac{U_{2\to 1}^{*(1)}(\mathbf{r},z=0)}{\left|U_{2\to 1}^{(1)}(\mathbf{r},z=0)\right|}\right] \times \mathcal{P}_2 \end{cases}$$

$$\vdots\vdots\vdots$$

$$\text{Iteration i}\begin{cases} U_{2\to 1}^{(i)}(\mathbf{r}, z=0) & = \mathcal{G}_{2\to 1}\left[U_0(\mathbf{r}, z=0)\frac{U_{1\to 2}^{*(i-1)}(\mathbf{r}',z=L)}{\left|U_{1\to 2}^{(i-1)}(\mathbf{r}',z=L)\right|}\right] \times \mathcal{P}_1 \\ U_{1\to 2}^{(i)}(\mathbf{r}', z=L) & = \mathcal{G}_{1\to 2}\left[U_0(\mathbf{r}, z=0)\frac{U_{2\to 1}^{*(i)}(\mathbf{r},z=0)}{\left|U_{2\to 1}^{(i)}(\mathbf{r},z=0)\right|}\right] \times \mathcal{P}_2 \end{cases}$$

Where:

- $U_0(\mathbf{r}, z=0)$ is the initial field;
- $\mathcal{P}$ represents the pupil;
- $\mathcal{G}_{j\to k}[.]$ symbolises the propagation through turbulence from telescope j towards telescope k;
- $|A_0|$ represents total intensity of the emitted field;
- $U_{j\to k}$ is the field received in k after propagation from j;
- The ratio $\frac{U_{j\to k}^{*(i)}(\mathbf{r}',z=L)}{\left|U_{j\to k}^{(i)}(\mathbf{r}',z=L)\right|} = e^{-i\varphi_j}$ represents phase correction in k.

Without loss of generality the total intensity will be fixed to $|A_0|^2 = 1$. In other words, the emitted field after each iteration will be normalised to a value of 1. Each round trip between one telescope and the other will be considered as a single iteration step. Results are presented for telescope $T2$ only.

6.2.2 Optimisation of the Emitted Intensity Distribution

We suppose that laser beams are emitted through un-obscured circular pupils. We also suppose the beams to be monomode Gaussian beams. The initial emitted beam waist can have an important impact on the total collected flux after propagation with iterative phase-only pre-compensation. We first optimise the beam waist without turbulence based on PIB values. We will then jointly optimise mean PIB and normalised intensity fluctuations with atmospheric turbulence.

6.2.2.1 Without Turbulence

We first focus on optimising the emitted beam waist for sub-optimal correction without any atmospheric turbulence. From figure 6.17 it is clear that final PIB values and using an iterative correction are only loosely dependent on the initial Gaussian beam waist. When the emitted

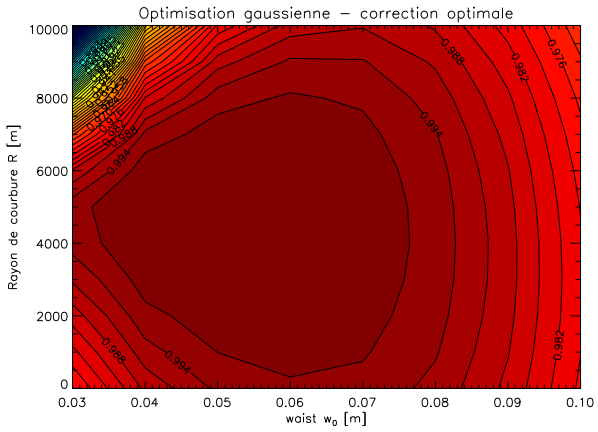

Figure 6.17: Iso-intensity curves after propagation: Gaussian beam parameters optimisation for a sub-optimal correction. Non-turbulent propagation with pupil truncation at both emission and reception of $D = 30\,\text{cm}$. Propagation distance $L = 10\,\text{km}$, $\lambda = 1.5\ \mu\text{m}$.

beam has a small waist or a small radius of curvature, the beam is highly divergent. It will then suffer from strong energy losses imposed by pupil truncation at reception. Inversely, when the beam is much larger than the emission pupil, the beam is only slightly divergent. Diffraction by the edge of emission pupil also leads to energy losses. In an intermediate regime, approximately between $5\,\text{cm} < w_0 < 9\,\text{cm}$, energy losses are minimised. The beam waist position relative to the propagation path has little impact on the collected energy.

Nevertheless, it appears that a beam of waist $w_0 = 5\,\text{cm}$ focalised in the middle of the path($z_{w_0} = 5\,\text{km}$), will minimise energy losses. In addition, iso-intensity curves are relatively flat. Small parameters variations w_0, z_{w_0} or D will not strongly impact the final PIB value after iterations. By, for example, doubling the beam size w_0 or by choosing a collimated beam with waist in the pupil ($z_{w_0} = 0$), energy losses will be kept below the percent. However, when strongly changing the wavelength or the pupil size, the beam natural divergence and diffraction by the pupil edge will no longer be negligible. Optimal parameters will then be modified.

Initial parameters for sub-optimal correction are taken as $w_0 = 5\,\text{cm}$ for the beam waist focalised at $z_{w_0} = 5\,\text{km}$. This means that the radius of the emitted beam in the pupil is $w_{z=0} \simeq 7\,\text{cm}$. Both optimal and sub-optimal approaches lead to very similar results.

6.2.2.2 Impact of Atmospheric Turbulence

By adding atmospheric turbulence both, intensity fluctuations and mean intensity must be studied. Figure 6.18 presents a parametric study used to optimise the size of the beam for differ-

ent turbulence strengths.

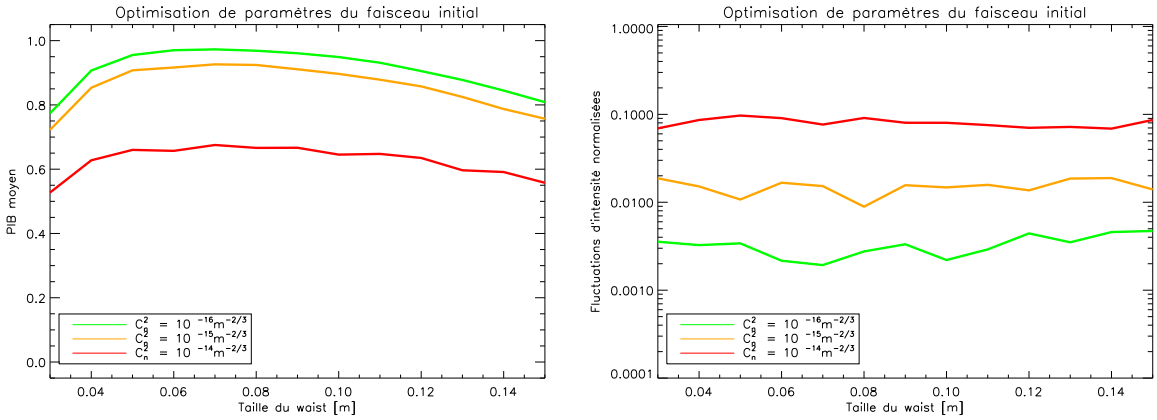

Figure 6.18: Gaussian beam parameters optimisation for iterative phase-only correction. Pupils diameter $D = 30\,\text{cm}$, propagation distance $L = 10\,\text{km}$, $\lambda = 1.5$ µm. . Left: mean Power in the Bucket (PIB), right: normalised intensity fluctuations.

Figure 6.18 only shows cases where the beam waist is in the emitting pupil, that is $z_{w_0} = 0$. Iterative phase-only correction is capable of directly modifying the beam focusing power; the waist position has a limited effect on final optimisation values. Results of the parametric study show an optimal beam waist between approximately $5 < w_0 < 10\,\text{cm}$ with turbulence. For the range of beam waist studied, intensity fluctuations do not depend on the size of the beam.

6.2.3 Performances Function of Turbulence Strength

6.2.3.1 Correction Effect on Energy Distribution

An example of short-exposure intensity distribution after propagation is presented figure 6.19. It illustrates phase-only iterative correction efficiency after 10 iterations. For $C_n^2 = 10^{-14}\,\text{m}^{-2/3}$ and this particular turbulence realisation, phase correction lead to an improvement from $I_0 = 25\%$ to $I_9 = 41\%$ of the total collected flux in only 10 iterations. Qualitatively, phase correction is able to increase the collected flux but does not enable, as with the optimal correction, a concentration of the major party of the flux within the aperture.

6.2.3.2 Influence of Turbulence Strength

We first study the evolution of mean intensity and intensity fluctuations for three turbulence strength as a function of number of iterations i (see figure 6.20). We observe that correction efficiency (i.e. final values of both metrics after convergence of the sub-optimal correction) depends on turbulence strength. This has already been observed for optimal correction as well. By first considering $C_n^2 = 10^{-14}\,\text{m}^{-2/3}$, we observe that phase-only iterative correction can noticeably increase mean PIB. It goes from $\langle I_0 \rangle = 0.30$ to $\langle I_4 \rangle = 0.63$ after five iterations. This

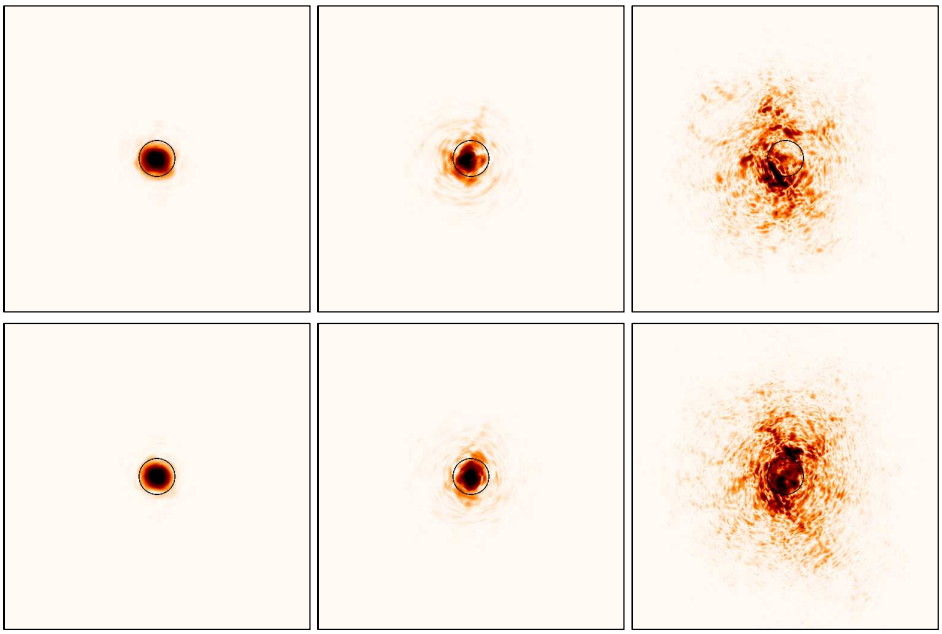

Figure 6.19: Sub-optimal iterative phase correction influence. Top: short-exposure images without any correction; bottom: short-exposure images with phase correction and 10 iterations. Propagation distance $10\,\text{km}$, $\lambda = 1.5$ µm. From left to right: $C_n^2 = 10^{-16}$, 10^{-15} and $10^{-14}\,\text{m}^{-2/3}$. For same turbulence strength, intensity distributions are obtained with the same turbulence realisation. Logarithmic colour scale for better contrast visualisation.

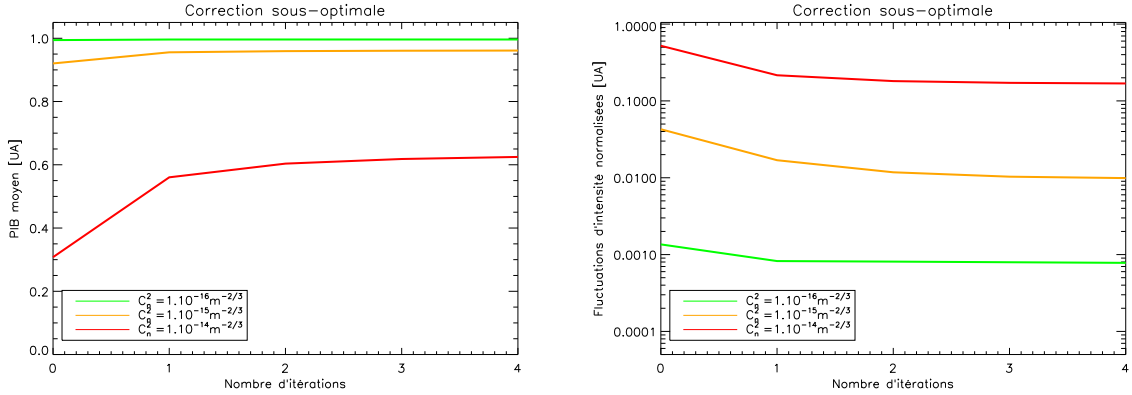

Figure 6.20: Iterative phase correction efficiency. Propagation distance $10\,\text{km}$, $\lambda = 1.5$ µm and $D = 30\,\text{cm}$. Left: mean PIB function of number of iterations. Right: normalised intensity fluctuations function of number of iterations.

is equivalent to an average increase of 110%. We recall that the value obtained for the optimal correction was $\langle I_4 \rangle = 0.82$ for the same configuration. Similarly to the optimal correction, we

observe that correction efficiency for mean PIB increases with turbulence strength. However, link quality is already excellent for the weaker turbulence cases.

If we now look at residual PIB fluctuations, we can observe that they are reduced whatever the turbulence strength considered. For $C_n^2 = 10^{-14}\,\mathrm{m}^{-2/3}$, intensity fluctuations go from $\frac{\sigma_{I_0}}{\langle I_0 \rangle} = 0.5$ to $\frac{\sigma_{I_4}}{\langle I_4 \rangle} = 0.18$ after five iterations. This is equivalent to an average decrease of 64% (resp. $\frac{\sigma_{I_4}}{\langle I_4 \rangle} = 0.08$, or 84% for optimal correction).

Concerning convergence speed, the first iteration step is always the most efficient. However, if one iteration is sufficient for weak turbulence and for average PIB, it appears that a larger number of iterations is required for other cases. This has already been shown for optimal correction. For all considered cases, it has been noticed that only 5 iterations are generally sufficient to reach convergence. For sub-optimal correction, the final value after convergence is always lower than the value reached using an optimal correction scheme. This observation is valid both for $\langle I \rangle$ or $\frac{\sigma_I}{\langle I \rangle}$ and regardless of turbulence strength.

6.2.3.3 Average Error Rate

In figure 6.21 is presented the impact of sub-optimal correction on mean error rate. This figure shows results for a turbulent propagation with $C_n^2 = 10^{-14}\,\mathrm{m}^{-2/3}$ (in red) et $C_n^2 = 10^{-15}\,\mathrm{m}^{-2/3}$ (in orange), with and without sub-optimal correction. Curves show for the weakest

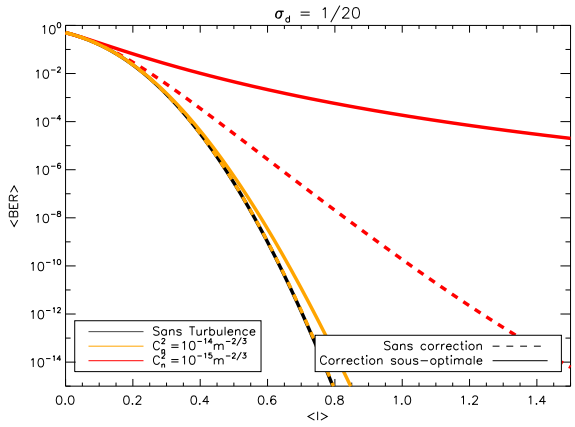

Figure 6.21: Average BER evolution function of mean received intensity. Orange: $C_n^2 = 10^{-15}\,\mathrm{m}^{-2/3}$, red: $C_n^2 = 10^{-14}\,\mathrm{m}^{-2/3}$ Dashed lines: without correction; full lines: sub-optimal correction.

perturbation studied here, that sub-optimal correction can reduce the error rate significantly and up to levels approximately equal to levels obtained without turbulence. For $C_n^2 = 10^{-14}\,\mathrm{m}^{-2/3}$, sub-optimal correction cannot sufficiently reduce fluctuations ($\frac{\sigma_I}{\langle I \rangle} > 0.1$). However, mean BER is still much lower than without correction and a normalised optical power of $\langle I \rangle = 1.2$ will be sufficient to reach $\langle BER \rangle = 10^{-12}$. This optical power requires the emitted power to be doubled because the received intensity after sub-optimal correction convergence is equal to

$\langle I \rangle_{C_n^2=10^{-14}\,\mathrm{m}^{-2/3}} = 0.63$. These considerations are to be taken with precautions because delimited by the validity domain of the log-normal probability density.

6.2.4 Pupil Diameter Influence on Performance

Similarly to optimal correction, efficiency after convergence of the sub-optimal correction depends on turbulence strength, pupil diameters, wavelength and propagation distance. The dimensioning value is still the reduce parameter $\sqrt{\lambda L}$ for weak turbulence. We recall that these effects are purely diffractive without any relation with turbulence. When pupil diameters are too small, diffraction imposes loses between the two ends of the link. Oppositely, for an infinitely large pupil, all the flux is collected by the pupil and correction is unable to improve the already extremely good link. Figure 6.22 shows pupil diameter influence for a wavelength of $\lambda = 1.5$ µm and several propagation regimes.

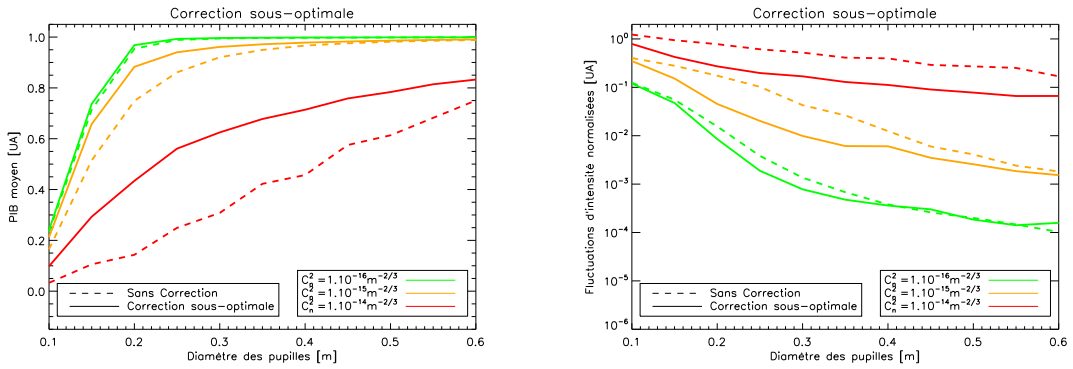

Figure 6.22: Phase-only sub-optimal correction efficiency as a function of telescope pupil diameters for several turbulence strength. Propagation distance $L = 10\,\mathrm{km}$ and $\lambda = 1.5$ µm. Full lines: sub-optimal correction; dashed lines: no correction. Left: average PIB; right: normalised intensity fluctuations.

Lets first focus on average PIB $\langle I \rangle$ as a function of pupil diameters D. We can observe that for weak perturbations (i.e. diffractive regime), when pupil diameters are smaller than $L_F = \sqrt{\lambda L}$ and greater than $2L_F$, phase-only correction is inefficient and unnecessary relative to $\langle I \rangle$. This result has already been presented for optimal correction

We present figure 6.23 correction gain as function of pupil size. We recall that the chosen conventions for PIB gain and intensity fluctuation gain are given by equations 6.3 and 6.4.

Concerning intensity fluctuations, the correction gain for weak turbulence regimes seem to saturate from approximately $3L_F$. The real gain brought by sub-optimal correction relative to no correction at all lies between $L_F < D < 3L_F$. Beyond these limits, phase-only iterative correction is unnecessary relative to intensity fluctuations. In a strong perturbation regime ($\sigma_R^2 = 14$), fluctuations decrease proportionally to D^{-1} or equivalently inversely proportionally to the

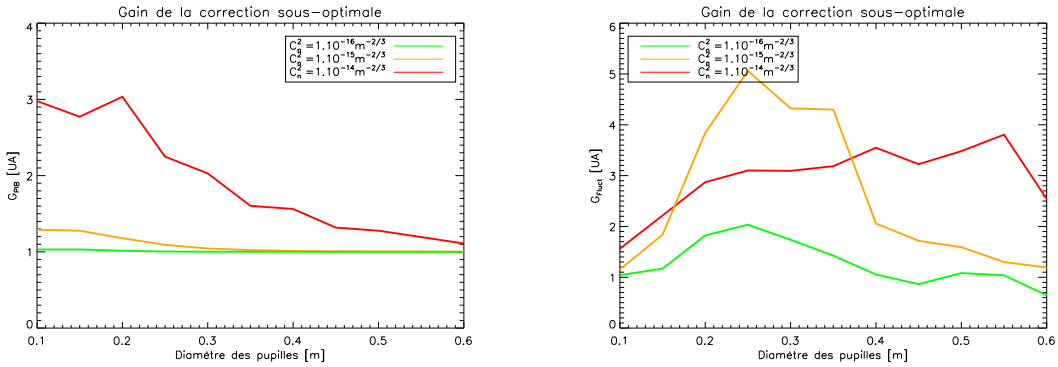

Figure 6.23: Gain brought by phase-only iterative correction function of telescope pupil diameter and turbulence strength. Propagation distance $L = 10\,\text{km}$, $\lambda = 1.5$ µm. Left: average PIB gain; right: normalised intensity fluctuations gains.

square root of the number of independent speckles in the pupil. For $\sigma_R^2 = 0.14$ and $\sigma_R^2 = 1.4$ the behaviour is different since most of the perturbations are introduced by beam wander.

We can observe that the slopes are similar to the one presented figure 6.9 for optimal correction. However, they show much lower values in the present case. For intensity fluctuations, the gain in PIB stays lower than $G_{PIB} < 1.3$ for the entire range of pupil diameters studied. Sub-optimal correction efficiency relative to propagation without correction decreases as a function of the optics size.

Concerning intensity fluctuations gain, they present an intermediate area where gain is maximal. This area is approximately located between $15\,\text{cm} < D < 40\,\text{cm}$ for weak turbulence, values identified earlier. By selecting a pupil diameter of $D = 30\,\text{cm}$, the intensity fluctuation gain is approximately 14 (resp. 19 and 8) for optimal correction. For sub-optimal correction gain drops to 3 (resp. 4.5 et 1.7) with turbulence strength of $C_n^2 = 10^{-14}\,\text{m}^{-2/3}$ (resp. $C_n^2 = 10^{-15}$ and $10^{-16}\,\text{m}^{-2/3}$). This clearly illustrates the loss, in terms of correction quality, when only controlling the phase part of the emitted field.

6.2.5 Probability Density

Figure 6.24 illustrates PDF modification created by iterative sub-optimal phase-only correction. The global distribution seems to be modified towards a log-normal distribution as predicted for weak perturbations or when pupil averaging is sufficiently important. Dashed curves represent a log-normal fit to the simulation curves respectively for $C_n^2 = 10^{-15}\,\text{m}^{-2/3}$ and $C_n^2 = 10^{-14}\,\text{m}^{-2/3}$. The improvement brought by the sub-optimal correction is clearly visible for all studied turbulence strengths and when comparing to a propagation without correction. For comparison see figure 2.16. However, discrepancies with the log-normal distribution, relatively reduced for the first case, are fairly important for strong turbulence conditions and that despite the correction.

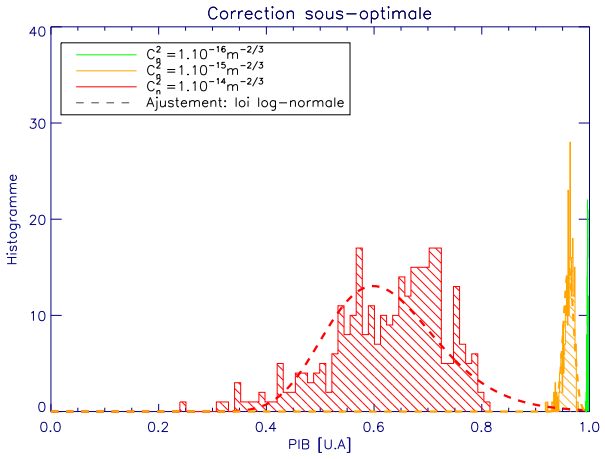

Figure 6.24: PIB histograms for various turbulence strength with sub-optimal correction. Propagation distance $L = 10\,\text{km}$, $\lambda = 1.5$ µm and pupil diameter $D = 30\,\text{cm}$. Dashed curves represent a log-normal fit to the simulated data.

6.3 Conclusion

In this chapter, we have re-interpreted Bachers work in order to understand the ultimate limits of adaptive optics correction for FSO systems [Schwartz-p-09]. This study has been performed in the framework of the Fortune43G project, a typical example of long-distance endo-atmospheric propagation in the near infrared. The analysis carried out in this chapter enabled us to identify phase and amplitude (i.e. full-wave) iterative correction as the optimal correction between two telescopes composing an optical atmospheric link. It shows that optimal control efficiency goes largely beyond weak perturbation regime. Enabling both an increase in mean PIB and an important reduction in intensity fluctuations, it appears to be well adapted to FSO applications. Correction performance has been evaluated according to those two criterions and to the mean bit error rate of the link. We have observed that correction performance is in particular limited by pupil truncation and turbulence strength. In the diffractive regime, that is when the pupil diameter $D > \sqrt{\lambda L}$, it is possible to create a propagation mode. A propagation mode is temporally and spatially invariant. In addition, we have established that when the coupling coefficient between the two telescopes is already excellent without correction (i.e. weak perturbations and $D > \sqrt{\lambda L}$), the improvement brought by correction is small in terms of average PIB but can be quite substantial for residual intensity fluctuations (a factor of approximately 10). For strong perturbations ($\sigma_R^2 > 1$) correction is able to improve both values simultaneously. However, when turbulence increases even more (i.e. saturation regime), only PIB improves significantly. Intensity fluctuations on the other hand are also reduced but to a lesser extent.

To the best of our knowledge, no optimal correction implementation has yet been proposed. Its study has been limited to a theoretical examination only. Nevertheless, it enables us to establish theoretical limitations in terms of correction quality that we hope to achieve with adaptive

optics correction. The fundamental reason for the lack of implementation is linked to the difficulty of jointly controlling phase and amplitude of the emitted field. This argument led to the study of the so-called sub-optimal correction limited to a phase-only control of the field. This chapter enabled us to characterise the Gaussian beam parameters optimising the optical link quality with atmospheric turbulence and adaptive optics correction. We have observed, regardless of the poorer performance of the phase-only correction relative to the optimal correction, that is enables a clear improvement both in terms of PIB and intensity fluctuations. Sub-optimal correction can be used to establish theoretical limits of a correction limited to the phase part of the field in the pupil plane. In particular, we have shown that:

- Pupil plane phase modification can be used to stabilise intensity distribution after propagation over a long distance.
- Phase-only correction is a less powerful correction strategy than phase and amplitude correction. However, it can effectively be used to monotonously increase mean received PIB (resp. decrease intensity fluctuations).
- Improvement (gain) brought by the correction is proportional to pupil size and turbulence strength C_n^2.

However, in strong perturbation regimes, phase-only correction does not enable a sufficient reduction in residual intensity fluctuations. We have previously set the acceptable intensity fluctuation limit to $\frac{\sigma_I}{\langle I \rangle} = 0.1$. For a typical pupil diameter of $D = 30\,\text{cm}$, this limit is not achievable. It is necessary to increase thes diameter to $D \simeq 40\,\text{cm}$ to keep the performance above the desired threshold. In the two following chapters, we will study various classical AO configurations implementing phase-only correction.

Chapter 7

Correction on Counter-Propagating Laser beam Probe

Contents

In the field of adaptive optics corrected atmospheric optical link, the classical approach consists in using a counter-propagating laser beam probe fixed at the other end of the link. The wavefront is analysed by the emitting telescope using the counter-propagating laser. This method is a classical AO implementation with a cooperative point source on which wavefront measurement is performed. In the theoretical work presented paragraph 6.2, we have shown that iterative phase correction, or sub-optimal correction, can be used to increase link quality significantly. The first

iteration was identified as the most effective with regards to the studied metrics $\langle I \rangle$ and $\frac{\sigma_I}{\langle I \rangle}$. Phase correction on a counter-propagating beam presents the double advantage of making the AO loop bandwidth requirements less difficult while suffering only marginally from performance degradation relative to the full sub-optimal correction. Bandwidth requirements relaxation comes from the fact that only one iteration is necessary between emitter and receiver to reach the desired solution. The goal of this chapter is to understand limitations imposed by AO correction on a laser beam probe and analyse its performance relative to optical communication systems.

We will first study the expected performance for a perfect phase control without any iterations using a divergent counter-propagating laser beam. This type of correction requires a exact knowledge of the received phase and the ability to reproduce its shape perfectly. Secondly, we compare these results with correction obtained with SH wavefront sensor measurements (paragraph 7.2). Results are compared with two different configurations: perfect non-iterative correction on counter-propagating beam (paragraph 7.1) and iterative phase correction (paragraph 7.4). We show that the improvement brought by AO correction is limited in strong perturbations. This limitation is mainly due to scintillation. We suggest, paragraph 7.3, a simple implementation that can partially overcome this limitation by using several counter-propagating laser beams instead of a single one.

7.1 Counter-Propagating Beam Correction using True Phase

In this paragraph, we present results of correction using a counter-propagating laser beam as presented paragraph 4.2.1 and by supposing perfect knowledge of the phase of the complex field $U_s(r, z = 0)$. We remind figure 7.1 the correction diagram, specifying the different laser beams used and positions of telescope 1 and 2. We consider, as a first approximation, that

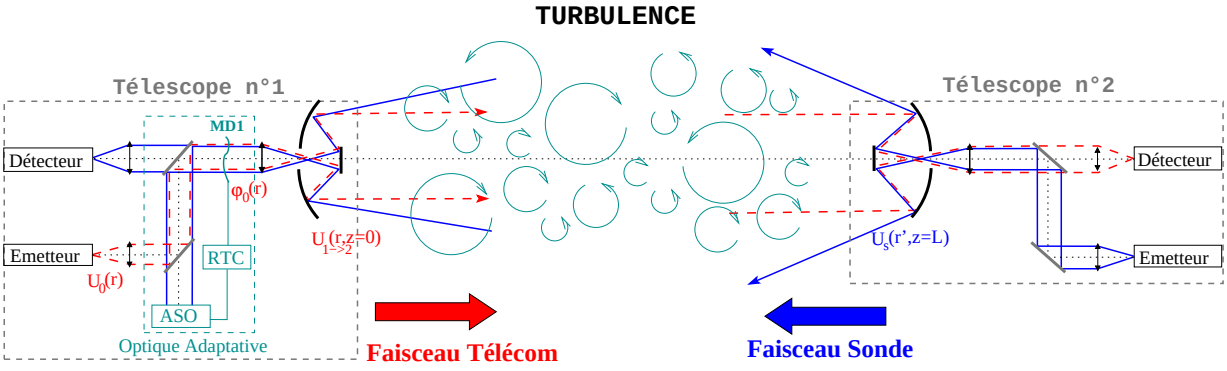

Figure 7.1: Diagram of phase correction using a counter-propagated laser beam.

the adaptive optics system located at telescope 1 (also called emitting telescope) can be used to correct phase perfectly. Various errors introduced by the use of a SH wavefront sensor (see paragraph 7.2.1.1) are neglected. In this paragraph we present the probe beam and telecom beam

geometry optimisation (cf. §7.1.1). The influence of pupil diameter on the metrics $\langle I \rangle$ and $\frac{\sigma_I}{\langle I \rangle}$ are discussed paragraph 7.2.2.2.

7.1.1 Laser Beam Geometry

7.1.1.1 Probe Beam

In theory and in this configuration, the probe should be a spherical beam. In practice, the beam divergence is limited by energetic considerations. The beam divergence must be sufficiently large to ensure that an important part of the flux arrives at the wavefront sensor detector in $T1$. The probe beam is not corrected and will directly be affected by turbulence. It will mainly suffer from beam wander. When the beam wander is too strong, the probe beam will not be able to reach the emission pupil. Wavefront sensing will be impossible. In order to overcome this problem, the use of a very divergent beam is necessary to cover a large area at the level of the emitting pupil. This area must be sufficiently large so that, even with atmospheric turbulence, the spatially limited beam arrives at the other end of the communication link. We choose the divergence of the beam U_s such that its diameter after propagation in free-space without atmospheric turbulence is $w_{z=0}(U_s) = 2\,\text{m}$. This approximately corresponds to a emitting beam radius of $w_{z=L}(U_s) = 5\,\text{mm}$.

Moreover, for a spherical geometry, the beam is infinitely small near $T2$. This particular geometry can be justified by the fact that we know that turbulence creating scintillation on $U_{1\to2}(r', z = L)$ near $T2$ is located near telescope $T1$. Phase perturbations near $T2$ mainly leads to phase modifications but little scintillation. Emitting a beam $U_s(r', z = L)$ of small diameter will only suffer marginally from perturbations located in the vicinity of $T2$. We are trying here to approximate a spherical wave by a Gaussian beam with limited waist size. Figure 7.2 presents laser beam probe and telecom beam geometry as well as the impact of turbulence on $U_{1\to2}$ as a function of propagation distance. The beam carrying the information to be transmitted from tele-

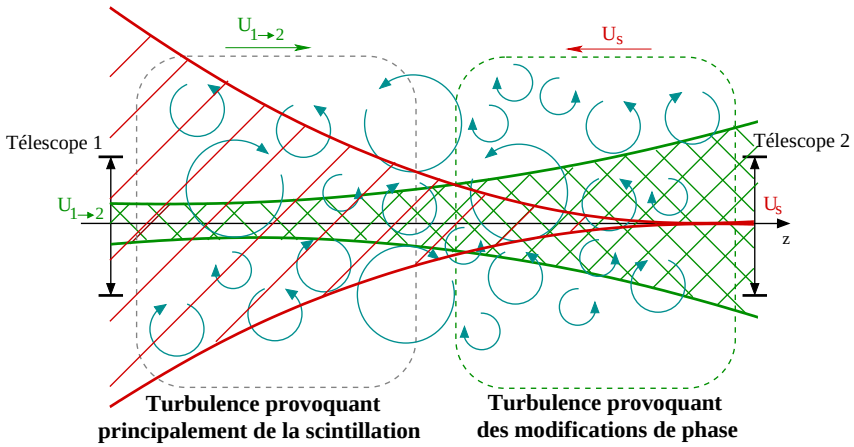

Figure 7.2: Geometry of the probe beam U_s, telecom beam $U_{1\to2}$ and impact of the turbulence position relative to the telescopes on the telecom beam.

scope 1 to telescope 2 (telecom beam) must have the maximum of its energy within the reception aperture. Its divergence must therefore be limited. We will consider in the rest of the document that the beam waist is in the plane $z = 0$.

7.1.1.2 Optimisation of Telecom Beam Parameters

In this paragraph we search for the telecom beam waist value that optimises both $\langle I \rangle$ and $\frac{\sigma_I}{\langle I \rangle}$ by using a perfect phase correction. Optimisation is preformed with an aperture diameter of $D = 30\,\text{cm}$, a propagation distance of $L = 10\,\text{km}$ and a wavelength of $\lambda = 1.5$ µm. Figure 7.3 presents the optimisation results with these propagation parameters and phase-only correction. The correction phase used is the opposite of the received laser beam probe phase. For an FSO sys-

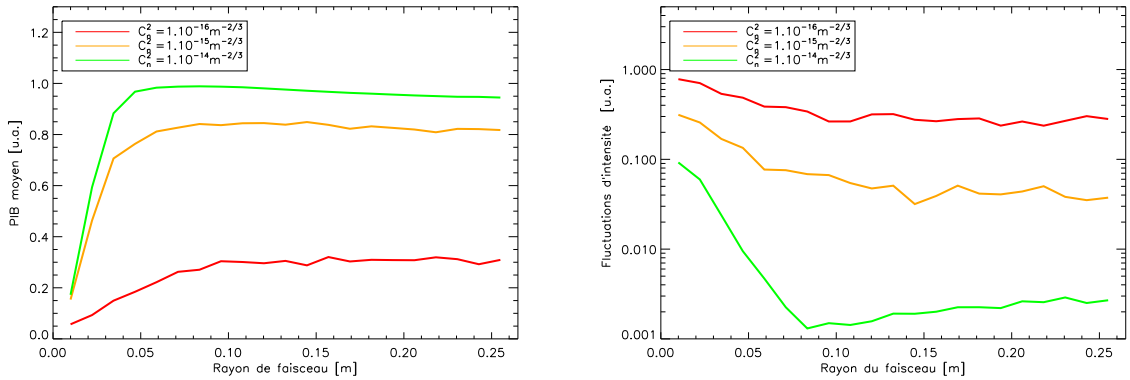

Figure 7.3: Gaussian beam parameters optimisation for a perfect phase correction using a counter-propagating beam. Left: mean PIB, right : normalised intensity fluctuations.

tem using propagation through atmospheric turbulence, it is important to jointly optimise mean intensity and intensity fluctuations. It can be noticed that small telecom beams result in strong flux loses due to geometrical truncation by telescope $T2$. In fact, for beams $w_{z=0}\,(U_{1\to 2}) \lesssim 7\,\text{cm}$ divergence is such that flux losses is important even for low turbulence. From a certain beam size (approximately $w_0 = 9\,\text{cm}$) the loss is reduced regardless of turbulence strength. For larger beam size and for the range of beam sizes studied, diffraction effects by the edges of telescope $T1$ are negligible. For the remainder of the document we will use a telecom beam with $w_0 = 10\,\text{cm}$. This result is similar to the optimisation results obtained for optimal and sub-optimal corrections.

7.1.2 Influence of Pupil Diameter

7.1.2.1 Example of Correction Efficiency

Figure 7.4 gives an example of phase-only correction using a counter-propagating beam. It shows short-exposure images both without any correction (upper part of the figure) and with a perfect phase correction (lower part of the figure) for three different turbulence strengths. For

same turbulence strengths, images with and without correction are obtained using the same turbulence realisation. A direct comparison between uncorrected and corrected images is therefore possible. For these specific turbulence realisations and for a turbulence strength of $C_n^2 =$

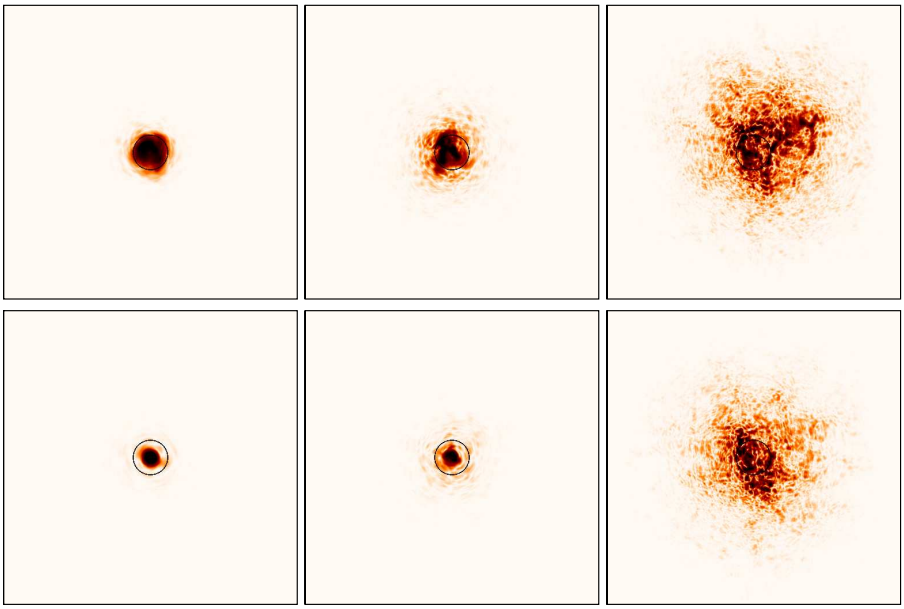

Figure 7.4: Influence of perfect phase correction. Top: short-exposure images without correction, bottom: short-exposure images with perfect phase correction. From left to right: $C_n^2 = 10^{-16}\,\mathrm{m}^{-2/3}$, $C_n^2 = 10^{-15}\,\mathrm{m}^{-2/3}$ and $C_n^2 = 10^{-14}\,\mathrm{m}^{-2/3}$. Propagation distance $L = 10\,\mathrm{km}$, wavelength $\lambda = 1.5$ µm and pupil diameter $D = 30\,\mathrm{cm}$. Logarithmic colour scale.

$10^{-14}\,\mathrm{m}^{-2/3}$, the total intensity integrated of the pupil aperture of $D = 30\,\mathrm{cm}$ is $I_{without\ Corr} = 0.27$ in absence of correction and $I_{Corr} = 0.39$ after perfect phase correction. The $C_n^2 = 10^{-15}\,\mathrm{m}^{-2/3}$ case leads to an increase of $I_{Without\ Corr} = 0.90$ to $I_{Corr} = 0.94$. For the weakest turbulence strength studied, the intensity goes from $I_{Without\ Corr} = 0.95$ to $I_{Corr} = 0.99$ after correction.

7.1.2.2 Influence of Pupil Diameter

Figure 7.5 represents the quality evolution for a perfect phase correction using a counter-propagating laser probe. Several turbulence strengths and pupil diameters are studied. On the left hand side of figure 7.5 is studied mean PIB and on the right hand side normalised intensity fluctuations both using perfect phase correction. We recall that the Gaussian beam used has been optimised for a pupil diameter of $D = 30\,\mathrm{cm}$.

As presented in chapter 6 when the pupil diameter D is too small, the improvement brought by correction is small. In the diffractive regime ($\sigma_R^2 = 0.14$), the limit when correction seems superfluous relative to $\langle I \rangle$ is approximately located around $2\sqrt{\lambda L}$. This value has already been identified using optimal and sub-optimal corrections. For intermediate regimes, correction is

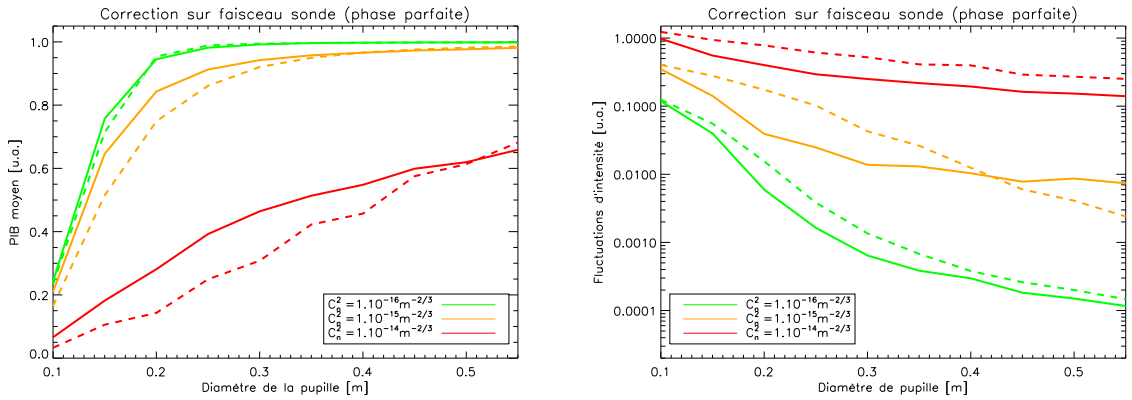

Figure 7.5: Correction quality evolution for a perfect phase correction using a counter-propagating laser beam probe. Different turbulence strengths and pupil diameters are studied. Left: Mean Power in the Bucket, right: normalised intensity fluctuations. Solid lines: with perfect phase correction ; dashed lines: without any correction.

unnecessary above $D \simeq 35\,\text{cm}$. For $\sigma_R^2 = 14$ the limit is located around $D < 55\,\text{cm}$. We recall that $\frac{\lambda L}{\pi \rho_0} \simeq 50\,\text{cm}$ for the studied strong turbulence case. Above this limit mean PIB cannot be improved by correction.

If we set the acceptable limit in terms of intensity fluctuations to $\frac{\sigma_I}{\langle I \rangle} = 0.1$, as identified in introduction chapters, this value cannot actually be reached for the studied pupil diameters if $C_n^2 = 10^{-14}\,\text{m}^{-2/3}$. Correction is not sufficient to achieve this value. It is necessary to use a larger telescope with $D > 55\,\text{cm}$ to reach this goal. Unfortunately, for these diameters the improvement brought by phase-only correction is minimal when looking at mean PIB. For intermediate turbulence strength (i.e. $C_n^2 = 10^{-15}\,\text{m}^{-2/3}$), pupil diameters of $10 < D < 45\,\text{cm}$ can be used to reach the desired fluctuations value. The most interesting area where correction enable a decrease below the $\frac{\sigma_I}{\langle I \rangle} = 0.1$ threshold is between $20 < D < 30\,\text{cm}$ for $C_n^2 = 10^{-15}\,\text{m}^{-2/3}$. Above $D = 30\,\text{cm}$ no correction is required as the optical link is already excellent.

As a conclusion, even by using a perfect wavefront measurement and control, the range where non-iterative methods can be used seems limited. This technique should be seen more as a method to increase working range of optical communication links in an intermediate perturbation regime.

7.2 Correction Using A Counter-Propagating Beam: Shack-Hartmann Case

So far we has only estimated performance (either iteratively or not) by considering perfect both the wavefront measurement and the correction systems. Adaptive optics requires at the minimum a deformable mirror and a wavefront sensor capable of reconstructing the incoming

phase. In this paragraph we will mainly concentrate on the impact of wavefront reconstruction on phase-only correction (§7.2.2). Firstly, we describe the correction system (§7.2.1) and in particular the choice and the geometry of Shack-Hartmann wavefront sensor. In addition, we give the hypotheses used for wavefront reconstruction in order to undertake the necessary numerical simulations.

7.2.1 Description of the Correction System

7.2.1.1 Errors Analysis

Correction quality is contaminated by errors that do not enable us to perfectly reconstruct the true wavefront (i.e. perfect phase). The residual error σ^2_{res} between the true phase and the reconstructed phase is the sum of several errors:

$$\sigma^2_{res} = \sigma^2_{fit} + \sigma^2_{alias} + \sigma^2_{temp} + \sigma^2_{noise} + \sigma^2_{scintillation} \tag{7.1}$$

With:

- σ^2_{fit}: AO can only compensate for a finite number of spatial frequencies. Spatial under-sampling of the wavefront leads to a fitting error.
- σ^2_{alias}: The Shack-Hartmann wavefront sensor (i.e. SH-WFS) is sensitive to high spatial frequencies creating an aliasing error of the high frequencies into the lower measured ones.
- σ^2_{temp}: Temporal errors is due to the limited bandwidth of the AO loop; that is that turbulence evolves between the time when the slopes measurements are made and the time when the voltage is applied to the DM.
- σ^2_{noise}: Slope measurement is affected by noise (photon, electronic, detector ...).
- $\sigma^2_{scintillation}$: Wavefront measurements are affected by scintillation creating scintillation error.

In order to simplify the study and discriminate between different errors impacting correction quality, we will neglect temporal error of the AO loop, that is we consider an infinite bandwidth: $\sigma^2_{temp} = 0$. In addition, as mentioned in the previous chapter, we will also neglect and only for the time being measurement noise: $\sigma^2_{noise} = 0$. Only spatial under-sampling of the wavefront σ^2_{fit}, aliasing σ^2_{alias} and scintillation $\sigma^2_{scintillation}$ will be taken into account for the time being.

7.2.1.2 Selection of the Wavefront Sensor

A large number of wavefront sensors exists. In addition, for atmospheric free space communication links, several WFSs can potentially be used. Curvature wavefront sensor, Shack-Hartmann or phase diversity techniques are possible options. Phase diversity requires heavy calculations and is currently ill-adapted to FSOs. We will concentrate on SH-WFS for this study.

This type of wavefront sensor is the most commonly used wavefront sensor in current AO systems and its limitations are representatives of most pupil plan WFSs. The limited number of reconstructed modes (Zernikes) and in particular the influence of scintillation of the reconstructed phase is studied in the following chapters.

7.2.1.3 Wavefront Sensor Geometry

The conventional rule for characterising the SH-WFS in AO is done by choosing the lenslets diameter to be equal to r_0 where r_0 is the Fried diameter. This leads to a value of $2\,\text{cm}$ (resp. $8.3\,\text{cm}$) for turbulence of $C_n^2 = 10^{-14}\,\text{m}^{-2/3}$ (resp. $10^{-15}\,\text{m}^{-2/3}$). The number of lenslets depends on the number of mode one wants to correct (aliasing and fitting error) and scintillation error. The final choice will also depend of the correction strategy (iterative or not). We consider that the correction is limited to the first 38 modes. A justification of this choice will be presented paragraph 7.3.6. A 7×7 lenslets SH-WFS array will be used which enables to reconstruct 38 mode. 7×7 lenslets is the minimum number to achieve an acceptable σ^2_{fit} and σ^2_{alias}. The SH-WFS is presented figure 7.6. The greyed area represents the strongly truncated lenslets by the pupil. Measurements for these lenslets won't be taken into account.

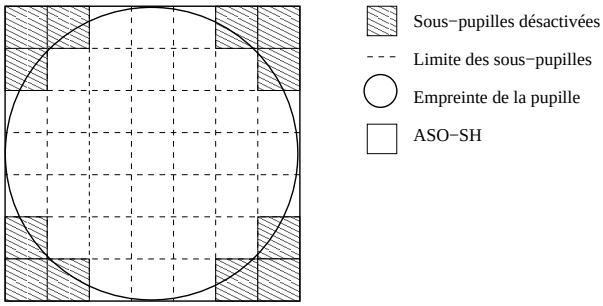

Figure 7.6: Wavefront sensor geometry and pupil imprint with deactivated lenslets.

7.2.1.4 Wavefront Reconstruction

SH-WFS slope measurements are performed by measuring displacement of focal images observed at the focus of each lenslets. These measurements are affected by detector and photon noise. Local slopes measurement of the wavefront is measured by centre-of-gravity (COG) of non noisy images. Temporal error is not taken into account.

Lets $\mathbf{M}$ be the measurement slope matrix. When the influence of scintillation is negligible on COG measurements, the operator $\mathbf{M}$ is linear. The slopes vector s can then be linked to the phase φ of the field in the lenslet by:

$$s = \mathbf{M}\varphi \tag{7.2}$$

Going from slopes to phase is performed by the generalised inverse of matrix $\mathbf{M}$. $\mathbf{M}$ represents here the interaction matrix of Zernike modes on SH slopes.

Phase reconstruction is affected by scintillation (some active lenslets can randomly over time receive virtually no flux) and by issues related to COG measurements in strong perturbations regimes. Figure 7.7 shows the influence of turbulence on SH images for different turbulence strengths. Methods have been developed [Nicolle-a-04] to be more robust to these effects.

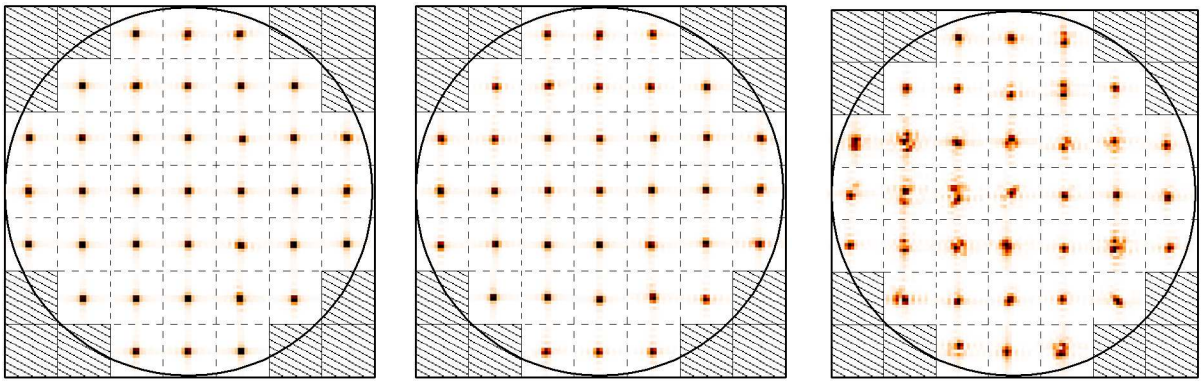

Figure 7.7: Influence of turbulence strength of SH noiseless images on a single turbulence occurrence. Left: $C_n^2 = 10^{-16}\,\mathrm{m}^{-2/3}$, centre: $C_n^2 = 10^{-14}\,\mathrm{m}^{-2/3}$ and right: $C_n^2 = 10^{-14}\,\mathrm{m}^{-2/3}$. The laser beam is divergent.

7.2.2 Wavefront Sensing on Counter-propagating Laser Beam Probe

After having studied perfect true phase correction, we now examine the same correction strategy when phase perturbations estimation is performed by a SH-WFS with a finite number of modes. We recall that this is realised by a SH-WFS with a 7×7 lenslets enabling the reconstruction of the first 38 Zernike modes.

7.2.2.1 Optimisation of Telecom Laser Beam Parameters

Similarly to perfect wavefront correction, parameters of the telecom beam have been chosen to optimise $\langle I \rangle$ and $\frac{\sigma_I}{\langle I \rangle}$. The optimisation is presented figure 7.3 using a SH-WFS for the wavefront reconstruction. It can be seen from figure 7.8 that the optimal parameters identified previously for a perfect phase correction are still valid for SH-WFS limited to the reconstruction of the first 38 Zernike modes. Similarly to perfect phase correction, we use a beam waist of $w_0 = 10\,\mathrm{cm}$ in radius for the telecom beam. The waist is still in the pupil.

7.2.2.2 Influence of the Pupil Diameter

We present figure 7.9 the evolution of correction quality for a phase-only correction based on a counter-propagating laser beam as a function of turbulence strength and pupil diameter. Propagation distance is $L = 10\,\mathrm{km}$ and wavelength is set to $\lambda = 1.5\ \mu\mathrm{m}$. We study both mean

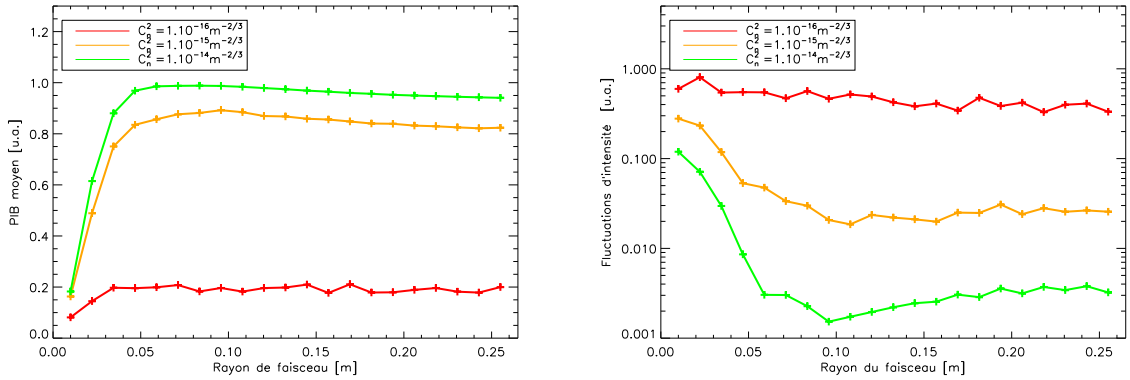

Figure 7.8: Correction quality function of the Gaussian beam waist size using a phase-only correction of a counter-propagating beam. Left: Mean Power in the Bucket, right: normalised intensity fluctuations.

PIB (see left hand side of the figure) and normalised intensity fluctuations (see right hand side of the figure).

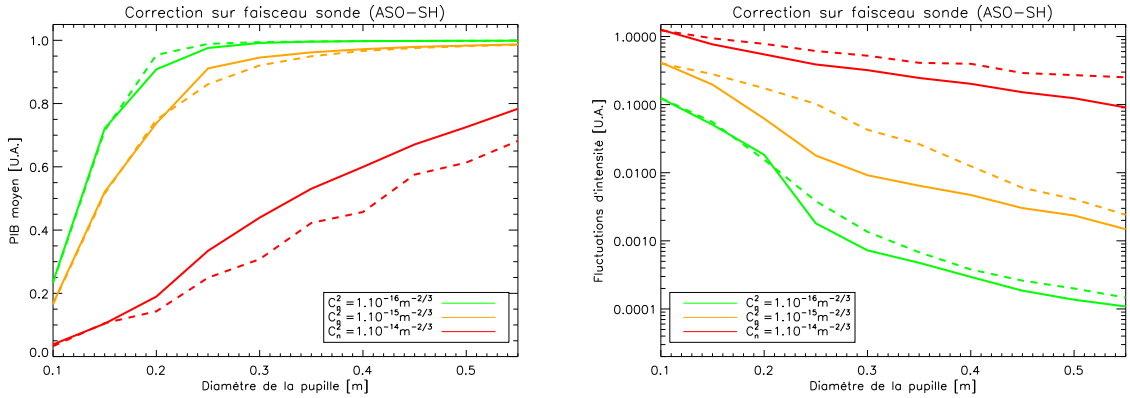

Figure 7.9: Evolution of correction quality for a phase-only correction based on a counter-propagating laser beam as a function of turbulence strength and pupil diameter. Left: Mean Power in the Bucket, right: normalised intensity fluctuations. Correction of the first 38 Zernike modes. Solid line: with phase-only correction, dashed lines: without any correction. $w_0 = 10\,\mathrm{cm}$.

Figure 7.10 shows the gain in terms of mean PIB and intensity fluctuations using phase-only correction on a counter-propagating probe and a finite number of Zernike modes. For the $C_n^2 = 10^{-16}\,\mathrm{m}^{-2/3}$ case and for both correction cases (i.e. perfect phase correction and phase correction using a SH-WFS) as expected, it can be seen that for mean PIB the gain brought by

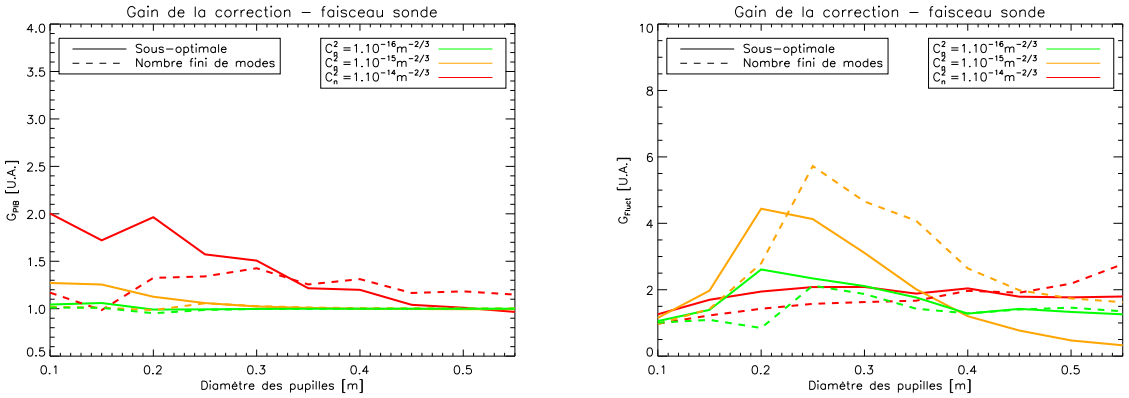

Figure 7.10: Gain of phase-only correction on a counter-propagating probe and a finite number of Zernike modes function of turbulence and pupil diameter. Left: mean Power in the Bucket, right: normalised intensity fluctuations. Propagation distance $L = 10\,\text{km}$ and $\lambda = 1.5\ \mu\text{m}$. Solid lines: correction on an infinite number of Zernike modes, dashed lines: correction of the first 38 Zernike modes.

AO in minimal ($G_{Fluct} \simeq 1$). For the $C_n^2 = 10^{-15}\,\text{m}^{-2/3}$ and $C_n^2 = 10^{-14}\,\text{m}^{-2/3}$ cases the gain of the SH-WFS is significantly less than with perfect phase measurement. However, conclusions drawn from perfect phase measurement and correction are still valid here. For $C_n^2 = 10^{-14}\,\text{m}^{-2/3}$ AO does not bring sufficient improvement to reach to required FSO system performance of a bit error rate of 10^{-12}. For $C_n^2 = 10^{-15}\,\text{m}^{-2/3}$ AO brings a small gain that can be used to increase the usability range of FSO systems for these typical conditions.

7.2.2.3 Conclusion

The impact of wavefront sensing techniques on correction performance is small. This conclusion has two explications:

- the AO performance for perfect non-iterative phase-only correction is mediocre;
- the influence or measurement noise has not been taken into account.

We will now concentrate on the impact of noisy wavefront measurement. Secondly, we will study the impact of wavefront measurement of iterative correction.

7.3 Correction Using a Counter-Propagating Beam: Multi-Probe Analysis

We did not take into account detection noise effects on wavefront measurement while simulating a non-iterative phase-only correction using a counter-propagating beam. In practice,

scintillation considerably reduces signal levels on some of the lenslets making noise levels no longer acceptable.

7.3.1 Correction Principal

In order to circumvent problems related to SH-WFS measurements we propose to take advantage of angular decorrelation of scintillation, also called scintillation anisoplanatism, by placing several laser beam probes [Kim-p-97, Polynkin-a-07, Schmidt-p-09] distributed over the field of view. The idea is to average scintillation effects in the field of view (FoV) for each lenslet. Phase correction diagram using multi-probe counter-propagation is presented figure 7.11. Probes are

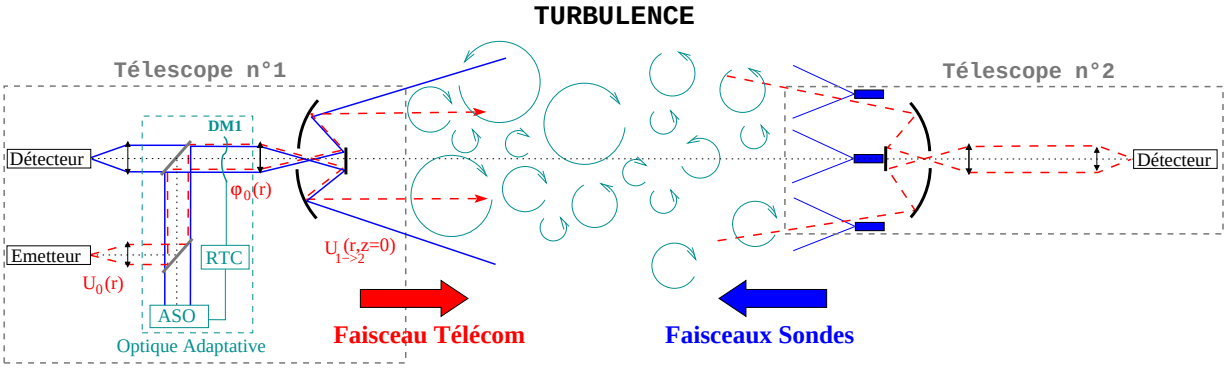

Figure 7.11: Diagram of phase correction using multi-probe counter-propagation.

depicted in blue on the diagram. We have previously seen that scintillation is mainly caused by phase perturbations close to the source. The goal of the wavefront measurement is here to measure perturbations close to $T1$ that are seen by all laser beam probes in the same way. This configuration can be seen as similar to ground layer adaptive optics (GLAO) used in astronomy. In order to optimise beam density in the plan of the reception pupil, we use six beams distributed in circle around the optical axis and one single laser on the optical axis. The geometry is described in figure 7.12. We therefore use 7 counter-propagating laser beam probes in the pupil plan of telescope 2. Let R_c be the distance between the optical axis and the position of the outer laser beams.

7.3.2 Optimal Seperation Distance Between Laser Probes

Spatial statistics of turbulence effects will determine the optimal distance between the probes in order to achieve the best averaging effect. The more we separate the beams, the more the turbulence effects are decorrelated and scintillation is reduced. However, as we move the beam outwards, not only scintillation effects of the different beams become decorrelated but phase effects also become decorrelated. A compromise is required between phase anisoplanatism and scintillation anisoplanatism that is between angular decorrelation of phase effects and angular decorrelation of scintillation effects. Each laser probe will pass through a slightly different part

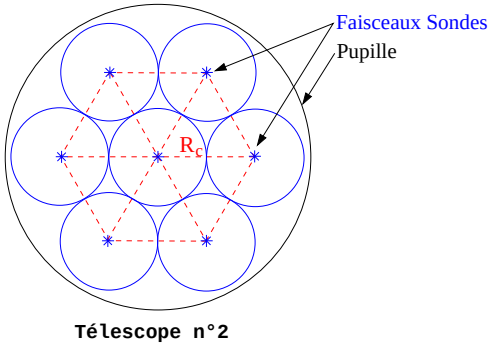

Figure 7.12: Distribution of laser probes.

of atmospheric turbulence (see. figure 7.13). The SH-WFS will only be sensitive to part of

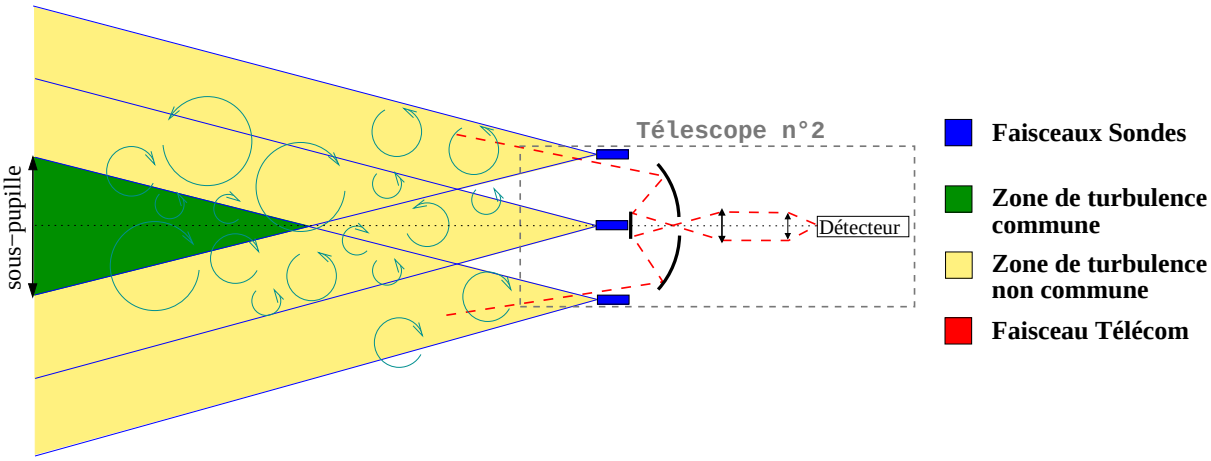

Figure 7.13: Common turbulence volume for each beam probe. Green: common turbulence, blue: probes, red: telecom beam, yellow: non-common turbulence.

the phase perturbation along the optical path and will not be able to correct it all. This area is determined by the turbulence area where all probes pass through (green area on figure). Phase effects in the non-common area (yellow part on the figure) will be averaged and will not be measured. Before saturation the following inequality is true: $r_0\,(\text{spherical waves}) > \alpha\sqrt{\lambda L}$ (typically $\alpha \simeq 3$), with:

- r_0: the characteristic size of phase angular decorrelation,
- $\sqrt{\lambda L}$: the characteristic size of intensity angular decorrelation.

After saturation, r_0 becomes the characteristic angular decorrelation size of both amplitude and phase. As we will only focus on the non-saturated case ($C_n^2 = 10^{-15}\,\mathrm{m}^{-2/3}$), it is best to separate

sources by a value around r_0. Numerical simulations are necessary to evaluate the actual gain of the correction.

7.3.3 Signal-to-Noise Ratio

The calculation of centre of gravity (COG) in the focal plan of each SH-WFS lenslets is impacted by noise. We haven't taken its impact so far. This paragraph is dedicated to its study. The signal-to-noise ratio (SNR) is defined by:

$$SNR = \frac{I_{max}}{\sqrt{\sigma_{ph}^2 + \sigma_d^2}}, \tag{7.3}$$

where I_{max} is the maximal value received by pixel in the lenslet without any atmospheric turbulence, σ_{ph}^2 is the photon noise variance and σ_d^2 the detector noise variance. In order to improve COG measurements in the presence of noise and scintillation, we will use the approach proposed by Nicolle [Nicolle-a-04]. It consists in an iterative weighted COG estimation.

7.3.4 Performances as Function of the Distance Between Beam Probes

In order to quantify the optimal distance between sources, numerical simulations were under taken with the simulation code PILOT. The pupil diameter is set to $D = 25\,\text{cm}$. Figure 7.14 illustrates typical intensity distribution in the reception pupil plan for cases without any atmospheric turbulence (see left hand side of figure), with non-iterative perfect correction of the true phase (see central part) and SH-WFS correction (see right hand part of figure). A $R_c = 9\,\text{cm}$ separation between the sources has been used for this particular illustration with on signal-to-noise ratio of $SNR = 50$ for $C_n^2 = 10^{-14} m^{-2/3}$. This illustration clearly shows the efficiency of the perfect phase correction on energy concentration and the degradation when using a SH-WFS. The turbulence used is the same for the three studied cases.

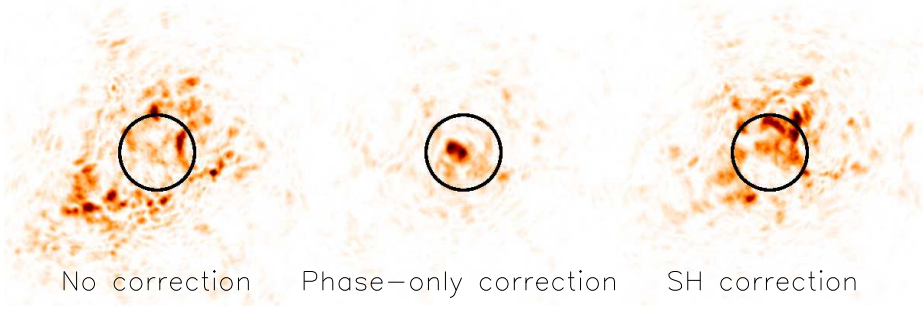

Figure 7.14: Influence of multi-probes on correction quality. Left: without any correction, middle: perfect phase correction, right: SH correction with $R_c = 9\,\text{cm}$, $SNR = 50$ and $C_n^2 = 1.10^{-14}$.

The SH correction efficiency as a function of the radius R_c between laser beam sources is presented figure 7.15 for different SNRs and turbulence strength. Simple propagation without any correction is noted 'No correction' and non-iterative true phase correction noted 'Phase only' on the figure. These two curves set the minimal and maximal limits of phase-only correction. With a strong signal-to-noise ratio (in green), the distance R_c does not have a strong impact on the studied metrics and for weak to intermediate turbulence levels. Conversely, when turbulence levels are high, an optimal separation between the laser probes appears optimising both $\langle I \rangle$ and $\frac{\sigma_I}{\langle I \rangle}$. Plots help us locate the optimal separation around $4 < R_c < 9\,\text{cm}$. The SH-WFS correction can lead to correction quality as least as good (and some time even better for intermediate turbulence strengths) as with perfect phase correction. This is possible only for SNR level superior to 25 for $C_n^2 = 10^{-15}\,\text{m}^{-2/3}$ and superior to 50 for $C_n^2 = 10^{-14}\,\text{m}^{-2/3}$. When SNR decreases, the link quality will naturally also decrease. However, even if no optimal beam separation appears for weak turbulence regimes, it appears that R_c has an impact on the studied metrics. For $SNR = 10$ (in blue on the figure) this optimum is located approximately between $7 < R_c < 9\,\text{cm}$. An increase in the number of laser probes in addition to an optimum separation ($7 < R_c < 9\,\text{cm}$) can lead to an improvement in correction quality.

7.3.5 Probability Density Function

By modifying the separation between sources, we have modified mean intensity and intensity fluctuations. Source separation will therefore also have an impact on intensity histograms received at the level of each lenslets. Figure 7.16 illustrates intensity histograms for the three studied turbulence levels and for different source separation. Five different separation distances are studied: $3\,\text{cm}$, $6\,\text{cm}$, $10\,\text{cm}$, $14\,\text{cm}$ and $17\,\text{cm}$. Gain is clearly visible when the separation goes from $R_c = 3\,\text{cm}$ to a separation of $R_c = 6\,\text{cm}$.

7.3.6 Influence of the Number of Corrected Modes

In the following paragraph influence of the number of corrected modes on both metrics will be studied. Decrease of the influence of scintillation in wavefront measurement is achieved by multi-beam spatial diversity. The SH-WFS simulation measurement model takes into account errors due to scintillation and aliasing. Other errors are neglected.

Figure 7.17 the two metrics are plotted for corrections respectively reconstructing 2 (tip-tilt), 3 (tip-tilt and focus), 20, 35 and 54 Zernike modes. We suppose that the number of SH lenslets is constant and equal to 8×8. In order of have an idea of the AO correction performance results are compared to simulations without any correction (crosses) and perfect phase correction (squares). It appears that with a sufficient number of corrected modes (over 20), AO correction and perfect phase correction can lead to similar performance.

In order to quantify the PIB improvement brought by AO and confront it to perfect phase correction (on-axis source), we define a mean PIB relative gain G_{av} and an intensity fluctuation gain G_{stdev} as:

$$G_{av} = \frac{\langle I \rangle - \langle I \rangle_{\text{Without Corr}}}{\langle I \rangle_{\varphi_{\text{perfect}}} - \langle I \rangle_{\text{Without Corr}}} \tag{7.4}$$

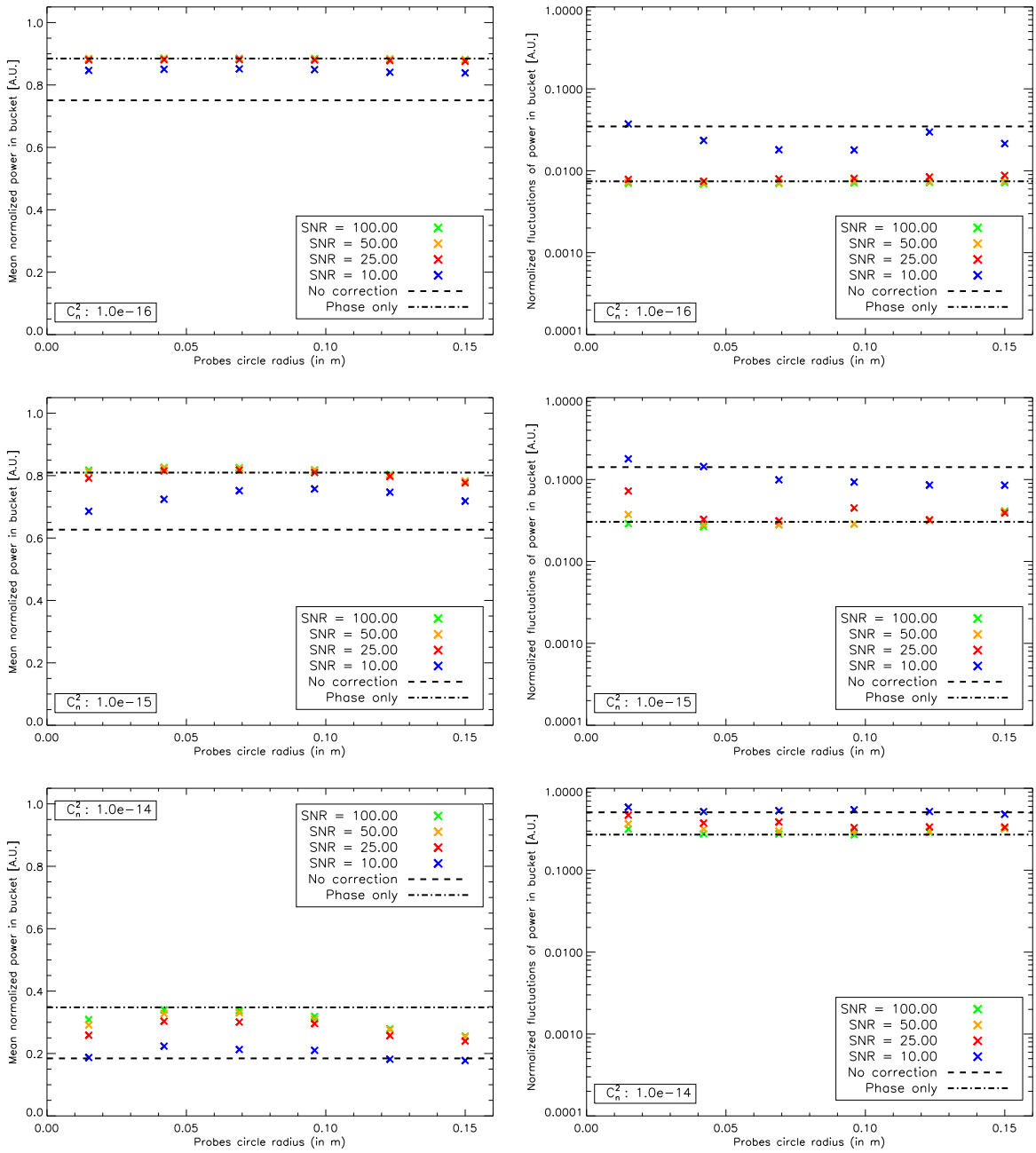

Figure 7.15: Correction efficient as a function of the circle of radius R_c (in meters), SNR levels and turbulence strength. Left: mean PIB $\langle I \rangle$, right: intensity fluctuations $\frac{\sigma_I}{\langle I \rangle}$.

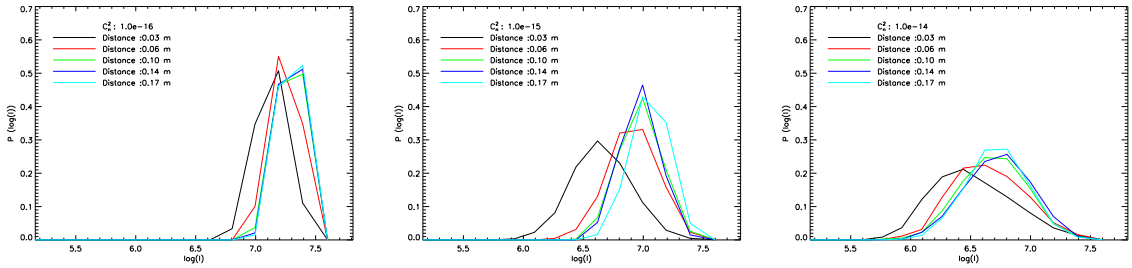

Figure 7.16: Illustration of intensity histograms for the three studied turbulence levels and for different source separation. From left to right: $C_n^2 = 1.10^{-16}\,\mathrm{m}^{-2/3}$, $C_n^2 = 1.10^{-15}\,\mathrm{m}^{-2/3}$ and $C_n^2 = 1.10^{-14}\,\mathrm{m}^{-2/3}$. The x-axis is given in logarithm scale o f I in arbitrary units.

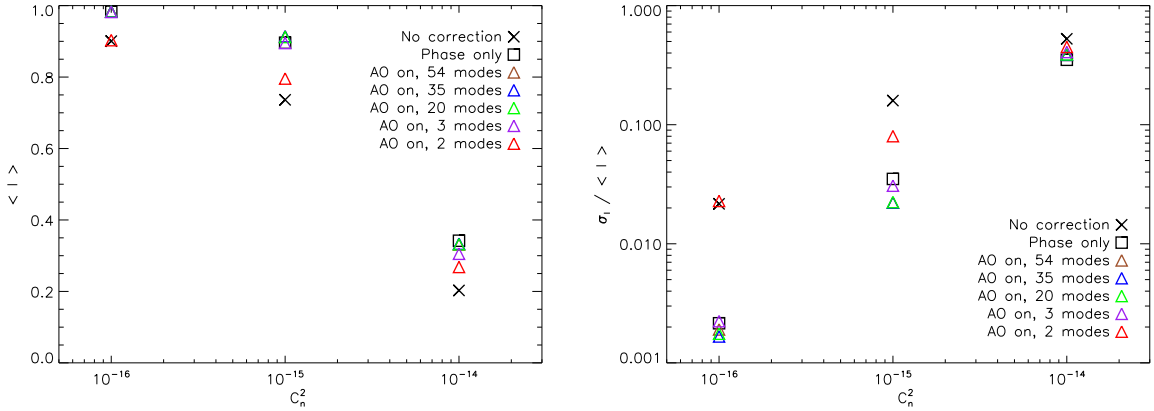

Figure 7.17: Influence of the number of correction Zernike modes. Left: mean Power in the Bucket (PIB), right: normalised intensity fluctuations. Propagation distance $L = 10\,\mathrm{km}$, $\lambda = 1.5$ µm and $D = 25\,\mathrm{cm}$.

$$G_{sdtdev} = \frac{\sigma_I / \langle I \rangle - \sigma_{I_{\text{Without Corr}}} / \langle I \rangle_{\text{Without Corr}}}{\sigma_{I_{\varphi_{\text{perfect}}}} / \langle I \rangle_{\varphi_{\text{perfect}}} - \sigma_{I_{\text{Without Corr}}} / \langle I \rangle_{\text{Without Corr}}}, \tag{7.5}$$

Where the index *Without Corr* indicates the value without correction and φ_{perfect} a perfect phase correction. Results are presented figure 7.18. This figure demonstrates that for most cases a correction of the first 35 modes is sufficient. In addition, it can be observed that for intermediate C_n^2 the relative gain is superior to 1. This phenomenon has already been observed several times in this paragraph and in paragraph 7.2.2.2. The average measurement on different points, even degraded by the WFS, can result in a better performance that one obtained with an on-axis source. If the number of corrected modes is increases to 54, one obtains similar results to those previously obtained with 35. This is the reason why the previous study (see paragraph 7.2) has been limited to the reconstruction of only the first 38 Zernike modes.

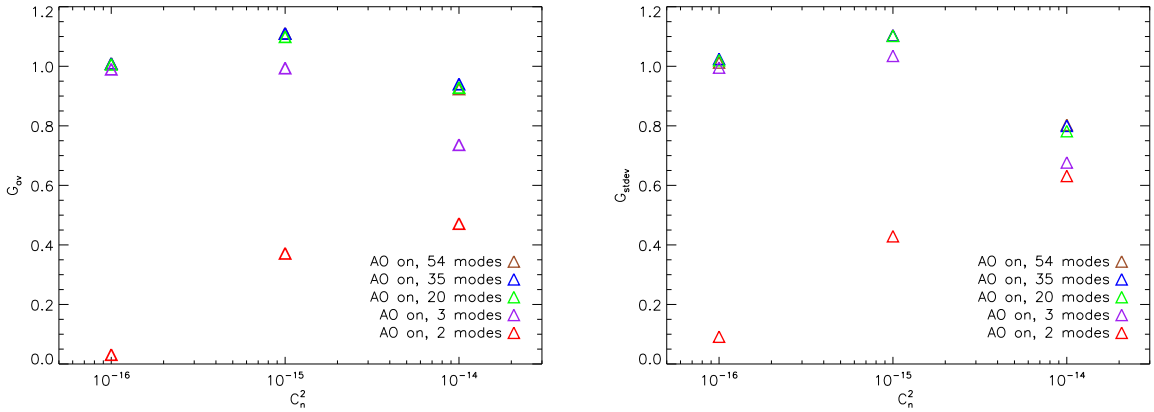

Figure 7.18: Relative gain brought by AO correction as function of the number of corrected Zernike modes. Left: mean Power in the Bucket (PIB), right: normalised intensity fluctuations. Propagation distance $L = 10\,\text{km}$, $\lambda = 1.5$ µm and $D = 25\,\text{cm}$.

7.3.7 Correction Stability to Temporal Variation

In a realistic implementation, winds perpendicular to the beam propagation axis $V_\perp$, also called transverse winds, creates a temporal evolution of phase perturbations. In previous cases, we considered turbulence to be static, or similarly that the adaptive optics sampling frequency (f_e) was infinite. Transverse wind, or again similarly sampling frequency, is an essential parameter to take into account relative to correction quality when designing an AO system along with static turbulence characteristics (C_n^2, r_0, ...). This paragraph tries to demonstrates the importance of f_e in an AO loop.

Let $t = t_0$ be the time when phase perturbations of the incoming electromagnetic field are measured and $t = t_1$ the time when phase correction is applied. Phase perturbations at the origin of the field perturbation at $t = t_0$ can be totally decorrelated of the perturbations at $t = t_1$ when correction is applied. Figure7.19 illustrates the pupil footprint during phase perturbation evolution under the influence of transverse winds. In the least favourable case ($t = t_1'$), phase perturbations are extremely decorrelated from those taken during measurement at $t = t_0'$. Applying a correction actually adds new phase perturbations which in return decreases the link quality.

In order to study the impact of temporal error (σ^2_{temp}) on mean PIB and intensity fluctuations, we present figure 7.20 the change of these metrics as a function of the AO sampling frequency. For comparison purposes, results obtained without any temporal errors ('SH no error' case) are also plotted. A $V_\perp = 10\,\text{m.s}^{-1}$ wind is considered with a pupil diameter of $D = 25\,\text{cm}$. When the first 35 Zernike modes are corrected, temporal errors are negligible as soon as the sampling frequency is higher than $4\,\text{kHz}$ for $C_n^2 = 10^{-15} m^{-2/3}$. This study shows the importance of sampling frequency on the correction quality of an OA system. This is the reason wavefront reconstruction based systems are usually favoured relative to iterative correction. Iterative usually have much higher constrains in terms of sampling frequency.

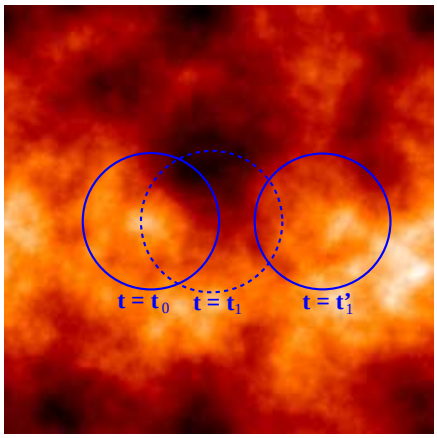

Figure 7.19: Pupil imprint during phase perturbation evolution when transverse winds modifies the phase perturbation distribution along the propagation path between time t_0 when the phase measurement is done and t_1 when the correction is actually applied.

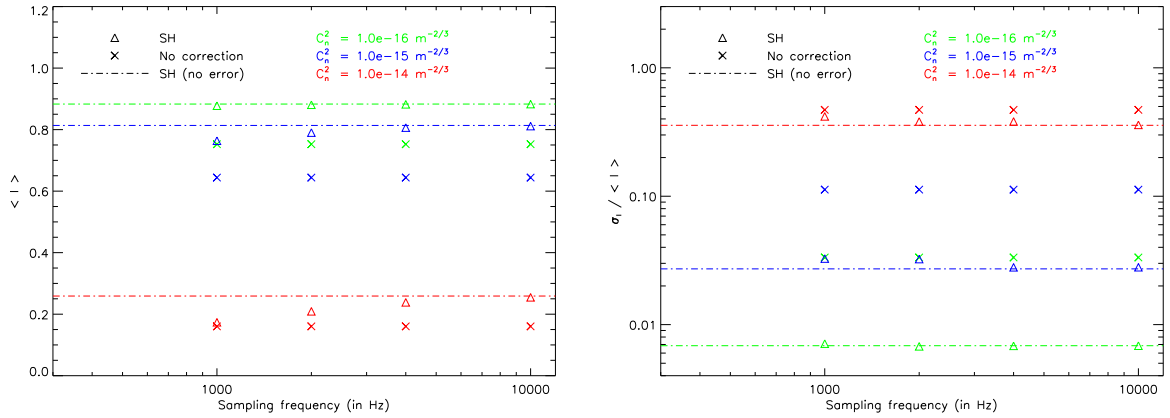

Figure 7.20: Influence of temporal errors on mean PIB and intensity fluctuations. Top: tip-tilt only correction, bottom: correction of the first 35 Zernike modes. Left: mean PIB, right: normalised intensity fluctuations. Propagation distance $L = 10\,\text{km}$, $\lambda = 1.5$ µm, $D = 25\,\text{cm}$ and a transverse wind of $V_\perp = 10\,\text{m.s}^{-1}$.

7.4 Phase-Only Iterative Correction

In this paragraph is presented results relative to phase-only iterative correction using wave-front reconstruction. This correction is similar to sub-optimal correction with the difference that the phase used for correction is not the true phase but the reconstructed phase. We address the question of the influence of pupil size and adaptive optics bandwidth. Noise effects are neglected.

7.4.0.1 Influence of the Pupil Size

A 7×7 SH-WFS measurement, reconstructing 38 mode with neither temporal nor spatial errors are considered. The SH-WFS is identical to the one used for count-propagating probe system. This enables us to make a direct comparison with identical system complexities. Optimisation of the number of reconstructed modes for $\langle I \rangle$ and $\frac{\sigma_I}{\langle I \rangle}$ needs to be undertaken independently for sub-optimal correction. Figure 7.21 presents performance function of pupil diameter. Results

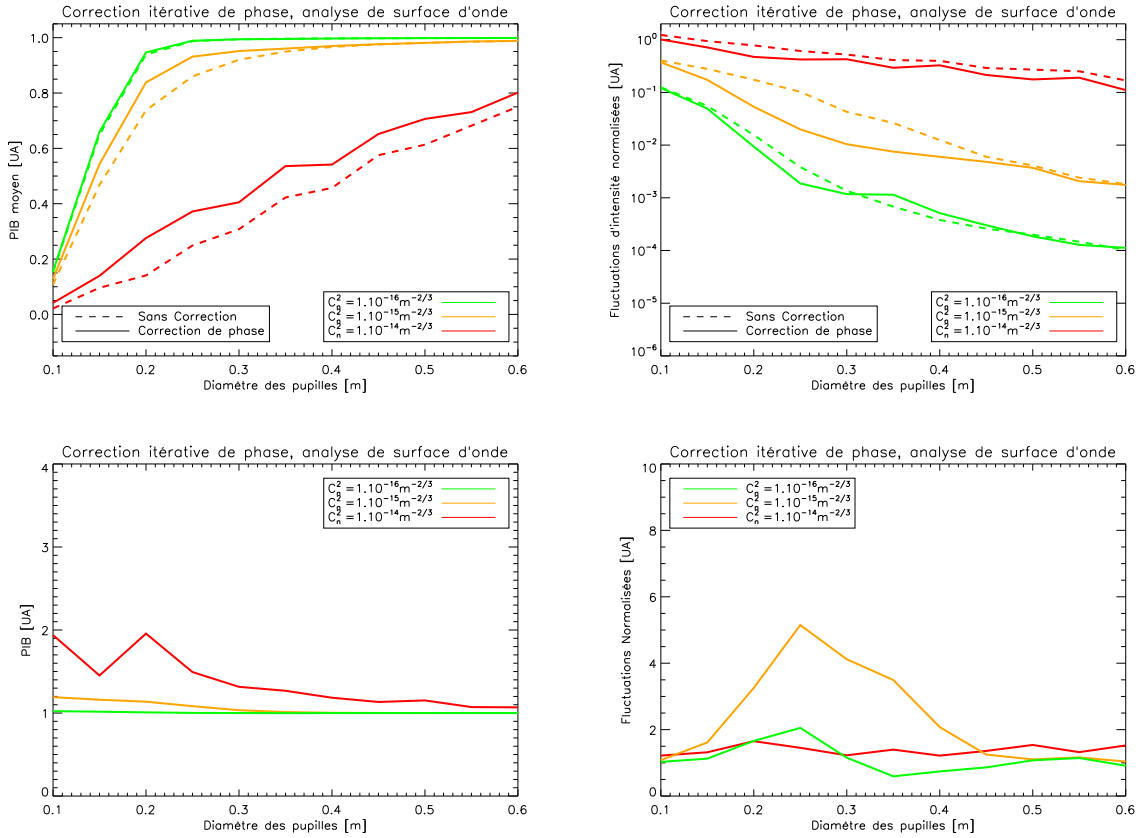

Figure 7.21: Efficiency (top) and gain (bottom) of iterative phase-only correction function of pupil diameter for different turbulence strengths. propagation distance $10\,\text{km}$, $\lambda = 1.5$ µm. Statistics were calculated over 300 propagations. Solid lines: correction on 38 Zernike modes, dashed lines: no correction. Left: PIB, right: normalised intensity fluctuations.

obtained are close to those obtained with sub-optimal correction in the case of weak perturbations. Degradation brought by SH-WFS measurements and by the limited number of corrected modes is relatively small.

Only intermediate turbulent regimes show an interesting prospect relative to phase-only iterative correction. In terms of intensity fluctuations gain G_{Fluct}, it grows up to a factor 5 for pupil diameters of approximately $25\,\text{cm}$. This is even more interesting in that it enables fluctuations

level to go below $\frac{\sigma_I}{\langle I \rangle} = 0.1$ after correction. By comparing these results with figure 6.23, it can be observed that the gain is similar to the one obtained with perfect phase correction and for this turbulence strength. This indicates quality losses introduced by the SH-WFS are negligible in this case. It therefore seems possible to neglect scintillation and under-sampling effects for the intermediate turbulent regimes. For $C_n^2 = 10^{-14}\,\mathrm{m}^{-2/3}$, improvement is not sufficient to consider using in FSO systems. This correction method looses all interest in strong perturbations.

7.4.0.2 Probability Density Functions

Figure 7.22 shows probability density functions (PDF) for different pupil diameters. They are to be compared with figure 6.24 for perfect phase correction. Strong correction quality degradation can be seen for strong turbulence confirming previous results obtained on mean PIB and intensity fluctuations. Weak turbulence PDF (resp. intermediate) are virtually unchanged.

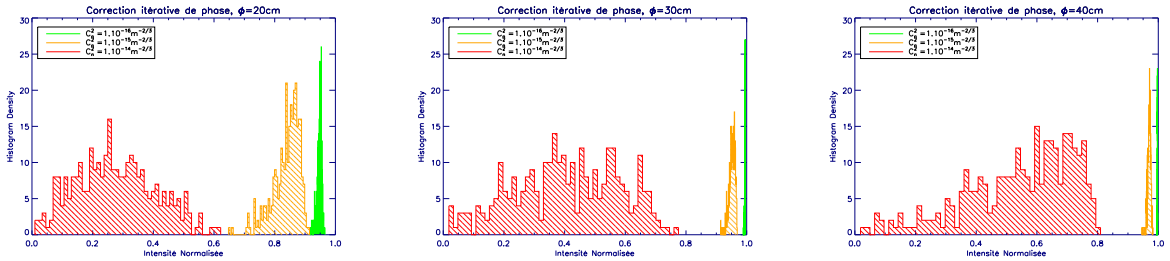

Figure 7.22: Evolution of the probability density functions for different pupil diameters and turbulence strengths. Iteration phase corrections by SH-WFS phase reconstruction. The pupil diameter is from left to right respectively $20\,\mathrm{cm}$, $30\,\mathrm{cm}$ and $40\,\mathrm{cm}$. Propagation distance: $10\,\mathrm{km}$ and wavelength of $\lambda = 1.5\ \mu\mathrm{m}$.

7.4.0.3 Impact of the Adaptive Optics Loop Sampling Frequency

Modelling of wind effects $V_\perp$ is performed by phase screen translation. Three different phase screen translation amplitudes by unit of time are studied: $d_1 = 0.78\,\mathrm{cm}$, $d_2 = 1.56\,\mathrm{cm}$ and $d_3 = 3.91\,\mathrm{cm}$. Each displacement is performed after a complete iteration between telescope 1 and telescope 2. We have considered a constant wind across the propagation length: all phase screens are translated by the same amount. It is possible, in order to quantify the problem to express the previous displacements in terms of wind speed or AO loop sampling frequency. As an example, by taking $f_e = 100\,\mathrm{Hz}$ we obtain for the first case a perpendicular wind of $V_\perp = 0.78\,\mathrm{m.s}^{-1}$. Similarly, by choosing a wind speed of $V_\perp = 5\,\mathrm{m.s}^{-1}$ a sampling frequency of $f_e = 640\,\mathrm{Hz}$ is obtained. Figure 7.23 gives transverse wind speed as a function of the adaptive optics loop sampling frequency for different displacement values.

In order to separate temporal and spatial effects, the study is performed with perfect phase-only sub-optimal correction. Figure7.24 shows evolution of sub-optimal correction (i.e. using true phase) function of the ratio of wind speed and sampling frequency. Convergence is obtained

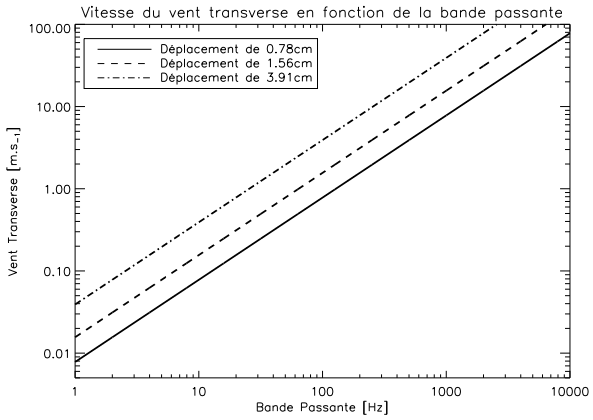

Figure 7.23: Transverse wind speed as a function of sampling frequency for different displacement values.

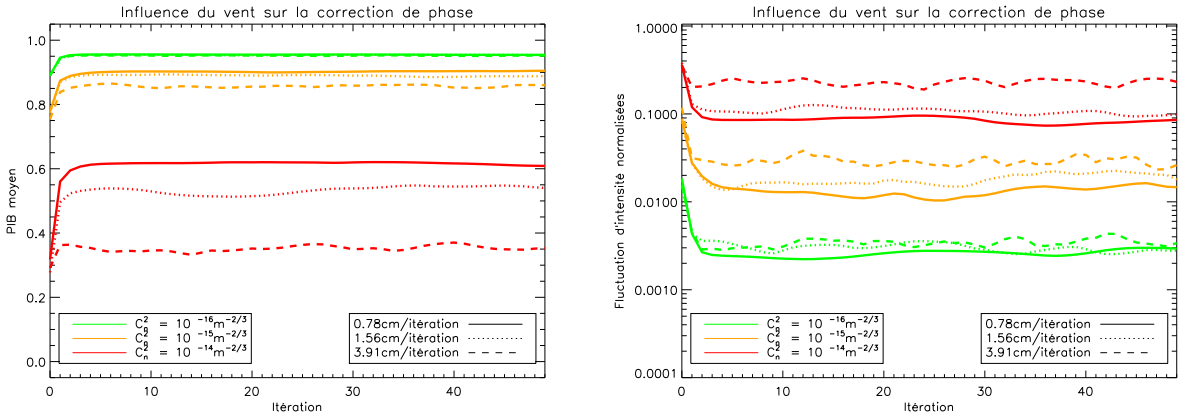

Figure 7.24: Mean intensity evolution (left) and normalised intensity fluctuations (right) after iterative phase correction. Phase screen displacement due to wind, solid lines: $d_1 = 0.78$ cm per iteration, dotted lines: $d_2 = 1.56$ cm per iteration and dashed lines: $d_3 = 3.91$ cm per iteration. Propagation distance of 10 km, $\lambda = 1.5$ µm, $D = 30$ cm.

in every case in less than three iterations, as in the static cases. The final value after convergence of the iterative correction depends on the sampling frequency. For example, sub-optimal phase-only correction can help achieve a mean PIB of $\langle I_{Corr} \rangle = 0.55$ (resp. $\langle I_{Corr} \rangle = 0.35$) for $C_n^2 = 10^{-14}\,\mathrm{m}^{-2/3}$ with displacement of d_2 (resp. d_3). The value obtained with an infinite sampling frequency is $\langle I_{Corr} \rangle = 0.63$. More importantly $V_\perp$ can strongly increase intensity fluctuations. In order to reach a level of correction close to the one obtain without any temporal errors, the following inequality must be satisfied $\frac{V_\perp}{f_e} < \frac{\rho_0}{\text{Number of Iterations}}$. As an example, for $V_\perp = 10\,\mathrm{m.s}^{-1}$ and $C_n^2 = 10^{-14}\,\mathrm{m}^{-2/3}$ it is necessary to have an AO system with a sampling frequency $f_e > 3$ kHz.

7.5 Conclusion

In this chapter, limitations of phase-only correction using a counter-propagating laser beam to probe atmopheric turbulence were studied. This correction only pre-compensates phase aberrations of the emitted field. It is performed by measuring the wavefront of a laser beam propagating in the opposite direction of the emitted field. First, the performance of such a correction device was studied with perfect phase correction. We have shown that for certain configurations, correction quality can be closed to sub-optimal correction. However, the lack of iterations reduces pre-compensation quality. We remind the reader that the first iteration is the most efficient, but each following ones helps to increase mean PIB and decrease residual fluctuations.

Secondly, a practical implementation solution using SH wavefront sensing was studied. We have seen that it deteriorates correction quality for strong turbulence scenarios. This is mainly due to scintillation and phase dislocations. Correction in weak perturbation scenarios is similar for perfect true phase correction and phase correction using wavefront reconstruction. However, the use of such a system cannot be justified in strong turbulence. In addition, this is valid for both iterative phase-only correction (i.e. sub-optimal) and non-iterative phase correction (i.e. with a counter-propagating probe).

Scintillation of the laser beam probe (not corrected by AO) is strong and disrupts measurements. This is the reason why we have presented a solution to partially overcome this limitation. It extends the domain of validity of phase-only correction by multiplying the number of probes. It is therefore possible to average scintillation effects as well as minimising effects due to phase decorrelation is the field. We have shown an important gain for $\langle I \rangle$ and $\frac{\sigma_I}{\langle I \rangle}$ to the condition that the probes are positioned in an optimal configuration. The improvement brought by multi-lasers is limited for low SNRs and weak turbulence or for strong turbulence. The study we have led on the number of corrected Zernike modes (about 30) can lead to a good correction quality and in some cases better (for intermediate turbulence) than perfect phase correction. Studying temporal errors helped us set a lower limit to the necessary adaptive optics loop speed to minimise these errors. It brought into light the importance of AO sampling frequency, a strong constrain in FSOs. The sampling frequency for FSO systems is high and stresses the fact that it is important to minimise the number of iterations before convergence.

The method based on wavefront measurement of several counter-propagating probes has the advantage of improving correction quality in particular in the intermediate regime. In addition, it is simple to implement on a real system. This is the technical solution we have considered for the AO system of the Fortune43G project.

Chapter 8

Correction by Phase Modulation

Contents

Different correction strategies based on phase measurement (sub-optimal and with counter-propagating probe) have been studied so far. These methods rely on the knowledge of wavefront deformations and on phase conjugation principal to maximise collected flux in the pupil. We have presented limitations due to the use of a WFS, in particular for strong turbulence conditions. The direct PIB optimisation enables us to overcome problems related to wavefront sensing. However, it generates algorithmic related issues. The objective function J (also called cost function, here considered to be the instantaneous PIB) is generally not convex. It is important not to fall into

a local minimum during the optimisation process. In addition, the use of algorithms converging faster than the turbulence evolution time is important.

Existing optimisation methods were presented in introductory chapters. The goal of this chapter is to evaluates these methods in the chosen application framework for this manuscript and compare their performance with other correction strategies already studied. This chapter will enable to position optimisation techniques relatively to corrections using a wavefront sensor. It is expected to be less efficient than the sub-optimal perfect phase correction. Numerical simulations are necessary to evaluate differences in terms of mean intensity and intensity fluctuations. The approach taken for this chapter consists in firstly the study of optimisation using 'simples' criterions (see paragraph 8.1). We will study performance and principal limitations. Several pupil configurations will be studied: full pupils on both sides of the communication link and full aperture on the emission side and annular aperture for the reception. Central obscuration (see paragraph 8.2) is a frequently encountered case, in particular for larger pupil diameters D. AO systems with a WFS used on a counter-propagating probe does not deal with the central obscuration easily. Secondly, the main parameter influencing correction by direct optimisation will be studied: number of correction segments (necessarily finite). Direct optimisation techniques seem more adapted to noisy cases. Today, the most common algorithm in use is the SPGD and its performance will be studied paragraph 8.3.

8.1 Sequential Phase Perturbations

8.1.1 Principle

Vellekoop [Vellekoop-a-07] has recently developed a simple optimisation algorithm used for coherent light focalisation through a highly diffusing medium. The typical application for this technique is biological tissues. This algorithm modifies the emitted wavefront to focalise it after propagation through a diffusing medium. It supposes linearity the diffusion process. The received field is a linear combination of the field emitted by the N DM segments:

$$U_R = \mathcal{G}\left[U_E\right] = \mathcal{G}\left[\sum_{n=1}^{N} A_n e^{i\varphi_n}\right], \tag{8.1}$$

with A_n and φ_n the amplitude and phase of the field after reflection on the n^{th} DM segment and $\mathcal{G}\left[.\right]$ the propagation operator through diffusing or turbulence media. The algorithm can be decomposed into the following steps:

- Propagate the emitted field U_E through turbulence (or diffusing medium);
- Measure metric J after propagation;
- Modify the wavefront of the first DM segment ($n = 1$) in order to find the position maximising the metric J;
- Put the mirror back into original position (i.e. flat);

- Modify the wavefront of the second DM segment ($n = 2$) in order to find the position maximising the metric J;
- Go through all segments ($n = 3 \cdots N$) by repeating previous steps.

At the end of the optimisation process, the correction phase optimising metric J corresponds to the linear combination of all optimal positions obtained sequentially for the each of the mirror segments.

Figure 8.1 presents the deformable mirror geometry used for this study. Implementing this

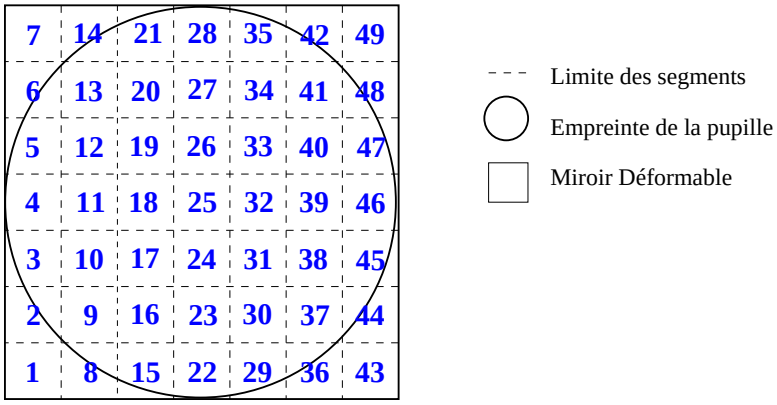

Figure 8.1: Segmented mirror geometry with 7×7 segments. Each segment can only be driven in piston with coupling coefficient equal to zero.

algorithm for the application used in this manuscript, we will sequentially address all DM segments in order to optimise instantaneous intensity integrated over the reception pupil I_R. We will modify the algorithm proposed by Vellekoop slightly in order to optimise the metric after each individual step. Instead of putting back the mean phasor to zero after each step, we will conserve the optimum position of the segment. The optimisation process will therefore become more continuous and slightly faster. Oppositely to the first method, this new sequential optimisation process might necessitate a second round after all the segments have been optimised a first time.

8.1.2 Influence of the Number of Correction Elements

Figure 8.2 shows the change in mean intensity $\langle I \rangle$ and normalised intensity fluctuations $\frac{\sigma_I}{\langle I \rangle}$ as function of turbulence strength and number of deformable mirror segments. Three different cases are presented: 4×4, 7×7 and 11×11 actuators. The deformable mirror is used to modify the phase of the electromagnetic wave. Each segment corrects for piston and has a zero coupling coefficient with neighbouring actuators. The pupils used for this simulation at both end of the propagation path have a $D = 30\,\text{cm}$ diameter with no central obscuration. The laser emitted beam is collimated with a waist of $w_o = 7\,\text{cm}$ in radius. Each elementary phase perturbation

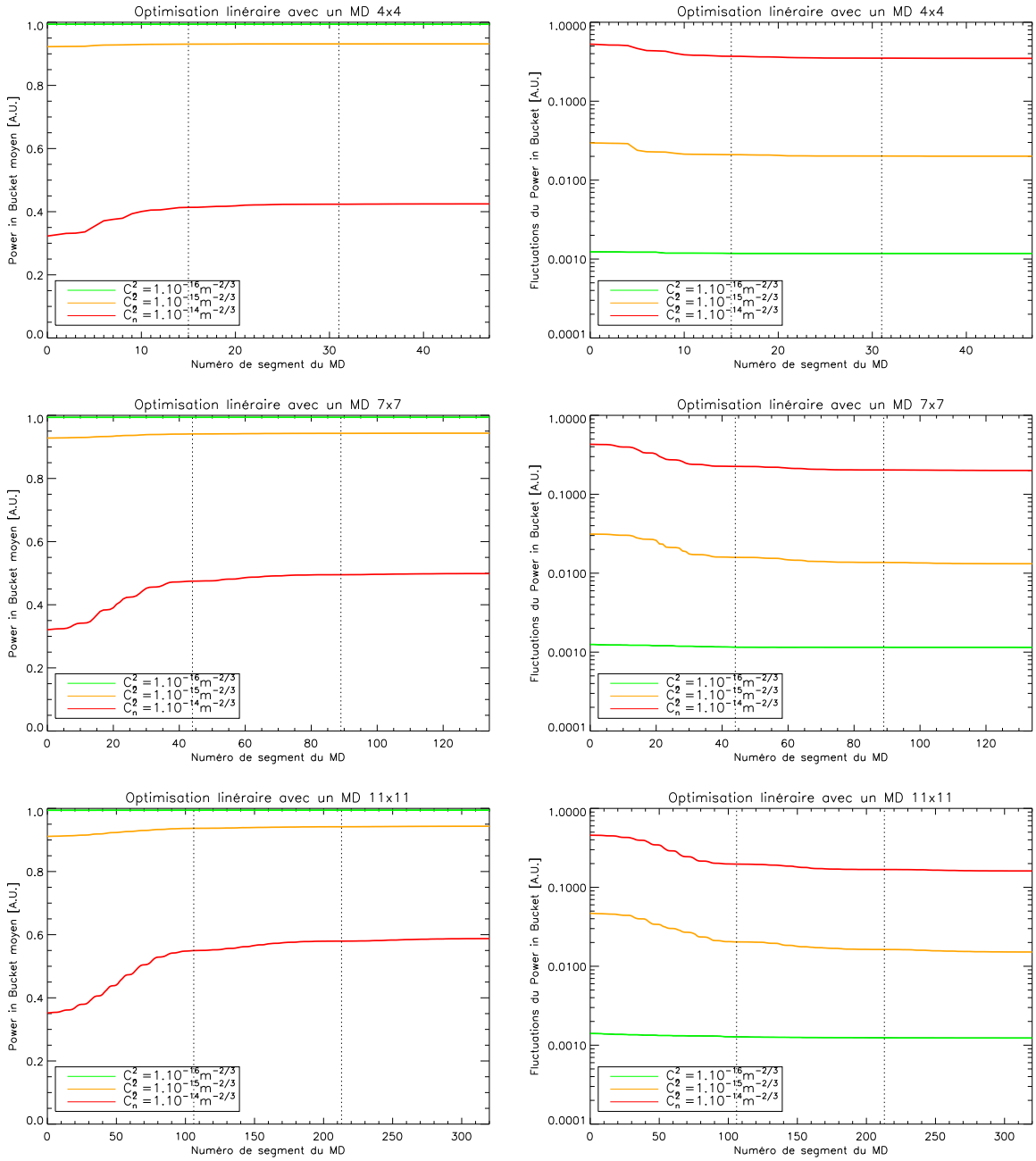

Figure 8.2: Influence of the Vellekoop algorithm on mean intensity $\langle I \rangle$ (left) and on intensity fluctuations $\frac{\sigma_I}{\langle I \rangle}$ (right) function of the number of iterations and C_n^2. From top to bottom, the number of DM segments is respectively of 4×4, 7×7 and 11×11. $D = 30\,\text{cm}$.

step is $\varepsilon = \frac{\pi}{21}$. It can be noticed that for weak turbulence this algorithm does not enable us to significantly improve neither mean intensity nor residual fluctuations. No improvement is

visible if the number of segments is increased. For $C_n^2 = 10^{-14}\,\mathrm{m}^{-2/3}$ however, 7×7 and 11×11 segments enables a noticeable improvement in link quality. The mean intensity goes from $\langle I \rangle \simeq 0.35$ to $\langle I \rangle \simeq 0.5$ for a 7×7 DM and up to $\langle I \rangle \simeq 0.6$ for a 11×11 DM. The number of segments clearly has an influence on mean intensity for strong perturbation regimes. For $C_n^2 = 10^{-15}\,\mathrm{m}^{-2/3}$, no improvement is visible and a 7×7 mirror seems sufficient.

For intensity fluctuations, the same observation can be made on the number of correction elements for $C_n^2 = 10^{-15}\,\mathrm{m}^{-2/3}$. Is goes from $\frac{\sigma_I}{\langle I \rangle} = 0.03$ to $\frac{\sigma_I}{\langle I \rangle} \simeq 0.015$ regardless of the number of actuators, except for 4×4 where only $\frac{\sigma_I}{\langle I \rangle} \simeq 0.02$ is achieved. This value is generally sufficient to ensure a good link quality. As for $C_n^2 = 10^{-14}\,\mathrm{m}^{-2/3}$, the influence of the number of segments (7×7 or 11×11) is equally relatively small. Only a small improvement can be seen when increasing the number of segments, but it is negligible. However, a small improvement is achieved when refraining from using a SH-WFS in strong turbulence conditions. This observation is in accordance with expectations because problems linked to wavefront sensing (scintillation, phase wrapping) are no longer an issue for direct optimisation methods.

In addition, the quasi-linearity of the propagation process through turbulence with regards to introduced phase perturbations is verified. After performing a complete round of correction (i.e. after addressing all DM segments) two other rounds are performed. The initialisation phase for each subsequent correction is the phase optimised at the previous step. Using two additional rounds of correction does not significantly improve link quality. In spite of implementation differences with the algorithm proposed by Vellekoop, one can observed that it is unnecessary to add additional rounds to improve correction. Even though phase correction for a number of actuators superior or equal to 7×7 is efficient, it is important to sequentially go over all phase point for each DM segments. This leads to long convergence times and justifies the search for more efficient algorithms in terms of convergence time.

Results obtained in strong perturbation regimes for an 11×11 DM both for intensity fluctuations and mean intensity are similar to those obtained with sub-optimal correction. In addition, despite the pupil diameter difference ($D = 25\,\mathrm{cm}$ versus $D = 30\,\mathrm{cm}$), it seems that multi-beam correction gives similar results for $C_n^2 = 10^{-16}\,\mathrm{m}^{-2/3}$ and $C_n^2 = 10^{-15}\,\mathrm{m}^{-2/3}$. On the other hand, performance seems slightly better when using sequential optimisation for $C_n^2 = 10^{-14}\,\mathrm{m}^{-2/3}$. However, the obtained results in strong perturbations for $D \simeq 30\,\mathrm{cm}$ are not sufficient to achieve the desired BER in typical FSO systems.

8.2 Performances with Central Obscuration

This paragraph is dedicate to the study of phase modulation performance in presence of central obscuration. We use a Nelder-Mead type algorithm (also called simplex algorithm) which is a classical non-linear optimisation method (or downhill search) for multidimensional spaces. It was first introduced by J. Nelder and R. Nead in 1965 [Nelder-a-65]. The minimising routine used during numerical simulations is based on *Numerical Recipes* [Press-l-86]. This algorithm requires the evaluation of the function to be optimised. Contrarily to some other minimisation algorithms it does not require the evaluation of its derivatives. This method is generally considered simple and robust. Using this technique will validate phase correction for an obscured pupil

without wavefront sensing and with a simple optimisation strategy.

8.2.1 Simulation Conditions

In this paragraph, we perform numerical simulations implementing the downhill simplex algorithm with a $D = 25$ cm diameter pupil and an obscuration of $OC_{\text{emission}} = 0\%$ and $OC_{\text{reception}} = 35\%$ respectively for the emitting telescope and the receiving telescope. Metrics measurements is performed without additional noise, the wavelength is set to $\lambda = 1.5$ µm and the propagation distance to $L = 10$ km. The emitted laser beam has a waist in the pupil of the emitting telescope of $w_o = 7$ cm in accordance to chapter 6.

The continuous representation used for phase is not longer justified in strong perturbations. We will therefore use a segmented mirror (zonal correction of the phase) with a zero coupling factor between the actuators. As previously, segments are only driven in piston. In order to decrease convergence time, we propose a hierarchical correction. It consists in gradually increasing the number of corrected segments. The Nelder-Mead algorithm is set to stop when the difference between two consecutive measurements of the metric I is less than 10^{-2}.

8.2.2 Hierarchical Algorithm

Hierarchical phase optimisation consists in starting first with a small DM (i.e. with a small number of actuators) and gradually increasing the number of segments as the convergence at each step is achieved. We first use a 2×2 DM to start the optimisation process. Once convergence is reached, we increase the number of segments to 4×4 to finally finish with an 8×8 DM. At each step when increasing the numbers of segments (i.e. when going from step N to step $N+1$) we use the previously obtained phase after convergence at step N to initialise the phase at step $N+1$. The idea is that by reducing the number of parameters we will reduce the complexity of the problem. It will in return reduce the global convergence time of the algorithm and reduce the number of local minimums. Figure 8.3 shows a diagram of the hierarchical phase optimisation. The red colour on the diagram is used to represent the 2×2 deformable mirror geometry. We then used the 4×4 segments mirror represented in blue. Finally, the 8×8 configuration is used (in black on the diagram). The pupil imprint on the DM is represented by the light gray circle. Some of the actuators are actually sitting outside the emitting pupil (in particular numbers 1, 8, 57 and 64) and will have no or limited impact on the final optimisation value.

Figure 8.4 illustrates the evolution of mean intensity and normalised intensity fluctuations as the number of iterations increase.

The influence of the amplitude of the new phase perturbations (ε) applied to the DM at each iteration step of the algorithm was studied (not shown here). Two different cases were examined. The first case where phase perturbations are small compared to the wavelength λ with $\varepsilon = \frac{\pi}{21}$, the second where $\varepsilon = \frac{\pi}{2}$. Only the case where the amplitude of phase perturbations are equal to $\varepsilon = \frac{\pi}{2}$ is presented because it enables a more effective correction, especially for strong perturbations. In addition, the study was limited to $C_n^2 = 10^{-15}\,\text{m}^{-2/3}$ and $C_n^2 = 10^{-14}\,\text{m}^{-2/3}$ cases. The $C_n^2 = 10^{-16}\,\text{m}^{-2/3}$ case has only a limited interest since the optical link is already excellent without correction.

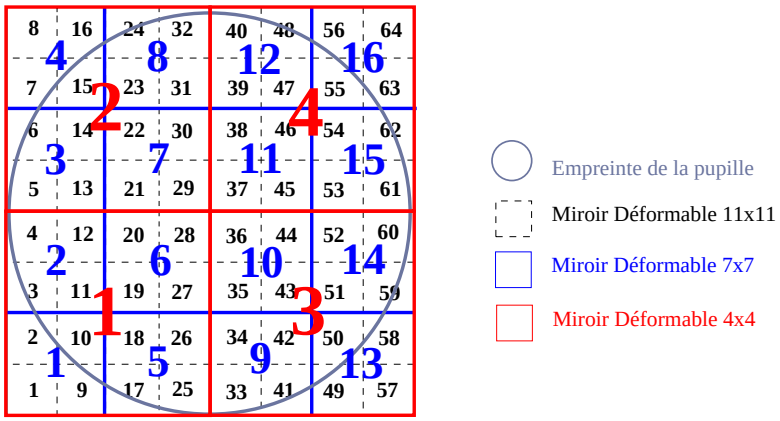

Figure 8.3: Diagram of the hierarchical phase optimisation. In red: the first optimisation level. In blue: the second and in black the final optimisation stage.

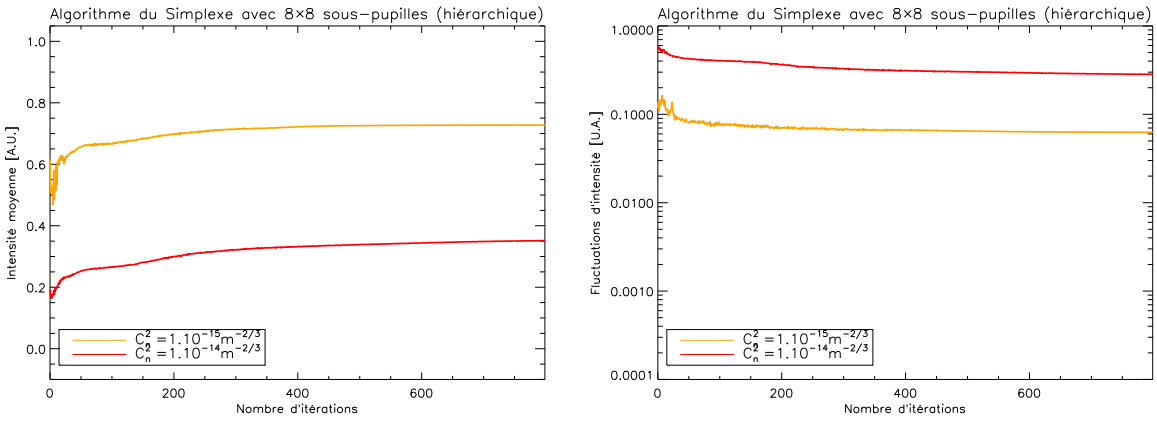

Figure 8.4: Hierarchical downhill simplex algorithm: influence of turbulence strength of mean intensity $\langle I \rangle$ (left) and on intensity fluctuations $\frac{\sigma_I}{\langle I \rangle}$ (right) as function of the number of iterations. The hierarchical downhill simplex algorithm is implemented using (2×2), (4×4) then (8×8) segments and elementary phase perturbations of $\varepsilon = \frac{\pi}{2}$. $D = 25\,\text{cm}$.

By comparing obtained results without a hierarchical configuration (not shown here) it can be observed that modifying the correction strategy does not influence the final values after convergence of the algorithm. The final values are therefore intrinsically linked to the final number of elements of DM and not the intermediate steps.

The number of iterations necessary to reach convergence goes from an average of $N \simeq 850$ (resp. $N \simeq 1200$) for $C_n^2 = 10^{-15}\,\text{m}^{-2/3}$ (resp. $10^{-14}\,\text{m}^{-2/3}$) with a classical non-hierarchic correction using a (8×8) DM to $N \simeq 450$ (resp. $N \simeq 850$) for a hierarchic correction. The comparison between the two methods was performed using a deformable mirror with (8×8) segments and a perturbation amplitude of $\varepsilon = \frac{\pi}{2}$. As expected, the hierarchic correction enables

a reduction in convergence time. The reduction can go as high as a factor tow (resp. 1.3 for strong turbulence).

8.2.3 Conclusion

The impact of central obscuration was studied using a simple phase modulation algorithm that optimises instantaneous intensity I. The necessary number of DM elements (approximately 8×8 segments) leads to a high required number of iterations. Moreover, the final level for intensity fluctuations after correction in strong turbulence is not compatible with typical bit error rates required in FSO systems. When used in intermediate turbulence regimes, it can however be used to get the intensity fluctuations below the threshold of 0.1. Degradation in correction quality is brought by the central obscuration of $OC = 35\%$ for the reception telescope. We have in parallel presented results using a hierarchic optimisation that help reduce the number of iterations required to reach convergence. It was observed that modifying the algorithm for a hierarchical one does not change the final values for $\langle I \rangle$ and $\frac{\sigma_I}{\langle I \rangle}$ after convergence. These values are mainly related to the number of actuation points (i.e. number of actuators).

8.3 Stochastic Parallel Gradient Descent Optimisation

8.3.1 Introduction

An alternative approach was proposed by Vorontsov *et al.* [Vorontsov-a-97, Weyrauch-a-05] consisting in the direct optimisation of the objective function by using a Stochastic Parallel Gradient Descent (SPGD) algorithm. Let J be the objective function to be optimised defined on a finite reel vector space $\mathbb{R}^d$ or a vector subspace Ω of $\mathbb{R}^d$. We here look for the maximum x^* of function J in Ω. Stochastic optimisation methods (or metaheuristic) are often used in cases where:

- The objective function J has no analytical expression (the specific values are reached by either a calculation code or a direct measurement by which J can be noisy).
- The gradient of J can be inaccessible.
- Function J can comprise many non-linearities.
- Number of correlations between variables can exist but are not precisely identified.
- Function J is multimodal. It has many local minimums.

A stochastic approach seems to be appropriate to the problem of propagation through turbulent atmosphere when one is using the total integrated intensity over the pupil as objective function. In addition, the proposed downhill algorithm is a parallel algorithm where each element of the vector sub-space is optimised simultaneously. This greatly increases convergence speed compared to the previous sequential optimisation methods.

The stochastic descent consist in sending an elementary phase perturbation δu_j (where δu_j can be either positive of negative) to each mirror segment. $|\delta u_j| = \varepsilon$ is identical for each DM actuator. Let N be the number of mirror segments. The perturbation vector at time n is $\sum_{j=1}^{N} \delta u_j^n$. The sign of phase perturbation follows Bernoulli law: $\delta u_j^n = \pm\varepsilon \,\forall\, j \in [1 \cdots N]$. After applying the perturbation vector and measuring the metric J_+^n, the perturbation signs are inverted to measured J_-^n. Perturbations applied for J_+^n and J_-^n are of opposite sign. Let $J_\pm^n$ be the metric at time n after application of one of the perturbations. At time n one obtains:

$$J_\pm^n = J\left(u_1^n \pm \delta_1^n, \cdots, u_j^n \pm \delta_j^n, \cdots, u_N^n \pm \delta_N^n\right), \tag{8.2}$$

with u_j^n the voltage applied to segment j of the DM at time n and $\pm\delta_j^n$ the elementary perturbation created by the same segment. Voltage vector values to send to the mirror at time $n+1$ is calculated by the following equation:

$$\left\{u_j^{n+1}\right\}_{j=1}^{N} = \left\{u_j^n + \gamma(J_{j,+}^n - J_{j,-}^n) sign(\delta u_j^n)\right\}_{j=1}^{N}, \tag{8.3}$$

where $sign(\delta u_j^n)$ the elementary perturbation sign during calculation of metric J_+^n, γ is an update coefficient and $\{\cdots\}_{j=1}^{N}$ a vector with N elements. We use a constant γ update parameter for the optimisation of J.

8.3.2 Correction Efficiency: An Example

In the following paragraph we concentrate on numerical simulations of an AO system implementing an SPGD optimisation algorithm. The propagation distance is set to $L = 10\,\text{km}$, the wavelength to $\lambda = 1.5$ µm and the pupil diameter to $D = 30\,\text{cm}$. In order to illustrate correction efficiency of the SPGD algorithm, short and long-expose images are presented figure 8.5. The energy concentration between non-corrected and corrected images is clearly visible. For this particular realisation of turbulence (short exposure) the SPGD algorithm helps improving the integrated energy from 0.45 to 0.65 after 200 iterations. The turbulence strength is set to $C_n^2 = 10^{-14}\,\text{m}^{-2/3}$.

Figure 8.6 illustrate the typical evolution of metric J as a function of the iteration number. We have considered that turbulence does not change during the optimisation process. The corresponding short-exposure image before and after correction is given figure 8.5. It can be seen that a strong improvement is brought by the correction at the beginning of the optimisation process (i.e. strong slope of the curve, in particular between iteration 0 and 20). It seems to reach a local maximum around approximately iteration number $70 - 80$. After that, metric improvement is much slower and the optimisation process cannot reach the global maximum easily. The slope at origin is favourable for rapid turbulence evolution where the system needs to 'hook on' rapidly. Oppositely, once the system is engaged, the metric progression is much slower and chaotic. The SPGD algorithm does not seem particularly adapted when J is close to the global optimum but only when it is relatively far away from it.

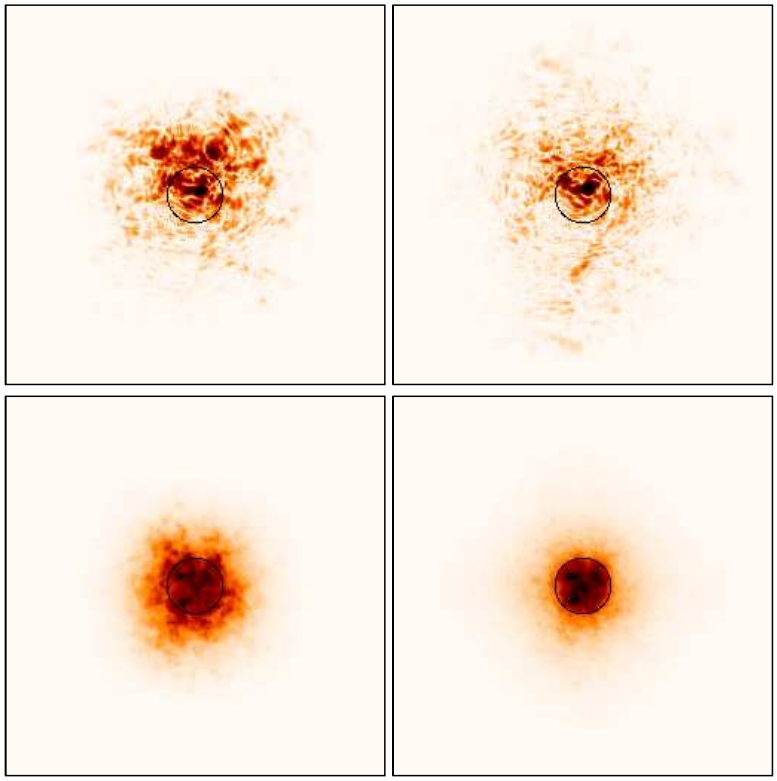

Figure 8.5: Illustration of SPGD correction efficiency. Left: before correction, right: after convergence. Top: short-exposure, bottom: long-exposure. Colour scale: logarithmic for short-exposure and linear for long-exposure.

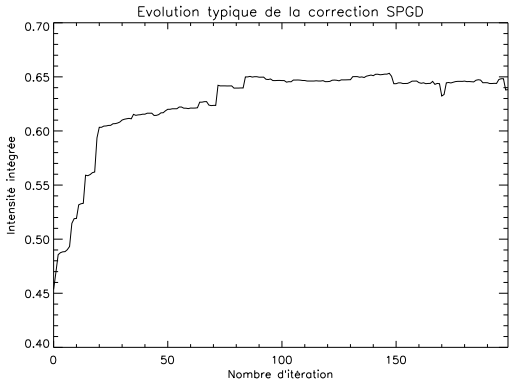

Figure 8.6: Typical integrated intensity evolution during the optimisation process.

8.3.3 Impact of Turbulence Strength

Figure 8.7 presents optimisation the instantaneous intensity I as a function of turbulence strength and iteration number. The classical statistical quantities are shown: mean intensity (left) and normalised intensity fluctuations (right). The deformable mirror can apply pure piston to each of its segments. The number of segment is limited to 7×7. Statistics are calculated over

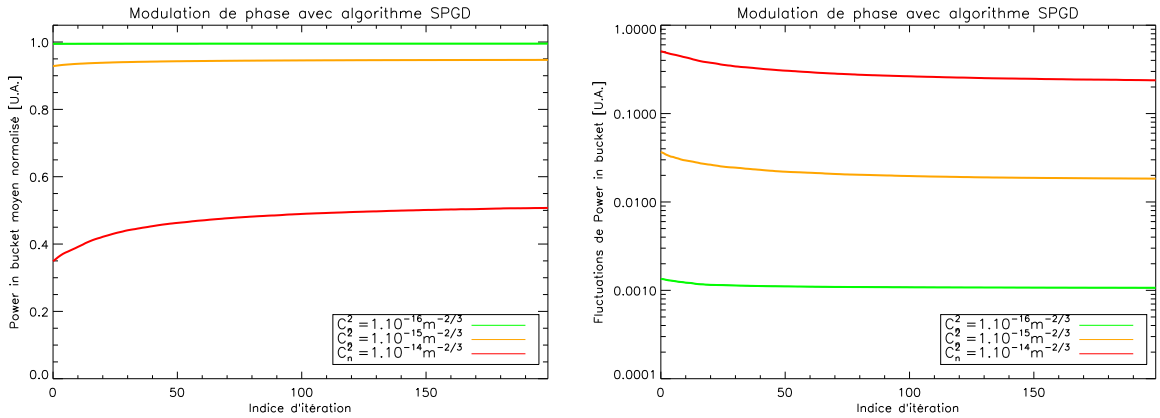

Figure 8.7: SPGD correction efficiency function of turbulence strength. Left: mean intensity. Right: normalised intensity fluctuations. $D = 30$ cm without central obscuration.

independent turbulence realisations. It can be seen that SPGD optimisation can lead to a mean intensity increase and a reduction in intensity fluctuations. As mentioned previously (on a single iteration), optimisation is quick at the beginning of the optimisation process and slows down after about 30 iterations in strong turbulence conditions.

For $C_n^2 = 10^{-14}\,\mathrm{m}^{-2/3}$, mean intensity increases from $\langle I_0 \rangle = 0.35$ to slightly above $\langle I \rangle = 0.5$ after about a hundred iterations. Intensity fluctuation on the other side go from $\frac{\sigma_I}{\langle I \rangle} = 0.5$ to $\frac{\sigma_I}{\langle I \rangle} \simeq 0.2$. We remind that the values obtained with Vellekoop's algorithm where approximately of $\frac{\sigma_I}{\langle I \rangle} \simeq 0.2$ after convergence. The two methods give similar results. However, the results obtained with an SPGD optimisation are slightly better than the SH analysis on a counter-propagating probe (see paragraph 7.2) in strong perturbation. It is comparable with the multi-probe method. Nevertheless, these results are still not compatible with the goal of obtaining a BER of 10^{-12}, that is to have $\frac{\sigma_I}{\langle I \rangle} < 0.1$.

The SPGD algorithm converges more rapidly than the algorithms proposed by Vellekoop or Nelder-Mead. It can reach convergence after approximately 50 iterations only. We recall that the number of necessary iterations for convergence of the Vellekoop algorithm is obtain by multiplying the number of segments in the DM by the number of elementary steps ε. In addition, we have implemented an algorithm with a constant update parameter γ. It has been shown [Weyrauch-a-01] that using an adaptive γ help reduce the convergence time at the same time as keeping the correction quality.

8.3.4 Impact of Pupil Geometry

In this paragraph is presented the ability of the SPGD algorithm to take into account a central obscuration in the reception pupil (pupil at emission stays un-obscured). More generally, this paragraph shows the capacity of the SPGD algorithm to take into account any pupil shape (other than circular for example). Figure 8.8 shows 5 different turbulence realisation all implementing a SPGD correction with $D = 30\,\text{cm}$ and a central obscuration of 50%. Intensity distribution is ob-

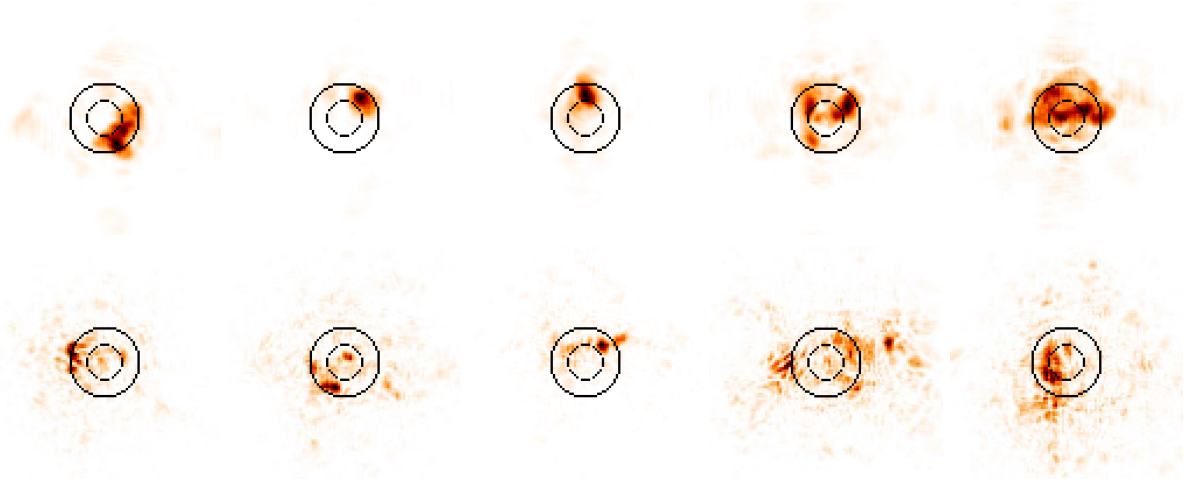

Figure 8.8: Intensity distribution (different turbulence realisation) after SPGD convergence. Two turbulence strengths are studied: $10^{-15}\,\text{m}^{-2/3}$ (top) and $10^{-14}\,\text{m}^{-2/3}$ (bottom). Central obscuration is 50 percent, propagation distance $10\,\text{km}$, wavelength $\lambda = 1.5$ µm and pupil diameter $30\,\text{cm}$.

tained after optimisation for $C_n^2 = 10^{-15}\,\text{m}^{-2/3}$ (upper part of the figure) and $C_n^2 = 10^{-14}\,\text{m}^{-2/3}$ (lower part of the figure). From these illustrations, it seems that some turbulence realisations are favourable and enable the algorithm to concentrate a speckle in the pupil. Other realisations seem less favourable for energy concentration. For the least favourable cases, the intensity distribution is more uniform throughout the reception plane.

Figure 8.9 presents correction efficiency as function of the number of iterations. Phase modulation based on a SPGD type algorithm seems capable of taking into account the shape of the pupil, whichever its shape. However, the correction quality seems much lower than without obscuration. We have shown paragraph 6.1.6 that the chosen set of parameters leads to a reduction of correction quality due only to the reducing of the collecting surface area. In fact, the mean intensity goes from $\langle I \rangle = 0.51$ to 0.36 with a 50% central obscuration. In addition, it seems that the algorithm cannot distribute the intensity over the entire pupil but concentrates the major part of the energy within a speckle on the side of the pupil. This observation is particularly true for realisation 1, 2 and 3 for $C_n^2 = 10^{-15}\,\text{m}^{-2/3}$ and case 3 for $C_n^2 = 10^{-14}\,\text{m}^{-2/3}$ (see figure 8.8 and by reading numbers from left to right).

As expected, results are clearly not as good as with the optimal correction. Remember that for the same set of parameters, mean intensity was $\langle I \rangle_{C_n^2 = 10^{-14}\,\text{m}^{-2/3}} = 0.6$ and residual intensity

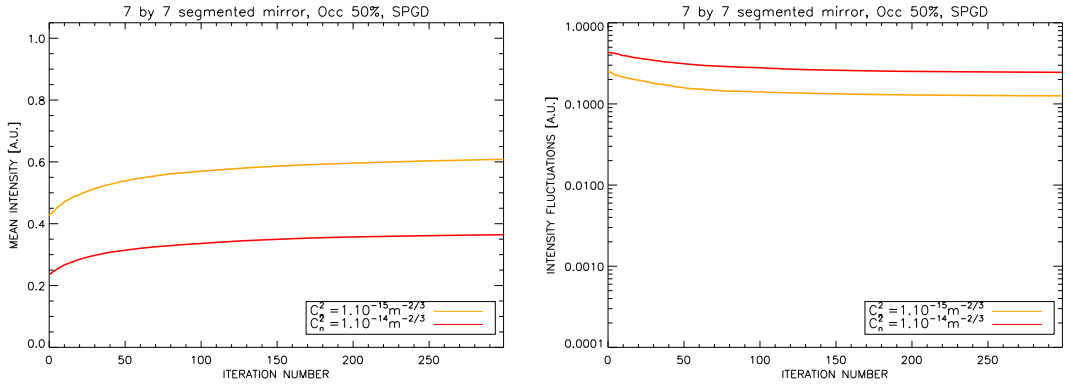

Figure 8.9: Mean intensity and intensity fluctuations function of the number of iterations for SPGD correction. Central obscuration of 50 percent. Propagation distance $10\,\text{km}$, wavelength $\lambda = 1.5$ µm, pupil diameter $30\,\text{cm}$.

fluctuations $\frac{\sigma_I}{\langle I \rangle_{C_n^2=10^{-14}\,\text{m}^{-2/3}}} = 0.1$ for the optimal correction. Here, they are respectively of $\langle I \rangle_{C_n^2=10^{-14}\,\text{m}^{-2/3}} = 0.36$ and of $\frac{\sigma_I}{\langle I \rangle_{C_n^2=10^{-14}\,\text{m}^{-2/3}}} = 0.25$ for the SPDG algorithm. In addition, convergence is reached only after approximately 150 iterations for SPGD whereas only about 10 iterations were sufficient for the optimal case.

8.3.5 Impact of Transverse Wind

In introductory chapters, the influence of transverse winds on laser propagation through turbulence was presented. In this paragraph, a numerical simulation of transverse wind $V_\perp$ effects on SPGD correction is also untaken. We simulate continuous wind by shifting phase screen by sub-pixels. These simulations can help us find the necessary correction speed in order to keep a sufficient correction gain. As these simulations are realised by shifting phase screens, the method is still valid either when considering transverse wind speed or adaptive optics loop speed. Simulations conditions are the following: constant γ parameter, laser beam diameter at emission $2w_0 = 14\,\text{cm}$, elementary phase perturbations $\varepsilon = \frac{2\pi}{21}$ and pupil diameter $D = 25\,\text{cm}$ with 35% central obscuration. Figure 8.10 shows simulations results for SPGD correction for three different wind speeds (or equivalently phase screen shifts). The wind speed increases from bottom to top on the figure.

In order to evaluate the correction quality as a function of wind speed (resp. correction loop speed) we introduce two new metrics: the mean intensity gain between the value before correction (at t_0) and the mean intensity after convergence if the algorithm (theoretically at t_∞) and the residual fluctuations after convergence (i.e. σ_I after convergence). Table 8.1 gives the results in terms of gain relative to the uncorrected case and residual fluctuations.

A one-pixel shift every 20 iteration seems the minimum to obtain an acceptable correction quality for the undertaken simulations. If a $10\,\text{m.s}^{-1}$ wind speed is considered the necessary loop update frequency is $f_{20} = 25.6\,\text{kHz}$ (resp. $f_{10} = 12.8\,\text{kHz}$ and $f_{30} = 38.4\,\text{kHz}$). The necessary

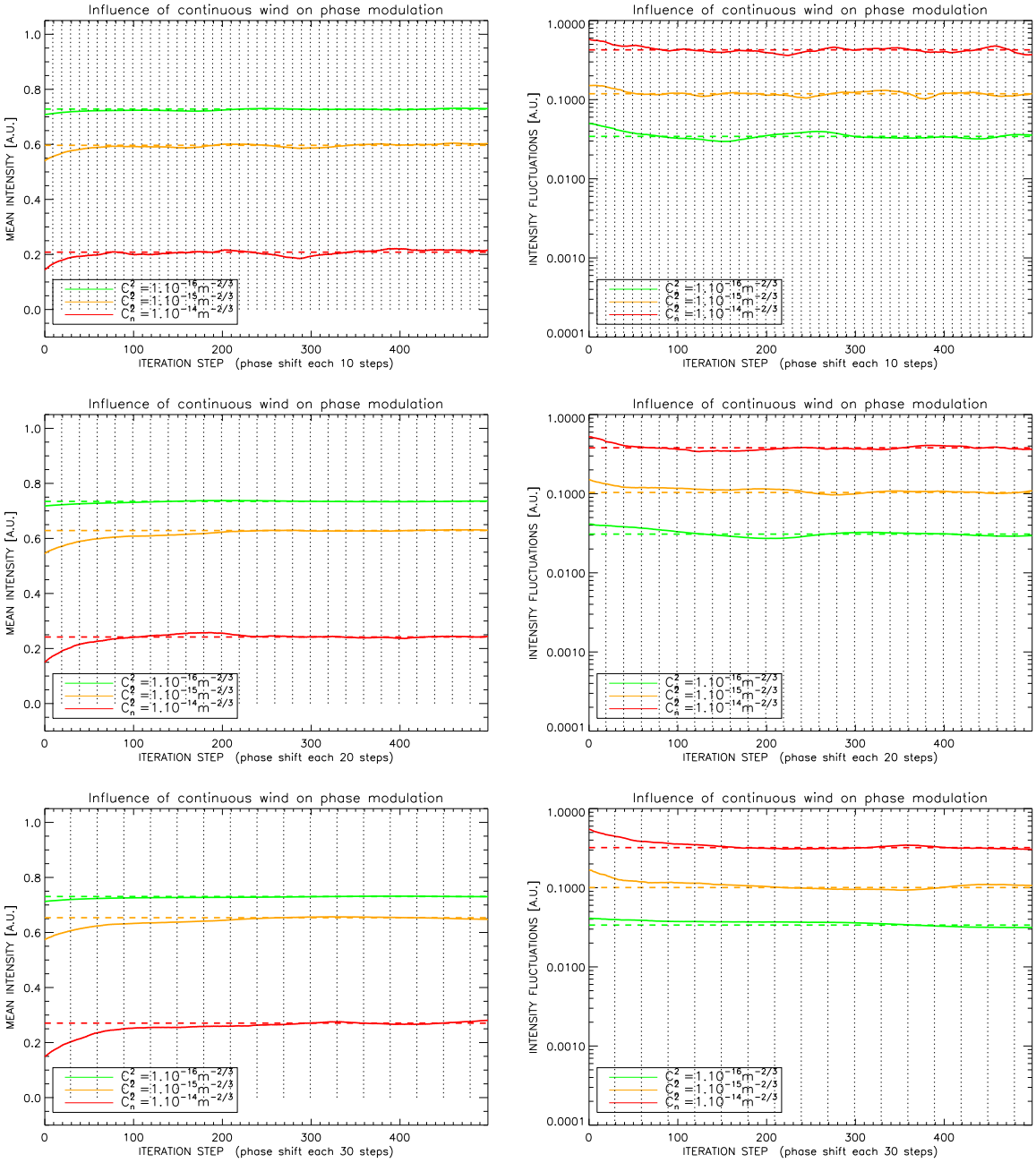

Figure 8.10: SPGD correction in presence of a continuous wind speed. From bottom to top the wind speed increases. Shift of one pixel is done respectively every 10, 20 and 30 iterations. Vertical lines represent a full pixel shift.

loop update frequency is crucial. Figure 8.11 illustrates correction evolution as a function of wind speed. The slower the wind (resp. loop frequency high) the higher the correction quality.

Type de correction	$C_n^2\ [\mathrm{m}^{-2/3}]$	Gain	Residual fluctuations
One pixel shift	10^{-16}	0.0202	0.0015
after 10 propagations	10^{-15}	0.0576	0.0056
	10^{-14}	0.0643	0.0102
One pixel shift	10^{-16}	0.0170	0.0008
after 20 propagations	10^{-15}	0.0848	0.0015
	10^{-14}	0.0920	0.0021
One pixel shift	10^{-16}	0.0186	0.0009
after 30 propagations	10^{-15}	0.0803	0.0025
	10^{-14}	0.1216	0.0040

Table 8.1: Table representing gain and residual fluctuations after correction converge, function of wind speed and turbulence strength.

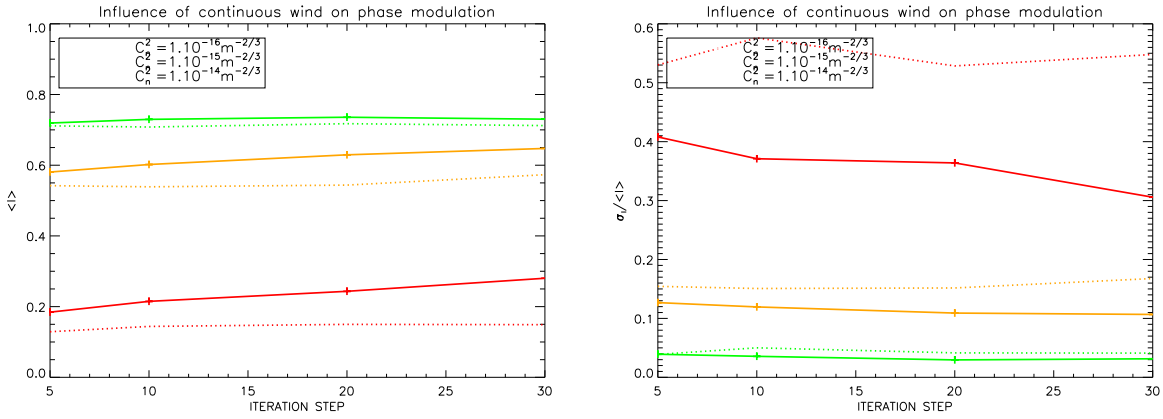

Figure 8.11: Correction efficiency as a function of wind speed. Dashed lines: without correction, solid lines: with correction. Horizontally is represented the number of propagation simulated before a one-pixel phase sift.

8.3.6 Noise Sensibility Study

Simulations presented so far did not take into account the effect of noise on the measurements. Adding noise will obviously disrupt the measurement of I and lead to a less effective optimisation process. In this simulation, we add noise in the measurement of the integrated intensity over the pupil area after propagation. The SNR is defined as:

$$SNR = \frac{I_{total}}{\sigma_{noise}}, \tag{8.4}$$

Where I_{total} is the total intensity received by the telescope and σ^2_{noise} the noise variance. Noise is considered Gaussian, with zero mean and a standard deviation of σ_{noise}.

Following figure 8.12, it is necessary to have signal-to-noise ratio higher than 40 for the SPGD algorithm to optimise integrated intensity after propagation. A low value will produce strong intensity fluctuations and for the worst case ($SNR < 20$) a reduction of mean intensity. When noise influence is negligible ($SNR > 100$), the obtained results are the same as without noise. By increasing update frequency of the adaptive optics loop we will increase system

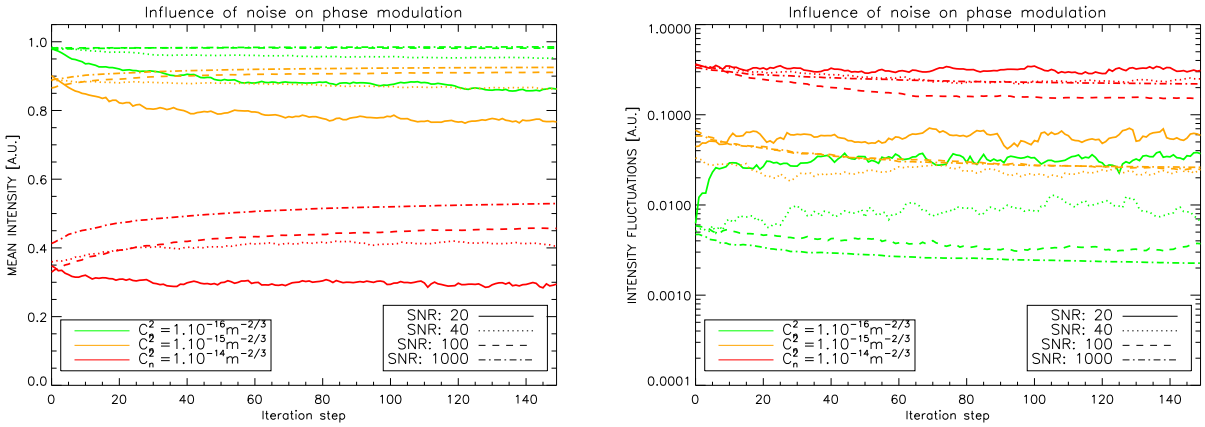

Figure 8.12: Mean intensity curves (left) and intensity fluctuations as a function of iterations (right) for SPGD correction and different noise levels. Propagation distance 10 km, wavelength $\lambda = 1.5$ µm and pupil diameter 30 cm.

robustness to temporal evolution of turbulence (i.e. transverse winds). On the other hand, the intensity received at each iteration step will be lower for higher loop frequencies. A compromise between small integration time and AO bandwidth is necessary.

8.3.7 Initialisation of the Correction Phase

8.3.7.1 Principle

In order to improve correction convergence speed, it is possible to add an a priori on the driven phase. By using an SPGD type optimisation algorithm, it is possible to initialise the correction phase before the iterative process begins by using a wavefront measurements [Vorontsov-a-02]. The idea is to increase algorithm convergence speed by using a phase that is as close as possible to the final correction phase calculated after convergence. Two different initialisation phases are studied: geometric phase and phase in the emission pupil. Geometric phase for a plane wave corresponds to the sum of all phase perturbations along the propagation path. It corresponds to the phase measured in weak perturbation regimes in the case of the sub-optimal correction. Phase in the emission pupil is considered to be the turbulent phase screen which closest to the emission plane. It corresponds to phase measured by the counter-propagative multi-probe approach. In the framework of geometric approximation, when phase perturbations are weak, it should enable the algorithm to be initialised with the phase obtain after convergence of the algorithm. On the

other hand, for strong perturbation regimes geometric phase is not longer the optimal solution. Phase perturbations near the emission pupil are responsible for scintillation after propagation. By pre-compensating for it, one can greatly overcome intensity fluctuations in the reception pupil.

A $D = 25$ cm pupil is used with a $2w_0 = 14$ cm diameter beam. The number of DM actuators is limited to 7×7 and the elementary step to $\varepsilon = \frac{2\pi}{21}$. Measurement of I is supposed noiseless. The phase initialisation for the SPGD correction is discretized on the DM basis which segments are only driven in piston. In order to take the mirror geometry into account, we use the average geometric phase (resp. the phase in the emission pupil) on each mirror segment. We project the phase on the DM basis (only driven in piston) which is equivalent to the mean light travel on the segment.

8.3.7.2 Initialisation with Geometric Phase and Phase in the Pupil

Figure 8.13 represents simulated results obtained for SPGD correction with an initialisation with the geometric phase (top) and the phase in the pupil (bottom). Initialisation the correction with a phase works well when the turbulence is weak because the final correction phase is close to the geometric phase. Correction by initialising the phase with the emission pupil phase does not significantly improve correction, despite a slight gain for the weakest turbulence studied. On the other hand, geometric phase seems to slightly improve correction both for $C_n^2 = 10^{-16}\,\mathrm{m}^{-2/3}$ and $C_n^2 = 10^{-15}\,\mathrm{m}^{-2/3}$. When turbulence is strong, the phase that optimises intensity in the reception pupil differs from the geometric phase. This is the reason why initialising correction with a non-zero phase (either geometric or the phase located in the emission pupil) is not efficient in strong turbulence.

To conclude, phase initialisation does not seem to increase convergence speed for iterative correction. Initialising the correction only slightly improve the overall correction quality. Geometric phase seems to be slightly more efficient than the phase in the emission pupil. By looking at the results obtained in this study, coupling wavefront sensing with a SPGD modulation technique is not justified. In order to reach sufficient gain, a bi-directional link might be useful (such as a sub-optimal correction).

8.4 Conclusion

Direct optimisation method by adaptive optics has been suggested for many years in the literature. These methods were the first to be implemented in adaptive optics system in the 1970s. Despite the relative simplicity of implementation (mainly by not using a complex optical element such as wavefront sensors), its practical implementation remains difficult. In fact, the required bandwidths are usually prohibitive for most FSO systems. When the required bandwidth is achieved (typically > 10 kHz), it is possible to correct atmospheric turbulence phase perturbations, for example by SPGD methods. These techniques have been around for a long time but can only recently be implemented in real systems because of the high bandwidth they require. This algorithm has been used successfully in a number of free-space communication systems [Weyrauch-a-05, Zhao-p-08] or validated for image restoration that have been degraded by

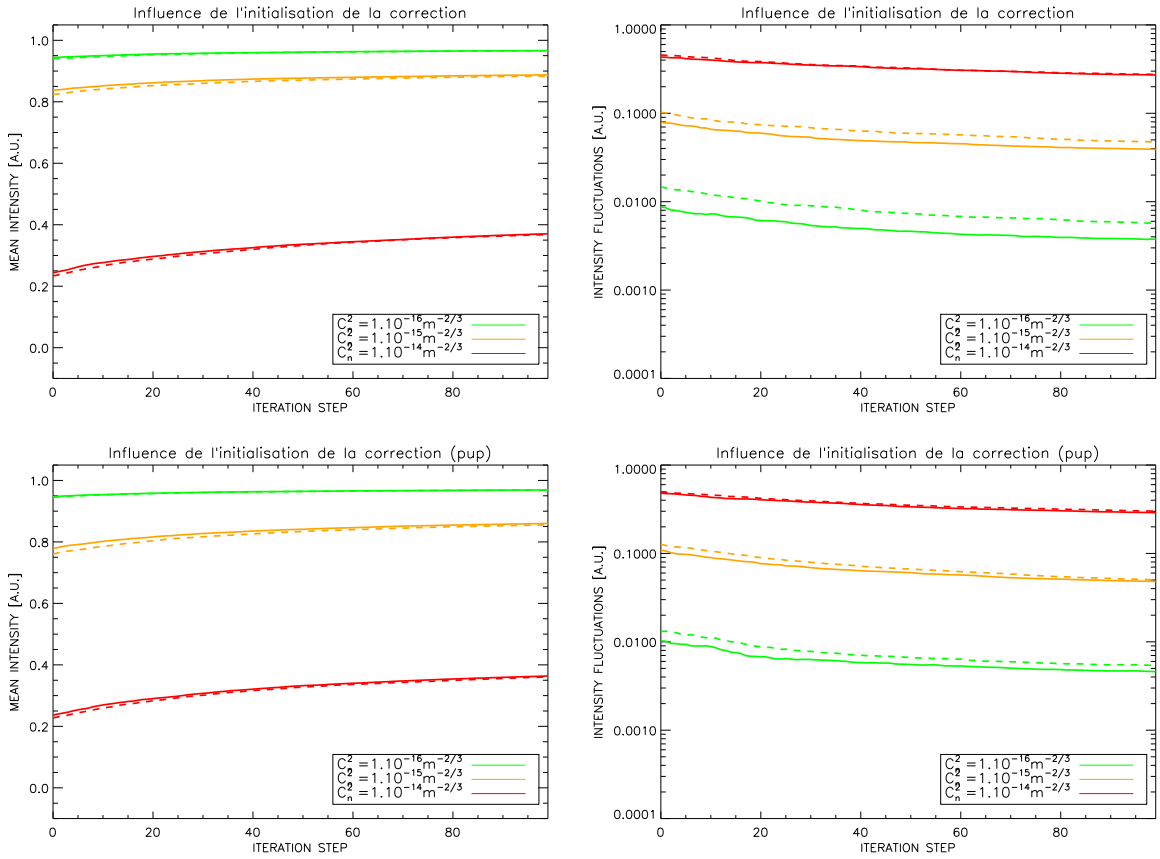

Figure 8.13: Top: intensity optimisation by SPGD with (solid line) and without (dashed lines) geometric phase initialisation. Bottom: intensity optimisation by SPGD with (solid line) and without (dashed lines) emission pupil phase initialisation.

turbulence [Vorontsov-a-97, Aubailly-a-08, Yang-a-09]. The implementation of more efficient algorithms and the rise of faster adaptive optics loops has renewed interest in phase modulation techniques. In addition, these techniques seem particularly adapted when data construction model is not known and when temporal constrains are limited (for example for laser focalisation though biological tissues).

This chapter enabled us to study several basic concept of phase modulation in the context of endo-atmospheric optical communication link on long distances. Stochastic methods seem the most appropriate methods for FSOs where temporal constrains impose large bandwidths. Static performances are satisfactory and correspond to those obtained for sub-optimal correction. No theoretical limit has been demonstrated as for the limits of algorithms such a SPGD for FSO systems. A number of other algorithms can be used and their performance estimation is still to be undertaken. Phase modulation methods can obtain similar results to those produced by a multi-probe analysis system. The technical problems encountered during implementation of multi-beam correction (i.e. optical complexity, number of laser sources, scintillation) are transposed to

an algorithmic and technological complexity (i.e. bandwidth of deformable mirror and real-time controller). We have seen in this chapter that SPGD type algorithms can take the geometry of the pupil into account (central obscuration for example). It is important to have enough bandwidth to converge faster that the time evolution of turbulence. In addition, we have seen that the signal-to-noise ratio can sufficiently reduce the signal quality to no longer enable optimisation. Signal-to-noise ratio is directly linked to integration time on the detector. The necessary loop frequency is dictated by the characteristic time evolution of phase perturbations. In other words, the loop frequency is a compromise between two temporal constrains. However, oppositely to SH-WFS where the flux is limited to the size of the lenslet, the flux used for optimisation is the total collected flux in the pupil.

It appears possible to improve the SPGD algorithm by several methods. Firstly by making the γ parameter adaptive, enabling a reduction in convergence time but by keeping performance at the same level [Weyrauch-a-01]. Secondly, we have shown an improvement in convergence time for the Nelder-Mead algorithm thanks to a hierarchical optimisation. However, the problem of convergence speed remains. In addition, phase perturbations applied to the DM segments follow a Bernouilli law that is not adapted to atmospheric turbulence. The study statistics more appropriate to turbulence could improve the convergence speed of the algorithm.

Performance obtained by phase correction remain significantly below performance of a phase and amplitude correction. Driving both phase and amplitude of the field could improve correction quality.

Chapter 9

Practical Implementation of Pseudo-Phase Conjugation

Contents

In chapter 6 we have presented amplitude and phase pre-compensation and showed how it can be used to reach the so-called optimal correction. Other types of correction, limited to the phase part of the wave, cannot reach the same correction levels. This is even clearer for strong perturbations where amplitude variations are not longer negligible. In strong turbulence and even by using an iterative true-phase correction, losses can be important. To the best of our knowledge, no system currently implements the optimal correction. In this chapter, we will

study different implementations for an iterative phase and amplitude correction of the emitted field. The proposed solutions will however represent a degradation of the perfect optimal pre-compensation strategy.

A possible solution to modulate phase and amplitude in the pupil plane is to use two deformable mirrors. In paragraph 9.1 a simple implementation strategy for phase and amplitude correction based on two tip-tilt mirrors is presented. This method takes advantage of the speckle distribution of the received intensity to concentrate the maximum flux within the most energetic speckle. In the following paragraph (paragraph 9.2) influence of pupil spatial sampling on optimal correction is evaluated from a theoretical point of view. In the same paragraph, we investigate the possibility off increasing wavelength to relax system constrains related to turbulence. Finally, with the idea of building a system using iterative phase and amplitude conjugation, we propose paragraph 9.3 a practical implementation. This is performed by sampling the pupil with a monomode waveguide matrix that can be used to modulate phase and amplitude of an electromagnetic field. The re-emitted wave after correction corresponds to the complex conjugate of the received electromagnetic wave (iterative correction principle). Limitations related to the use of waveguides are also investigated.

9.1 Phase and Amplitude Correction Using Two Deformable Mirrors

In previews chapters, we emphasised the importance of correcting both phase and amplitude of the field. In fact, after having evaluated the performance of different correction methods and in particular the optimal and sub-optimal approaches, we clearly demonstrated that using a phase-only correction is often not appropriate. Our best option is therefore to perform a phase and amplitude correction. In this chapter several concept are presented.

9.1.1 Introduction

No systems have been presented so far that can correct phase and amplitude of the field. We have therefore based our reasoning on a perfect system. In order to implement this type of correction, some authors [Roggemann-a-98] have proposed the use of two deformable mirrors. The first deformable mirror DM_1 is positioned in the pupil plan P and controls the phase part of the wave. It is driven by measurements taken by a WFS in a pupil-conjugate plan. The second mirror DM_2 is located a distance d away from the pupil. DM_2 enables by the phase aberrations it introduces and after propagation to modify the amplitude distribution in pupil P. Figure 9.1 shows a schematic of phase and amplitude correction with two deformable mirrors. One of the major issues for this type of correction is computing the control to apply to the second mirror DM_2. This problem cannot be solves in an exact way. In order to circumvent this problem, Roggemann proposed to position DM_2 in the far field of DM_1 and use a phase retrieval algorithm. In weak perturbation regimes, the resulting study showed a gain when compared to phase-only correction of approximately 1.5 on the amplitude of the field on the optical axis. When phase perturba-

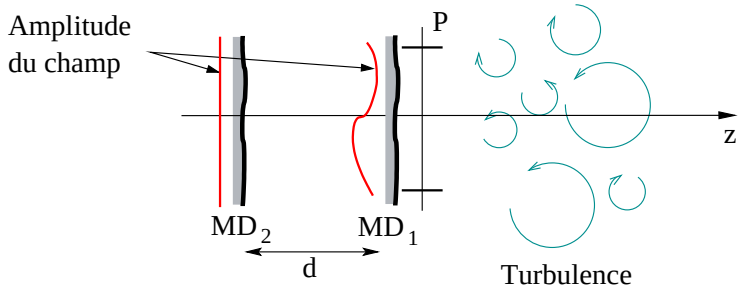

Figure 9.1: Schematic for two deformable mirrors DM_1 and DM_2 correction used to drive both phase and amplitude in the pupil plan P.

tions distributed over the entire volume are sufficiently strong, amplitude fluctuations in the field disrupt the wavefront sensing process [Mahe-p-00, Voitsekhovich-a-01]. Problems (phase dislocation, scintillation) found in the phase measurement in strong perturbations are found again in driving several DMs. The problem of generating control signals to drive mirrors DM_1 and DM_2 in an optimal way is still to be answered.

9.1.2 Tip-Tilt Correction

In this paragraph is presented a phase and amplitude pre-compensation method based on modal decomposition of perturbations. It focuses on a simple implementation with only two tip-tilt mirrors.

9.1.2.1 Correction Principle

We have shown in introductory chapters that the low orders modes of turbulence are the most energetic ones. When perturbations are weak, the primarily impact is beam wander and tilting of the incident beam. We here study the implications of compensating for both effects. The practical implementation of such a correction is relatively simple. For correcting tip-tilt and re-centring the beam, only two tip-tilt mirrors are necessary. The first is placed outside the pupil plane and is used to centre the emitted beam on the incoming beam's COG as received in the pupil plane. The second in a conjugated pupil plane corrects for phase. These mirrors are relatively cheap optical elements with high bandwidths. The wave tilting is measured by a low resolution detector placed in the focal plane. Measurement of the beam position requires a low-resolution detector located in the pupil plane. The importance of correcting for beam wander lies in the fact that tilt is only measured where the received intensity is maximal. Phase can vary greatly from one point to the other in the pupil. We need to re-emit the beam where the tip-tilt has been measured, i.e. where the intensity is maximal. Figure 9.2 illustrates a two tip-tilt mirror concept to shift the beam to the maximal received intensity (by using DM_2) and perform phase correction (using DM_1).

The optimal position for the emitted laser beam is calculated using the most energetic scintillation speckle from a counter-propagating beam. The correction therefore consists only in

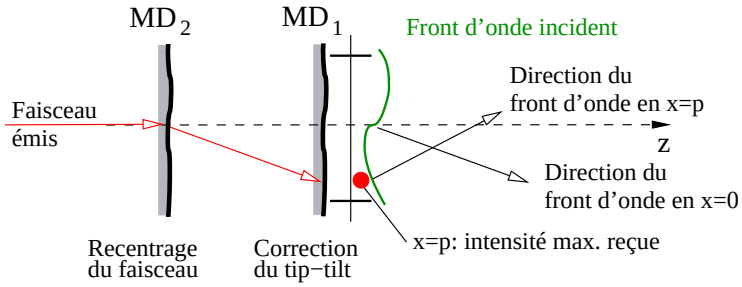

Figure 9.2: Illustration of the two tip-tilt mirror correction for beam re-centring and phase correction.

correcting for a single speckle and concentrating all the energy in this one only. It enables us to use phase conjugation principles on a reduced part of the emission plane. Figure 9.3 presents typical intensity distribution in the pupil plan $T2$ after propagation through turbulence of a laser beam emitted from $T1$. Figure 9.3 presents simultaneously pupil $T2$ and the position where the

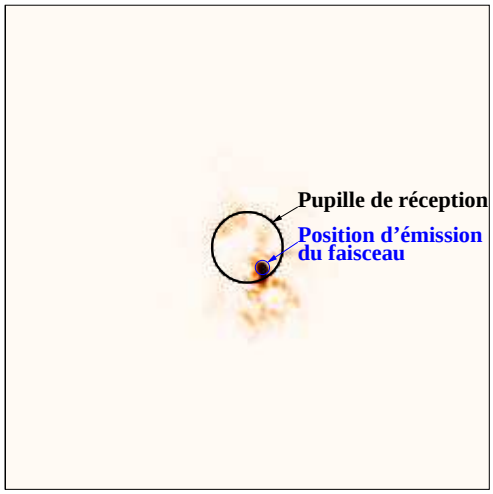

Figure 9.3: Typical intensity distribution after propagation with position (in blue) of the emitted beam at the following iteration step.

counter-propagating beam will be sent from $T2$.

Calculation of the position for the most energetic scintillation speckle is done by thresholding and centre of gravity. This helps, among other things, to limit the noise impact on measures. Centre of gravity measurements are weighted by a function (typically a top-hat) in order to privilege an energy distribution minimising pupil truncation effects [Zhao-p-08]. This restoring force favours configurations where the beam emission is close to the optical axis. From this position, the emitted beam is re-centred in order to be super-imposed to the previously calculated position. To a first approximation, the emitted intensity distribution is expressed as a Gaussian.

Optimisation of the emitted beam size will be presented in the following paragraph. In order to improve correction performance, an iterative correction between the communication extremeties $T1$ and $T2$ is used. The algorithm we have used for numerical simulations is summarised below:

- An initial divergent Gaussian beam is sent from $T1$ to $T2$. The divergent beam is used to increase the probability of interception by $T2$.
- Calculation of position p in telescope $T2$ where the incoming beam has maximal energy.
- Measurement of global tip-tilt value over the reception pupil.
- The pre-compensated (tip-tilt only) beam is emitted from $T2$ to $T1$ in position p. The laser beam is collimated and its beam waist w_0 optimised.
- From this moment on the iterative correction is in place. The two telescopes both emit a re-centred collimated beam. The centring position is calculated at every iteration step.

9.1.2.2 Impact of Beam Waist

Figure 9.4 presents intensity distribution at the level of telescope $T1$ for various correction methods. The turbulence strength is set to $C_n^2 = 10^{-14}\,\mathrm{m}^{-2/3}$ and the chosen turbulence distribution for this particular illustration is clearly favourable for a tip-tilt correction with beam re-centring. The first iteration is without any correction (left of the figure). The overall collected intensity for this particular turbulence realisation is $I_{\text{without corr}} = 0.33$. The first correction strategy (upper level on the figure) shows the impact of a phase and amplitude optimal iterative correction as presented in chapter 6. It enables the best correction quality possible with $I_9 = 0.83$ (only the first 4 iterations are shown). Sub-optimal correction (central part) presented chapter 6.2 and beam re-centring correction (lower part of the figure) give similar results. The received intensity after 9 iterations is increased to $I_9 = 0.55$. The presented numerical simulations presented all make use the same turbulent phase screens and enable a direct comparison of correction methods (for this particular case).

Optimisation of the beam waist w_0 for the emitted beam after re-centring is presented figure 9.5. This optimisation is based on both the mean intensity (left part of the figure) and normalised intensity fluctuations (right part of the figure). We have chosen a collimated laser beam because the influence of focalisation is not very strong. Pupil diameter for both $T1$ and $T2$ is set to $D = 25\,\mathrm{cm}$. Two turbulence strengths are studied: $C_n^2 = 10^{-15}m^{-2/3}$ (red) and $C_n^2 = 10^{-14}m^{-2/3}$ (orange)

For the $C_n^2 = 10^{-15}m^{-2/3}$ case, optimisation using both metrics gives a beam waist between 5 and $7\,\mathrm{cm}$. When beam size is too small, natural divergence produces strong flux losses due to strong truncation by the reception pupil. Inversely, when the beam size is too large, energy is distributed over an area much larger than the speckle size. Using a correction limited to tip-tilt and re-centring only cannot be justified in this case.

For $C_n^2 = 10^{-14}m^{-2/3}$, tip-tilt limited correction cannot sufficiently increase link quality regardless of the beam size w_0. Without any correction we obtain $\langle I \rangle = 0.26$ (resp. $\frac{\sigma_I}{\langle I \rangle} = 0.56$).

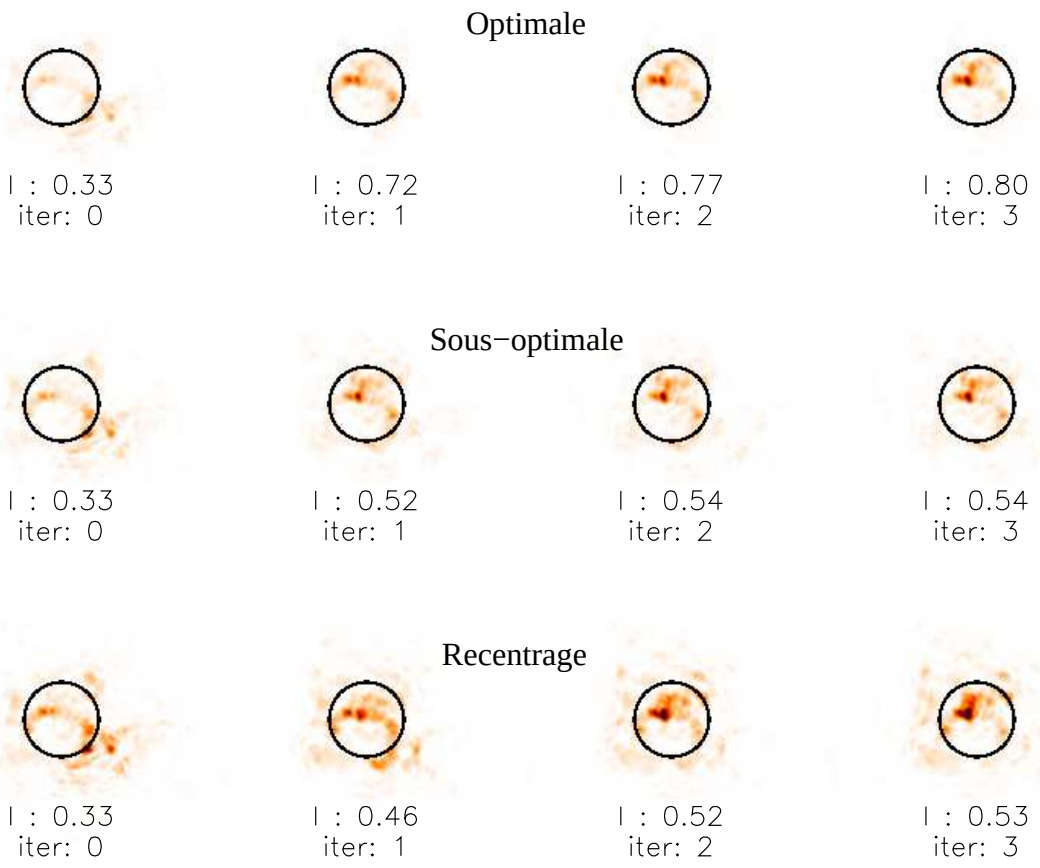

Figure 9.4: Intensity distribution at the level of telescope $T1$. From top to bottom: optimal correction, sub-optimal correction and tip-tilt correction with beam re-centring. Pupil limits are shown in black with a diameter of $D = 0,25\,\mathrm{m}$ and turbulence strength is $C_n^2 = 10^{-14}\,\mathrm{m}^{-2/3}$.

After correction we respectively obtain $\langle I \rangle = 0.4$ and $\frac{\sigma_I}{\langle I \rangle} = 0.3$. Despite a reduction by a factor of approximately 2, the desired intensity fluctuations level cannot be reached.

Conclusion

The correction strategy presented here relies on beam re-centring and tip-tilt correction at each iteration step. The position of the emitted Gaussian beam corresponds to the position of the most energetic speckle received from the incoming wave. The system we have implemented is relatively simple since it only requires two pointing mirrors. A restoring force favouring positions in the centre of the pupil can be used to minimise truncation effects. A static study was undertaken by the use of decorrelated turbulent phase screens. We have observed that certain turbulence realisation are clearly favourable and other clearly not (few or no energetic speckles in the pupil). We have found that the correction quality is below the typical requirements for FSO systems.

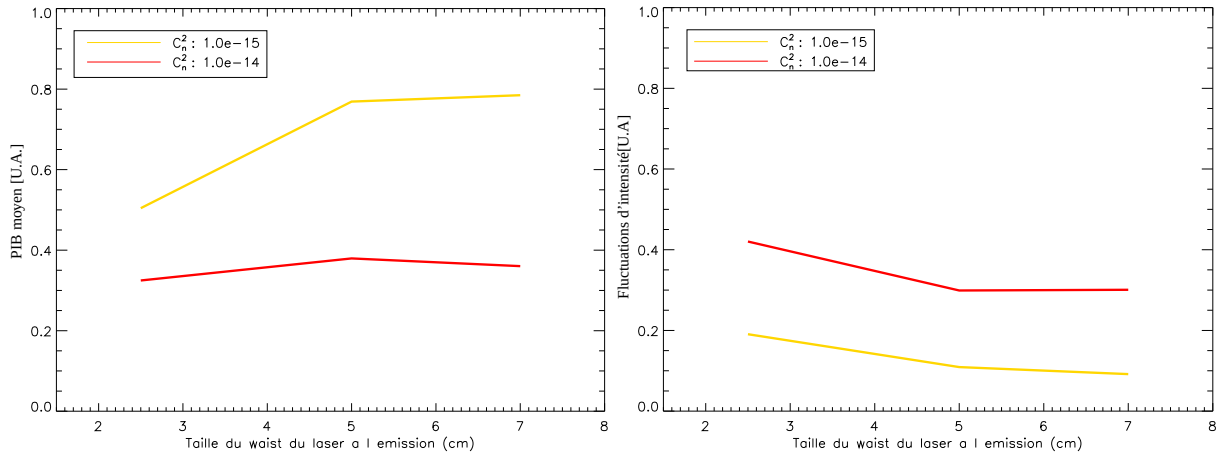

Figure 9.5: Mean intensity (left) and normalised intensity fluctuations (right) evolution function of the emitted laser beam waist for a tip-tilt correction on both telescopes. Two turbulence strengths are studied: $C_n^2 = 10^{-15} m^{-2/3}$ (red) and $C_n^2 = 10^{-14} m^{-2/3}$ (orange).

9.2 Influence of Wavelength and Field Sampling

When turbulence strength increases beyond the weak perturbation regime, phase dislocations and wrapping appear. In addition, scintillation increases creating a strong spatial and temporal variability of the amplitude of the field. An analysis based on a modal decomposition of phase and amplitude does not make sense anymore. It becomes increasingly interesting to drive phase and amplitude by a zonal approach. This paragraph studies the influence of the number of elements that control phase and amplitude for an optimal correction type. In this chapter is presented, on the one hand the influence of electromagnetic field sampling and on the other hand the influence of wavelength. Table 9.1 reminds the reader of the values for σ_R^2 and ρ_0 for the two wavelengths under study in this chapter: $\lambda = 1.5$ µm and $\lambda = 4$ µm.

C_n^2	$10^{-16}\,\mathrm{m}^{-2/3}$	$10^{-15}\,\mathrm{m}^{-2/3}$	$10^{-14}\,\mathrm{m}^{-2/3}$	$7.10^{-14}\,\mathrm{m}^{-2/3}$
σ_R^2 ($\lambda = 1.5$ µm)	0.14	1.4	14	98.6
σ_R^2 ($\lambda = 4$ µm)	0.04	0.45	4.49	31.4
ρ_0 ($\lambda = 1.5$ µm)	14.3 cm	3.6 cm	0.9 cm	0.3 cm
ρ_0 ($\lambda = 4$ µm)	46.3 cm	11.6 cm	2.9 cm	0.9 cm

Table 9.1: Comparison of σ_R^2 and ρ_0 for $\lambda = 1.5$ µm and $\lambda = 4$ µm.

9.2.1 Principle

Figure 9.6 presents a schematic of how the emitted field is calculated from the incoming field by using a finite number of correction elements. It is supposed that a single measurement

element evaluates the mean incident field on its surface. We will later show a justification of this hypothesis. In our explanation we go here from a pupil with $N = 16$ correcting elements to $N = 4$. From a practical point of view, in order to under-sample the number of elements in

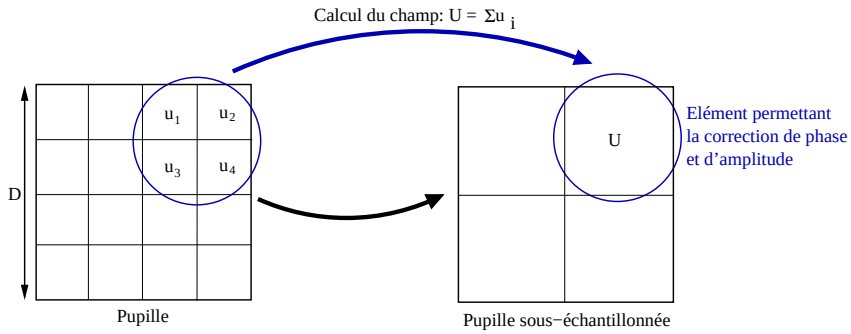

Figure 9.6: Schematic for calculating field in the pupil after correction.

the pupil (i.e. compared to a perfect optimal correction), we calculate the mean field U from the sum of the fields u_i in the initial pupil:

$$U = \sum_{i=0}^{n} u_i$$

Every emitting element is supposed capable of emitting a spatially uniform field on its surface. Phase and amplitude of this field is calculated from phase and amplitude over the same surface element. The size of the pupil D stays the same in the process. Without loss of generality a square pupil is used in this study.

9.2.2 Performance Function of Sampling

We first concentrate on performance at $\lambda = 1.5$ µm. Figure 9.9 presents mean PIB evolution (left part of the figure) and intensity fluctuations (right part) as a function of the number of actuation points N controlling both phase and amplitude of the emitted field. The square pupil has sides of approximately $D = 23.5$ cm. From figure 6.8 showing correction quality function of pupil size, the chosen D enables us be in a regime beyond $L_F = \sqrt{\lambda L} = 12$ cm. L_F has been identified as the minimal dimension that can be used to establish a propagation mode in weak perturbations regime. It is obvious that increasing N will help improving correction quality for both studied metrics: mean PIB and intensity fluctuations. From a particular number of elements N_{sat} correction quality saturates. The saturation seems to arrive earlier for mean PIB than for fluctuations. In fact, for intensity fluctuations the plateau does not seems related to turbulence strength. It is reached for approximately twenty actuators. The weaker the turbulence the smaller the number of elements N is required to reach saturation of the correction quality. This can be explained by the fact that ρ_0 increases as C_n^2 decreases. It is therefore possible to relax spatial sampling constrains.

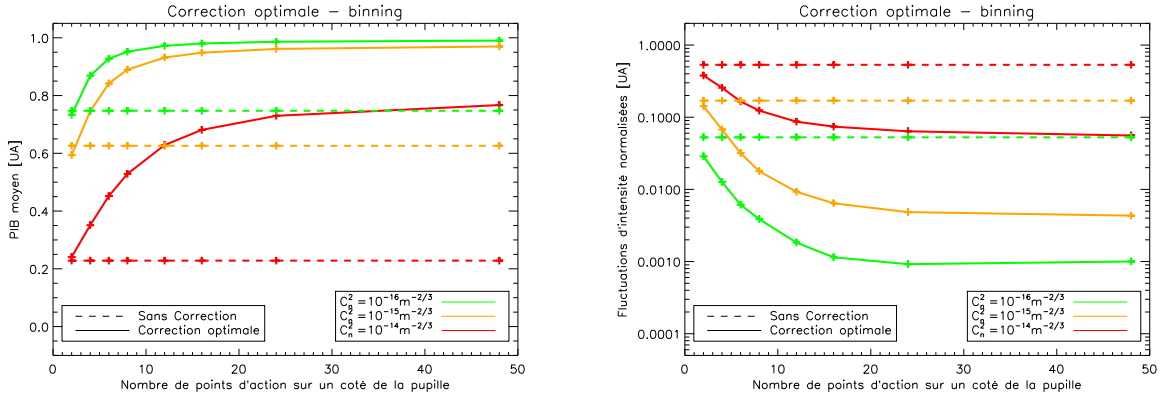

Figure 9.7: Mean PIB (left) and intensity fluctuations evolution (right) function of the number of correction elements and turbulence strength. $D = 23.5\,\text{cm}$.

In figure 9.8 is evaluated the ratio between mean intensity as a function of N over the mean intensity for an infinite number of elements N $\frac{\langle I\rangle(N)}{\langle I\rangle(N=\infty)}$ (left hand side), and the ratio $\frac{\frac{\sigma_I}{\langle I\rangle}(N)}{\frac{\sigma_I}{\langle I\rangle}(N=\infty)}$ (right hand side) for intensity fluctuations. These ratios can be linked to the loss due to pupil sampling.

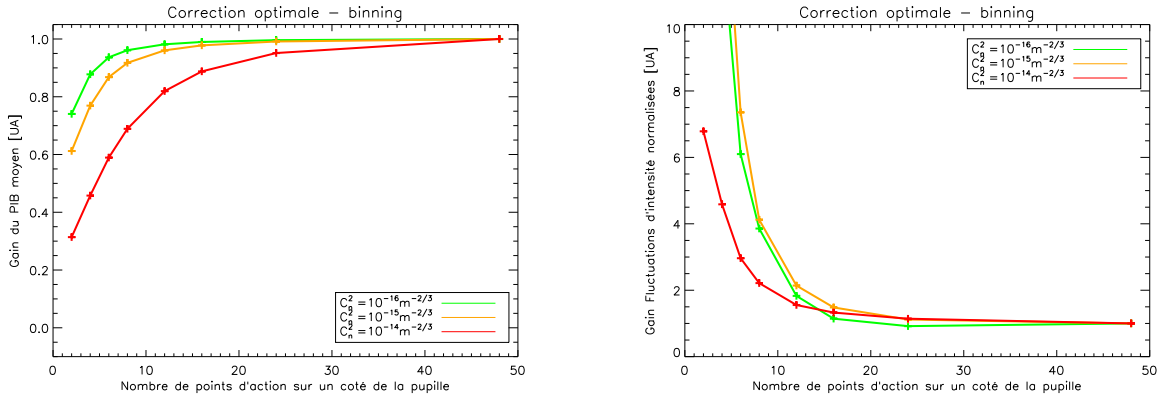

Figure 9.8: Mean PIB Evolution (left) and intensity fluctuations (right) as a function of the number of correction elements and turbulence strength.

Table 9.2 recalls $\frac{D}{\rho_0}$ values for the different turbulence strengths studied and indicates the necessary number of correction elements to achieve mean intensity and intensity fluctuation saturation.

We can observe that for $N \propto \left(\frac{D}{\rho_0}\right)^2$ (where N is the number of correction elements), we cannot reach the same performance levels for the three studied turbulence strengths. In fact, the

C_n^2	$10^{-16}\,\mathrm{m}^{-2/3}$	$10^{-15}\,\mathrm{m}^{-2/3}$	$10^{-14}\,\mathrm{m}^{-2/3}$
$\frac{D}{\rho_0}$	1.6	6.5	26
N_{sat} on intensity	16×16	24×24	$> 48 \times 48$
N_{sat} on fluctuations	24×24	24×24	24×24

Table 9.2: $\frac{D}{\rho_0}$ values for $\lambda = 1.5$ µm and $D = 23.5$ cm function of turbulence strength and the necessary number of correction elements required to reach saturation levels.

calculated values for $N = \left(\frac{D}{\rho_0}\right)^2$ are not enough the reach saturation level neither for $\langle I \rangle$ nor for fluctuations. This indicates that the sampling estimation cannot be evaluated from this quantity. Performance evaluation by numerical simulation means is essential. We remind the reader that dimensioning an adaptive optics systems with ρ_0 value is only valid for the first iteration step. Each successive field correction step modifies both phase and amplitude perturbations statistics. As a consequence, it changes the number of required correction elements.

Figure 9.9 presents mean intensity and intensity fluctuations as a function of iteration number between both ends of the optical link. It enables us to illustrate correction effectiveness for different numbers of correction elements. Convergence seems to be reached for a limited number of iterations (< 5). Only cases with a large degree of freedom take slightly longer to converge. Limiting the number of correction elements has the double advantage to make the correction easier and reduce the convergence time of the iterative process.

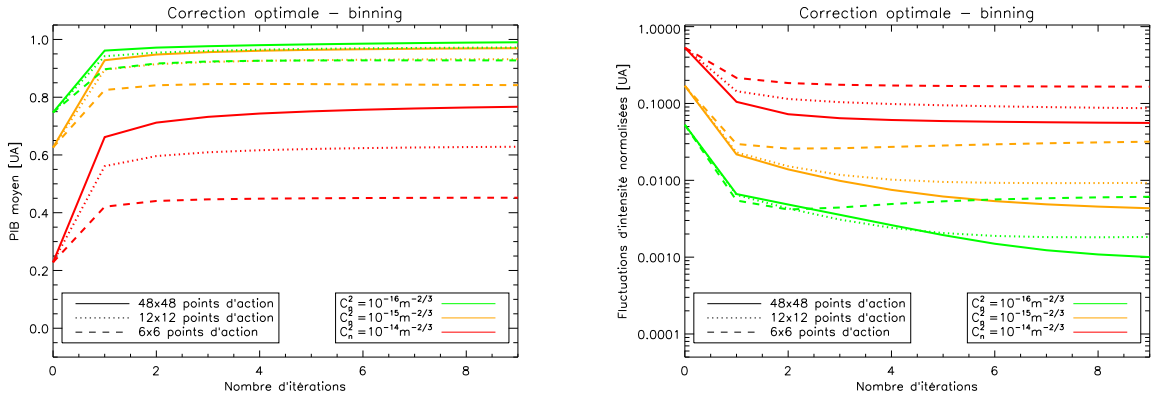

Figure 9.9: Mean PIB (left) and intensity fluctuations (right) function of the number of iteration, turbulence strength and phase and amplitude action points.

In order to reach an acceptable performance level, we need to limit intensity fluctuations to $\frac{\sigma_I}{\langle I \rangle} < 0.1$ for all turbulence strengths. In the studied cases, it means using a system with at least $N = 10 \times 10$ correction elements. This configuration leads to a mean intensity level of $\langle I \rangle \simeq 0.55$ for the worst case scenario.

9.2.3 Influence of Wavelength on Optimal Correction

In chapter 6.1 we have studied the optimal correction for a wavelength of $\lambda = 1.5$ µm. This wavelength corresponds to an atmospheric window and is a wavelength typically used in telecommunications. We have studied the influence of pupil diameter and turbulence strength. Mid-infrared $3 < \lambda < 5$ µm is generally considered as an atmospheric window with low attenuation. In addition, increasing the wavelength reduces the impact of turbulence. However, the actual gain obtained by using a $\lambda = 4$ µm wavelength is still to be quantified.

Despite its benifits, it is still to be understood how results obtained at $\lambda = 1.5$ µm can be translated to $\lambda = 4$ µm. Since wavelength is different, the influence of diffraction will also be different. System parameters (pupil size, reachable propagation distance, beam diameter) will be modified. In addition, implementation of FSO communication systems for $\lambda = 4$ µm still poses technological issues (laser source, matrix detector). The question we ask ourselves in this paragraph is that of the theoretical gain brought by changing the wavelength to a longer one.

9.2.3.1 Impact of Turbulence Strength

In this chapter the optimal phase and amplitude correction for $\lambda = 4$ µm is studied. We have seen that the initial phase or intensity distribution does not impact the studied metrics (i.e. mean PIB and intensity fluctuations) after convergence. Optimal correction can indeed modify both phase and amplitude of the field. In the following we will the optimum Gaussian parameters found for $\lambda = 1.5$ µm.

Firstly, figure 9.10 studies the evolution of $\langle I_i \rangle$ and $\frac{\sigma_{I_i}}{\langle I_i \rangle}$ for four different turbulence strengths and for each iteration step i. The pupil diameter is set to $D = 30$ cm. Final metric values after convergence strongly depend on C_n^2. It can be seen that for weak perturbations (i.e. $C_n^2 = 10^{-16}\,\mathrm{m}^{-2/3}$) optimal correction cannot achieve the maximal PIB. The size of the pupil is too small to enable it. For the three weakest turbulence the optimal correction at $\lambda = 1.5$ µm (see figure 6.6) gives better results than at $\lambda = 4$ µm. However, when turbulence is further increased (i.e. $C_n^2 = 7\ 10^{-14}\,\mathrm{m}^{-2/3}$) correction at $\lambda = 4$ µm achieves a slightly better PIB (i.e $\langle I \rangle = 0.4$ against 0.34 at $\lambda = 1.5$ µm) but still keeping similar intensity fluctuations values.

Residual PIB fluctuations have also been characterised. Regardless of the turbulence regime, a reduction by a factor 4 is observed after 10 iterations. This factor is relatively constant throughout the studied turbulence conditions. Concerning convergence speed, if only one iteration is sufficient for weak perturbations and mean PIB, it appears that larger number of iterations is required for the other cases and in particular for $C_n^2 = 7\ 10^{-14}\,\mathrm{m}^{-2/3}$. The same observation can be made for $\lambda = 1.5$ µm, where the required number of iterations for convergence was increasing with turbulence strength. However, the required number of iterations seems slightly smaller than for at $\lambda = 1.5$ µm and for weak turbulence. This relaxes the constrains in terms of bandwidth for the correction system.

9.2.3.2 Impact of Pupil Diameter

It has been observed during the $\lambda = 1.5$ µm study that correction quality depends on pupil size and propagation distance. All other things being equal this will also be dependent on wave-

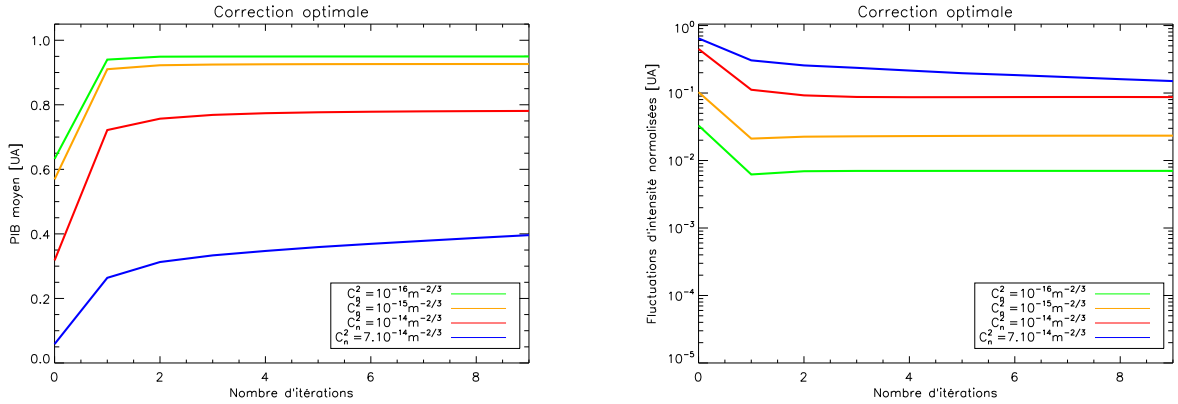

Figure 9.10: Optimal correction efficiency function of the number of iterations. Left: mean PIB, right: normalised intensity fluctuations. Propagation distance 10 km, $\lambda = 4$ µm. Green: $C_n^2 = 10^{-16}\,\mathrm{m}^{-2/3}$, orange: $C_n^2 = 10^{-15}\,\mathrm{m}^{-2/3}$, red: $C_n^2 = 10^{-14}\,\mathrm{m}^{-2/3}$ and blue: $C_n^2 = 7\ 10^{-14}\,\mathrm{m}^{-2/3}$. $D = 30$ cm.

length. Figure 9.11 shows metrics evolution for different pupil diameters and wavelengths of $\lambda = 4$ µm (top) and $\lambda = 1.5$ µm (bottom). It is reminded that the characteristic parameter $L_F = \sqrt{\lambda L} = 20$ cm at $\lambda = 4$ µm ($L_F = 12$ cm at $\lambda = 1.5$ µm) had been identified as the parameter defining the minimal pupil size. This is the reason the propagation mode appears for a larger telescope diameter in the diffractive cases (weak perturbations $C_n^2 = 10^{-16}\,\mathrm{m}^{-2/3}$ and $C_n^2 = 10^{-15}\,\mathrm{m}^{-2/3}$) for $\lambda = 4$ µm than for $\lambda = 1.5$ µm. As previously, it can be observed that from $D = 2L_F$ the correction in terms of PIB is near perfect. Beyond these values the reduction in terms of intensity fluctuations is however still important.

For strong turbulence (i.e $\sigma_R^2 = 4.5$ and $\sigma_R^2 = 31.4$) L_F is replaced by the ratio $\frac{\lambda L}{\pi \rho_0} \propto L^{8/5}\lambda^{-1/5}$. This ratio is not strongly dependent on wavelength but is strongly dependent propagation distance. A strong improvement for these turbulent conditions is not expected in terms of PIB with a constant D by increase the wavelength. Only the case with $C_n^2 = 7\ 10^{-14}\,\mathrm{m}^{-2/3}$ sees a slight improvement in PIB. On the other side, saturation appears much latter because σ_R^2 depends on wavelength. Increasing wavelength reduced fluctuations without any correction. After optimal correction both wavelength seem to give the same correction quality in terms of residual fluctuations and for strong turbulence.

9.2.3.3 Density Probability

Figure 9.12 puts forward the PDF evolution for different pupil sizes, turbulence conditions and with or without correction. Results obtained for $\lambda = 4$ µm are presented without correction (upper part of the figure) and with optimal correction (lower part). PDF is presented for two pupil diameters: $D = 30$ cm (left) and $D = 40$ cm (right).

By comparing these results to those obtained figure 6.10 for a $D = 30$ cm telescope diameter

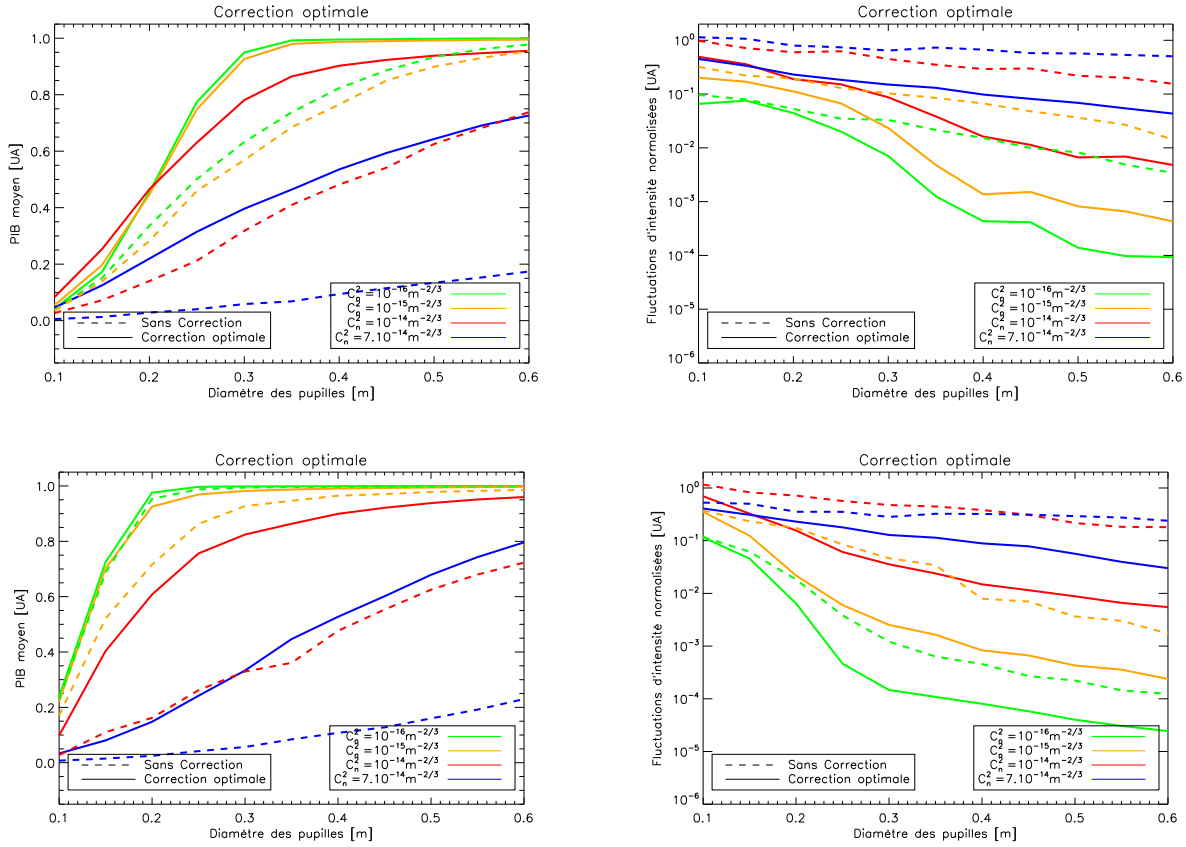

Figure 9.11: Optimal correction efficiency for various telescope diameter, turbulence strength and wavelengths. Solid lines: optimal correction, dashed: no correction. Left: PIB, right: normalised intensity fluctuations. Propagation distance 10 km with $\lambda = 4$ µm (top) and $\lambda = 1.5$ µm (bottom). Green: $C_n^2 = 10^{-16}\,\mathrm{m}^{-2/3}$, orange: $C_n^2 = 10^{-15}\,\mathrm{m}^{-2/3}$, red: $C_n^2 = 10^{-14}\,\mathrm{m}^{-2/3}$ and blue: $C_n^2 = 7\ 10^{-14}\,\mathrm{m}^{-2/3}$.

and $\lambda = 1.5$ µm wavelength, it seems that no improvement is expected by increase the wavelength. Only for very strong turbulence perturbations can the improvement brought by increasing the wavelength be seen.

9.2.3.4 Impact of Sampling

For a constant telescope diameter and propagation distance increasing the wavelength does not seem to improve performance. However, the importance of going up to $\lambda = 4$ µm does not only lie in efficiency improvement but also in reducing constrains in the implementation of the AO system. Figure 9.13 presents the sampling influence on optimal correction performance. In order to compare the results to the $\lambda = 1.5$ µm case we choose a square pupil of $D = 23.5$ cm of side. Unfortunately, this size is too small to reach intensity fluctuations lower than 0.1 for

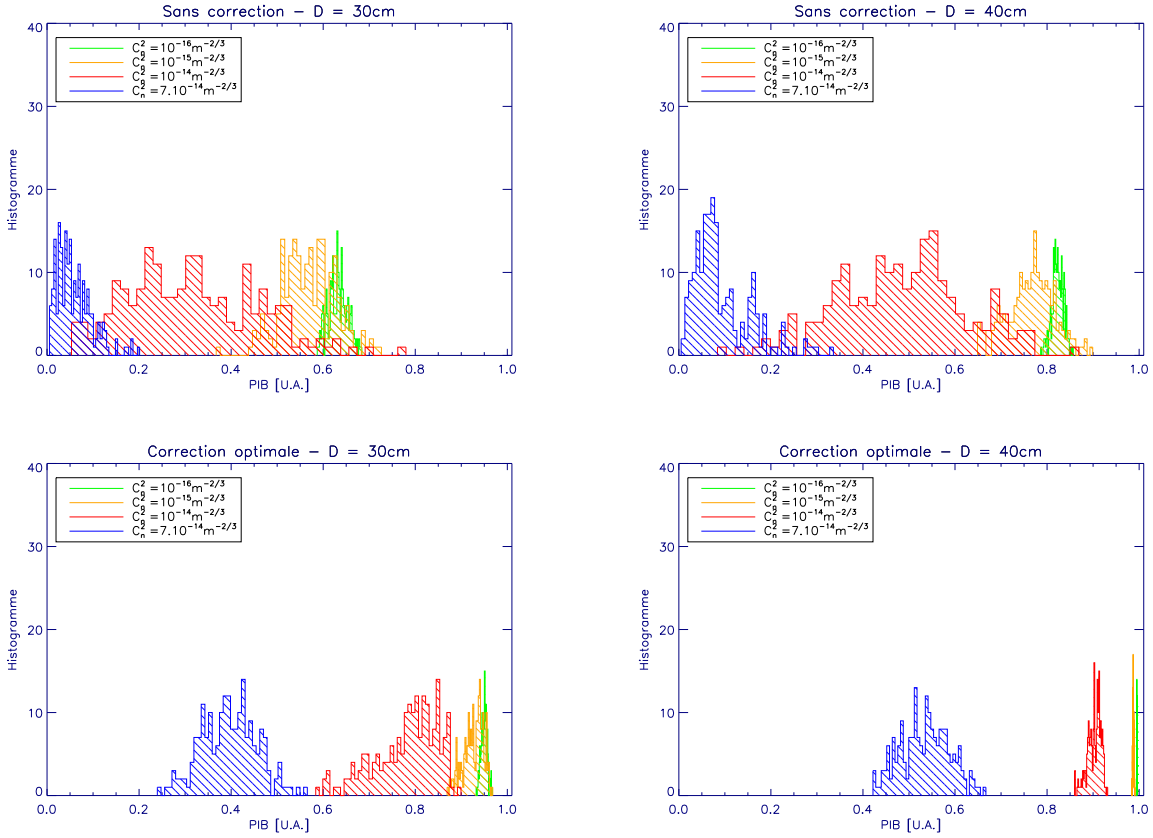

Figure 9.12: Probability density function changes for different pupil sizes, turbulence and correction. Top: no correction, bottom: optimal correction. Pupil diameter $D = 30\,\text{cm}$ (left) and $D = 40\,\text{cm}$ (rigth). Propagation distance $10\,\text{km}$, wavelength $\lambda = 4\ \mu\text{m}$.

$C_n^2 = 10^{-14}\,\text{m}^{-2/3}$. However, intensity fluctuations saturation arrives clearly before: $N_{sat} = 6$ regardless of the turbulence strength.

The small optics (i.e a $D = 23.5\,\text{cm}$ pupil) prevent the correction of reaching the required level of $\frac{\sigma_I}{\langle I \rangle} < 0.1$. Figure 9.14 presents the impact of optimal correction for different spatial sampling and for a diameter of $D \simeq 49\,\text{cm}$. The implementation difficulty brought by the use of a larger telescope is compensated by an important reduction in the number of required correction elements. In fact, only $N = 8 \times 8$ correction points are required to go from $\frac{\sigma_I}{\langle I \rangle} < 0.32$ to $\frac{\sigma_I}{\langle I \rangle} < 0.06$. If the desired limit is set to $\frac{\sigma_I}{\langle I \rangle} = 0.1$ only a $N = 5 \times 5$ system is sufficient. We remind the obtained results for $\lambda = 1.5\ \mu\text{m}$ helped us define $N = 10 \times 10$ correction element as the minimum to reach this value. Using a 5×5 correction system increases the mean intensity up to $\langle I \rangle \simeq 0.65$. The value before correction is $\langle I \rangle = 0.51$. The mean intensity value with correction is slightly larger than for $\lambda = 1.5\ \mu\text{m}$ where the value was $\langle I \rangle = 0.60$.

When wavelength is increased from $\lambda = 1.5\ \mu\text{m}$ to $\lambda = 4\ \mu\text{m}$, N goes from approximately one hundred elements to twenty five, or a factor 4. We remind that when changing wavelengths

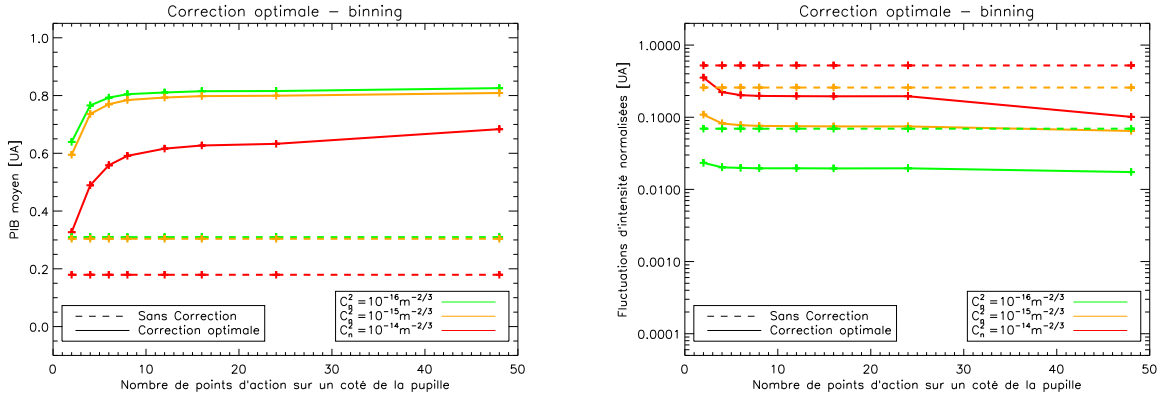

Figure 9.13: Mean PIB evolution (left) and fluctuations (right) function of number of phase and amplitude correction elements and turbulence strength. Square pupil $D = 23.5\,\text{cm}$ and $\lambda = 4$ µm.

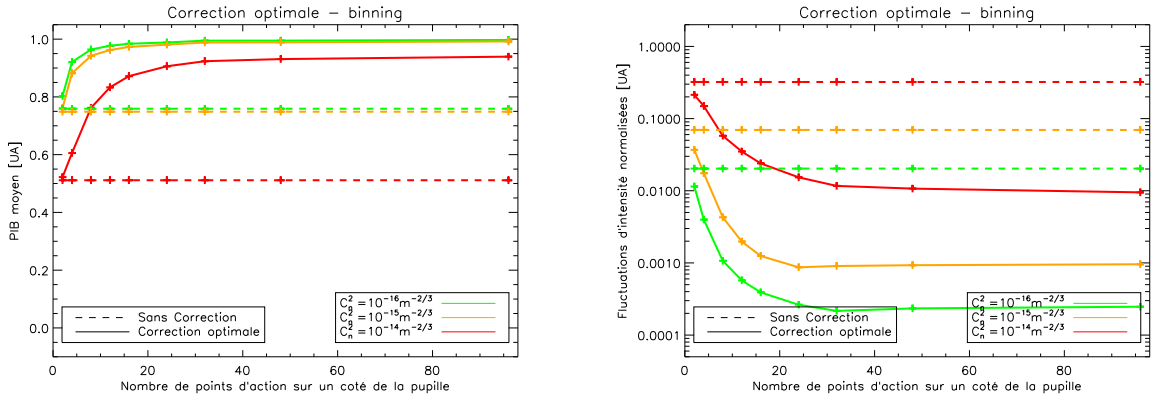

Figure 9.14: Mean PIB (left) and fluctuations (right) function of phase and amplitude correcting elements and turbulence strength. Square pupil $D \simeq 49\,\text{cm}$ and $\lambda = 4$ µm.

$\left(\frac{D}{\rho_0}\right)^2$ is divided by a factor 9. The elementary surface of correction between a $\lambda = 1.5$ µm and a $\lambda = 4$ µm correction is only divided by 4. Even if the pupil sizes are not identical for both cases, it can be observed that ρ_0 is not the scaling factor for the number of elements. In addition, it cannot be used to justify the reduction in N by changing the wavelength. Even if ρ_0 seems an appropriated scaling parameter without any correction, it completely losses interest when implementing an optimal iterative correction.

Figure 9.15 presents the change in mean intensity and intensity fluctuations as a function of the number of iterations between the two extremities of the link. Convergence seems reached after only a limited number of iterations (< 5). Only the case of large degrees of freedom takes

slightly longer. The behaviour is similar for both wavelengths studied.

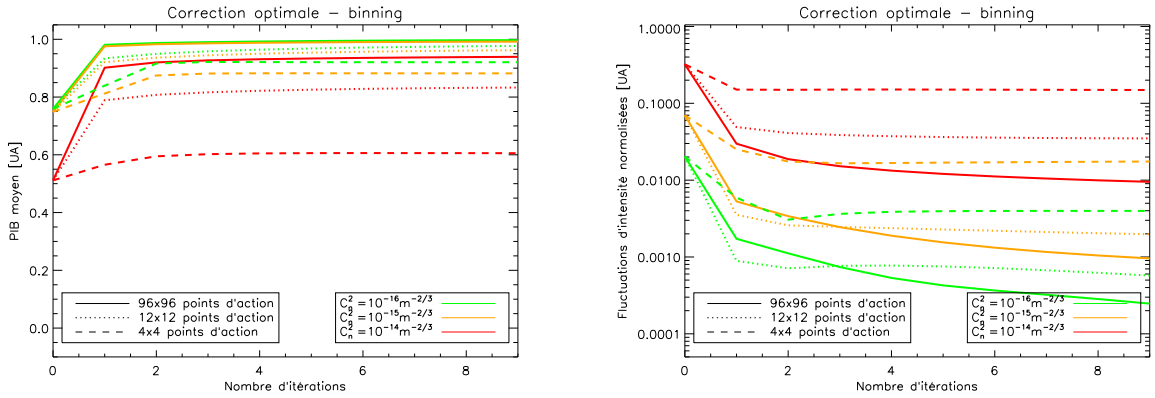

Figure 9.15: Mean PIB (left) and intensity fluctuations (right) changes as a function of the number of iteration, turbulence strength and number of phase and amplitude action points. Square pupil with $D \simeq 49\,\text{cm}$ and $\lambda = 4$ µm.

9.2.4 Conclusion

In the previous paragraphs the influence of wavelength on optimal correction was presented. We has seen that the scaling parameter $\sqrt{\lambda L}$, increased with increasing wavelength, requiring an increase in telescope diameter in order to maintain performance obtained at $\lambda = 1.5$ µm. Despite the negative impact related to diffraction, a study of the required number of correction elements shows a strong reduction for the longer wavelength. Changing wavelength helps us to divide the number of elements by a factor 4 by only doubling the optics size D. It goes from $N = 100$ correcting elements at $\lambda = 1.5$ µm to only $N = 25$ at $\lambda = 4$ µm. ρ_0 can no longer be considered as a scaling parameter for the number of actuation point for an iterative optimal correction.

9.3 Iterative Conjugation by Injection into a Waveguide

We are investigating means of measuring phase and amplitude on an incoming wave. In addition, we are also interested in creating a wave resulting from a finite sum of spatial modes than can be controlled both in phase and in amplitude in order to re-emit a conjugated wave. Most of existing systems (deformable mirrors, liquid crystals, and electro-optical systems) can only control the phase part of the spatial mode. In parallel, it is possible to control their amplitude by attenuation devices. Let the intensity $|E_0|^2$ be defined as the quadratic sum of the n modes' amplitudes: $|E_0|^2 = \sum_{i=1}^{n} |E_i|^2$. The device described in the following text can modulate phase and amplitude of each mode of beam without affecting the total intensity of the beam. The optical power is therefore not modified. We will later see how this device can be used to measure phase and amplitude of the incoming beam.

9.3.1 Correction Principle

The problem is similar to the duplication of a unique mode with total control over phase and amplitude of each of the duplicated modes. The total intensity is kept unchanged. Figure 9.16 shows the device used to split the initial beam E_0 into two beams E_1 and E_2. The two beams can be controlled in phase and amplitude by means of three dephasing elements (φ_0, φ_1 and φ_2). The three phase-shifting elements control the phase of the beams in an absolute fashion. Only two phase-shifting elements are needed if one only needs to control the relative phase which is only the differential phase between the beams. Only phase-shift φ_0 and φ_1 (or φ_2) are useful in this case. The phase-shifting element φ_0 is used to control the energy distribution between E_1 and E_2. This system verify energy conservation: $|E_1|^2 + |E_2|^2 = |E_0|^2$

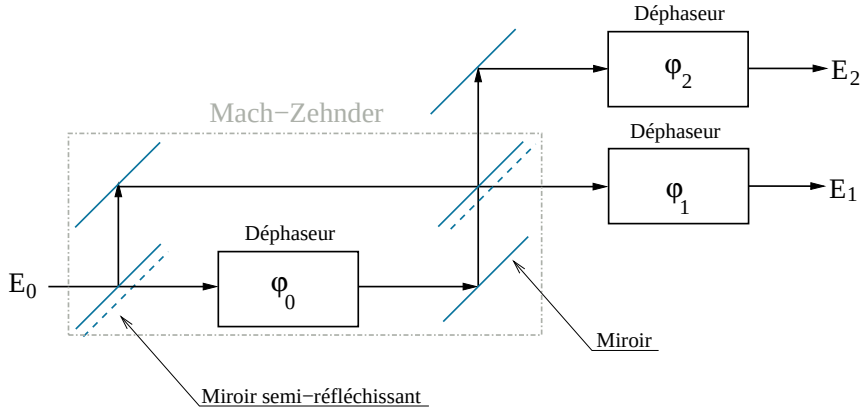

Figure 9.16: Diagram of the phase and amplitude control of two complex fields from a single coherent source.

It is equally possible to recombine E_1 and E_2 in order to create field E_0. If one needs to drive n complex amplitude beams, it is not possible to recombine them two-by-two because all beams much interfere. We propose to put these elements in cascade in order to realise this function. Figure 9.17 shows the implementation diagram based on elements presented figure 9.16. Each elementary function is depicted as a rectangle used to divide the beam in two beams controlled in phase and amplitude. By using this device a de-multiplexing device is realised and a unique beam is split into several beams. By reversal of the light path and by using the same device a combination system can be realised.

When phases and amplitudes are known (by using the de-multiplexing device) the phase-shift estimation to be applied is simple because based on a direct model perfectly known. In its principle the resolution relies on the knowledge of the amplitudes. Theses amplitudes give directly access to the phase-shifts by reasoning by levels (i.e. elementary function). Estimation of the other values is then straightforward. When phases and amplitudes are unknown, when used in recombination mode, one must add measurements to estimate the phase-shifts to apply. Spatial and temporal modulation techniques can be used and/or combined to realise this measurement. It can be realised on the final re-combined beam or the recombined beams at each level. If n beams

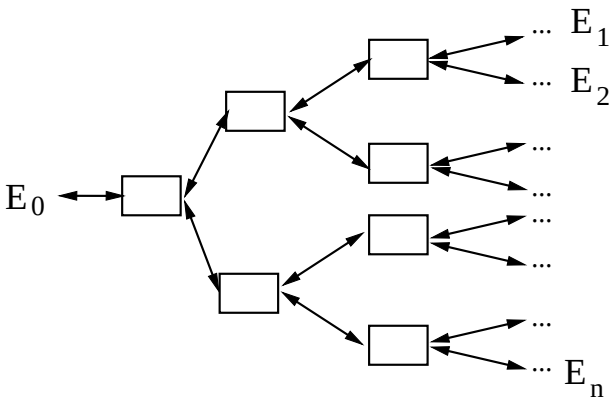

Figure 9.17: Diagram of the phase and amplitude control of n complex fields from a single coherent source. Each rectangle represents an elementary function presented figure 9.16.

need to be controlled in phase and amplitude, $n-1$ basic functions are required. Therefore, in order to drive one hundred modes we will typical need one hundred elementary systems. This relatively high value is a justification for studying integrated optics implementation strategies.

In the framework of FSO pre-compensation, the system described above is a practical implementation of the iterative phase and amplitude correction [Barchers-a-01-a, Barchers-a-01-b]. The proposed configuration is symmetrical, meaning that emission and reception are identical. Reception plane (resp. emission) is spatially sampled by a lenslet matrix (see figure 9.18). The field is focalised after each lenslet into a monomode optical fibre. The fibres are coupled to system described above. In re-combination mode it is used to measure phase and amplitude. In reverse, it is used to emit a phase conjugated wave.

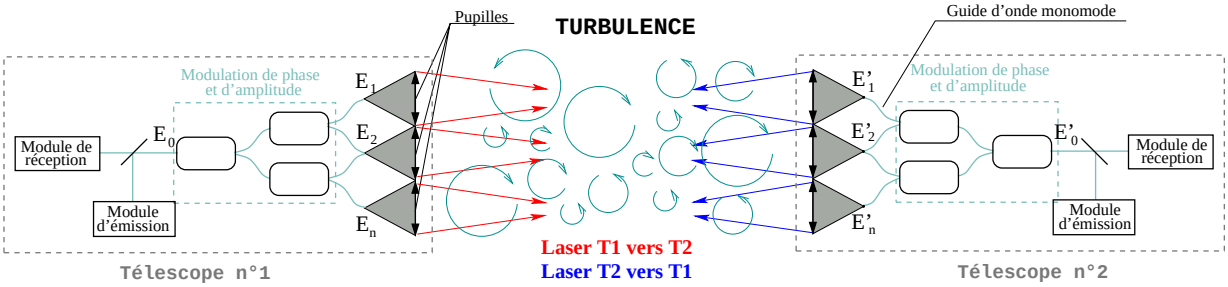

Figure 9.18: Diagram of phase and amplitude correction realised by injecting into monomode fibre optics.

9.3.2 Injection into a Single-Mode Waveguide

In ordre to realise the elementary function presented previously, one must inject the received wave into a finite number of single-mode optical fibres at reception. For example, we place

ourselves in the case where single-mode fibres are used. A single-mode fibre is a spatial filter selecting the part of the incoming field equal to its eigenmode. References for single-mode fibre injection are found in Ruillier and Cassaing [Ruillier-a-01]. Let $M_0(r)$ be the normalised single-mode fibre mode in the pupil plane ($\|M_0\| = 1$). The scalar product corresponds to:

$$\langle X|Y\rangle \triangleq \frac{\int\int X(r).Y^*(r).P_0(r)dr}{\int\int P_0(r)dr}, \tag{9.1}$$

and the norm:

$$\langle X\rangle \triangleq \langle X|1\rangle \tag{9.2}$$

$$\|X\| \triangleq \sqrt{\langle X|X\rangle}, \tag{9.3}$$

where P_0 is the pupil transmittance. A single-mode fibre only transmits the energy from the incoming field E corresponding to its eigenmode. Coupling efficiency is given by [Ruillier-a-01]:

$$\Omega(E) = \frac{\langle E|M_0\rangle}{||E||} \tag{9.4}$$

From Ruillier [Ruillier-a-01], the Gaussian mode that optimises coupling coefficient can couple approximately 80% of the energy of E. The fibre mode chosen is therefore a Gaussain beam where approximately 80% of the energy is transmitted through the lenses composing the matrix.

The measured amplitude and phase will be used to make the correction. The correction field $E'' = conj(E') = A * \Omega^* * M_0$ is simply the complex conjugate that will be propagated in reverse direction. Defocalisation due to propagation of the Gaussian fibre-mode M_0 is neglected between the fibre exit and the emitting lens.

9.3.3 Numerical Simulation Conditions

Firstly, we present numerical simulation results for a lenslet distribution as shown figure 9.19. Emission and reception pupils of diameter D are considered to be sampled by lenses of diameter d adjacent to each other.

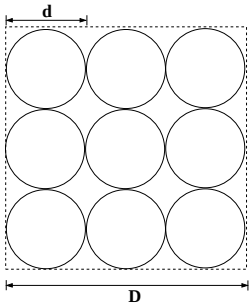

Figure 9.19: Pupil configuration.

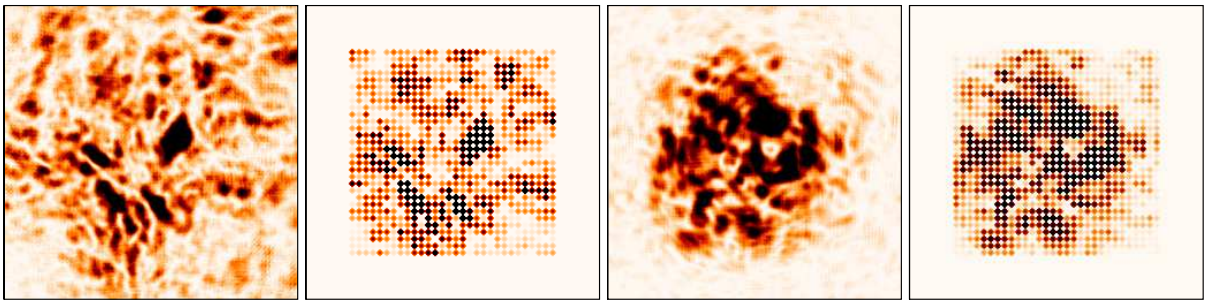

Figure 9.20: Illustration of received intensity distribution in the reception pupil plane after propagatioN and with and without correction; $C_n^2 = 10^{-14}\,\mathrm{m}^{-2/3}$.

Figure 9.20 represents a single realisation for the intensity distribution in the reception pupil plane after propagation without any correction (images on the left) and with correction (the two images on the right). Illustrations represent on the one side intensity distribution in reception plane and on the other the same distribution after injection into a matrix of fibres. Turbulence strength is set to $C_n^2 = 10^{-14}\,\mathrm{m}^{-2/3}$ and the individual pupil diameters to $d = 1\,\mathrm{cm}$ with a wavelength of $\lambda = 1.5$ µm and a propagation distance of $L = 10\,\mathrm{km}$. For this particular turbulence distribution, the total collected intensity without correction is $I_0 = 16.8\%$ and goes up to $I_3 = 33.1\%$ after correction (4 iterations). In spite of the low level of received intensity (limited surface, limited filling factor in both emission and reception pupils) a 92% increase in the collected intensity is obtained after only 4 iterations.

9.3.4 Performance Without Turbulence

In this study, we will use different sizes d for lenslets and different pupil sizes D. First, we will look at performance in the absence of turbulence. Figure 9.21 represents numerical simulation results for various pupil configurations without atmospheric turbulence. It can be observed that integrated intensity remains small in spite of the increase of pupil diameter D. However, correction gain is clearly visible when comparing results to the uncorrected case with the exception of $D = 10\,\mathrm{cm}$ where correction does not help improving quality. This low value of means PIB comes from various factors such as filling factor and fibre injection. Firstly, the chosen pupil geometry leads to a factor $\frac{\pi}{4}$ reduction when compared to a full square pupil (geometrical losses). Secondly, the empty spaces in the reception pupil create interferences such that part of the energy is ejected outside the pupil after propagation over a long distance (diffraction losses). After a long propagation distance, the energy contained the secondary lobes increases. Finally, injection into the single-mode fibre optics creates another loss (injection losses, see paragraph 9.3.2). We remind the reader that injection losses are of the order of 20%. Geometrical and diffractive losses can be in part compensated by a correction; however its gain is hard to evaluate because depending on turbulence strength.

Besides the above mentioned losses, an additional loss is observed for $D = 20\,\mathrm{cm}$ and $D = 30\,\mathrm{cm}$ when the diameter d is reduced from $2\,\mathrm{cm}$ to $1\,\mathrm{cm}$. Those losses are due to numerical

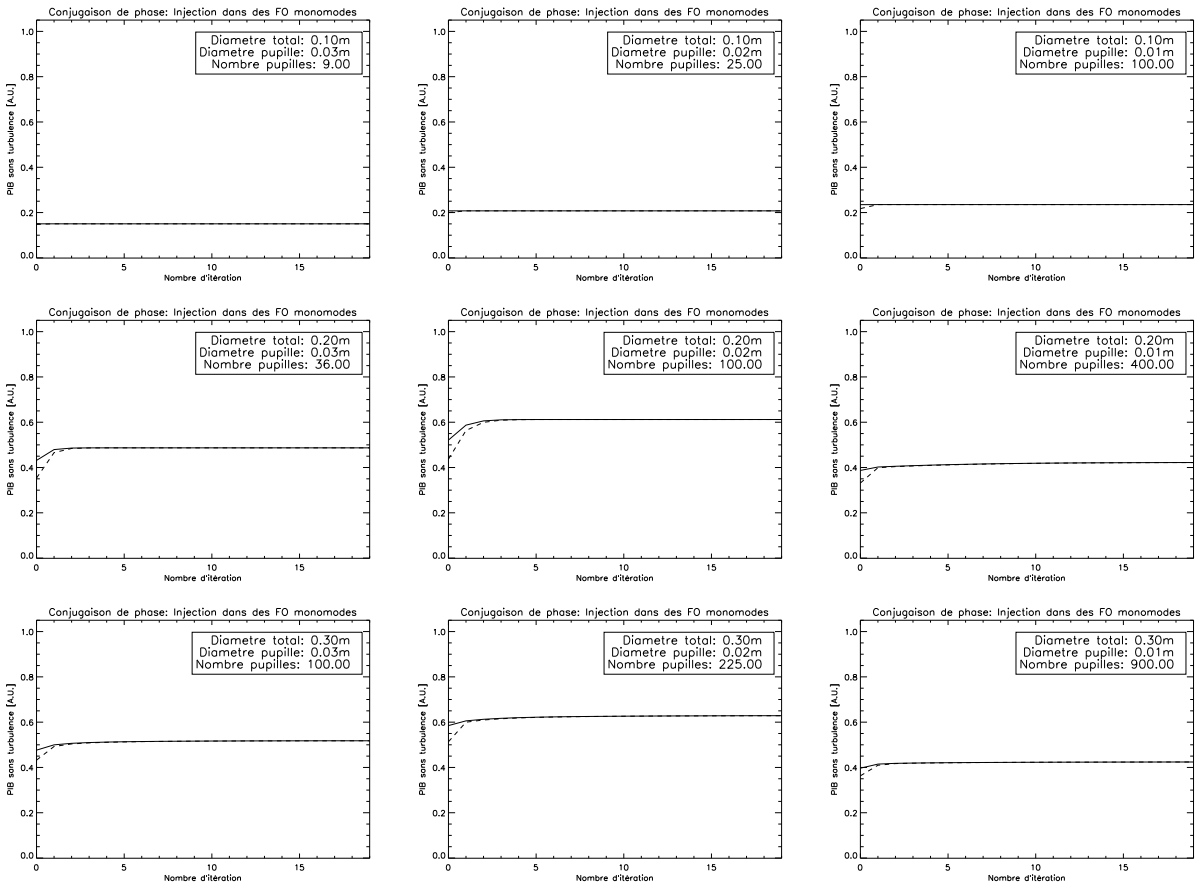

Figure 9.21: Numerical simulation results without turbulence for lenslets of diameter $d = 3\,\text{cm}$ (left), $d = 2\,\text{cm}$ (middle) and $d = 1\,\text{cm}$ (right). Pupil diameter D is $D \simeq 10\,\text{cm}$ (top), $D \simeq 20\,\text{cm}$ (middle) and $D = 30\,\text{cm}$ (bottom). Solid lines represent reception and dashed lines emission. Wavelength $\lambda = 1.5$ µm and propagation distance $L = 10\,\text{km}$.

issues related to aliasing. In fact, during emission the pupil acts as a grating. For a linear plane diffraction grating of step p and slit width a, the diffracted intensity at a point x in the Fraunhofer approximation is given by:

$$I \propto sinc^2\left(\frac{\pi X a}{\lambda L}\right)\left(\frac{sin\left(\frac{N\pi X p}{\lambda L}\right)}{sin\left(\frac{\pi X p}{\lambda L}\right)}\right)^2, \tag{9.5}$$

Where N in the number of slits and L the propagation distance. As a result, the smaller the pupil diameter d the more the secondary lobes will be far for the optical axis. These secondary lobes will therefore be more likely to be aliased for smaller diameter d. Figure 9.22 shows the diffraction pattern of a linear plan grating for a propagation distance of $L = 10\,\text{km}$ calculated form equation 9.5.

Unfortunately, the propagation model using turbulent phase screens (of finite dimension) that

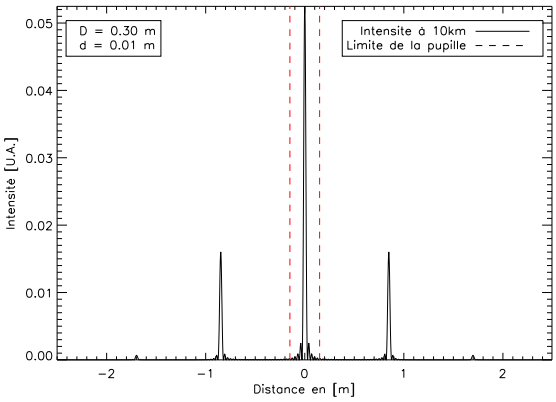

Figure 9.22: Diffraction pattern of a linear plan grating for a propagation distance of $L = 10\,\text{km}$ with $a = 1\,\text{cm}$, $p = 1.25\,\text{cm}$ and $N = 30$.

are used in simulation create aliasing. As a result, numerical simulations lead to a different diffraction pattern for a pupil $D = 30\,\text{cm}$ with $d = 1\,\text{cm}$ than the one presented figure 9.22. In addition, Fresnel formalism is used for propagation which also slightly modifies the diffraction pattern. Figure 9.23 presents on the one side intensity distribution (on the left-hand side) after a $L = 10\,\text{km}$ propagation and cut going through the optical axis (right-hand side). We can see

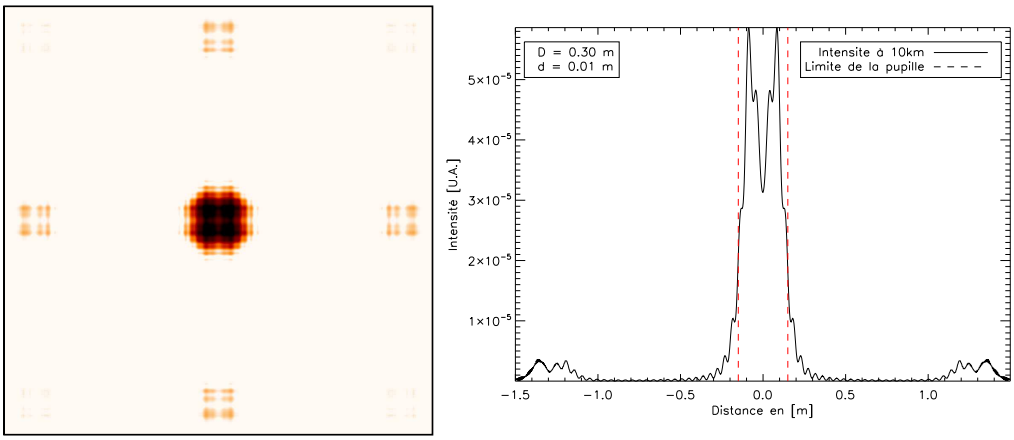

Figure 9.23: Left: intensity distribution in reception plane. Right: Intensity distribution cut though the optical axis.

that intensity is lower on the optical axis that next to it. Secondary lobes in this simulation case have been aliased on the optical axis because of digitalisation on a finite grid. The secondary lobes come from a coherent source (the emitted wave) and their phase is opposite to the principal lobe phase. This is the reason, by reasoning in amplitude, that the contribution of the aliased lobes can either be additive or subtractive. For the studied case it is subtractive and the intensity

integrated over the pupil area decreases. On the other hand, the other pupil configuration ($d = 2$ cm and $d = 3$ cm) do not have this issue as the influence of aliasing is weaker for the simulation parameters chosen.

In the absence of turbulence or when it is weak, the emitted wave is strongly coherent. The results obtained are strongly impacted by the negative effects of aliasing. Conversely, for strong turbulence, the emitted wave rapidly losses coherence. Results for strong perturbations will suffer less from aliasing effects. In addition, for the application of interest (i.e. endo-atmospheric long-distance FSOs) only strong perturbations are really of interest.

9.3.5 Impact of the Total Pupil Diameter

In the following paragraph results relating to the influence of pupil size D on correction quality in turbulence are presented. The study was performed with three different spatial sampling diameter d ($d = 1$, 2 and 3 cm), making the number of correcting elements vary. This study is similar to the one presented paragraph 9.2.

9.3.5.1 Impact of Diameter D for $d = 1$ cm

Figure 9.24 shows numerical simulation results for a pupil matrix composed of pupil of $d = 1$ cm in diameter. Three sizes of square pupil D are represented; from top to bottom by increasing size ($D \simeq 10$ cm (upper part of the figure), $D \simeq 20$ cm (central part) and for $D \simeq 30$ cm (lower part)).

As expected, when increasing the global collecting area D the correction quality improves. The difference is clearly visible between $10\,\text{cm} \times 10\,\text{cm}$ and $20\,\text{cm} \times 20\,\text{cm}$. This fact has already been noticed in paragraph 6. When $D \simeq 10$ cm intensity fluctuations stay superior to $\sigma_I / \langle I \rangle = 0.1$ for the least favourable cases. In the following paragraph we will mainly focus on matrices of size $D > 10$ cm. In fact, we have seen that pupils of $D < 10$ cm cannot be used to establish a propagation mode in weak perturbations. From $D = 20$ cm fluctuations are strongly reduced and go below the threshold (i.e. $\frac{\sigma_I}{\langle I \rangle} = 0.1$) whatever the turbulence strength studied.

The left part of figure 9.24 present mean intensity $\langle I \rangle$. For $D \simeq 30$ cm correction helps to improve intensity from $\langle I \rangle = 0.12$ to $\langle I \rangle = 0.34$ after 19 iterations and for $C_n^2 = 10^{-14}\,\text{m}^{-2/3}$. The final value depends on D (even if it can be observed that correction gain is very limited between $D = 20$ cm and $D = 30$ cm for cases $C_n^2 = 10^{-16}\,\text{m}^{-2/3}$ and $C_n^2 = 10^{-15}\,\text{m}^{-2/3}$). In fact, for $D \simeq 20$ cm the improvement brought by the correction creates an improvement from $\langle I \rangle = 0.09$ to $\langle I \rangle = 0.3$ for $C_n^2 = 10^{-14}\,\text{m}^{-2/3}$.

Concerning intensity fluctuations (right-hand side), they are equally dependent on the number of correction elements N. It evolves form $\frac{\sigma_{I_0}}{\langle I_0 \rangle} \approx 0.2$ (resp. $\frac{\sigma_{I_0}}{\langle I_0 \rangle} \approx 0.4$) without correction to $\frac{\sigma_{I_{19}}}{\langle I_{19} \rangle} \approx 0.03$ (resp. $\frac{\sigma_{I_{19}}}{\langle I_{19} \rangle} \approx 0.06$) with correction for $D \simeq 30$ cm (resp. $D \simeq 20$ cm). Even if pupil geometries are slightly different, we approximately encounter the same values obtained previously for perfect optimal correction. In fact, as seen paragraph 9.2.2 when the number of correction elements is greater than $N \approx 20 \times 20$ for a $D = 20$ cm pupil we reach optimal correction values for intensity fluctuations.

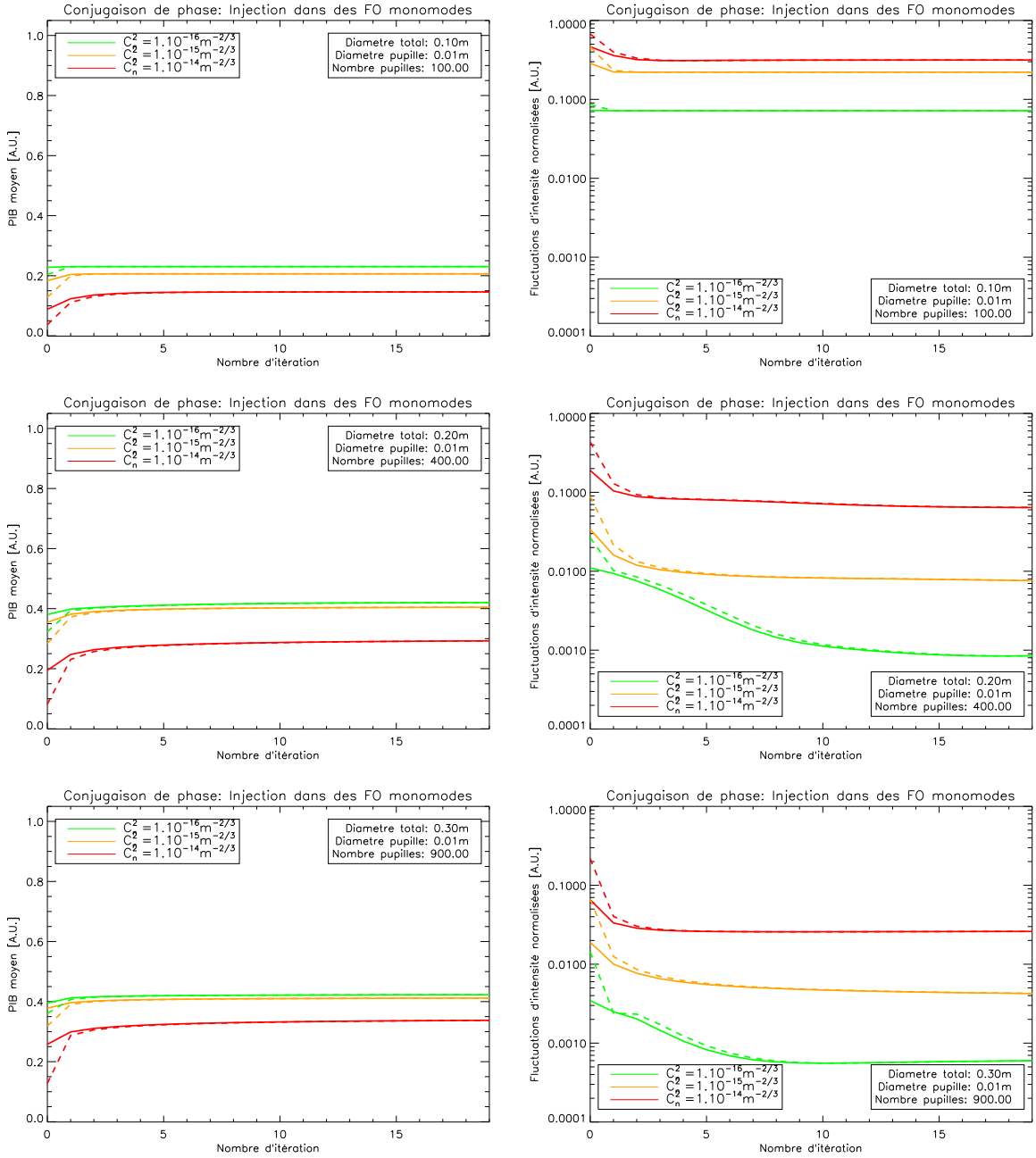

Figure 9.24: Simulation results for a matrix with pupils each of $d = 1$ cm in diameter. Solid lines represent results for telescope $T1$ and dashed lines for $T2$. Wavelength is set to $\lambda = 1.5$ µm and propagation distance to $L = 10$ km.

Convergence speed for mean intensity is high for all studied parameters. Convergence speed for intensity fluctuations depends on turbulence strength and pupil diameter. The stronger the

turbulence the fewer iterations are required. However, above 10 iterations it can be considered that convergence as been reached. The value is reduce (convergence is reached after 5 iterations) when the turbulence strength is increased.

Despite the strong gain, it must be noticed that a large number of fibres is required (approximately 900 for the best correction scenario) which can be a limitation when implementing this solution. We remind that the parameter $\rho_0 = 1$ cm for $C_n^2 = 10^{-14}\,\mathrm{m}^{-2/3}$ which is approximately the size of the pupils d. Perturbations are therefore well sampled. By increasing diameter d we will decrease the useful number of fibres by making the sampling coarser.

9.3.5.2 Impact of Diameter D for $d = 2$ cm

In order to relax constrains related to the high number of elements, figure 9.25 shows numerical simulation results for a matrix where each pupil has a diameter of $d = 2$ cm. Two different sizes of overall collecting areas are studied: $D \simeq 20$ cm (upper curves), $D \simeq 30$ cm (lower curves). Similarly to the 1 cm case, the more we increase the total collecting area the better the correction. For $D = 20$ cm the same results are obtained in terms of normalised intensity fluctuations as in paragraph 9.2 for $N = 100$. We remind that the size of the correcting elements is here of $d = 2$ cm and is identical to the $N = 100$ case presented previously. Oppositely, mean intensity is smaller than the case presented paragraph 9.2 confirming the small impact of the filling ratio on mean intensity (and not fluctuations). The reasoning done on intensity fluctuations with a simplified study (i.e. full square pupil and not fibre injection) is still valid for the present case with a different pupil geometry and taking into account injection in single-mode fibres.

Increasing d from1 cm to 2 cm helps increasing $\langle I \rangle$ but not $\frac{\sigma_I}{\langle I \rangle}$. Increasing the diameter d of the correction elements can relax system constrains. If the goal is set in terms of intensity fluctuations, 100 pupils of $D = 20$ cm with $d = 2$ cm seems sufficient. This is enough to reduce intensity fluctuations from $\frac{\sigma_I}{\langle I \rangle} = 0.3$ to $\frac{\sigma_I}{\langle I \rangle} = 0.1$ in only approximately 5 iterations. In addition, for weak turbulence convergence is reached sooner than for $d = 1$ cm.

9.3.5.3 Impact of Diameter D for $d = 3$ cm

In this paragraph results for lenslets of $d \simeq 3$ cm are presented. It can be observed, even if a $D \simeq 20$ cm pupil is sufficient for $d = 2$ cm, that the required pupil diameter is now $D = 30$ cm. Correction for weak and intermediate turbulence strength cannot reach the correction quality obtained with $d = 2$ cm. The area of the correcting elements being too large it cannot sample the field in the pupil sufficiently, leading to a loss in quality for the two studied metrics. In fact $d > \rho_0$ and the correction on a single correction element is limited to piston only. This approximation is not longer valid for large sizes of d. It can be noticed that the same value is obtained in terms of intensity fluctuations for $D = 20$ cm with $d = 2$ cm and for $D = 30$ cm with $d = 3$ cm. For these two cases, the number elements used for correction is $N = 100$. To a first approximation, it seems that $\frac{\sigma_I}{\langle I \rangle}$ is relatively independant of D but strongly depends on N. This is not the case for $\langle I \rangle$ which depends both on D and on N.

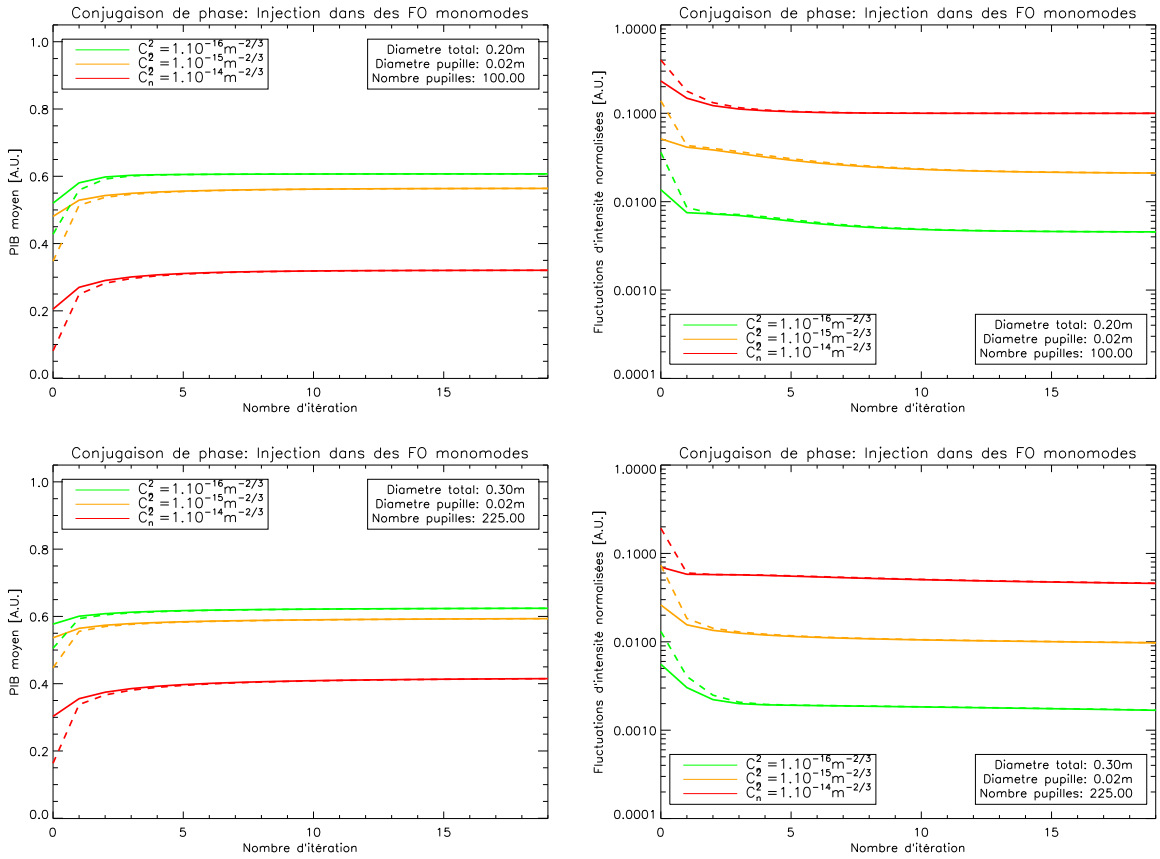

Figure 9.25: Simulation results for a matrix with pupils each of $d = 2$ cm in diameter. Solid lines represent results for telescope $T1$ and dashed lines for $T2$. Wavelength is set to $\lambda = 1.5$ µm and propagation distance to $L = 10$ km.

9.3.5.4 Conclusion

The reduction in mean collected intensity can be much higher than using a full pupil. The maximum mean intensity that one can hope to reach is approximately $\langle I \rangle \simeq 0.63$ (geometrical losses of $\frac{\pi}{4}$ and injection losses of 20%). This is the actual factor found in the best correction cases. In order to improve mean intensity values which have dropped from the perfect optimal case, one must densify the pupil plane. It is possible, for example, to use square lenslets capable of filling the entire aperture surface. However, the optical fibres eigenmode is Gaussian. Changing from a circular geometry to a square geometry will not enable a significant increase except if the eigenmode of the waveguide is square (i.e. the waveguide itself is square). In addition, the drop in $\langle I \rangle$ is not particularly prejudicial as intensity fluctuations are less sensitive to the pupil filling ratio. Moreover, even if mean intensity is an important factor for the BER, the resulting losses are negligible compared to losses produced by atmospheric absorption. Minimising intensity fluctuations is on the other hand of prime importance.

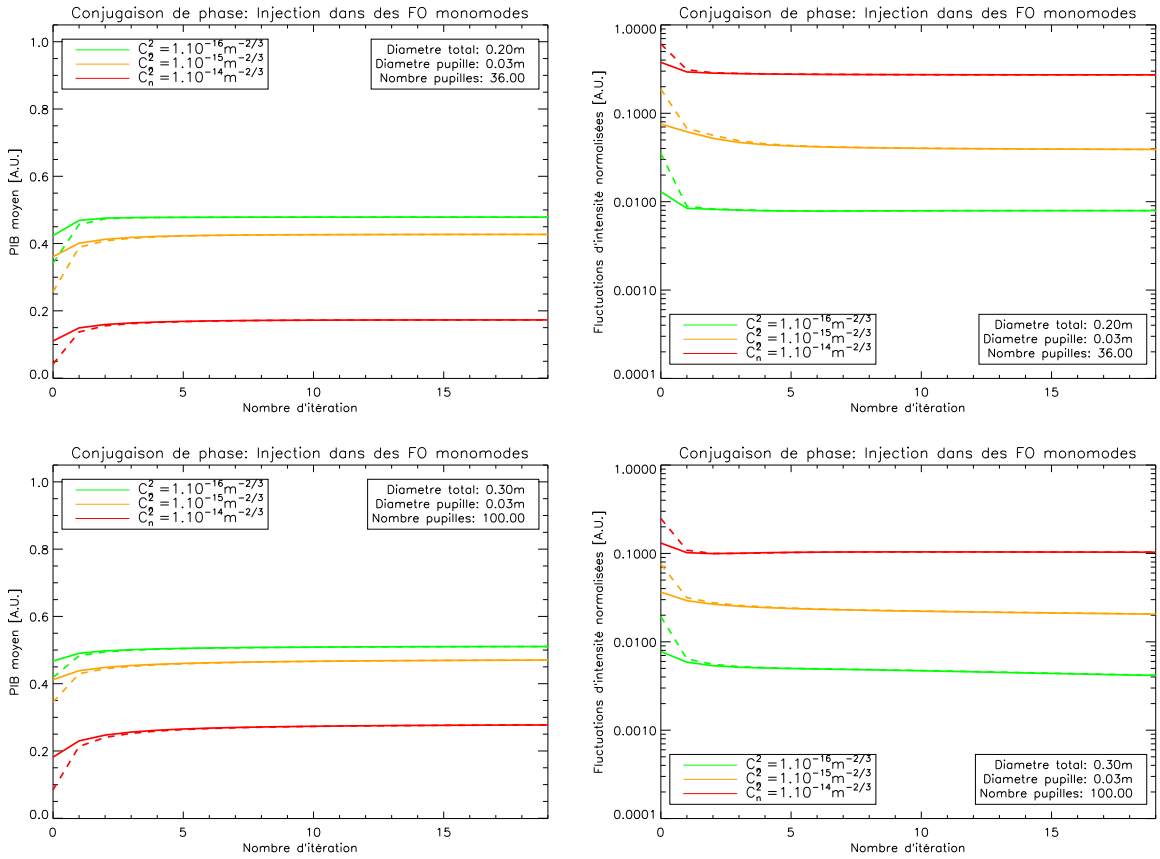

Figure 9.26: Simulation results for a matrix with pupils each of $d = 3\,\text{cm}$ in diameter. Solid lines represent results for telescope $T1$ and dashed lines for $T2$. Wavelength is set to $\lambda = 1.5$ µm and propagation distance to $L = 10\,\text{km}$.

Various pupil sizes D were studied with various combination of correction elements sizes d. For each of these cases, optimal correction improves the link budget. In order to design a FSO system using such a correction device, it is important to set an acceptable threshold in terms of intensity fluctuations. This particular threshold will then set the necessary number of correction elements and the required total optical surface. If high performance is desired, one must use a large optical aperture D with a large number of optical fibres. In this study, controlling a hundred modes is sufficient which with the proposed technology solution seems feasible.

9.3.6 Impact of the Pupil Filling Ratio

Correction on a total surface of approximately $30\,\text{cm} \times 30\,\text{cm}$ has a better correction quality because it performs phase conjugation on a large part of the field in the reception plane. Previously, we studied an iterative correction with pupils of $d = 1$, 2 and $3\,\text{cm}$ in diameter. The correction with the finest spatial sampling (i.e. producing the best correction) requires a lot of

correction elements.

However, by taking as a design goal $\frac{\sigma_I}{\langle I \rangle} < 0.1$ only $N = 100$ correction points are necessary. In this paragraph, we focus on the reduction of the lenslet size which is equivalent to diluting the pupil (see figure 9.27). Cases with $D = 20\,\text{cm}$ et $D = 30\,\text{cm}$ are presented. Figure 9.28 shows the simulation results.

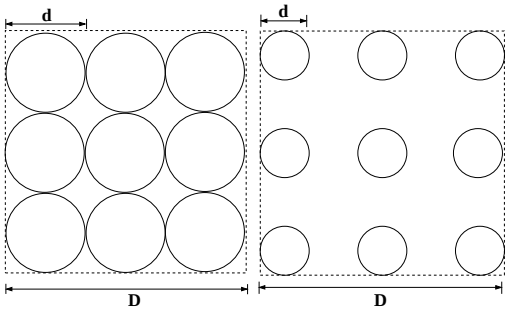

Figure 9.27: Illustration for the pupil configuration in the reception plane. Left: non-diluted pupil, right: diluted pupil.

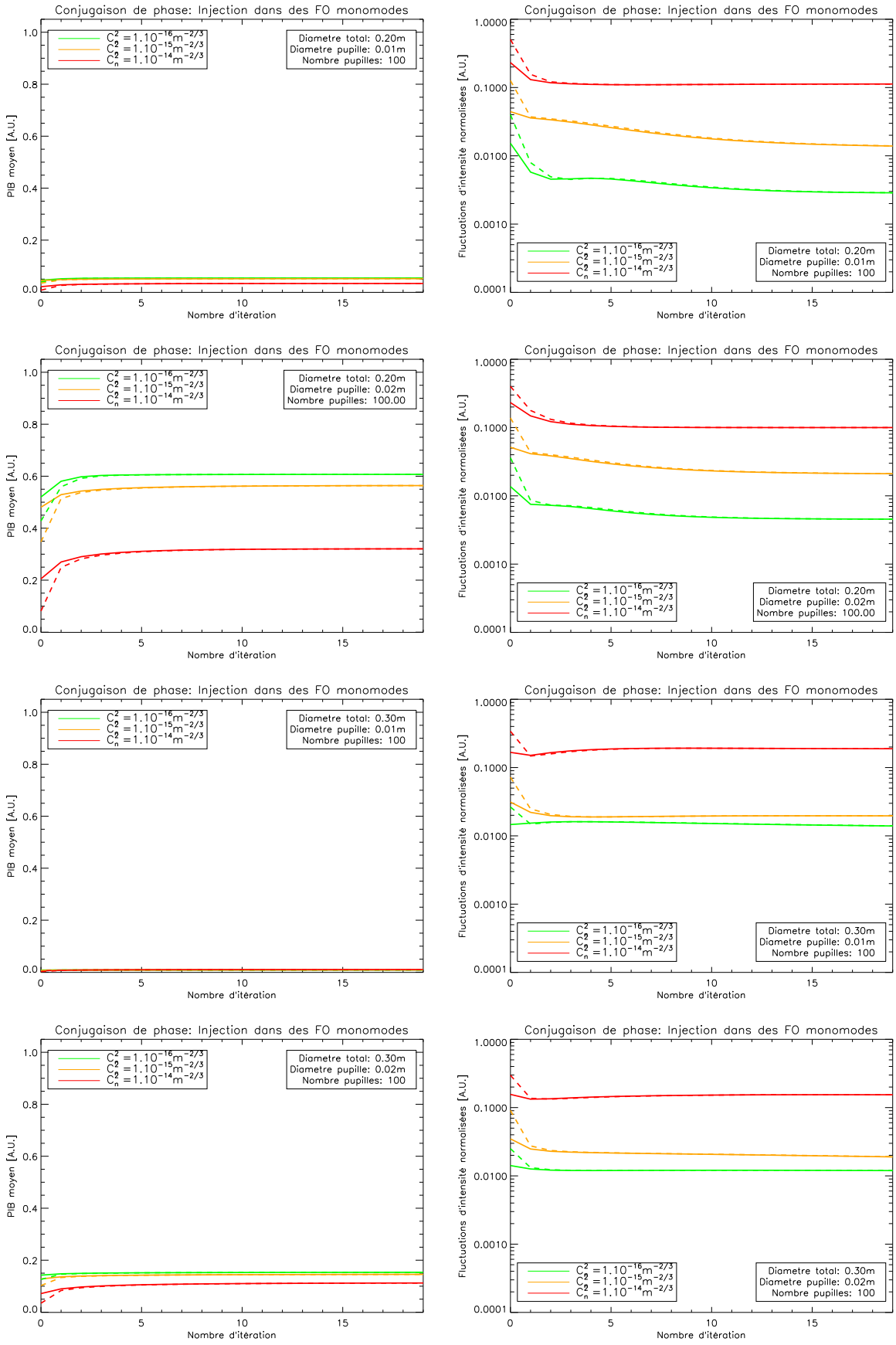

Figure 9.28: Simulation results for a matrix with 100 lenslets. Each lenslet is either $d = 1\,\text{cm}$ or $d = 2\,\text{cm}$ in diameter with $D = 20\,\text{cm}$ and $D = 30\,\text{cm}$. Solid lines represent emission and dashed lines reception. The wavelength is set to $\lambda = 1.5$ µm and propagation distance to $L = 10\,\text{km}$.

Pupil dilution strongly reduces mean collected intensity. As a matter of fact, reducing the paving density increases geometrical losses by also diffraction related losses. The cases $D = 30\,\text{cm}$ and $d = 1\,\text{cm}$ shows the limit for pupil dilution where the received mean intensity is almost zero. Conversely, normalised intensity fluctuations do not seem to be strongly affected by the increase of gaps in the pupil. This is what we have shown in the previous paragraph: $\frac{\sigma_I}{\langle I \rangle}$ depends on N but not so much on D. Fluctuations seem more directly related to diameter D for a fixed N, whereas mean intensity seems more to be fixed by the total collecting surface and gap factor.

The shown geometry with gaps is clearly not optimal. It cannot be used to reach $\frac{\sigma_I}{\langle I \rangle} = 0.1$ for $C_n^2 = 10^{-14}\,\text{m}^{-2/3}$. A better lenslet distribution is necessary. The use of denser optical fibre configurations, with for example square of hexagonal lenslets, can be used to achieve of pupil plan without any gaps. In order to fully benefit from the correction, it is possible to develop pupils with large gaps but with a geometry minimising fluctuations. As an example, it is possible to use lenslets of varying sizes throughout the pupil (see figure 9.29). Such a configuration has

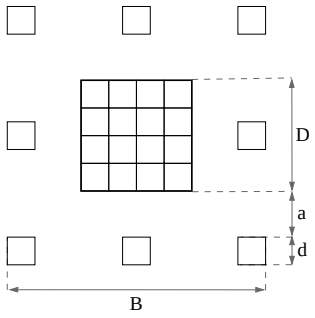

Figure 9.29: Pupil configuration with gaps.

a good sampling factor near the optical axis used to achieve an important flux collection. It also has a large base B capable of focalising and stabilising the beam after propagation. However, the optimisation of the geometry and the design of such pupil are still to be undertaken.

9.4 Conclusion

In this chapter we have proposed different novel implementation strategies of phase and amplitude correction. First, we have studied the influence of tip-tilt iterative correction combined with beam re-centring. This system is easy to implement as only two tip-tilt mirrors can be used. However, this iterative correction does not seem powerful enough because the number of corrected modes is insufficient. In addition, for strong perturbations it seems that a modal correction is not longer suitable and a zonal approach is more efficient.

Paragraph 9.2 impact of spatial sampling on non-diluted pupils (square lenslets without gaps) was studied theoretically for optimal correction. This result was used as a reference and we have showed that $\frac{\sigma_I}{\langle I \rangle}$ mainly depends of N whereas $\langle I \rangle$ depends on N but also on D. It has been

shown that a high number of correction elements N is required to reach sufficient correction quality. In terms of intensity fluctuations, the plateau where no improvement is obtained by increasing N does not seem to depend on turbulence strength. However, if one is to set the required performance to say $\frac{\sigma_I}{\langle I \rangle} = 0.1$ and wavelength to $\lambda = 1.5$ µm, a minimum of $N = 100$ correction elements is necessary. Increasing the wavelength can help reduce the number of elements but one need to simultaneously increase the overall pupil size. Increasing the wavelength from $\lambda = 1.5$ µm to $\lambda = 4$ µm reduces by 4 the number of necessary correction points when the pupil diameter D is doubled.

Finally, we proposed a novel approach for implementing iterative phase and amplitude correction by injecting into single-mode optical fibres. We first used circular lenslets with no gaps in between (geometrical losses of $\frac{\pi}{4}$). We then studied the impact of increasing the gaps between individual lenslets. Three different losses origins have been identified: losses introduced by injecting into single-mode optical fibres, geometrical losses due to gaps in the pupil and diffraction losses. The last ones are created by gaps within the pupil which increases secondary lobes density outside the reception pupil. Pupil density (i.e. the presence of gaps or not in the pupil) has a strong impact on mean received intensity. Intensity fluctuations however mainly depend on N when gaps between lenslets increase (no important variation between the studied cases with diluted pupils). Mean intensity is strongly modified and it seems necessary to optimise the pupil geometry when using a pupil with gaps between lenslets. However, it has been observed that the design in terms of normalised intensity fluctuations as showed paragraph 9.2 is identical for this type of correction despite important geometrical modifications. We have shown that to the first order, $\frac{\sigma_I}{\langle I \rangle}$ mainly depends on N and that $\langle I \rangle$ depends on N but also on D and on d. This is only the first evaluation step and a more advanced study needs to be carried out. In spite of these losses, correction using injection into an optical fibre can reach a satisfactory level of correction in return for a sufficient total collection surface and spatial sampling. It seems that from $N = 100$ and above, intensity fluctuations can be reduced down to $\frac{\sigma_I}{\langle I \rangle} < 0.1$ for all studied turbulence strengths. In the framework of our study, controlling a hundred modes is sufficient. With the proposed correction solution it seems entirely feasible technologically.

General Conclusion

Summary

The work presented in this document has focused on the impact of atmospheric turbulence in free-space optical links and on adaptive optics (AO) correction to reduce its impact.

In the first part, I have presented the problem and evaluated the correction efficiency levels to reach typical free-space optics (FSO) requirements. In order to quantify correction quality, I have proposed the use of mean power in the bucket (PIB) and normalised intensity fluctuations. These metrics are easily linked to classical FSO metrics such as the bit error rate (BER). However, the relation between these parameters is exact only in the weak perturbation case, for an important pupil averaging effect or when an efficient adaptive optics correction is in place. We have shown that in order to achieve an efficient correction it is important to increase the mean collected flux to assure sufficient signal-to-noise ratio. More importantly it is essential to reduce temporal intensity fluctuations. We have set the threshold for normalised fluctuations (i.e. $\frac{\sigma_I}{\langle I \rangle}$) to 0.1 or less based on a study on mean BER values. In these conditions, BER curves are similar to the theoretical curve obtained in absence of turbulence. It enables us to reach mean BERs typically between 10^{-9} and 10^{-12}. In typical conditions (i.e. in terms of turbulence strength, optics diameters, wavelength) and for long-distance endo-atmospheric links as we have studied, the order of magnitude of fluctuations is $\frac{\sigma_I}{\langle I \rangle} \simeq 0.5$. A reduction in intensity variance of a factor 25 is hard to achieve with methods such as diversity. Correction by an adaptive optics system has the potential of delivering the desired reduction.

The second part of the document focused on the detailed analysis and extension to all perturbation regimes of the work initially proposed by Barchers on optimal and sub-optimal correction. Truncation by pupil D and turbulence strength C_n^2 were established as the main limiting parameters. These corrections are worked out iteratively and enable, when D and C_n^2 enable it, the creation of a propagation mode. We have shown that the relevant scaling parameter for pupil diameter in weak perturbations is $L_F = \sqrt{\lambda L}$. For pupil diameters larger than $2L_F$ and smaller than L_F correction is superfluous when compared to an uncorrection optical link. For strong perturbations $\frac{\lambda L}{\pi \rho_0}$ was identified as the scaling parameter for the pupil size. As long as D stays smaller than $\frac{\lambda L}{\pi \rho_0}$ the link budget of the system is strongly improved by correction. Extension of the optimal correction efficiency was demonstrated in very strong perturbations and even saturation. For a Rytov scintillation variance rate σ_R^2 of about 100, correction is still able to improve the link. However, correction efficiency drops when we reach such variances. We have shown that intensity fluctuations can be reduced by up to a factor 30 (depending on turbulence strength

and pupil size) and that mean intensity can be increased by up to a factor 6 (equally dependent on C_n^2 and D).

We subsequently addressed sub-optimal correction, where only the phase part of the field is corrected. For the sub-optimal case we observe the same scaling factors and limitations introduced by turbulence strength and pupil diameter as we have observed for optimal correction. Performance is clearly below that of the optimal correction and that for all the studied situations.

The third part of this document addressed classical AO corrections for FSO. We first studied an approach based on wavefront sensing which is typical of AO techniques used in astronomy. This approach is based on the measurement and the reconstruction of phase perturbations. It is strongly sensitive to scintillation. The relevance of this technique lies mainly in its correction capability in low scintillation regimes, typically for $\sigma_R^2 < 1$. We have shown that restricting the number of corrected Zernike modes can be sufficient to reach the correction levels achieved by a perfect phase-only correction. Within the studied framework, only the first 35 modes are indispensable. In order to partially alleviate scintillation issues, we have proposed the use of several beam probes. This configuration helps averaging scintillation effects and increases the usability domain where correction is useful.

The second approach studied was phase modulation. It completely removes problems related to scintillation but on the other hand requires a much higher bandwidth for the deformable mirror. Such a correction system cannot guaranty the optimality of the solution after convergence. In addition, obtained performance is on average only slightly higher that with a wavefront sensor (if the multi-beam approach is used, reducing the impact of scintillation).

The three correction methods that we have presented (i.e. sub-optimal, counter-propagating laser beam probe and modulation) can only correct for the phase part of the emitted field. We have shown that for strong perturbations and for all studied strategies it is not possible to reduce intensity fluctuations below the require threshold set in terms of error rate. This observation demonstrates the importance of the optimal method and the necessity of pre-compensating for both phase and amplitude.

This is the reason why the last part of the document focuses on the implementation of the optimal correction. We demonstrated the importance of pupil plan spatial sampling. A large number of correction elements, approximately one hundred for a pupil of $D = 30cm$ in diameter, is required. An implementation of the optimal correction by sampling the pupil plane with a matrix of fibre optics has been proposed. This method reaches much higher correction levels than those limited to phase only. It can reach optimal correction levels in terms of intensity fluctuations. However, the large number of correction elements imposes either an important technological development or the study of ways of reducing this number. We have proposed two different approaches. The first consisted in increasing the wavelength. By increase wavelength from $\lambda = 1.5$ µm (hypothesis used for this work) to $\lambda = 4$ µm, it is possible to reduce the degrees of freedom up to a factor 4. The second approach consisted in diluting the pupil in order to use only a limited number of correction elements judiciously placed over a large area. This approach is similar to certain aspects of optical synthetic aperture used in multi-aperture instruments.

Perspectives

The results developed in this document are the first steps of the establishment of a more global phase and amplitude correction such as one could wish for FSO systems.

Field test for the Fortune43G project will take place mid-2010. During the system design, we have chosen a pupil diameter of $D = 25$ cm with no central obscuration in order to limit effects of pupil truncation at the reception. The impact of pupil truncation was established during the study of AO correction using a counter-propagating probe. In addition, seven counter-propagating beams were chosen in order to attenuate scintillation effect on wavefront measurement and extend the usability domain of the sytem. The SH-WFS is composed of a 8×8 lenslets array used to correct approximately the first fifty Zernike modes. These field tests will enable an experimental validation of the design and test the method based on wavefront measurement. We have seen in particular that for intermediate perturbations ($\sigma_R^2 = 1.4$) this correction is better than the perfect phase-only correction. The fundamental reasons are still to be evaluated.

Concerning wavefront measurements for FSO applications, we have concentrated our work on the SH-WFS. A number of other WFSs currently exist such as: the pyramid[Ragazzoni-a-96], curvature [Roddier-a-88], YAW [Gendron-a-07] or phase diversity [Mugnier-l-06, Gonsalves-a-82]. A detailed study on the usefulness of each system for FSO applications must be undertaken in order to extend the phase-only correction validity domain. Using a wavefront sensor more adapted to strong perturbations associated with a deformable mirror capable of reconstructing phase steps can possibly significantly improve final performance.

Even if SPGD algorithms are promising, nothing can guaranty that they are the best possible algorithms. Unfortunately, no theoretical study can compare different algorithms for AO correction of a terrestrial optical link. An improvement of current algorithms is still to be undertaken. In addition, we only focused on phase-only modulation of the emitted field. On the other hand, we have shown the usefulness of driving both phase and amplitude. Several deformable mirrors can be used to control both phase and amplitude at the same time. The control or the optimisation algorithm is still to be developed. During this thesis work, we have built an optical bench experimentally implementing adaptive optics correction using phase modulation. Unfortunately, due to supply issues of certain parts it was not possible to extensively explore the setup, and especially test the phase modulation method. As stressed previously, this strategy can improve link budget. The optical bench is an ideal tool to study both experimentally and numerically phase-only modulation and phase and amplitude modulation of the emitted field.

Concerning AO correction of a FSO system, I mainly focused my activity on the study at a wavelength of $\lambda = 1.5$ µm. We have showed that increasing the wavelength to $\lambda = 4$ µm, can have certain advantages. If this solution seems very promising for reducing the degrees of freedom, the design of such an instrument is still to be undertaken. Diffraction related effects, attainable distance and required optical diameters are modified by the change of wavelength and are still to be quantified. A theoretical study must be undertaken for all presented correction methods, and in particular for the last part on the implementation of the optimal correction.

In this manuscript we have only briefly mentioned the problem related to optimal configuration of a multi-pupil system. This multi-aperture system can be used to implement the iterative phase and amplitude correction (i.e. an approximation of the optimal correction). A thorough

study in order to optimise pupil geometry is essential. As a matter of fact, the goal is twofold and contradictory. The first is to minimise the correction pupil total surface as much as possible in order to reduce complexity and implementation costs. The second goal is to maximise the collected flux and minimise intensity fluctuations in order to reach the required FSO specifications.

Appendix

Appendix A

Reminder

A.1 Error Function

Let the function $erf(x)$ be the error function and $erfc(x)$ its complementary function:

$$\begin{aligned} erf(z) &\triangleq \frac{2}{\sqrt{\pi}} \int_0^z e^{-t^2} dt \\ erfc(z) &\triangleq 1 - erf(z) \triangleq \frac{2}{\sqrt{\pi}} \int_z^\infty e^{-t^2} dt \end{aligned}$$

A.2 Calculating BER by counting

How many bits *n* are to be sent so that if *k* errors are detected, one can ensure a specific *BER* with confidence level *CL*?

$$CL = P(k > N|BER) \, , \tag{A.1}$$

Where BER is the probability error for each bit, k the number of errors and N the number of specified errors. For each transmission either we obtain an error with a probability of error BER or the transmission is correct (binomial distribution):

$$P_n(k) = \frac{n!}{k!(n-k)!} BER^k (1 - BER)^{n-k} \tag{A.2}$$

Where n is the number of transmitted bits. The probability that at least N errors occur is:

$$P_n(k > N) = 1 - P_n(k \leq N) = 1 - \sum_{k=0}^{N} \left(\frac{n!}{k!(n-k)!} BER^k (1 - BER)^{n-k} \right) \tag{A.3}$$

As n approached infinity and BER approaches 0 with $n \times BER = \epsilon$, the binomial distribution approaches a Poisson distribution with parameter $n \times BER$:

$$P_n(k) \underset{n \to \infty}{\longrightarrow} \frac{(n \times BER)^k}{k!} e^{-n \times BER} \tag{A.4}$$

And so:

$$CL = P(k > N|BER) = 1 - \sum_{k=0}^{N} \frac{(n \times BER)^k}{k!} e^{-n \times BER} \tag{A.5}$$

Then:

$$n = -\frac{\ln(1 - CL)}{\times BER} + \frac{\ln\left(\sum_{k=0}^{N} \frac{(n \times BER)^k}{k!}\right)}{BER} \tag{A.6}$$

A.3 Conditional Probability

The conditional probability is defined in the general case as:

$$Pr(Y) = \int P_r(Y|X = x)\, p_X(x)\, dx \tag{A.7}$$

Appendix B

Mitigation of Atmospheric Effects by Adaptive Optics for Free-Space Optical Communication

Mitigation of Atmospheric Effects by Adaptive Optics for Free-Space Optical Communications

Noah H. Schwartz[a], Nicolas Védrenne[a], Vincent Michau[a], Marie-Thérèse Velluet[a] and Frédéric Chazallet[b]

[a] ONERA - Optics Department, 29 avenue de la division Leclerc, 92332 Châtillon, France
[b]Shaktiware, 27 boulevard Charles Moretti Bat B, 13014 Marseille, France

ABSTRACT

Data-rates of long-range free-space optical communication links are deteriorated by atmospheric turbulence which causes power in the bucket fluctuations. In order to compensate for those effects the use of adaptive optics is envisioned. Different solutions have been proposed for the correction. We study here the performances of several compensation methods, encompassing both amplitude and phase and phase-only precompensation. In the case of phase-only precompensation we studied two system designs, one which is dedicated to symmetrical communication systems and the other to dissymmetric systems. In the dissymmetric case we studied two ways of driving the deformable mirror : the use of a Shack-Hartmann wavefront sensor and a model-free phase modulation. For each compensation architecture simulation results covered weak, moderate and strong turbulence conditions.

Keywords: Atmospheric turbulence, adaptive optics, free-space optical communication, Monte Carlo simulations, optical propagation

1. INTRODUCTION

Local refractive index inhomogenities (i.e. atmospheric turbulence) disturb the phase of electromagnetic waves propagating through the atmosphere. In the case of a laser beam, they notably give rise to random displacement of the center of gravity (beam wander), significantly broader beams than predicted by the diffraction theory (beam spreading) and illumination fluctuations (scintillation) [1]. These intensity fluctuations can seriously increase bit-error rates [2, 3] of optical communication systems, thus limiting the practical distance and throughput of Free-Space Optical Communications Systems (FSOCS). The rapid growth of FSOCS, and in particular the need to increase their range and data-rate, stimulates the need to study means of mitigating intensity fluctuations. Indeed, optical communication systems have many advantages over their RF-based counterparts. They allow a smaller size and weight, a narrower beam (providing a secure channel), and enable a potential increase in total throughput.

A real-time modification of the emitted beam, can significantly reduce intensity fluctuations [4]. This technique is called precompensation. One of the main issues of phase precompensation is to determine the adequate shape to give to the phase correctors (usually Deformable Mirrors (DM)) in order to optimize the criterion we are interested in, that is to say power in the bucket. Two different methods arise from this precompensation need: phase measurement and phase modulation. Phase measurement supposes that the correction phase optimizing our criterion is the actual measured phase by the wavefront sensor (WFS). The behavior the the most currently used wavefront sensor (WFS), the Shack-Hartmann (SH), is usually poorly know under strong turbulence conditions. On the other hand, phase modulation techniques require compensation devices significantly faster than the turbulence evolution time-scale [5, 6].

In the present work, we investigated an adaptive optics (AO) system approach to correct for atmospheric disturbances by means of numerical simulations. In section 2 we present a brief description of the FSO system context. In section 3 we present an iterative method to estimate the optimal correction. This correction is based

Further author information:
Noah.Schwartz@onera.fr, Telephone:+33 (0)1 46 73 48 82
Vincent.Michau@onera.fr, Telephone: +33 (0)1 46 73 47 80

on perfect phase conjugation. We also discuss the possibility of altering the performance by means of simple phase-only correction. A non-iterative correction and its implementation based on a SH phase measurement is reported in section 4. A model-free phase modulation precompensation is described in section 5.

2. LONG-DISTANCE TERRESTRIAL FSO SYSTEMS

2.1 Context of Study

The context of the study is a $10km$ terrestrial commercial Free-Space Optical (FSO) communication link. Selecting the wavelength for such a system is a trade-off between atmospheric absorption (i.e. atmospheric windows), scattering, turbulence effects and available technology. The maximum operating wavelength will be set to $1.5\mu m$. Furthermore, as turbulence strength (characterized by the index of refraction structure constant C_n^2) is a decreasing function of height, it is best to place the FSO system as high above the ground as possible. On the other hand, wind speed tends to increase with altitude as well as the needed bandwidth of the correction system. The system should be placed approximately at an altitude of $30m$. A constant C_n^2 can be considered because the communication link will be horizontal. Various cases of turbulence strength will be studied in this paper: $C_n^2 = 1.10^{-16}m^{-2/3}$, $C_n^2 = 1.10^{-15}m^{-2/3}$ and $C_n^2 = 1.10^{-14}m^{-2/3}$, corresponding respectively to a Rytov variance for a plane wave of $\sigma_1^2 = 0.14$, $\sigma_1^2 = 1.4$ and $\sigma_1^2 = 14$, where $\sigma_1^2 = 1.23k^{7/6}C_n^2L^{11/6}$. The scope of this work will thus encompass weak to strong perturbation regimes. Normalized power in the bucket can be used as a first approximation to estimate the link quality:

$$I = \frac{\int d\mathbf{r}U(\mathbf{r}).U^*(\mathbf{r}).\mathcal{P}(\mathbf{r})}{\int d\mathbf{r}U(\mathbf{r}).U^*(\mathbf{r})}, \tag{1}$$

where $\mathcal{P}$ is the pupil of the receiving telescope and $U(\mathbf{r})$ is the received electromagnetic field. Losses due to incomplete focalization into an optical fiber, atmospheric absorption and the such are not taken into account. The mean power in the bucket will be noted $< I >$, where $< . >$ is the statistical average. For the remainder of the paper we will use mean intensity (mean power in the bucket) and of the normalized intensity fluctuations ($\frac{\sqrt{<I^2>-<I>^2}}{<I>}$) to estimate the communication link quality.

3. OPTIMAL LASER BEAM SHAPING BY MEANS OF ITERATIVE CORRECTION

The general purpose of this paragraph is to present an optimal laser beam shape in order to maximize transmission of a laser beam propagation through a turbulent atmosphere. This method, based on an approach proposed by Barchers [7], enables an increase in mean power in the bucket and a decrease in intensity fluctuations. This type of correction leads to a symmetrical system where both emitter and receiver are identical.

3.1 Optimal Correction based on a Amplitude and Phase Iterative Correction

Figure 1 illustrates the basic concept of the iterative amplitude and phase correction. The electromagnetic field is propagated back and forth across the turbulent volume. At the level of each telescope a pseudo-phase conjugation is performed. The correction necessitates the use of two or more phase compensation devices in order to control both emitted amplitude and emitted phase. The implemented algorithm utilizes an iterative

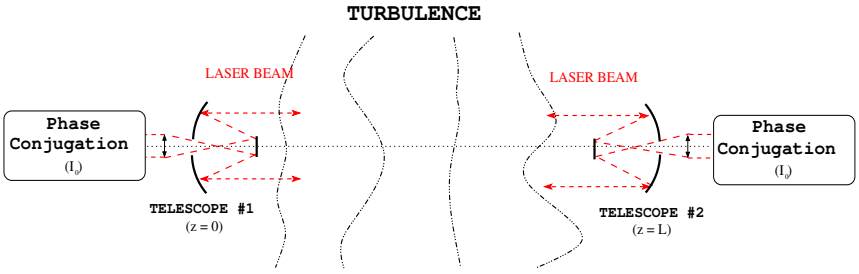

Figure 1. Basic concept of the optimal amplitude and phase iterative correction.

propagation between the two telescopes of the communication link. The different steps in the iterative correction are presented below, where: $z = 0$ (resp. $z = L$) corresponds to the position of telescope number 1 (resp. 2), I_0 is the nominal intensity emitted by the laser beams ($\int |U_0(\vec{r}, z = 0)|^2 d\vec{r} = I_0$), $\mathcal{P}_1$ (resp. $\mathcal{P}_2$) corresponds to the pupil of telescope number 1 (resp. 2), D is the pupil diameter. The operator $\mathcal{G}^+$ (resp. $\mathcal{G}^-$) represents the propagation through atmospheric turbulence along increasing (resp. decreasing) z. The subscript for each complex field depicts the iteration index and the complex conjugate of U_i is U_i^*:

$$U_i(\vec{r}, z = 0) = \mathcal{G}^- \left[\frac{I_0}{\int |U_{i-1}(\vec{r}, z = L) d\vec{r}|^2} U_{i-1}^*(\vec{r}, z = L) \times \mathcal{P}_2 \right] \tag{2}$$

$$U_i(\mathbf{r}, z = L) = \mathcal{G}^+ \left[\frac{I_0}{\int |U_i(\vec{r}, z = 0) d\vec{r}|^2} U_i^*(\vec{r}, z = 0) \times \mathcal{P}_1 \right], \tag{3}$$

The nominal beam shape injected to the system is $U_0(\mathbf{r}, z = 0) = A_0 exp\left(-\frac{\mathbf{r}^2}{{w_{z=0}}^2} - i\frac{k\mathbf{r}^2}{2F_{z=0}}\right)$, where $w_{z=0}^2$ is the beam width at the emitter and $F_{z=0}$ the radius of curvature. After each propagation, a normalization by I_0 is performed to take into account the initial laser beam power. This simulation algorithm was used to compute the effectiveness of the optimal correction as a function of the pupil diameters (Figure 2). The purpose of this optimal iterative correction is to attain a propagation mode of the system composed by {*telescope* #1, *turbulent atmosphere, telescope* #2} . This approach can be compared to a spatial mode selection in laser beam cavity. When this mode is obtained, losses due to atmospheric turbulence and pupil truncation are minimized. As expected [7], the pupil diameter has a fundamental effect on link quality. When pupil diameters are too small, this type of a propagation mode is impossible to reach due to the prominent constraints imposed on the spatial limitation of the beam. When the diffraction effects are negligible this mode can be obtained. If they are no longer negligible (longer wavelength or smaller pupil diameter), this mode will not be attained. This is why we observe that the uncorrected beam can yield even better results than the corrected beam for very small pupils. On the other hand, it can be observed that for large pupils the gap between optimality and beam propagation without correction decreases; this is due to the pupil averaging effect. As the pupil diameter increases, more energy is collected by the pupil. For large enough pupils, all the energy will be collected and the correction effectiveness will lose interest. Plain pupils are used for this simulation ; telescopes with a central occultation

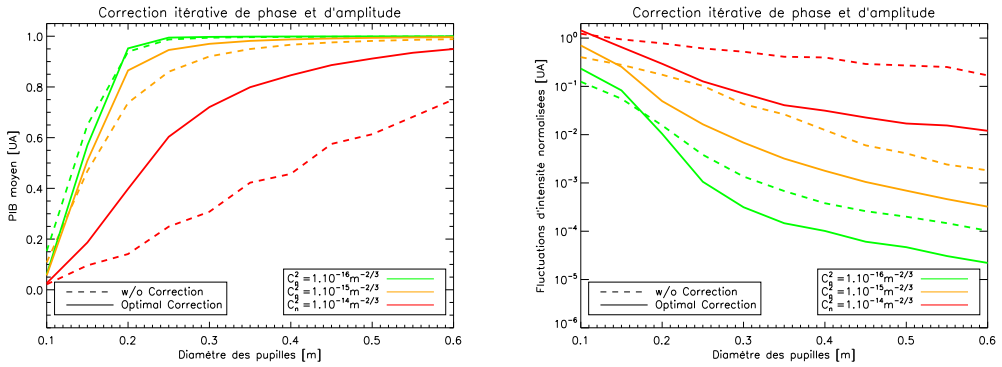

Figure 2. Effectiveness of optimal correction as a function of pupil diameters. Propagation length: $10km$, $\lambda = 1.5\mu m$. Statistics are calculated on 300 propagations. Green: $C_n^2 = 1.10^{-16} m^{-2/3}$, yellow: $C_n^2 = 1.10^{-15} m^{-2/3}$, red: $C_n^2 = 1.10^{-14} m^{-2/3}$. Solid lines: optimal correction, dashed lines: no correction. Left: Mean power in the bucket as a function of pupil diameter and turbulence strength. Right: intensity fluctuations as a function of pupil diameter and turbulence strength.

have not yet been taken into account. The authors are currently addressing this issue. According to Figure 2, a pupil diameter between $20cm$ and $50cm$ seems to be a good compromise. To minimize the general bulk of the system while maintaining a decent correction, a $30cm$ pupil can be judiciously chosen.

Figure 3 presents the evolution of mean power in the bucket and mean intensity fluctuations as a function of the iteration index. Clearly the first iteration has the most effect. Nevertheless, each step refines the correction

towards optimality. Only a few iterations are necessary to achieve a reasonable correction. For example, in the strongest turbulence simulated case (i.e. $C_n^2 = 1.10^{-14} m^{-2/3}$), mean intensity evolves from 0.30 to 0.72 in only five iterations. The iterative correction changes normalized intensity fluctuations from 0.52 to 0.071. Based on these curves, we see that intrinsic limitations of the optimal correction are both set by the pupil diameter and by the turbulence strength.

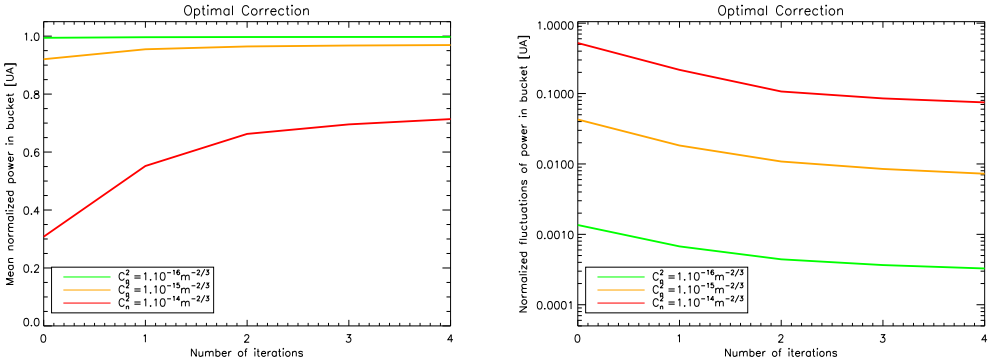

Figure 3. Effectiveness of optimal correction as a function of iterations. Pupil diameter: $30cm$. Propagation length: $10km$, $\lambda = 1.5\mu m$. Statistics are calculated on 300 propagations. Green: $C_n^2 = 1.10^{-16} m^{-2/3}$, yellow: $C_n^2 = 1.10^{-15} m^{-2/3}$, red: $C_n^2 = 1.10^{-14} m^{-2/3}$.

Upper part of Figure 4 illustrates a typical realization of energy distribution after a $10km$ propagation of a laser through atmospheric turbulence. Side by side are presented the propagation of a laser beam without any correction and the laser beam after optimal correction. The $30cm$ pupil is presented on these images to illustrate the effectiveness of the correction. After 10 iterations most of the energy is contained within the pupil. Optimal correction can be used as a reference to understand the performances of other precompensation devices. As mentioned earlier, a correction that needs to compensate for both phase and amplitude requires at least two deformable mirrors to operate. Each additional mirror increases the cost of the correction device. With this perspective in mind, one can investigate the eventual loss of correction quality by use of a phase-only correction. Correcting only the phase of an electromagnetic field can be performed by means of a single deformable mirror.

3.2 Iterative Phase-Only Correction

Phase-only correction is obtained by replacing the phase conjugation $U_i^*(\mathbf{r})$ (equations (2) and (3)) at the i^{th} iteration by the phase-only correction. For example, equation (3) then becomes:

$$U_i(\mathbf{r}, z = L) = \mathcal{G}^+ \left[\frac{I_0 U_0(\vec{r}, z = 0)}{\int |U_i(\vec{r}, z = 0) d\vec{r}|^2} \times \frac{U_i^*(\vec{r}, z = 0)}{|U_i(\vec{r}, z = 0)|} \times \mathcal{P}_1 \right] \tag{4}$$

Figure 4 illustrates a typical phase-only correction result. After 10 iterations, a notable gain can be achieved. Side by side, we illustrate the propagation of a laser beam without any correction, and the laser beam after phase-only correction. Phase-only correction seems to yield poorer results than the optimal phase and amplitude correction. Nevertheless, phase-only correction still leads to a more noticeable improvement than without precompensation. Figure 5 plots phase-only results as a function of the pupil diameters for 300 statistically independent realizations. Figure 6 illustrates phase-only efficiency as a function of iteration index. Only a few iterations are necessary to achieve a good correction. For example, in the strongest turbulent case (i.e. $C_n^2 = 1.10^{-14} m^{-2/3}$), mean intensity increases from 0.3 to 0.64 in only five iterations and changes normalized intensity fluctuations from 0.52 to 0.156. Limitations of the phase-only correction are set both by the pupil diameter and the turbulence strength. These results compare well with the optimal correction. For a $30cm$ pupil and $C_n^2 = 1.10^{-14} m^{-2/3}$, the mean power in the bucket (resp. intensity fluctuations) is 0.64 (resp. 0.1568) for phase-only and 0.72 (resp. 0.071) for optimal correction after iteration. The simulations performed for phase-only correction used a narrow collimated beam ($exp(-1)$ amplitude beam radius at pupil level $w_0 \approx 7cm$).

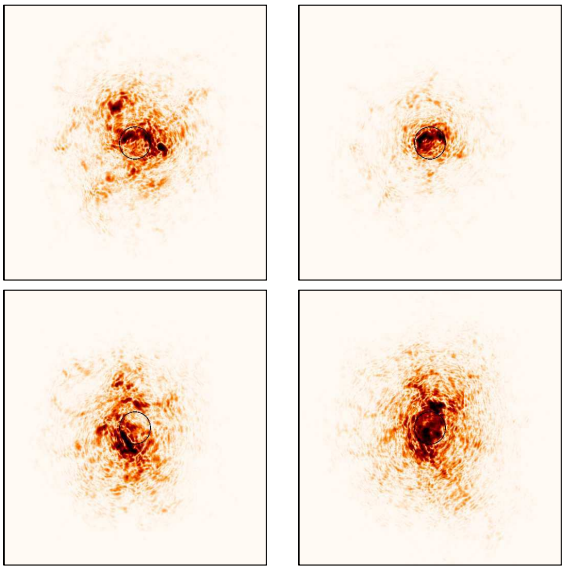

Figure 4. Typical energy distribution for iterative optimal and phase-only correction. Top: optimal correction. Bottom: phase-only correction. Left: No correction; right: optimal (reps. phase-only) correction after 10 iterations. Circles represent a $30cm$ pupil diameter. Propagation length: $10km$, $\lambda = 1.5\mu m$. $C_n^2 = 1.10^{-14}m^{-2/3}$. These two figures have been obtained under the same atmospheric turbulence conditions. Logarithmic scaling.

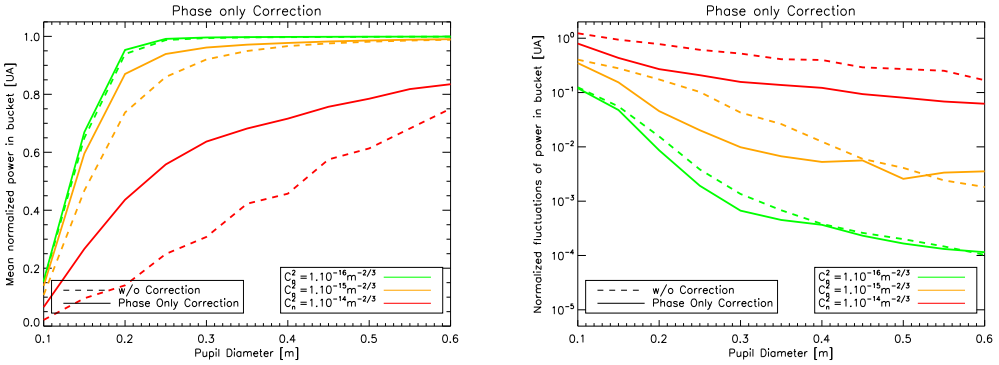

Figure 5. Effectiveness of iterative phase-only correction as a function of pupil diameters. Propagation length: $10km$, $\lambda = 1.5\mu m$. Statistics calculated on 300 propagations. Left: Mean normalized power in the bucket ($< I >$); right: normalized fluctuations of power in the bucket ($\frac{\sigma_I}{<I>}$). Green: $C_n^2 = 1.10^{-16}m^{-2/3}$, yellow: $C_n^2 = 1.10^{-15}m^{-2/3}$, red: $C_n^2 = 1.10^{-14}m^{-2/3}$. Solid lines: phase-only correction; dashed lines: no correction.

An optimization of the initial laser beam radius in the case of a phase-only iterative correction is presented Figure 7. When the beam waist is too small, natural beam divergence induces a strong reduction in the total collected energy at the receiver pupil. On the other hand, when the beam waist is too big an important truncation will be introduced by the emitter pupil. These simulations place an upper limit on phase only correction efficiency. However, the development of a system based on an iterative correction requires two AO systems. Before considering such a complex device, we need study more classical approaches.

4. PHASE-ONLY CORRECTION WITH DISSYMMETRIC BEAMS

4.1 Concept of Correction

The aim of this paragraph is to present a particular type of phase-only correction [8]. The interest of this type of configuration is that only one AO system is necessary, and not two as for the iterative approach. This correction circumvents the iteration process and will precompensate the emitted beam in a single propagation.

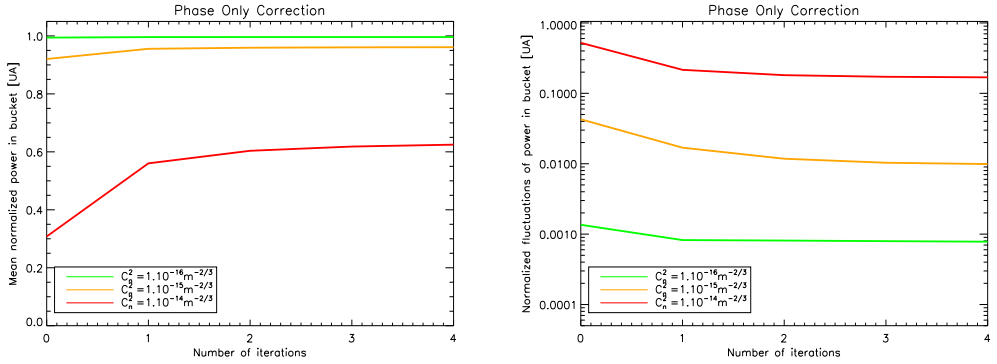

Figure 6. Effectiveness of iterative phase-only correction as a function of iteration index. Propagation length: $10km$, $\lambda = 1.5\mu m$, pupil diameter: $30cm$. Statistics are calculated on 300 propagations. Green: $C_n^2 = 1.10^{-16}m^{-2/3}$, yellow: $C_n^2 = 1.10^{-15}m^{-2/3}$, red: $C_n^2 = 1.10^{-14}m^{-2/3}$.

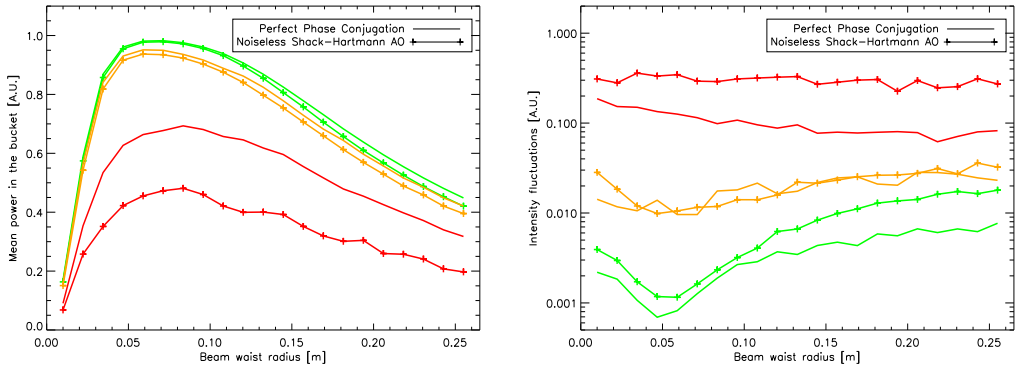

Figure 7. Evolution of the figures of merit as a function of the initial laser beam radius in the case of a phase-only iterative correction. Propagation length: $10km$, $\lambda = 1.5\mu m$. Statistics are calculated on 300 propagations. Left: mean normalized power in the bucket ($< I >$); right: normalized fluctuations of power in the bucket ($\frac{\sigma_I}{<I>}$). Green: $C_n^2 = 1.10^{-16}m^{-2/3}$, yellow: $C_n^2 = 1.10^{-15}m^{-2/3}$, red: $C_n^2 = 1.10^{-14}m^{-2/3}$. Solid lines: optimization with exact phase-only correction, pluses: optimization with a noiseless SH-WFS.

More precisely, a back-propagating laser beam (from receiver to emitter) will probe atmospheric disturbances. To prevent effects of beam wander, this uncorrected beam should be chosen to be largely divergent. Scintillation

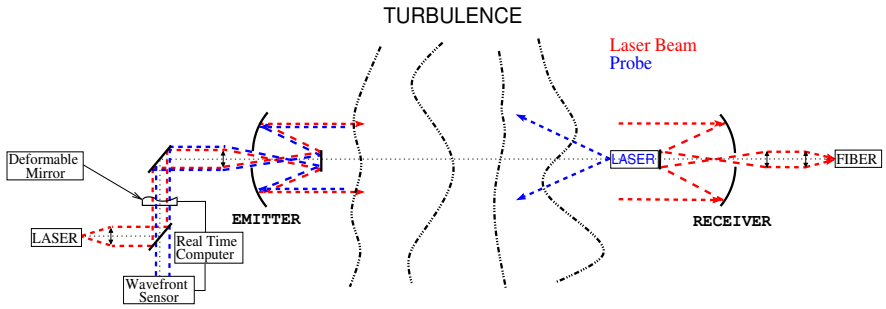

Figure 8. Configuration of the single-source probe precompensation device with a WFS. The mirror surface is updated by the real time computer (RTC) based on the WFS measurements.

effects are caused by the propagation of phase aberrations. Scintillation will thus not be affected by phase disturbances that are close to the receiver. Therefore, a largely divergent beam is appropriate as a probe because it will poorly probe this region of space while still properly probing turbulence close to the emitter. On the

other hand, the forward propagating beam (from emitter to receiver) will be a collimated beam to insure that a maximum of the energy is collected through the receiver. For the rest of the paper a $w_0 = 10cm$ beam will be chosen. Figure 8 presents the system configuration.

Figure 9 plots the evolution of the correction as a function of the pupil diameter. In the strongest turbulence

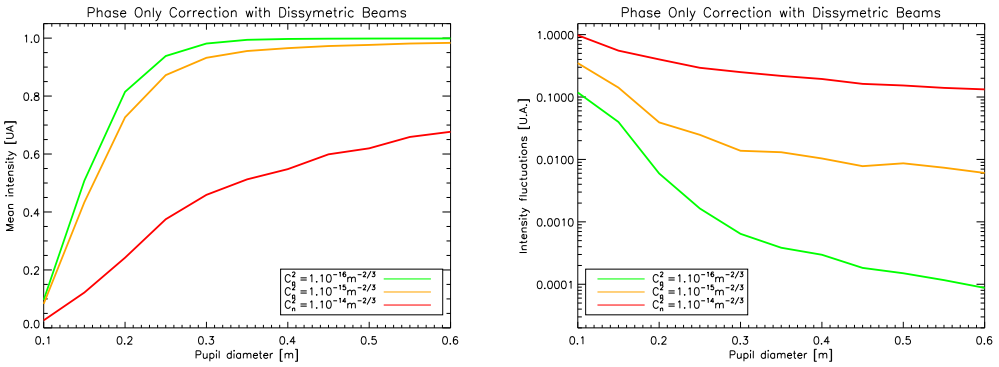

Figure 9. Performance of a phase-only dissymmetric beam correction as a function of pupil diameter. Propagation length: $10km$, $\lambda = 1.5\mu m$. Statistics calculated on 300 propagations. Left: mean normalized power in the bucket ($< I >$); right: normalized fluctuations of power in the bucket ($\frac{\sigma_I}{<I>}$).

studied case (i.e. $C_n^2 = 1.10^{-14} m^{-2/3}$), mean power in the bucket increases from 0.3 to 0.46 and brings normalized intensity fluctuations from 0.52 to 0.25. A typical realization of a phase-only correction utilizing dissymmetric beams is presented Figure 10.

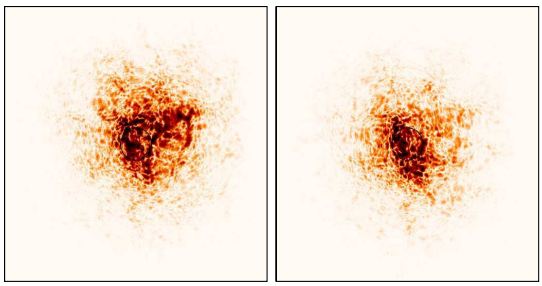

Figure 10. Typical energy repartition of a phase-only dissymmetric beam correction in the receiver plane. Left: No correction; right: correction. Circle represent a $30cm$ pupil. Propagation length: $10km$, $\lambda = 1.5\mu m$. $C_n^2 = 1.10^{-14} m^{-2/3}$. These two figures have been obtained under the same atmospheric turbulence conditions. Logarithmic scaling.

A summary of the different correction types is presented Table 1 where optimal, iterative phase-only and dissymmetric phase-only corrections can be compared. Although the dissymmetric phase-only precompensation gives poorer results than optimal iterative correction, it still provides a clear amelioration. For example: normalized intensity fluctuations are halved and mean power in the bucket is multiplied by 1.5 for $C_n^2 = 1.10^{-14} m^{-2/3}$.

Until now the exact phase has been used to perform the correction. Phase analysis problems have so far been discarded. WFS's are known to function poorly in strong scintillation regimes (see Figure 10). The next paragraph addresses the use of such a phase measurement.

4.2 Shack-Hartman Based Correction : noiseless case

A noiseless SH WFS is used to measure the phase of the back-propagating laser probe beam. The simulated SH is composed of 7 by 7 lenslets. Slopes are estimated from lenslet images. The correction is performed by a DM correcting 38 Zernike modes. Figure 11 illustrates the correction effectiveness as a function of pupil

	$C_n^2[m^{-2/3}]$	$< I >$	σ_I		$C_n^2[m^{-2/3}]$	$< I >$	σ_I
No Correction	1.10^{-16}	0.99	0.001	**Phase-Only**	1.10^{-16}	0.99	0.0007
	1.10^{-15}	0.92	0.04	**Iterative**	1.10^{-15}	0.96	0.01
	1.10^{-14}	0.31	0.5	**Correction**	1.10^{-14}	0.64	0.15
Optimal	1.10^{-16}	0.99	0.0003	**Phase-Only**	1.10^{-16}	0.98	0.0006
Iterative	1.10^{-15}	0.97	0.007	**Dissymmetric**	1.10^{-15}	0.93	0.01
Correction	1.10^{-14}	0.72	0.07	**Correction**	1.10^{-14}	0.46	0.25

Table 1. Comparative table of correction efficiency. Statistics are calculated from 300 propagations. Wavelength $1.5\mu m$, propagation distance: $10km$, pupil diameter: $30cm$.

diameter. Surprisingly under certain conditions of turbulence strength and pupil diameters the noiseless SH based correction can lead to better performances than with a perfect dissymmetric phase-only correction. The difference is small and this slight gain can be explained by the spatial filtering performed by each lenslet. This spatial filtering actually filters modes that deteriorate the quality of correction.

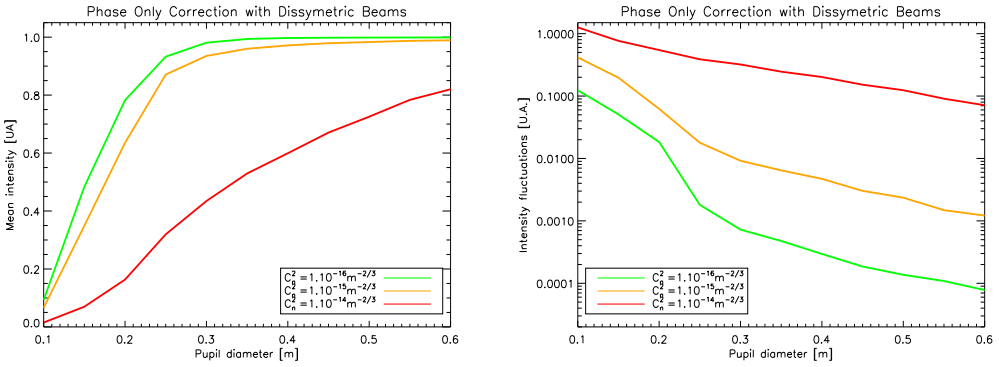

Figure 11. Performance of a phase-only dissymmetric beam correction as a function of pupil diameter. The phase measurement is performed by a noiseless 7 by 7 Shack-Hartmann WFS. Propagation length: $10km$, $\lambda = 1.5\mu m$. Statistics are calculated on 300 propagations. Left: mean normalized power in the bucket ($< I >$); right: normalized fluctuations of power in the bucket: ($\frac{\sigma_I}{<I>}$).

5. CORRECTION BY MODEL-FREE PHASE MODULATION

As previously shown, strong scintillation conditions deteriorate the accuracy of phase reconstruction. This leads to poor correction quality. Alternative methods, like phase modulation, avoiding the use of wavefront measurements, have been proposed in the early developments of AO [9, 10]. The main drawback of this technique lies in the convergence time of the correction. For this study, we use a segmented mirror in which each element can be driven in piston. Figure 12 illustrates a typical segmented mirror used for the simulations with addresses for each mirror segment. Phase modulation precompensation technique needs both a low data-rate feedback and an ultra-fast DM.

5.1 Sequential Perturbations

Optimization is done sequentially by addressing one mirror segment at a time. The figure of merit is estimated for the 21 positions of each segment. We keep the mirror element in the position that maximizes the received energy in the bucket. After having addressed all mirror segments, another round is performed. The first round of optimization gives excellent results and demonstrates that, when using a sequential perturbation correction, it is unnecessary to continue any further [11]. Figure 13 shows the evolution of both metrics as a function of addressed mirror segment.

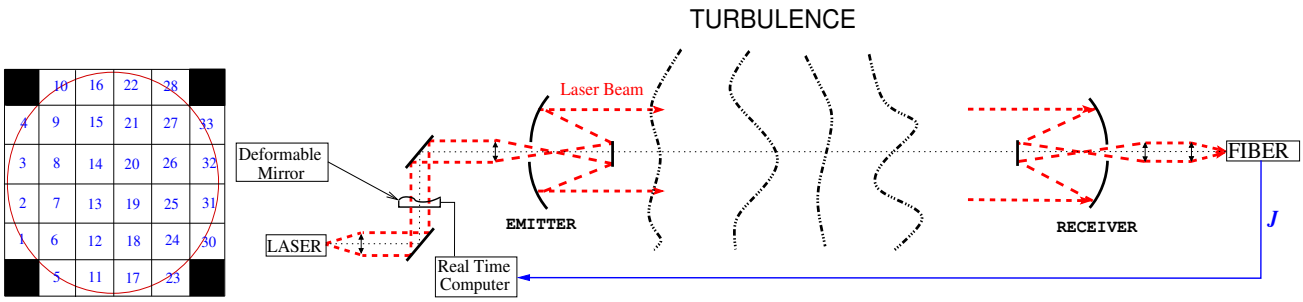

Figure 12. Left: sketch of segmented mirror and address of each mirror element for a 6 by 6 mirror. Numbers represent the address of each element. Right: Configuration of a phase modulation precompensation device. The real time computer (RTC) updates the mirror surface by knowing metric J.

The correction is performed with a 7 by 7 segments mirror, that is with roughly the same number of degrees of correction as in the previous case (probe plus WFS). The correction performed by a sequential perturbation correction yields similar results. Nonetheless, under strong turbulence conditions, phase modulation seems to perform even better. The evolution curves as a function of the segment number evolves slowly at the beginning

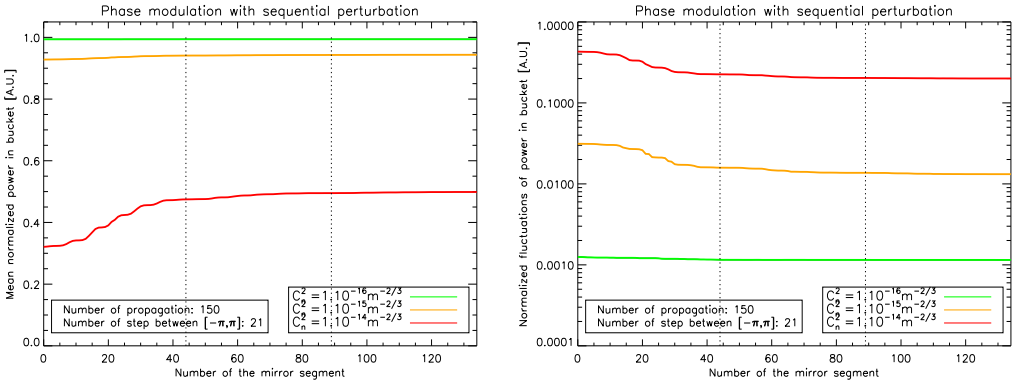

Figure 13. Performance of a sequential perturbations correction. Precision of piston steps: $\lambda/21$. Vertical dashed lines design when all segments have been addressed; another round of correction is then performed starting by element number 1. Propagation length: $10km$, $\lambda = 1.5\mu m$, pupil diameter: $30cm$. Statistics are performed on 150 propagations. Left: mean normalized power in the bucket ($< I >$); right: normalized fluctuations of power in the bucket ($\frac{\sigma_I}{<I>}$). Number of segments for the deformable mirror: $7 * 7$.

and slowly at the end of a cycle. Only the middle part, progressing by steps, seems to evolve rapidly. This is due to the way we address the mirror segments. The mirror segments located at the center correspond to the most energetic part of the beam.

5.2 Parallel Perturbations: SPGD

The main drawback of phase modulation is its response time. To diminish the time of convergence, an algorithm based on stochastic parallel gradient descent (SPGD) has been proposed [6, 12]. For each mirror segment, an elementary perturbation ϵ is applied; this perturbation has a given amplitude but a random sign $\delta u_I = \mp\epsilon$. The obtained power in the bucket after precompensation and propagation through turbulence is given by I_+. Next, the exact opposite of the previous elementary perturbations is applied and the obtained power in the bucket is then noted I_-. Let u_I^n be the mirror position at iteration n. Correction updates of mirror segments at step $n+1$ is done according to the rule [12]:

$$u_I^{n+1} = u_I^n + \gamma(I_+^n - I_-^n) sign(\delta u_I^n)\,, \tag{5}$$

where γ can either be a constant or a variable. A constant γ has been used. A variable γ has been proposed [13] to increase the convergence speed of the SPGD algorithm and this issue is currently being address by the

authors. We can observe that the results obtained are comparable to those obtained by sequential perturbations. Only a ten or so iterations seem necessary to converge to a good correction quality, as compared to a few hundred for sequential perturbations.

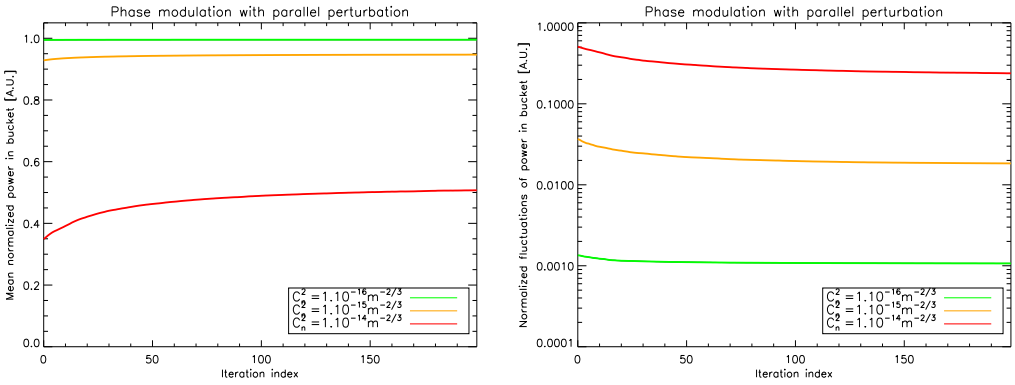

Figure 14. Performance of a SPGD perturbations correction. Precision of piston steps: $\lambda/21$. Vertical dashed lines designateq when all segments have been addressed; another round of correction is then performed starting by element number 1. Propagation length: $10km$, $\lambda = 1.5\mu m$, pupil diameter: $30cm$. Statistics are performed on 150 propagations. Left: mean normalized power in the bucket ($< I >$); right: normalized fluctuations of power in the bucket ($\frac{\sigma_I}{<I>}$). Number of segments for the deformable mirror: $7 * 7$.

6. DISCUSSION

We studied the impact of different correction strategies for a Free-Space optical communication system. These strategies were compared to an optimal correction based on iterative phase conjugation precompensation. These correction types comprise of a phase-only iterative correction, a dissymmetric phase-only correction and a phase modulation correction. It has been shown that a simple correction implementing a single mirror and thus a phase-only correction is possible. Moreover it has been shown that both dissymmetric and phase modulation can produce good correction quality. Nevertheless, none of these techniques is a clear winner. The turbulence coherence time is of the order of $5ms$ to $10ms$ for classical turbulence strength and medium wind speed ($\approx 10m/s$) for the case studied here. In order to use a phase modulation correction, the deformable mirror will have to be frequently updated during the lifetime of atmospheric turbulent cells. On the other hand techniques based on SH-WFS are not robust and lose accuracy in strong turbulences.

A pupil of approximately $30cm$ has been shown to be sufficient to enable good correction quality. If the correction needs to be improved further (even longer distances, stronger turbulence) then it will be necessary to implement at least a two mirror precompensation. A test bench is currently under development at ONERA to study phase modulation correction.

ACKNOWLEDGMENTS

This work has been realized in the framework of a Ph.D. thesis. Funding for this work was provided by ONERA and the Provence Alpes Côte d'Azur region.

REFERENCES

[1] Andrews, L. C. and Phillips, R. L., [*Laser Beam Propagation through Random Media*], SPIE Press, Bellingham, Wash. (1998).

[2] Bloom, S., Korevaar, E., Schuster, J., and Willebrand, H., "Understanding the performance of free-space optics [invited]," *J. Opt. Netw.* **2**, 178–200 (2003).

[3] Ricklin, J., Bucaille, S., and Davidson, F. M., "Performance loss factors for optical communication through clear air turbulence," in [*Free-Space Laser Communication and Active Laser Illumination III*], Voelz, D. G. and Ricklin, J. C., eds., *Proc. SPIE* **5160**, 1–12 (2004).

[4] Tyson, R. K., "Bit-error rate for free-space adaptive optics laser communications," *J. Opt. Soc. Am. A* **19**, 753–758 (2002).

[5] Yu, M. and Vorontsov, M. A., "Compensation of distant phase-distorting layers. I. narrow-field-of-view adaptive receiver system," *J. Opt. Soc. Am.* **21**, 1645–1658 (Sep 2004).

[6] Vorontsov, M. A., Carhart, G. W., and Ricklin, J. C., "Adaptive phase-distortion correction based on parallel gradient descent optimization," *Opt. Lett.* **22**, 907–909 (1997).

[7] Barchers, J. D. and Fried, D. L., "Optimal control of laser beams for propagation through a turbulent medium," *J. Opt. Soc. Am. A* **19**, 1779–1793 (2002).

[8] Tyson, R. K., Canning, D. E., and Tharp, J. S., "Measurement of the bit-error rate of an adaptive optics, free-space laser communications system, part 1: tip-tilt configuration, diagnostics, and closed-loop results," *Optical Engineering* **44**(9) (2005).

[9] Hardy, J. W., "Active optics: a new technology for the control of light," *Proc. IEEE* **66**, 651–697 (1978).

[10] O'Meara, T. R., "The multidither principle in adaptive optics," *J. Opt. Soc. Am.* **67**, 306–315 (1977).

[11] Vellekoop, I. M. and Mosk, A. P., "Focusing coherent light through opaque strongly scattering media," *Opt. Lett.* **32**, 2309–2311 (2007).

[12] Weyrauch, T. and Vorontsov, M. A., "Atmospheric compensation with a speckle beacon in strong scintillation conditions: directed ernergy and laser communication applications," *Appl. Opt.* **44**, 6388–6401 (2005).

[13] Weyrauch, T., Vorontsov, M., Bifano, T., Hammer, J., Cohen, M., and Cauwenberghs, G., "Microscale adaptive optics: wave-front control with a μ-mirror array and a VLSI stochastic gradient descent controller," *Appl. Opt.* **40**, 4243–4253 (2002).

Appendix C

List of Publications

Peer Reviewed Articles

A. Khalighi, **N. Schwartz**, N. Aitamer, S. Bournnane, *Fading Reduction by Aperture Averaging and Spatial Diversity in Optical Wireless Systems*, J. Opt. Commun. Netw., 1, pp. 580-593, 2009.

Conference Articles

A. Khalighi, N. Aitamer, **N. Schwartz**, S. Bournnane, *Turbulence Mitigation by Spatial Diversity in Optical Wireless Systems*, ConTel09, June 2009.

N. Schwartz, N. Vedrenne, V. Michau, M.-T. Velluet, and F. Chazallet, *Mitigation of atmospheric effects by adaptive optics for free-space optical communications*, Proc. SPIE 7200, Janurary 2009.

Bibliography

Bibliography

[Achour-a-03] M. ACHOUR, Free-space optics wavelength selection: 10 μm versus shorter wavelengths [invited], J. Opt. Netw., 2(6):127–143, June 2003.

[Al-Habash-a-01] M. A. AL-HABASH, L. C. ANDREWS, ET R. L. PHILLIPS, Mathematical model for the irradiance probability density function of a laser beam propagating through turbulent media, Optical Engineering, 40:1554–1562, August 2001.

[Aljada-p-06] M. ALJADA, K. ALAMEH, ET K. AL-BEGAIN, Distributed wireless optical communications for humanitarian assistance in disasters, Proc. of IEEE, Jan. 2006, pp. 4 pp.–.

[Andrews-a-01] L. C. ANDREWS, M. A. AL-HABASH, C. Y. HOPEN, ET R. L. PHILLIPS, Theory of optical scintillation: Gaussian-beam wave model, Waves in Random Media, 11:271–291, Juil. 2001.

[Andrews-a-99] L. C. ANDREWS, R. L. PHILLIPS, C. Y. HOPEN, ET M. A. AL-HABASH, Theory of optical scintillation, J. Opt. Soc. Am. A, 16(6):1417–1429, 1999.

[Andrews-l-01] L. C. ANDREWS, R. L. PHILLIPS, ET C. Y. HOPEN, Laser beam scintillation with applications, SPIE Press, Bellingham, 2001.

[Andrews-l-98] L. C. ANDREWS ET R. L. PHILLIPS, Laser beam propagation through random media, Proc. Soc. Photo-Opto. Instrum. Eng., 1998.

[Andrews-p-08] L. C. ANDREWS ET R. L. PHILLIPS, Recent results on optical scintillation in the presence of beam wander, vol. 6878, Proc. Soc. Photo-Opto. Instrum. Eng., 2008, p. 687802.

[Aubailly-a-08] M. AUBAILLY ET M. A. VORONTSOV, Imaging with an array of adaptive subapertures, Opt. Lett., 33(1):10–12, 2008.

[Babcock-a-53] B. BABCOCK, The possibility of compensating estronomical seeing, Astronomical Society of the Pacific, 65:229–236, 1953.

[Barchers-a-01-a] J. D. BARCHERS ET B. L. ELLERBROEK, Improved compensation of turbulence-induced amplitude and phase distortions by means of multiple near-field phase adjustments, J. Opt. Soc. Am. A, 18:399–411, February 2001.

[Barchers-a-01-b] J. D. BARCHERS, Evaluation of the impact of finite-resolution effects on scintillation compensation using two deformable mirrors, J. Opt. Soc. Am. A, 18:3098–3109, December 2001.

[Barchers-a-02-a] ——, Closed-loop stable control of two deformable mirrors for compensation of amplitude and phase fluctuations, J. Opt. Soc. Am. A, 19:926–945, May 2002.

[Barchers-a-02-b] J. D. BARCHERS ET D. L. FRIED, Optimal control of laser beams for propagation through a turbulent medium, J. Opt. Soc. Am. A, 19:1779–1793, September 2002.

[Baykal-a-09] Y. BAYKAL, H. T. EYYUBOĞLU, ET Y. CAI, Scintillations of partially coherent multiple gaussian beams in turbulence, Appl. Opt., 48(10):1943–1954, 2009.

[Begley-p-02] D. BEGLEY, "free-space laser communications: a historical perspective", vol. 2, LEOS, Proc IEEE, Nov. 2002, pp. 391–392 vol.2.

[Bell-a-1880] A. G. BELL, The photophone, Science, 1:130–134, September 1880.

[Belmonte-a-97] A. BELMONTE, A. COMERÓN, J. A. RUBIO, J. BARÁ, ET E. FERNÁNDEZ, Atmospheric-turbulence-induced power-fade statistics for a multiaperture optical receiver, Appl. Opt., 36(33):8632–8638, 1997.

[Bissonnette-a-79] L. R. BISSONNETTE ET P. L. WIZINOWICH, Probability distribution of turbulent irradiance in a saturation regime, Appl. Opt., 18(10):1590–1599, 1979.

[Bloom-a-03] S. BLOOM, E. KOREVAAR, J. SCHUSTER, ET H. WILLEBRAND, Understanding the performance of free-space optics [invited], J. Opt. Netw., 2(6):178–200, June 2003.

[Borgnino-a-92] J. BORGNINO, F. MARTIN, ET A. ZIAD, Effect of finite spatial-coherence outer scale on the covariances of angle-of-arrival fluctuations, Opt. Commun., 91, 1992.

[Bouchet-l-04] O. BOUCHET, H. SIZUN, C. BOISROBERT, F. DE FORNEL, ET P. FAVENNEC, Optique sans fils, Hermès - Lavoisier, Collection Technique et Scientifique des Télécommunications, Paris, 2004.

[Breguet-a-1880] B. ANTOINE, Le photophone de bell, J. Phys. Theor. Appl, 9:369–375, 1880.

[Bruesselbach-a-95] H. BRUESSELBACH, D. C. JONES, D. A. ROCKWELL, R. C. LIND, ET G. VOGEL, Real-time atmospheric compensation by stimulated brillouin-scattering phase conjugation, J. Opt. Soc. Am. B, 12:1434–1447, August 1995.

[Buffington-a-77] A. BUFFINGTON, F. S. CRAWFORD, R. A. MULLER, A. J. SCHWEMIN, ET R. G. SMITS, Correction of atmospheric distortion with an image-sharpening telescope, J. Opt. Soc. Am. A, 67(3):298–303, 1977.

[Cai-a-08] Y. CAI, H. T. EYYUBOGLU, ET Y. BAYKAL, Scintillation of astigmatic dark hollow beams in weak atmospheric turbulence, J. Opt. Soc. Am. A, 25(7):1497–1503, July 2008.

[Carbon-p-03] M. CARBON, Laser beam shaping in space using adaptive optics, vol. 5087, Proc. Soc. Photo-Opto. Instrum. Eng., 2003, pp. 83–86.

[Churnside-a-90] J. H. CHURNSIDE ET R. J. LATAITIS, Wander of an optical beam in the turbulent atmosphere, Appl. Opt., 29(7):926–930, 1990.

[Clifford-a-74] S. F. CLIFFORD, G. R. OCHS, ET R. S. LAWRENCE, Saturation of optical scintillation by strong turbulence, J. Opt. Soc. Am. A, 64(2):148–154, 1974.

[Clifford-l-78] S. F. CLIFFORD, The clasical theory of wave propagation in a turbulent medium, Springer-Verlag, Berlin, 1978, pp. 9–43.

[Davis-p-02] C. C. DAVIS ET I. I. SMOLYANINOV, Effect of atmospheric turbulence on bit-error rate in an on-off-keyed optical wireless system, vol. 4489, Proc. Soc. Photo-Opto. Instrum. Eng., 2002, pp. 126–137.

[Dios-a-08] F. DIOS, J. RECOLONS, A. RODRIGUEZ, ET O. BATET, Temporal analysis of laser beam propagation in the atmosphere using computer-generated long phase screens, Opt. Express, 16(3):2206–2220, February 2008.

[Eardley-p-95] P. EARDLEY ET D. WISELY, 1 gbit/s optical free space link operating over 40 m system and applications, vol. 143, Proc IEEE, Dec 1996, pp. 330–333.

[Eyyuboglu-a-06] H. T. EYYUBOGLU, ÇAGLAR ARPALI, ET Y. K. BAYKAL, Flat topped beams and their characteristics in turbulent media, Opt. Express, 14(10):4196–4207, 2006.

[Fante-p-75] R. L. FANTE, Electromagnetic beam propagation in turbulent media, vol. 63, IEEE Proceedings, December 1975, pp. 1669–1692.

[Flatte-a-94] S. M. FLATTÉ, C. BRACHER, ET G.-Y. WANG, Probability-density functions of irradiance for waves in atmospheric turbulence calculated by numerical simulation, J. Opt. Soc. Am. A, 11(7):2080–2092, 1994.

[Frehlich-a-00] R. FREHLICH, Simulation of laser propagation in a turbulent atmosphere, 39:393–397, January 2000.

[Fried-a-66] D. L. FRIED, Optical resolution through a randomly inhomogeneous medium for very long and very short exposures, J. Opt. Soc. Am. A, 56:1372–1379, 1966.

[Fried-a-67] ——, Aperture averaging of scintillation, J. Opt. Soc. Am. A, 57:169–175, 1967.

[Fried-a-72] D. L. FRIED ET H. T. YURA, Telescope-performance reciprocity for propagation in a turbulent medium, J. Opt. Soc. Am. A, 62(4):600–602, 1972.

[Fried-a-82] D. L. FRIED, Anisoplanatism in adaptive optics, J. Opt. Soc. Am. A, 72(1):52, January 1982.

[Fried-a-92] D. L. FRIED ET J. L. VAUGHN, Branch cuts in the phase function, Appl. Opt., 31(15):2865–2882, 1992.

[Gagliardi-l-76] R. M. GAGLIARDI ET S. KARP, Optical communications, 1976.

[Gendron-a-07] E. GENDRON, F. POUPLARD, F. VIDAL, Z. HUBERT, D. PERRET, ET G. ROUSSET, A new linear optical differentiation wavefront sensor for laser tomography on elts, in Adaptive Optics: Analysis and Methods/Computational Optical Sensing and Imaging/Information Photonics/Signal Recovery and Synthesis Topical Meetings on CD-ROM, Optical Society of America, 2007, p. ATuB4.

[Giggenbach-p-02] D. GIGGENBACH, F. DAVID, R. LANDROCK, K. PRIBIL, E. W. FISCHER, R. G. BUSCHNER, ET D. BLASCHKE, Measurements at a 61-km near-ground optical transmission channel, vol. 4635, Proc. Soc. Photo-Opto. Instrum. Eng., 2002, pp. 162–170.

[Gochelashvily-a-71] K. S. GOCHELASHVILY ET S. V. I., Laser beam scintillation beyond a turbulent layer, Journal of Modern Optics, 18:131–320, 1971.

[Gonsalves-a-82] R. A. GONSALVES, Phase retrieval and diversity in adaptive optics, Optical Engineering, 21:829–832, Oct. 1982.

[Goodman-l-85] J. W. GOODMAN, Statistical Optics, Wiley-Interscience, 1985.

[Gracheva-a-65] M. E. GRACHEVA ET A. S. GURVICH, Strong fluctuations in the intensity of light propagated through the atmosphere close to earth, Soviet Radiophysics, 8:511–515, 1965.

[Hardy-a-77] J. W. HARDY, J. E. LEFEBVRE, ET C. L. KOLIOPOULOS, Real-time atmospheric compensation, J. Opt. Soc. Am. A, 67(3):360–369, 1977.

[Hardy-p-78] J. W. HARDY, Active optics: a new technology for the control of light, vol. 66 of Proc. IEEE, 1978, pp. 651–697.

[Henderson-p-08] B. G. HENDERSON ET J. D. MANSELL, Laser beam shaping with membrane deformable mirrors, vol. 7093, Proc. Soc. Photo-Opto. Instrum. Eng., 2008, p. 70930I.

[Hufnagel-p-74] R.-E. HUFNAGEL, Variations of atmospheric turbulence, in Proc. of Topical Meeting on Optical Propagation through the Turbulence, 1974.

[Hutchinson-l-08] D. P. HUTCHINSON ET R. K. RICHARDS, All-weather long-wavelength infrared free space optical communications, in Majumdar et Ricklin [Majumdar-l-08], pp. 407–417.

[Khalighi-a-09-b] M.-A. KHALIGHI, N. SCHWARTZ, N. AITAMER, ET S. BOURENNANE, Fading reduction by aperture averaging and spatial diversity in optical wireless systems, J. Opt. Commun. Netw., 1(6):580–593, 2009.

[Kiasaleh-a-06] K. KIASALEH, On the scintillation index of a multiwavelength gaussian beam in a turbulent free-space optical communications channel, J. Opt. Soc. Am. A, 23:557–566, 2006.

[Killinger-a-02] D. KILLINGER, Free space optics for laser communication through the air, Opt. Photon. News, 13(10):36–42, 2002.

[Kim-p-97] I. I. KIM, H. HAKAKHA, P. ADHIKARI, E. J. KOREVAAR, ET A. K. MAJUMDAR, Scintillation reduction using multiple transmitters, vol. 2990, Proc. Soc. Photo-Opto. Instrum. Eng., 1997, pp. 102–113.

[Kolmogorov-a-41] A. N. KOLMOGOROV, Local structure of turbulence in incompressible fluids with very high reynolds number, Dokl. Akad. Nauk. SSSR, 30(4):301–305, 1941.

[Lee-p-69] R. LEE ET J. HARP, Correction to "weak scattering in random media, with applications to remote probing", vol. 57, Nov. 1969, pp. 2094–2094.

[Li-p-05] Y. LI, Gaussian to annular beam shaping, vol. 5876, Proc. Soc. Photo-Opto. Instrum. Eng., 2005, p. 587609.

[Linnick-a-57] V. P. LINNICK, On the possibility of reducing the influence of atmospheric seeing on the image quality of stars (in russian), Optics and Spectroscopy, 3:401–402, 1957.

[Lipsett-a-69] M. LIPSETT, C. MCINTYRE, ET R. LIU, Space instrumentation for laser communications, Quantum Electronics, IEEE Journal of, 5(6):348–349, Jun 1969.

[Loizos-p-06] D. LOIZOS, P. SOTIRIADIS, ET G. CAUWENBERGHS, A robust continuous-time multi-dithering technique for laser communications using adaptive optics, Proc. IEEE, 2006, p. 3629.

[Lucy-a-68] R. F. LUCY ET K. LANG, Optical communications experiments at 6328 and 10.6 μ, Appl. Opt., 7(10):1965–1970, 1968.

[Lukin-a-02] V. P. LUKIN ET B. V. FORTES, Phase-correction of turbulent distortions of an optical wave propagating under conditions of strong intensity fluctuations, Appl. Opt., 41(27):5616–5624, 2002.

[Lutomirski-a-71] H. T. LUTOMIRSKI, R. F. AND. YURA, Propagation of a finite optical beam in an inhomogeneous medium, Appl. Opt., 10(7):1652–1658, 1971.

[Mahe-p-00] F. MAHÉ, V. M. G. ROUSSET, ET J.-M. CONAN, Scintillation effects on wavefront sensing in the rytov regime, in Propagation through the Atmosphere IV, M. Roggemann, ed., vol. 4125, Bellingham, Washington, Aug 2000, Proc. Soc. Photo-Opto. Instrum. Eng., pp. 77–86.

[Mahe-t-00] F. MAHÉ, Application d'un modèle atmosphérique à l'étude des fluctuations d'indice de réfraction dans la couche limite. Influence de la scintillation sur l'analyse de front d'onde, Thèse de doctorat, Université de Nice-Sophia Antipolis, France, February 2000.

[Majumdar-l-08] A. MAJUMDAR ET J. RICKLIN, eds., Free-Space Laser Communications, Principles and Advances, vol. 2, Springer, Berlin, 2008.

[Majumdar-p-07] A. K. MAJUMDAR, C. E. LUNA, ET P. S. IDELL, Reconstruction of probability density function of intensity fluctuations relevant to free-space laser communications through atmospheric turbulence, vol. 6709, Proc. Soc. Photo-Opto. Instrum. Eng., 2007, p. 67090M.

[Manor-a-03] H. MANOR ET S. ARNON, Performance of an optical wireless communication system as a function of wavelength, Appl. Opt., 42:4285–4294, 2003.

[Mansell-p-06] J. D. MANSELL, Beam shaping for relay mirrors, vol. 6290, Proc. Soc. Photo-Opto. Instrum. Eng., 2006, p. 62900K.

[Martin-a-88] J. M. MARTIN ET S. M. FLATTÉ, Intensity images and statistics from numerical simulation of wave propagation in 3-d media, Appl. Opt., 11:2111–2126, 1988.

[McAulay-p-99] A. D. MCAULAY ET J. LI, Improving bandwidth for line-of-sight optical wireless in turbulent air by using phase conjugation, vol. 3850, Proc. Soc. Photo-Opto. Instrum. Eng., 1999, pp. 32–39.

[McCall-a-77] S. L. MCCALL, T. R. BROWN, ET A. PASSNER, Improved optical stellar image using a real-time phase-correction system: initial results, Astrophysical Journal, 211:463–468, Jan. 1977.

[McGlamery-p-76] B. L. MCGLAMERY, Computer simulation studies of compensation of turbulence degraded images, Proc. Soc. Photo-Opto. Instrum. Eng., 1976, pp. 225–233.

[Miller-a-94] W. B. MILLER, J. C. RICKLIN, ET L. C. ANDREWS, Effects of the refractive index spectral model on the irradiance variance of a gaussian beam, J. Opt. Soc. Am. A, 11(10):2719–2726, 1994.

[Mironov-l-81] V. L. MIRONOV, Laser beam propagation in turbulence atmosphere, Nauka, Moscow, 1981.

[Monin-a-54] A. S. MONIN ET A. M. OBUKHOV, Basic regularity in turbulence mixing in the surface layer of the atmosphere, Trad. Geophys. Inst. ANSSSR, p. 163, 1954.

[Mugnier-l-06] L. M. MUGNIER, A. BLANC, ET J. IDIER, Phase diversity: a technique for wave-front sensing and for diffraction-limited imaging, in Advances in Imaging and Electron Physics, P. Hawkes, ed., vol. 141, Elsevier, 2006, ch. 1, pp. 1–76.

[Nelder-a-65] J. NELDER ET R. MEAD, A simplex method for function minimization, Computer Journal, 7:308–313, 1965.

[Nicolle-a-04] M. NICOLLE, T. FUSCO, G. ROUSSET, ET V. MICHAU, Improvement of shack-hartmann wave-frontsensor measurement for extreme adaptive optics, Opt. Lett., 29(23):2743–2745, 2004.

[Noll-a-76] R. J. NOLL, Zernike polynomials and atmospheric turbulence, J. Opt. Soc. Am. A, 66:207–211, March 1976.

[Northcott-p-07] M. J. NORTHCOTT, A. MCCLAREN, J. E. GRAVES, J. PHILLIPS, D. DRIVER, D. ABELSON, D. W. YOUNG, J. E. SLUZ, J. C. JUAREZ, M. B. AIROLA, R. M. SOVA, H. HURT, ET J. FOSHEE, Long distance laser communications demonstration, vol. 6578, Proc. Soc. Photo-Opto. Instrum. Eng., 2007, p. 65780S.

[Obukhov-a-49] A. M. OBUKHOV, Structure of the temperature field in a turbulent current, Izvestiya Akademia Nauk SSSR, Series Goegraficheskaya i Geograficheskaya, 13(6):58–69, 1949.

[Omeara-a-77] T. R. OMEARA, The multidither principle in adaptive optics, J. Opt. Soc. Am. A, 67:306–315, March 1977.

[Parzen-a-62] P. E., Estimation of a probability density fonction and its mode, Ann. Math. Statist., 33, 1962.

[Peleg-a-06] A. PELEG ET J. V. MOLONEY, Scintillation index for two gaussian laser beams with different wavelengths in weak atmospheric turbulence, J. Opt. Soc. Am. A, 23(12):3114–3122, 2006.

[Plett-t-07] M. L. PLETT, Free-space optical communication link across 16 kilometers to a modulated retro-reflector array, Thèse de doctorat, University of Maryland, College Park, 2007.

[Polynkin-a-07] P. POLYNKIN, A. PELEG, L. KLEIN, T. RHOADARMER, ET J. MOLONEY, Optimized multiemitter beams for free-space optical communications through turbulent atmosphere, Opt. Letters, 32(8):885–887, April 2007.

[Poyneer-a-03] L. A. POYNEER, Scene-based shack-hartmann wave-front sensing: Analysis and simulation, Appl. Opt., 42(29):5807–5815, 2003.

[Prasad-l-08] P. S. N., Optical communications in the mid-wave ir spectral band, in Majumdar et Ricklin [Majumdar-l-08], pp. 347–391.

[Press-l-86] W. PRESS, B. FLANNERY, S. TEUKOLSKY, ET W. VETTERLING, Numerical Recipes: the Art of Scientific Programming, Cambrigde University Press, New York, 1986.

[Primmerman-a-91] C. A. PRIMMERMAN, D. V. MURPHY, B. G. ZOLLARS, ET H. T. BARCLAY, Compensation of atmospheric optical distortion using a synthetic beacon, Nature, 353(6340):141–143, September 1991.

[Primmerman-a-95] C. A. PRIMMERMAN, T. R. PRICE, R. A. HUMPHREYS, B. G. ZOLLARS, H. T. BARCLAY, ET J. HERRMANN, Atmospheric-compensation experiments in strong-scintillation conditions, Appl. Opt., 34(12):2081–2088, April 1995.

[Ragazzoni-a-96] R. RAGAZZONI, Pupil plane wavefront sensing with an oscillating prism, Journal of Modern Optics, 43:289–293, Fev. 1996.

[Razavi-p-05] M. RAZAVI ET J. SHAPIRO, Wireless optical communications via diversity reception and optical preamplification, Wireless Communications, IEEE Transactions on, 4(3):975–983, May 2005.

[Ricklin-l-08] J. C. RICKLIN, S. M. HAMMEL, F. D. EATON, ET S. L. LACHINOVA, Atmospheric channel effects on free-space laser, in Majumdar et Ricklin [Majumdar-l-08], pp. 9–56.

[Roddier-a-88] F. RODDIER, Curvature sensing and compensation: a new concept in adaptive optics, Appl. Opt., 27:1223–1225, 1988.

[Roddier-a-97] F. RODDIER ET C. RODDIER, Stellar coronograph with phase mask, Publications of the Astronomical Society of the Pacific, 109:815–820, juillet 1997.

[Roddier-l-99] F. RODDIER, Adaptive optics in astronomy, Adaptive Optics in Astronomy, 1999.

[Roggemann-a-98] M. C. ROGGEMANN ET D. J. LEE, Two-deformable-mirror concept for correcting scintillation effects in laser beam projection through the turbulent atmosphere, Appl. Opt., 21:4577–4585, 1998.

[Rousset-a-90] G. ROUSSET, J. C. FONTANELLA, P. KERN, F. GIGAN, ET E. A. LENA, P., First diffraction-limited astronomical images with adaptive optics, Astron. Astrophys., 230:L29–L32, 1990.

[Rousset-l-99] G. ROUSSET, Wave-front sensors, [Roddier-l-99], pp. 91–130.

[Ruillier-a-01] C. RUILLIER ET F. CASSAING, Coupling of large telescopes and single-mode waveguides: application to stellar interferometry, J. Opt. Soc. Am. A, 18:143–149, 2001.

[Rytov-l-87] S. RYTOV, Y. KRAVTSOV, ET V. TATARSKII, eds., Principles of statistical radiophysics: Wave propagation through random media, vol. 4, Springer-Verlag, Berlin, 1960.

[Sandalidis-a-08] H. SANDALIDIS, T. TSIFTSIS, G. KARAGIANNIDIS, ET M. UYSAL, Ber performance of fso links over strong atmospheric turbulence channels with pointing errors, Communications Letters, IEEE, 12(1):44–46, January 2008.

[Schmidt-p-09] J. D. SCHMIDT ET J. A. LOUTHAIN, Integrated approach to free-space optical communication, vol. 7200, Proc. Soc. Photo-Opto. Instrum. Eng., 2009, p. 72000I.

[Schwartz-p-09] N. H. SCHWARTZ, N. VÉDRENNE, V. MICHAU, M.-T. VELLUET, ET F. CHAZALLET, Mitigation of atmospheric effects by adaptive optics for free-space optical communications, vol. 7200, Proc. Soc. Photo-Opto. Instrum. Eng., 2009, p. 72000J.

[Shack-a-71] R. B. SHACK ET B. R. PLATT, Production and use of a lenticular hartmann screen, J. Opt. Soc. A, 61, 1971.

[Shannon-l-49] C. E. SHANNON ET W. WEAVER, The Mathematical Theory of Communication, Illinois Press, Urbana, IL, 1949.

[Sova-p-06] R. M. SOVA, J. E. SLUZ, D. W. YOUNG, J. C. JUAREZ, A. DWIVEDI, N. M. I. DEMIDOVICH, J. E. GRAVES, M. NORTHCOTT, J. DOUGLASS, J. PHILLIPS, J. DRIVER, A. MCCLARIN, ET D. ABELSON, 80 gb/s free-space optical communication demonstration between an aerostat and a ground terminal, vol. 6304, Proc. Soc. Photo-Opto. Instrum. Eng., 2006, p. 630414.

[Tatarski-l-61] V. I. TATARSKII, Wave Propagation in a Turbulent Medium, Dover Publications Inc., New York, 1961.

[Tatarski-l-71] ——, The effects of the turbulent atmosphere on wave propagation, Jerusalem: Israel Program for Scientific Translations, 1971, 1971.

[Tyson-a-03] R. K. TYSON ET D. E. CANNING, Indirect measurement of a laser communications bit-error-rate reduction with low-order adaptive optics, Appl. Opt., 42(21):4239–4243, 2003.

[Tyson-p-05-b] R. K. TYSON, J. S. THARP, ET D. E. CANNING, Measurement of the bit-error rate of an adaptive optics, free-space laser communications system, part 2: multichannel configuration, aberration characterization, and closed-loop results, Optical Engineering, 44(9):096003, 2005.

[Vedrenne-t-08] N. VEDRENNE, Propagation optique et correction en forte turbulence, Thèse de doctorat, Université de Nice-Sophia Antipolis, 2008.

[Vellekoop-a-07] I. M. VELLEKOOP ET A. P. MOSK, Focusing coherent light through opaque strongly scattering media, Opt. Lett., 32:2309–2311, 2007.

[Velluet-p-07] M.-T. VELLUET, V. MICHAU, T. FUSCO, ET J.-M. CONAN, Coherent illumination for wavefront sensing and imaging through turbulence, in Atmospheric Optics: Models, Measurements, and Target-in-the-Loop Propagation, S. M. Hammel, A. M. J. van Eijk, M. T. Valley, et M. A. Vorontsov, eds., vol. 6708, 2007.

[Viterbi-l-79] A. J. VITERBI ET O. J. K., Principles of Digital Communication and Coding, McGraw-Hill, New York, 1979.

[Voelz-p-04] D. VOELZ ET K. FITZHENRY, Pseudo-partially coherent beam for free-space laser communication, vol. 5550, Proc. Soc. Photo-Opto. Instrum. Eng., 2004, pp. 218–224.

[Voitsekhovich-a-01] V. V. VOITSEKHOVICH, V. G. ORLOV, ET L. J. SANCHEZ, Influence of scintillations on the performance of adaptive astronomical systems with hartmann-like wavefront sensors, Astron. Astrophys., 368:1133–1136, mar 2001.

[Vorontsov-a-00] M. A. VORONTSOV, G. W. CARHART, M. COHEN, ET G. CAUWENBERGHS, Adaptive optics based on analog parallel stochastic optimization: analysis and experimental demonstration, J. Opt. Soc. Am. A, 17(8):1440–1453, 2000.

[Vorontsov-a-02] M. A. VORONTSOV, Decoupled stochastic parallel gradient descent optimization for adaptive optics: integrated approach for wave-front sensor information fusion, J. Opt. Soc. Am. A, 19:356–368, 2002.

[Vorontsov-a-97] M. A. VORONTSOV, G. W. CARHART, ET J. C. RICKLIN, Adaptive phase-distortion correction based on parallel gradient-descent optimization, Opt. Lett., 22(12):907–909, June 1997.

[Wakamori-a-07] K. WAKAMORI, K. KAZAURA, ET I. OKA, Experiment on regional broadband network using free-space-optical communication systems, J. Lightwave Technol., 25(11):3265–3273, 2007.

[Weyrauch-a-01] T. WEYRAUCH, M. VORONTSOV, T. BIFANO, J. HAMMER, M. COHEN, ET G. CAUWENBERGHS, Microscale adaptive optics: wave-front control with a μ-mirror array and a VLSI stochastic gradient descent controller, Appl. Opt., 40:4243–4253, 2001.

[Weyrauch-a-05] T. WEYRAUCH ET M. A. VORONTSOV, Atmospheric compensation with a speckle beacon in strong scintillation conditions: directed ernergy and laser communication applications, Appl. Opt., 44:6388–6401, 2005.

[Weyrauch-l-08] ——, Free-space laser communications with adaptive optics: Atmospheric compensation experiments, in Majumdar et Ricklin [Majumdar-l-08], pp. 247–271.

[Wheelon-l-01] A. D. WHEELON, Electromagnetic Scintillation, vol. 1 of Geometrical Optics, Cambridge University Press, Cambridge, 2001.

[Wilson-p-05] S. WILSON, M. BRANDT-PEARCE, Q. CAO, ET M. BAEDKE, Optical repetition mimo transmission with multipulse ppm, Selected Areas in Communications, IEEE Journal on, 23(9):1901–1910, Sept. 2005.

[Wright-a-08] M. W. WRIGHT, J. ROBERTS, W. FARR, ET K. WILSON, Improved optical communications performance combining adaptive optics and pulse position modulation, Optical Engineering, 47(1), 2008.

[Wyngaard-a-71] J. WYNGAARD, Y. IZUMI, ET C. S.A., Behavior of the refractive-index-structure parameter near the ground, J. Opt. Soc. Am. A, 61:1946, 1971.

[Xiao-p-07] X. XIAO ET D. VOELZ, Toward optimizing partial spatially coherent beams for free space laser communications, vol. 6709, Proc. Soc. Photo-Opto. Instrum. Eng., 2007.

[Xu-a-09] F. XU, M.-A. KHALIGHI, P. CAUSSÉ, ET S. BOURENNANE, Channel coding and time-diversity for optical wireless links, Opt. Express, 17(2):872–887, January 2009.

[Xu-p-08] ——, Performance of coded time-diversity free-space optical links, June 2008.

[Xu-p-09] F. XU, M. KHALIGHI, ET S. BOURENNANE, Pulse position modulation for fso systems: Capacity and channel coding, in Telecommunications, 2009. ConTEL 2009. 10th International Conference on, June 2009, pp. 31–38.

[Yaglom-a-49] A. M. YAGLOM, On the local structure of the temperature field in a turbulent flow, Doklady Acad. Nauk. SSSR Ser. Geograf. Geofiz., p. 73, 1949.

[Yang-a-09] H. YANG, X. LI, C. GONG, ET W. JIANG, Restoration of turbulence-degraded extended object using the stochastic parallel gradient descent algorithm: numerical simulation, Opt. Express, 17(5):3052–3062, 2009.

[Young-p-07] D. W. YOUNG, J. E. SLUZ, J. C. JUAREZ, M. B. AIROLA, R. M. SOVA, H. HURT, M. NORTHCOTT, J. PHILLIPS, A. MCCLAREN, D. DRIVER, D. ABELSON, ET J. FOSHEE, Demonstration of high data rate wavelength division multiplexed transmission over a 150 km free space optical link, Oct. 2007, pp. 1–6.

[Yu-a-04] M. YU ET M. A. VORONTSOV, Compensation of distant phase-distorting layers. i. narrow-field-of-view adaptive receiver system, J. Opt. Soc. Am. A, 21:1645–1658, September 2004.

[Yu-p-03] M. YU ET M. A. VORONTSOV, Multi-conjugate adaptive optical systems based on decoupled stochasitic parallel gradient descent technique, in Conference on Lasers and Electro-Optics/Quantum Electronics and Laser Science, Opt. Soc Am., 2003.

[Yura-a-74] H. T. YURA, Physical model for strong optical-amplitude fluctuations in a turbulent medium, J. Opt. Soc. Am. A, 64(1):59–67, 1974.

[Zhao-p-08] Z. ZHAO, S. LYKE, ET M. ROGGEMANN, Adaptive optical communication through turbulent atmospheric channels, May 2008, pp. 5432–5436.

[Ziad-a-04] A. ZIAD, M. SCHÖCK, G. A. CHANAN, M. TROY, R. DEKANY, B. F. LANE, J. BORGNINO, ET F. MARTIN, Comparison of measurements of the outer scale of turbulence by three different techniques, Appl. Opt., 43(11):2316–2324, 2004.